

University of Nottingham
UK | CHINA | MALAYSIA

Molecular Simulations of Porous Solids for Adsorption Applications

Joseph Glover

Thesis submitted to the University of Nottingham
for the degree of Doctor of Philosophy

January 28, 2021

Declaration

I hereby declare that the research in this thesis is the result of my own work which has been undertaken during my period of registration for this degree at The University of Nottingham.

Joseph A Glover

Abstract

The separation of gaseous mixtures plays a significant role across environmental, commercial, medicinal and analytical applications. In recent years, the emergence of metal-organic and covalent-organic frameworks has created a lot of attention within the material science community due to the versatile and highly tunable range of attractive physical and chemical properties that they possess. Due to the exceptionally large design space of these materials, it is often infeasible to synthesise and test each new material. Therefore, the viability of these materials for gas storage and separation applications is often predicted from computational modelling tools that can accurately characterise and assess the performance from molecular models of the adsorbent and adsorbates. In this thesis, different computational tool kits are employed to accurately characterise the structural properties of these materials and design a high-throughput protocol that can efficiently screen thousands of materials for membrane-based separations. The results may ultimately help the future design of novel membranes by providing relationships between the best performing materials and their structural design.

Acknowledgements

Firstly, i would like to thank my supervisor Prof. Elena Besley who has supported me through the past five years that i have spent in her group during my Msci and PhD studies. Her guidance, enthusiasm and belief that she has in all of her students has allowed myself and the remaining members of her group to truly grow in to better researchers. I am also especially grateful for the opportunities to co-supervisor student projects that have been both enjoyable and excellent learning experiences.

Next, I would like to thank all of the collaborators that i have worked with during my time in Elena's group, including Prof. Schroder at the University of Manchester, Prof. Patane in Physics at the University of Nottingham, and also Dr. Hainam Do and his PhD students at the Ningbo campus in China. I'd also like to acknowledge the efforts of all those who manage the computational facilities here at the University of Nottingham, for which many of the calculations presented in this thesis were performed.

I am grateful for all the past and current members of the computational chemistry groups at the University of Nottingham who have made the past five years a memorable and pleasant experience. I hope to stay in touch with many of you as we progress along our own career paths.

Finally, i would like to acknowledge the support of my family and i am especially grateful for my girlfriend Zara McLaren. Thank you for the support, patience and encouragement that you have shown over the past 9 years that have helped me to progress to this stage of my life; i am eternally grateful.

Joseph Glover

28-01-2021

List of Publications

A list of publications and manuscripts in preparation is presented below for the work contained in this thesis:

- J. Glover and E. Besley, "Pore-filling contamination in metal–organic frameworks" *Phys. Chem. Chem. Phys.*, 2018, **20 (36)**, 23616 - 23624 [Chapter 3]
- J. Glover and E. Besley, "A High-Throughput Screening of Metal-Organic Framework Based Membranes for Biogas Upgrading" 2020, in preparation. [Chapter 4]
- J. Glover, A. Manley and E. Besley, "Evaluating the performance of COF Based Membranes for Biogas Upgrading", 2020, in preparation [Chapter 5]

Contents

Declaration i

Abstract i

Acknowledgements iii

List of Publications iv

1 Introduction 1

1.1 Adsorption 1

1.1.1 Physisorption Isotherms 3

1.2 Porous Materials 6

1.2.1 Zeolites 6

1.2.2 Metal-Organic Frameworks 8

1.2.3 Covalent-Organic Frameworks 13

1.3 Gas separations 16

1.3.1 Pressure swing adsorption 16

1.3.2 Membrane separations 17

1.3.3 Computational modelling 20

1.4 High-throughput calculations 21

1.4.1 Membrane screenings 24

1.4.2 Calculations at infinite dilution 25

1.5 Thesis objectives and outline 27

2 Computational Methods 29

2.1 Statistical Mechanics 29

2.1.1 Entropy 32

2.1.2 The Boltzmann Distribution 33

2.1.3 The Grand Canonical Ensemble 35
2.2 Monte Carlo methods 37
2.2.1 Trial move acceptance criteria 39
2.2.2 Cavity and Energy Biasing 40
2.2.3 Generating an adsorption isotherm 42
2.3 Molecular Dynamics 43
2.3.1 Simulation Algorithm 43
2.3.2 Diffusion coefficients 44
2.4 Force-fields 46
2.4.1 Lennard-Jones Interactions 47
2.4.2 Electrostatic Interactions 49
2.4.3 Periodic Boundary Conditions 52
2.5 Structural Characterisation 53
2.5.1 BET Surface Area 53
2.5.2 Geometric Surface Area 57
2.5.3 Pore volume and Void Fraction 58
2.5.4 Pore size distribution 59
2.5.5 Topological features 60
3 Pore-Filling Contamination in Metal-Organic Frameworks 62
3.1 Introduction 62
3.2 Methods for quantifying PFC in MOFs 68
3.2.1 Computational Details 68
3.2.2 PFC in **rht** and **nbo** MOFs 70
3.2.3 Phenyl-Alkyne substitutions 80
3.2.4 Conclusions 84
3.3 Analysing the PFC effect in small and large pores 86
3.3.1 Computational Details 87
3.3.2 Small pores: ($4.1\mathring{A} \leq d \leq 15.0\mathring{A}$) 87
3.3.3 Large pores: ($15.0\ \mathring{A} \leq d \leq 30.8\ \mathring{A}$) 94
3.3.4 Conclusions 100

4 A high-throughput screening of MOF-based membranes for biogas upgrading 102

4.1 Introduction . . . 102

4.2 Computational Details . . . 107

4.2.1 Force-Field Validation . . . 111

4.2.2 Main assumptions and limitations . . . 113

4.3 Results and discussion . . . 116

4.3.1 Accuracy in evaluation of partial charges on metal sites . 116

4.3.2 Permeability at infinite dilution . . . 118

4.3.3 Separations at working conditions . . . 124

4.3.4 Top candidates . . . 126

4.3.5 Comparison with literature membranes . . . 130

4.3.6 Structure-Performance relationships . . . 132

4.3.7 Applying Structure-Performance relationships . . . 136

4.4 Conclusions . . . 138

5 Evaluating COF-based membranes for biogas upgrading: A comparative study 140

5.1 Introduction . . . 140

5.2 Screening COF membranes for biogas upgrading . . . 143

5.2.1 Computational Details . . . 143

5.2.2 Separations at infinite dilution . . . 144

5.2.3 Working conditions . . . 149

5.2.4 MOF- and COF-based separation performance at working conditions . . . 153

5.2.5 Top COF candidates . . . 156

5.3 Investigating the impact of feed pressure . . . 161

5.3.1 Impact on adsorption behaviour . . . 163

5.3.2 Impact on transport behaviour and membrane performance . . . 166

5.4 Conclusions . . . 171

6 Summary, conclusions and future outlook **174**

6.1 Overview of chapter 3 175

6.2 Overview of chapter 4 176

6.3 Overview of chapter 5 179

A Chapter 3 Appendix **182**

A.1 Force-field parameters 182

A.2 BET fitting parameters 183

A.3 Method 1 and method 2 monolayer comparison 185

B Chapter 4 Appendix **187**

B.1 UFF parameters, oxidation states and adsorbate force-field parameters 187

B.2 Experimental membrane conditions 189

B.3 Qeq partial charge criteria assessment 190

B.4 Infinite dilution calculation assessment 193

Bibliography **195**

Chapter 1

Introduction

The work carried out in this thesis demonstrates how molecular simulations can be employed as powerful tools to characterise and identify top-performing porous solids for adsorption-based applications. In this chapter, an introduction to basic adsorption concepts, several classes of porous materials and gas separation techniques is presented alongside how they can be modelled. At the end of this chapter, the objectives of this thesis are summarised and a brief outline of the subsequent chapters is given.

1.1 Adsorption

Adsorption is a surface phenomenon that can be defined as the enrichment of one or more components in the region next to an interface.[1] In the context of this thesis, it can be understood as a process by which molecules from the gas phase (adsorbates) adhere to a solid surface (adsorbent). Adsorption processes can be categorised into chemical adsorption and physical adsorption. Chemical adsorption or chemisorption usually involves the formation of strong chemical bonds between the adsorbate and adsorbent. The process can involve dissociative or non-dissociative bonding, leading to high heats of adsorption (Q_{st}) of 40 - 200 kJ/mol.[2] As such, chemisorbed molecules are typically confined to specific reactive regions of the surface.[1] On the other hand, physical adsorption

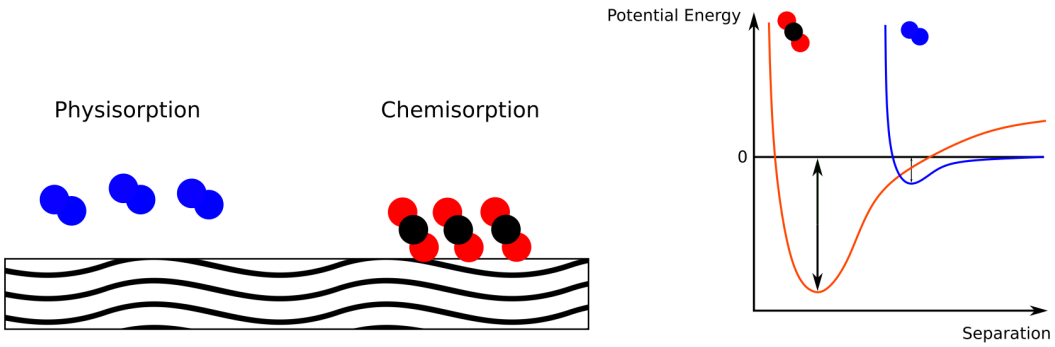


Figure 1.1: *Cartoon depicting the visual and energetic differences between chemisorption and physisorption.*

or physisorption is a much weaker phenomenon whereby adsorbates interact with the surface through intermolecular interactions such as dispersion, electrostatic interactions, hydrogen bonding and $\pi - \pi$ interactions.[1] As such, physisorption interactions are generally much weaker (Q_{st} of 10 - 40 kJ/mol), are highly reversible and have less specificity than chemisorption interactions. An example potential energy profile for both processes is shown in Figure 1.1. The attractive interactions between an adsorbate and adsorbent lead to an increased ordering of the adsorbates relative to the bulk gas, thus resulting in a decreased enthalpy and entropy - the relative balance of these two quantities dictates whether the adsorption process occurs spontaneously.

Gas adsorption has many applications from characterising adsorbent structural properties to describing the fundamentals of gas storage and separations. These are commonly performed using porous materials which are able to achieve much larger surface areas and adsorption capacities than non-porous surfaces. To differentiate between different porous materials, each structure can be categorised by the diameter, d, of its pores.[3] Micropores possess diameters in the range of 0 - 2 nm resulting in strong potential overlap between the adsorbate and each side of the pore. Mesopores possess diameters in the range of 2 - 50 nm and are often associated with adsorption hysteresis or capillary condensation. Capillary condensation is a phenomenon by which a gas under confinement condenses to a liquid-like phase below its saturation pressure (p^0) and is generally unique to mesopores as their pore diameters are of critical size

(not too small or large)[4]. Finally, macropores possess diameters greater than 50 nm and are often associated with layer-by-layer adsorption.

1.1.1 Physisorption Isotherms

Adsorption isotherms are often employed to understand a physisorption process between an adsorbate and a specific adsorbent. Adsorption isotherm models yield a function that describes the change in the adsorbed gas loading as a function of pressure or fugacity. It may also be presented as a function of relative pressure p/p^0.The curvature of an adsorption isotherm is dictated by the relative balance between the host-guest and guest-guest interaction strengths. Furthermore, the overall shape is an important feature that can provide a great deal of insight into the type of adsorbent and its structural features which impact the adsorption process. Physisorption isotherms can be classified into six types based on a number of recommendations from IUPAC (Figure 1.2).[5]

Type I isotherms display sharp and reversible gas uptake at relatively low pressures followed by a plateau in gas loading. These isotherms are typically observed for microporous materials which possess narrow pore diameters which enhance the host-guest interactions, leading to fast micropore filling at low pressure. The isotherm can be further categorised into type I(a) and type I(b) which depends on the pore-size distribution of the material; Type I(a) is usually observed for materials containing ultra-micropores ($d \leq 10$Å), while Type I(b) is usually observed for materials containing wider micropores or smaller mesopores ($10 \leq d \leq 25$Å).

Type II isotherms are observed for non-porous or macroporous materials where physisorption is described using a layer mechanism. The initial uptake of gas at low pressure corresponds to the formation of an adsorbed monolayer which quickly levels off and reduces to a gradual increase upon completion. This is often referred to as the 'knee' of the isotherm and its curvature often dictates the amount of overlap between monolayer coverage and multilayer

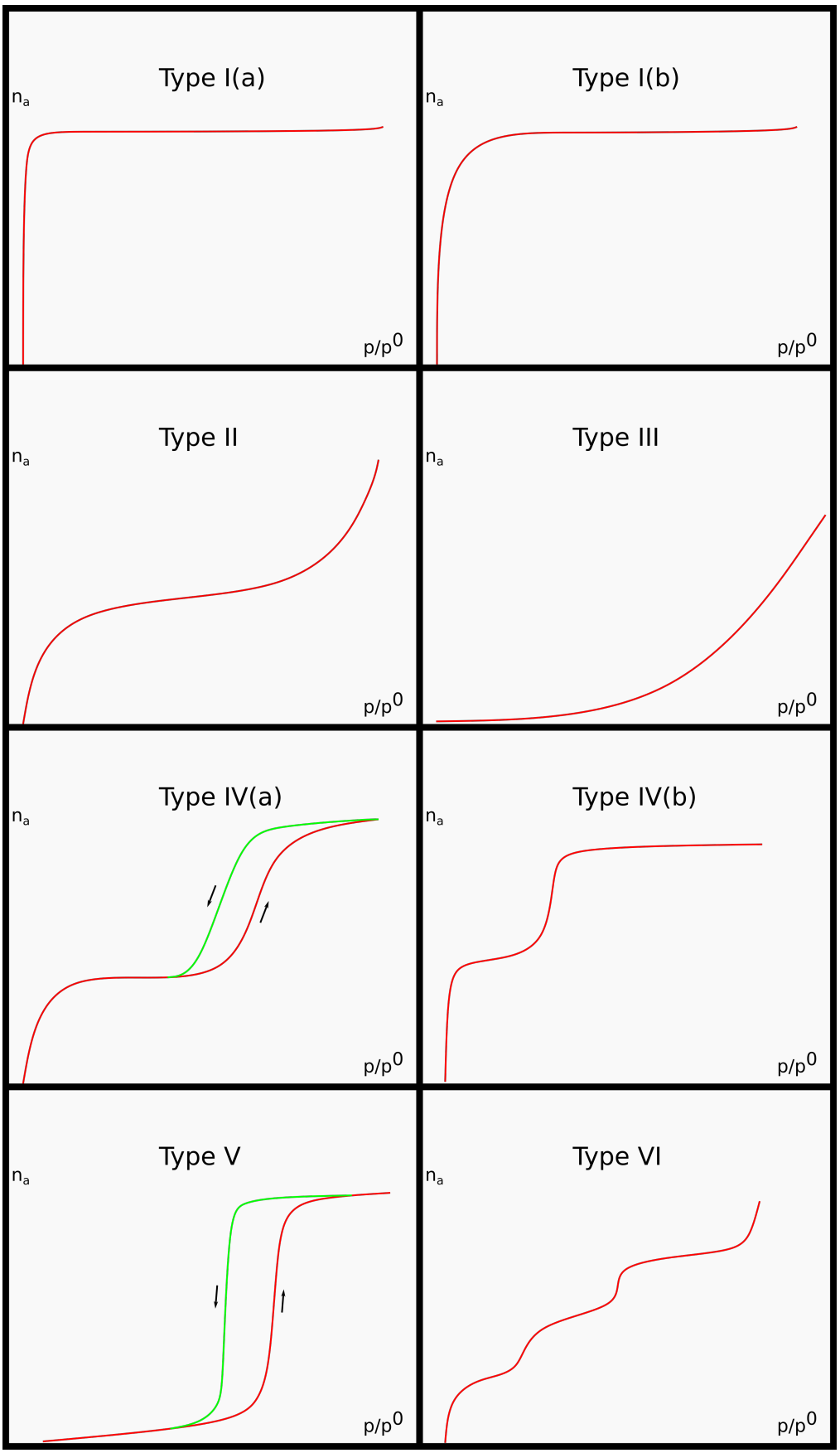


Figure 1.2: *IUPAC classification for physisorption isotherms.*

adsorption; a sharp curvature indicates a clear distinction between monolayer and multi layer adsorption, while a gradual increase indicates appreciable overlap.[5] As the pressure approaches p^0, the amount of adsorbed layers increases rapidly leading to the exponential shape observed on the isotherm.

Type III isotherms are observed for non-porous or macroporous materials and are relatively convex showing little gas uptake until higher pressures. Non-porous or macroporous materials possess relatively weak host-guest interactions that are unable to compete with the stronger guest-guest interactions, resulting in little to no surface coverage at low pressure. As the pressure is increased and some guests begin to adsorb, it becomes much easier for other guests to follow as a result of the strong guest-guest interactions, leading to larger uptakes at higher pressures. These isotherms are quite scarce but do exist for some host-guest systems such as iodine adsorption on silica gel.[6]

Type IV isotherms display many similar characteristics to the Type II isotherm but are typically observed for mesoporous adsorbents. Gas adsorption initially proceeds by monolayer-multilayer adsorption followed by capillary condensation which gives rise to a step on the isotherm at higher pressures. Capillary condensation may be accompanied with (type IV(a)) or without (type IV(b)) hysteresis depending on the mesopore width and temperature of the system. In addition, the shape of the hysteresis loop can change depending on the shape of the pores and also the pore connectivity. For example, ink-bottle shaped pores can be described by a series of wide pores that are connected to the surface through narrow channels. During desorption, the wide pores will remain filled until the narrower channels are emptied at a lower vapour pressure leading to wider hysteresis loop.[5]

Type V isotherms display many similar characteristics to the Type III isotherm but are accompanied by a capillary condensation hysteresis loop. This isotherm is typically observed for H_2O adsorption in hydrophobic adsorbents.[7]

Finally, Type VI isotherms display reversible and step-wise behaviour as a function of increasing pressure. This is typically observed for uniform

non-porous adsorbents in which adsorption occurs through a layer-by-layer mechanism.

1.2 Porous Materials

In this thesis, there are three main classes of porous material that will be encountered - zeolites, metal-organic frameworks and covalent-organic frameworks.

1.2.1 Zeolites

Zeolites are a class of crystalline, aluminosilicate materials containing well defined porous cavities and channels. These materials are formed from TO_4 tetrahedral building blocks, where T is a silicon or aluminium atom and each tetrahedron is linked together by sharing their oxygen atoms. The composition of a zeolite is generally expressed using the following formula:[8]

$$M^{n+}_{y/n}[(SiO_2)_x] \cdot (AlO^-_2)_y] \cdot zH_2O \tag{1.1}$$

where M is a cation with a charge $n+$, x and y are the number of silicon and aluminium tetrahedra respectively, and x/y is the Si/Al ratio. The fact that aluminium and silicon atoms both form tetrahedral building blocks means they can be readily replaced by one another; therefore, many zeolites can be synthesised with varying elemental compositions and Si/Al ratios. Almost all zeolite structures obey Löwenstein's rule which states that the formation of -Al-O-Al- linkages are unfavourable;[9] this implies that the Si/Al ratio of a zeolite shall be greater or equal to 1. The amount of aluminium in the zeolite can impact several properties including the unit cell dimensions, hydrophilicity, cation-exchange capacity, density and strength of Brønsted acid sites, and thermal stability.

Due to the net negative charge of the framework introduced by replac-

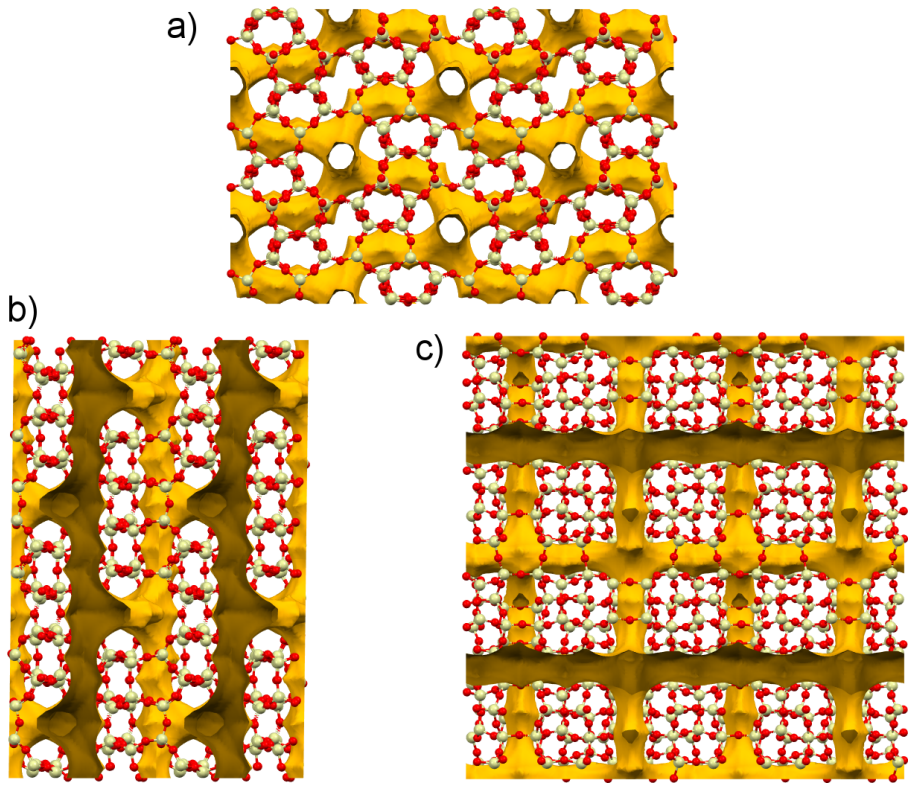


Figure 1.3: *2x2x2 supercell of ZSM-5 along the a, b and c axes. The void space forms a network of microporous channels that are visualised in yellow. Atom colour scheme: Red = O, Gold = Si*

ing a Si atom with an Al atom, the pore cavities of these materials are often occupied by charge balancing protons and water molecules. They may also be exchanged with other ions such as alkali or transition metals, which introduce new basic and redox active sites. Charge balancing protons can often initiate cracking and isomerisation reactions of alkanes that diffuse into the pore cavities of zeolites.[10,11] Furthermore, the pores of a zeolite provide shape and size selectivity for these reactions which has resulted in their widespread employment in the petrochemical industry as heterogeneous catalysts. For example, ZSM-5 is a microporous zeolite containing uni-dimensional pores that are constructed from pentasil units (Figure 1.3). These units link together to form a straight and sinusoidal series of intersecting ten-membered-ring pores of approximately 5.1 - 5.6 Å in diameter. ZSM-5 shows exceptional thermal stability up to temperatures of 1200 K and can be synthesised with high silicon content (Si/Al $\geq$ 10). This material was first patented by Mobil Oil in 1975 and has since been widely employed for hydrocarbon isomerisation reactions.[12]

The synthesis of new zeolite structures is a very important area of research and today, there are over 240 zeolite framework types that have been documented in the international zeolite association (IZA) database.[13]

1.2.2 Metal-Organic Frameworks

Metal-organic frameworks (MOFs) are a relatively new class of hybrid materials constructed from metal ions clusters (known as secondary building units (SBUs)) that are coordinated together by polydentate organic ligands. These typically form a series of periodic, 3-D crystalline frameworks that can achieve ultra-high surface areas and porosities[14]. Unlike traditional nanoporous materials such as zeolites, there is a wider variety of building blocks to choose from when developing new MOFs[15]. Therefore, a greater range of pore architectures, pore sizes and porosities can be achieved through judicious selection of the inorganic and organic building blocks, providing a more rational approach to design[16–18]. Figure 1.4 displays the crystal structure of MOF-5 - one of the most studied MOFs in the literature. This MOF consists of octahedral Zn_4O SBUs which are coordinated by terephthalate ligands to afford a cubic framework topology. By increasing the length and functionality of the organic ligands, Yaghi and co-workers were able to systematically increase the framework density, surface area and pore volume of the MOFs in small increments, creating an isoreticular series.[17] With such a wide variety of inorganic and organic moieties, it is hypothetically possible to design a near-infinite number of MOF structures. The structure and properties of a MOF can be further tailored towards applications of interest using post-synthetic modification (PSM) techniques, including ligand or metal exchanges and tandem PSM reactions which introduce multiple functionalities that may have been previously infeasible to incorporate through direct synthesis.[19,20]. As such, MOFs have been extensively studied for a wide array of applications including gas storage,[21] separation,[22] drug delivery,[23] catalysis,[24] and sensing.[25]

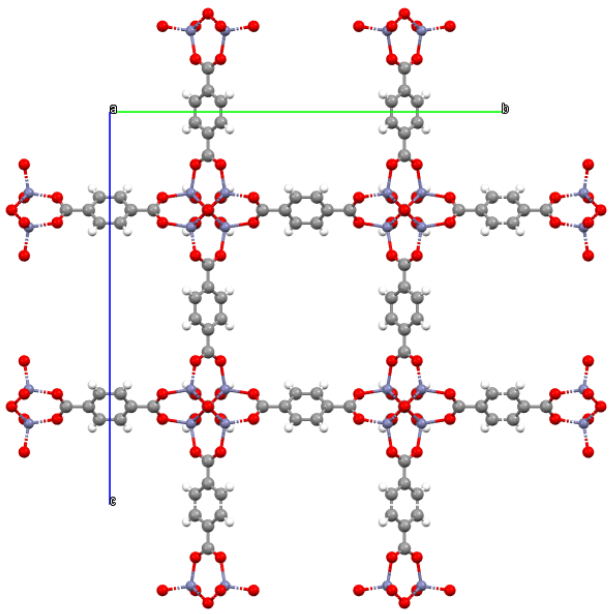


Figure 1.4: *Unit cell of MOF-5 viewed along the 'a' axis. Atom colour scheme: Red = O, Grey = C, White = H, Purple = Zn*

MOFs can be synthesised using a range of synthetic routes including solvothermal, microwave-assisted, electrochemical, mechanochemical, sonochemical, spray drying and flow chemistry setups.[26] To generate the permanent porosity of a newly synthesised MOF, any adsorbed solvent molecules must be evacuated from the pores in a process known as activation. In its simplest form this process involves a heating and vacuum treatment, however, for solvents that contain high boiling points (HBP), this process can be relatively challenging as significant surface tension may be generated leading to the loss of structural integrity.[27] One strategy to combat this problem is to submerge the sample in a bath containing a solvent with a lower boiling point (LBP). As LBP solvents have relatively weaker intermolecular forces than HBP solvents, they reduce the overall surface tension and capillary forces generated upon activation. Therefore, soaking the sample in another solvent can allow a solvent exchange to occur which can then be treated with a conventional heating and vacuum treatment. An alternative method is to exchange the solvent with liquid CO_2 which is subsequently turned into supercritical (sc) CO_2 and vented from the MOF, thus avoiding the liquid-to-gas phase transition that is

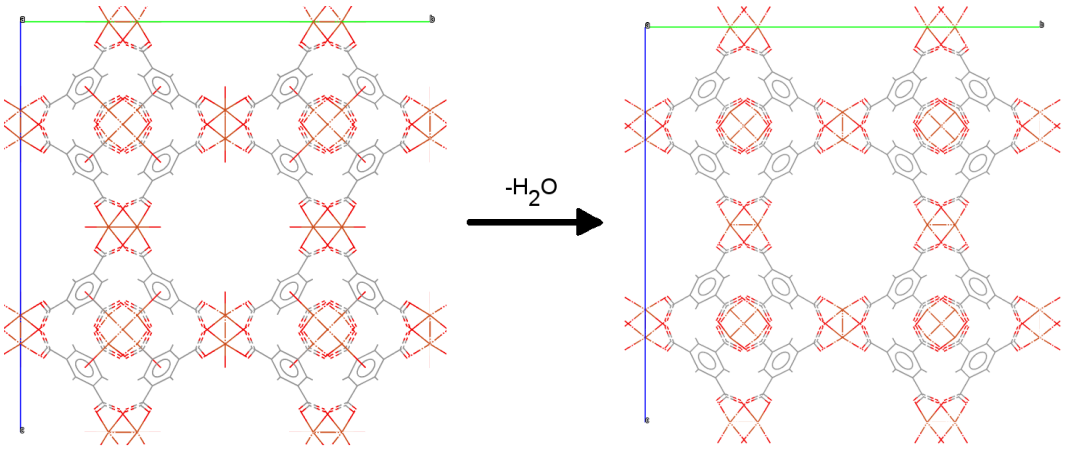


Figure 1.5: *Activation of HKUST-1 leading to the generation of two open metal sites per Cu(II) paddle-wheel SBU.*

associated with the generation of capillary force.[27]

Some SBUs allow guest solvent molecules to occupy coordination sites around their metal centres which upon activation, yield coordinately unsaturated sites (CUS) or open metal sites. HKUST-1 is constructed from trimesic acid (benzene-1,3,5-tricarboxylic acid) ligands that coordinate to Cu(II) ions forming a dicopper-tetracarboxylate paddle-wheel SBU.[28] The structure of HKUST-1 contains a series of small tetrahedral-shaped pores that surround a larger set of cuboctahedral-shaped pores. The cuboctahedral-shaped pores can be further classified into one of two types based on the alignment of the paddlewheel units in which the Cu-Cu axis points to the centre of the pore or aligns perpendicular. Each copper ion is occupied by a terminal axial water molecule that points towards the interior of the nanopores which can be removed upon thermal activation to yield two open metal sites per SBU. MOFs containing CUS have beneficial value in gas storage, separation and catalytic applications, where the CUS can act as potential binding sites for adsorbing guest species. The was demonstrated by Peterson et al. using in-situ neutron powder diffraction (NPD) when studying hydrogen binding sites in HKUST-1 from D_2 adsorption.[29] A total of six sites were identified, which are primarily located above the CUS with a Cu-D_2 distance of 2.39 Å, suggesting significant interaction between D_2 and the Cu(II) cations. Similar results have been

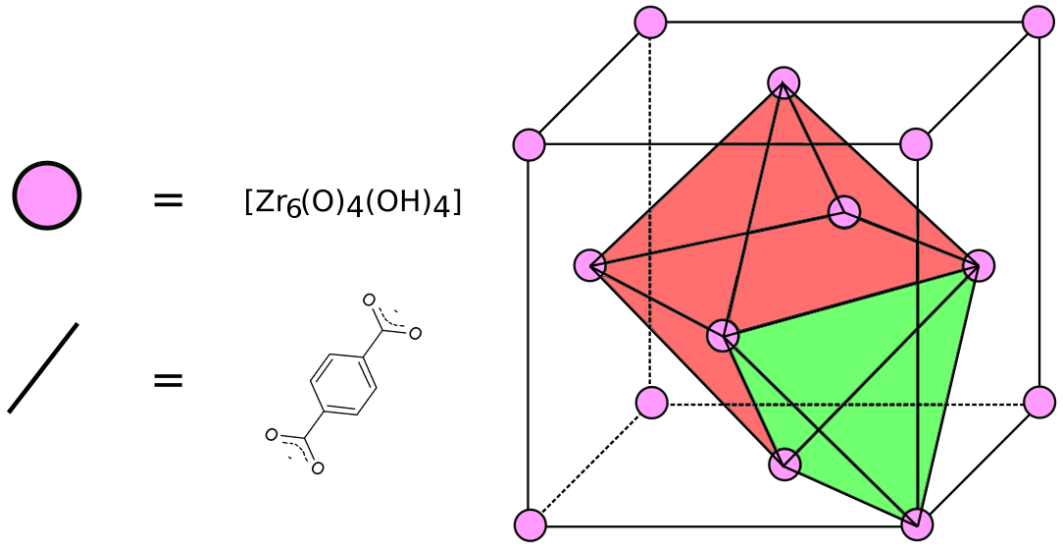


Figure 1.6: *The FCC UiO-66 unit cell depicting the small tetrahedral pores (green) and large octahedral pores (red).*

observed for several other molecules including CH_4, CO_2, alcohols, THF, and MeCN.[30–32]

In many MOFs, the presence of weak coordination bonds between the organic linkers and SBUs can be easily hydrolysed and displaced by water molecules that bind to reactive inorganic entities within the framework[33]. By choosing more sterically hindered and inert SBUs, it is possible to form robust frameworks that can retain their porosity even in the most humid conditions. Such a crucial property is needed for MOFs to be commercially viable, as without it, the long-term usage of MOFs becomes severely limited. One such example is UiO-66 - a MOF created from 12-coordinate $Zr_6O_4(OH)_4$ SBUs that are linked together by terephthalate ligands affording a 3-D network containing tetrahedral- and octahedral-shaped pores with diameters of approximately 8 and 11 Å respectively (Figure 1.6).[34,35] Due to the high connectivity of the network topology, this MOF is thermally stable up to 800 K, resistant to hydrolysis and able to retain its crystallinity under pressures of 10,000 kg/cm^2.

While most MOFs are characterised by their structural rigidity, there exists a class of MOFs which possess highly dynamical structural features or flexible frameworks in response to external stimuli such as heat, pressure, guest

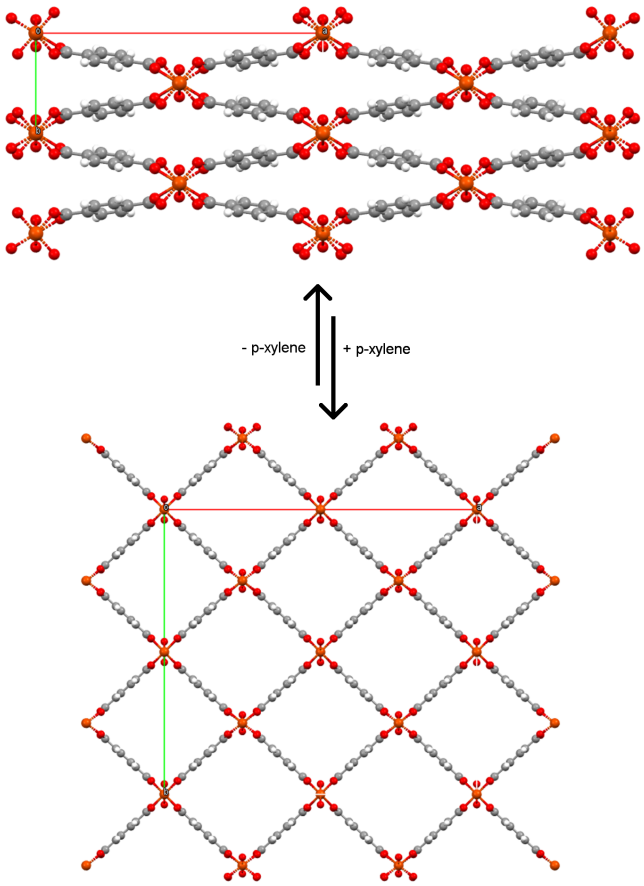


Figure 1.7: *Example of the 'breathing' effect in Mil-53(Fe) upon adsorption of p-xylene (guests removed from unit cell for clarity). Atom colour scheme: Red = O, Grey = C, White = H, Orange = Fe*

adsorption and light. The degree of structural flexibility can range from small local vibrations to large phase transitions such as swelling, "breathing" and "gate-opening" effects.[36–38] An archetypal example of the breathing effect is observed in the MIL-53 MOF series, pioneered by Férey and co-workers; these contain a series of 1-D chains of transition metals (e.g. Al, Ga, In, Fe, V, Cr and Sc) that are bridged together by μ-OH moieties and carboxylate ligands, affording a series of diamond shaped channels in a wine rack-shaped topology. Upon thermal activation; adsorption of small molecules; or application of pressure, these MOFs undergo a reversible transition between closed and open phases where the porosity, unit cell length and angles drastically change (Figure 1.7).[39] In the case of adsorption, these transitions can be observed on the adsorption isotherm by sharp inflections and hysteresis.[36]

1.2.3 Covalent-Organic Frameworks

In 2005, a new class of porous, crystalline materials known as covalent-organic frameworks (COFs) were introduced for the first time. These are comprised of extended organic structures that are linked together by strong covalent bonds, thus displaying excellent thermal and chemical stability across a wide range of conditions.[40] The pore geometry, size, structural properties and functional design of a COF are controlled through the choice of building blocks. Moreover, the structure of each COF can be predicted from topology diagrams which indicate the direction of covalent bond formation from the symmetry and planarity of the chosen building blocks. The wide diversity of organic building blocks and the facile approaches to introduce new pore functionalities has resulted in the extensive study of employing COFs as platforms for catalysis, gas storage, separation and as semi-conductors.[41–43]

The synthesis of ordered and crystalline organic structures relies on dy-

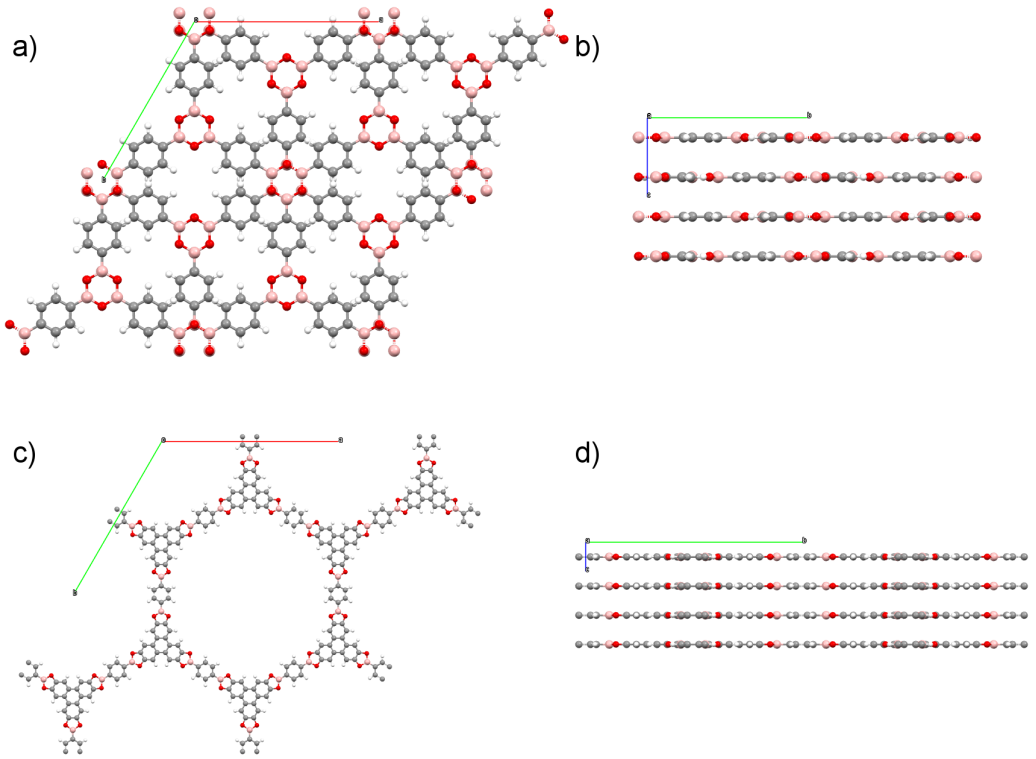


Figure 1.8: *Unit cells of COF-1 (a,b) and COF-5 (c,d) which demonstrate a staggered (AB) and eclipsed (AA) stacking pattern. Atom colour scheme: Red = O, Grey = C, White = H, Pink = B*

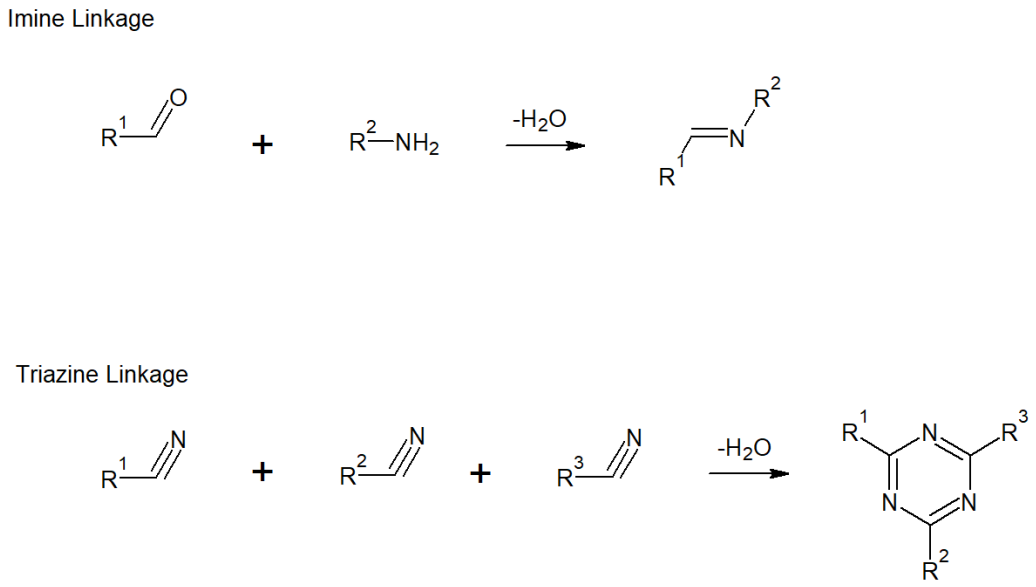


Figure 1.9: *Examples of imine and triazine linkages.*

namic covalent chemistry (DCC)[44] or reversible covalent bond formation. Based on the spatial arrangement of each building block and the intermediates that they form, a number of different products may be attained. Kinetic products such as amorphous polymers generally dominate the initial product distribution due to their low activation barriers and highly favourable entropic contributions.[45] By optimising the synthesis conditions, the reversibility of their covalent bond formation provides a self-healing characteristic that can shift the equilibrium towards the formation of thermodynamically stable products, which often are more ordered and contain crystalline arrays of building blocks.[44]

The use of rigid, planar building blocks restricts framework growth into 2-dimensions, thus forming a series of 2-D conjugated layers. These layers are able to stack on top of one another in an arrangement that maximises attractive forces while minimising repulsion. COF-1 is the earliest example of a 2-D COF that can be formed under solvothermal conditions from diboronic acid precursors.[40] These converge into a 2-D microporous network of boroxine rings (B_3O_3) forming an analogous structure to graphite where each C atom is replaced with a boroxine unit and each C - C bond by a phenyl ring (Figure

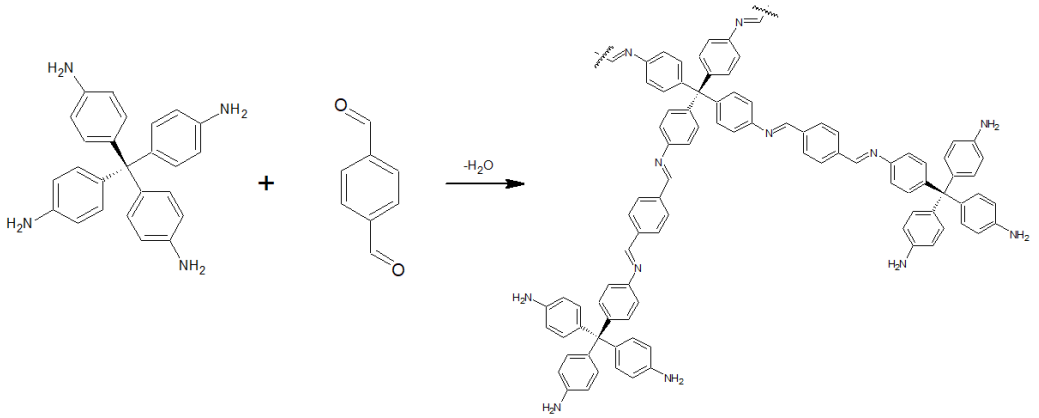


Figure 1.10: *Schematic depicting the condensation reaction of tetra-(4-anilyl)-methane and terephthaldehyde to afford COF-300.*

1.8). In this COF the layers stack in a staggered arrangement which limits the porosity of the material and restricts guest diffusion along the 'z' axis. However, by adding hexahydroxy-triphenylene to the diboronic acid precursors, the larger COF-5 structure can be formed which displays an eclipsed stacking arrangement with 1-D hexagonal channels along the 'z' axis (Figure 1.8).[40] In comparison to COF-1, COF-5 contains a larger number of $\pi - \pi$ interactions which favour the eclipsed stacking pattern. One of the main disadvantages of boron-based COFs is that their linkages may be hydrolysed in the presence of water vapour. Thus in recent years, new classes of porous COFs employing imine and triazine linkages has been synthesised leading to a diverse range of structures with enhanced stability (Figure 1.9).[46]

The use of tetrahedral or orthogonal building blocks directs the growth of the framework in all 3-dimensions leading to 3-D COFs. For example, the imine condensation reaction between tetra-(4-anilyl)-methane and terephthaldehyde affords the COF-300 structure, containing a **dia** topology.[47] Due to the large size of the bis-imine linkages, this COF undergoes five-fold interpenetration which reduces the pore size down to 7.2 Å. Despite advances in the synthesis of 3-D COFs, progress and reports of new structures are extremely limited in comparison to research on 2-D COFs. This arises from a number of reasons: (1) 3-D COFs have a much smaller diversity of building blocks and framework topologies than 2-D COFs; (2) 3-D COFs possess significant crystallisation

problems and the influence of kinetic and thermodynamic factors in their synthesis remain poorly understood; (3) 3-D COFs are typically less stable than 2-D COFs due to higher porosities and the absence of $\pi - \pi$ stacking.[48]

1.3 Gas separations

Gas separations play a significant role in several environmental and industrial applications.[49] For example, increases in atmospheric CO_2 emissions have urged the development of materials that can selectively remove CO_2 from flue gas mixtures. In the petroleum industry, olefin, paraffin, aliphatic and xylene separations are of high importance for generating chemical feedstocks. The separation of air provides O_2 and N_2 products that are used in many medical applications and chemical reactions such as the Haber process. Many noble gases are important in lighting and biomedical applications, but occur naturally in mixtures with other gases.[49–51] As an alternative to expensive and energy intensive distillation methods, research into the application of porous materials has led to the development of many adsorption-based technologies such as pressure swing adsorption (PSA) and membrane-based separations.

1.3.1 Pressure swing adsorption

PSA is a well-established gas separation technique that was first patented in the 1960s.[52] In this technique, the adsorbent is packed into a fixed bed and a gas mixture is streamed across it under ambient temperature. Depending on the molecular characteristics of each component, some may have strong affinity for the adsorbent and stick to its surface, while those with weaker affinities will pass over the bed.[53] To regenerate the adsorbent, the adsorbed phase must be desorbed by changing one of the conditions that leads to equilibrium; In a PSA process, this involves reducing the pressure of the system from high to low. Once regenerated, the system can be 'swung' back to a high pressure state in order to cycle the separation process. It is therefore crucial to select

an adsorbent that can be rapidly regenerated and that possesses large working capacities ΔN. Working capacity can be defined as the difference in adsorbate loading between the high and low pressure states of a PSA cycle. Materials with steep gas uptakes at low pressures may require vacuum conditions to regenerate the adsorption bed which can rapidly increase the power consumption of the PSA unit.[53] However, this also means that the high pressure part of the cycle can be conducted at ambient pressures which is essential in CO_2 capture from flue gas[54] and portable oxygen concentrators that perform O_2/N_2 separations from air.[55]

The adsorption selectivity $S_{i/j}$ of component i over component j is expressed as a function of the equilibrium gas phase pressure P, temperature T, and mole fraction y_i of component i:

$$S_{i/j} = \frac{ci}{y_j} \times \frac{y_i}{c_j} \tag{1.2}$$

where c_x represents the adsorbed concentration of component x under equilibrium conditions.

1.3.2 Membrane separations

Membrane separations offer a cheap and efficient alternative to traditional separation techniques such as cryogenic distillation, PSA and liquid absorption.[56] In these separations, a feed gas containing a mixture of adsorbates is driven through a membrane using a differential pressure gradient. The feed gas is separated into permeate and retentate phases by exploiting differences in physical properties or membrane-guest interactions of its components. The permeate phase corresponds to the component of the feed gas that passes through the membrane, while the retentate is the component adsorbed and retained by the membrane (Figure 1.11)

The overall separation performance of this process is governed by the permeability of each component and the selectivity of the membrane. The

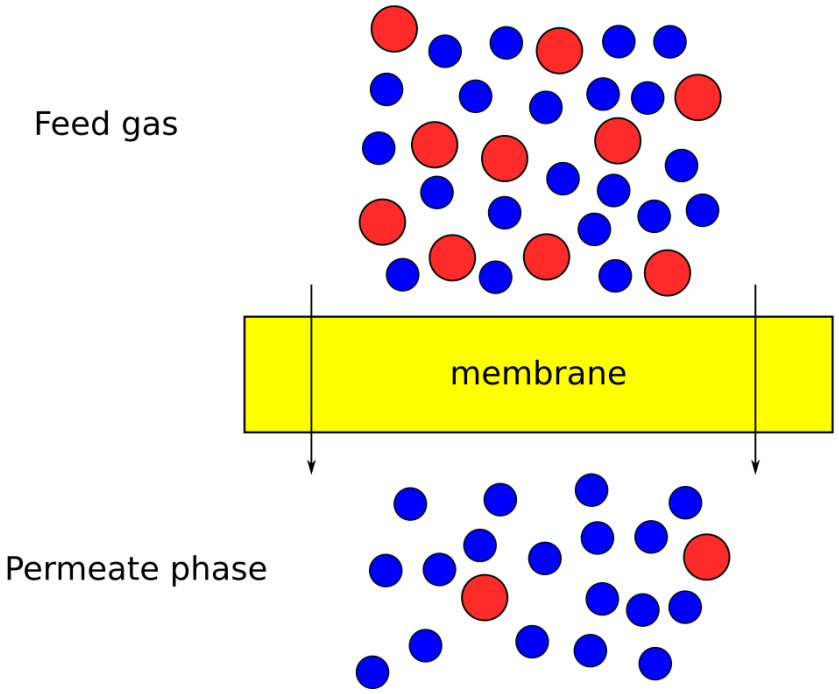


Figure 1.11: *Illustration of a membrane separation*

permeability describes how quickly a gas component passes through a membrane; it depends on the membrane's affinity for the gas component and the rate of which it diffuses through the pores. The selectivity is a measure of a membrane's relative affinity for one component over another. Membranes that simultaneously possess high selectivity and permeabilities are highly desirable. As such, the choice of material used to synthesise the membrane plays an important role.

Membranes can be synthesised from various materials, including organic polymers, molecular sieves, palladium alloys, amorphous silicas, ceramics and zeolites.[56] Polymer-based membranes currently dominate the membrane market as they are cheap, easily scalable, can be fabricated into hollow fibres or sheets and have been more extensively studied. However, they suffer from short lifetimes, low thermal and chemical stability, and low selectivity.[57] Furthermore, Robeson revealed that polymer membranes possess a trade-off relationship between the guest selectivity and guest permeability which limits their overall separation performance (i.e. polymers with high selectivity tend to possess low permeability and vice-versa).[58,59] After plotting a large amount

of experimental data for various small gas separations, Robeson observed that this relationship establishes an an upper bound that describes a boundary to the overall performance of these materials.[58,59] To overcome the stability and trade-off limitations of polymer membranes, the development of inorganic membranes using carbonaceous, silica-based or zeolitic materials has proven valuable. These materials typically possess much larger permeabilities and selectivities and can be used in much harsher conditions.[60] In addition to these, MOFs have received much attention due to their tunable structural properties, making them a versatile and highly competitive choice for a range of gas separations. However, many of these are fragile and suffer from poor mechanical properties which increases their processing costs.[56,61] More recently, approaches to combine the high permeability and selectivity of inorganic membranes with the processability of polymer membranes has been achieved by dispersing inorganic materials into polymer matrices, known as mixed matrix membranes (MMMs).[62]

Experimental studies of porous membranes typically report single component permeabilities for different gases which can be employed to determine its ideal separation performance. The permeability of gas species i, can be defined as:

$$P_i = \frac{N_i}{\Delta p L} \tag{1.3}$$

where N_i is the molar flux of species i as described by Fick's law[63] (equation 2.28), Δp is the pressure drop across the membrane and L is the membrane thickness. The ideal membrane selectivity of component i over component j is then expressed as the ratio of their permeabilities:[63]

$$S_{mem,i/j} = \frac{P_i}{P_j} \tag{1.4}$$

Although ideal calculations provide some estimates of the separation performance, it is well understood that the adsorption and diffusion properties in mixtures can be very different to their single-component behaviour.[64] As such,

it is necessary to determine multi-component adsorption isotherms and use a theoretical framework that can accurately describe mixture diffusion and correlation effects between different species.[62]

1.3.3 Computational modelling

A complete understanding of the fundamental interactions that control a separation process is often critical for the effective design of new adsorbents. With the advances of technology during the 21st century, computational modelling has become a ubiquitous and powerful tool across material science that provides a wide array of applications: from structural characterisation to providing microscopic insights of different processes that are generally challenging or near impossible to extract from using experimental methods. For example, the difficulties with measuring mixed-gas adsorption equilibria often results in the reliance on theoretical methods such as ideal adsorbed solution theory (IAST).[65] This method predicts the mixed-gas equilibria using only single-component adsorption isotherms, but often fails to accurately predict for gas mixtures containing components with large differences in their molecular size, polarity, or strength of host-guest interactions.[66] In these scenarios, molecular simulations can provide a platform to study such mixtures across any composition, temperature and pressure of choice while avoiding the heavy costs and safety concerns that are accompanied with experimental work. By varying each of the simulation parameters, a systematic study of their impact on the adsorption process can be employed. Molecular simulations can also be viewed as a hypothetical sandbox of sorts in which the user can augment the physics of reality by adjusting or completely removing specific intermolecular interactions - providing insight into their importance. Furthermore, hypothetical structures can be designed *in silico* and studied using molecular simulations to provide new predictive insights into their potential application.[67] The predictions made by any simulation are only as accurate as the underlying models -

Therefore, it is essential that these are able to capture the chemical and physical characteristics of the system. Many porous material models are typically generated from experimental methods including single-crystal x-ray diffraction (SCXRD) that can be used to provide an atomistic representation of crystalline materials.

1.4 High-throughput calculations

For many adsorption-based applications, finding a top performing candidate is a challenging task due to the large number of individual porous structures that exist or can be designed. Over the past decade, improvements in computational power have meant that large-scale screenings which efficiently determine the gas adsorption properties of a diverse set of materials can now be routinely performed. One of the most exciting prospects of high-throughput simulations (HTS) is that they can uncover structure-performance relationships on a vast scale that cannot be practically determined from experimental synthesis. For example, Bobbitt, Chen and Snurr performed a HTS to identify suitable candidates for cryogenic H_2 storage applications.[68] From 29,807 high-performing MOFs, the authors reported a number of optimal structure properties that maximised the ΔN_{H_2}. These included an optimal void fraction (VF) and volumetric surface area of 0.9 and 2000 m^2 cm^{-3} respectively, and an optimal pore size range from 12 to 15 Å. At higher pore sizes, the centre of the pore was found to be less saturated leading to inefficiencies in gas uptake. Finally, isosteric heats of adsorption (Q_{st}) values between 2.0 and 4.0 kJ/mol were found to be optimal for maximising ΔN_{H_2}.

In early screening studies, a diverse set of structures could be obtained by selecting well known materials in the literature. For example, Wu et al. performed two separate screenings for CH_4/H_2 and CO_2/N_2 separations using 105 MOFs, including IRMOFs, Cu-BTC, MILs, Zeolitic imidazolate frameworks (ZIFs), and some newly synthesized structures.[69,70]. Dubbeldam et al.

Table 1.1: Examples of structural databases for different real and hypothetical porous materials

Type	Number of Structures[(a)]	Notes/Alternative name	ref
Zeolites	2,000	Hypothetical Zeolites	72,73
	600,000		74
	2,700,000		75
	2,700,000		76
MOFs	5,109	CoRE-MOF 2014	77
	137,593	Northwestern hypotheticals	78
	116	MOF-5 analogues	79
	22,700	UM MOFs	80
	18,383	Mg MOFs	81
	13,512	ToBaCCo MOFs	82,83
	69,666	CSD MOF Subset	84
	14,142	CoRE-MOF 2019	85
COFs	4,147	3D porous COFs	86
	69,840	2D and 3D COFs	87
	319	CoRE COFs	88

(a) Number of structures in database upon publication

screened over 100 nanoporous adsorbents, including zeolites, MOFs, COFs, ZIFs and carbonaceous materials for separations of alkane mixtures.[71] As the number of experimentally synthesised structures increased, the opportunity to screen much large datasets presented itself. However, these relied on developing automation processes that could identify and select these materials out of experimental databases that contain hundreds of thousands of crystal structures. In recent years, a number of groups have performed data-mining exercises to identify porous materials and populate them in specific "computationally-ready" databases for use in HTS (Table 1.1).

These materials can then be analysed with the ultimate goal of discovering promising candidates that can be further validated in laboratory experiments. For example, Moghadam *et al.* recently screened over 82,000 compounds in

the MOF subset of the Cambridge Structural Database (CSD) for O_2 storage applications.[89] In this work, room-temperature single-component GCMC simulations were performed at 5 and 140 bar, corresponding to the desorption and adsorption pressures. From the analysis of the volumetric and gravimetric O_2 capacities, the authors identified UMCM-152,[90] a MOF which delivers 22.5% more O_2 than the record holding material (NU-125).[91] The MOF was then synthesised and the measured O_2 adsorption isotherms were in excellent agreement with those predicted from GCMC simulations.

Many of the databases shown in Table 1.1 have been generated by employing simulated annealing or *in silico* design principles to generate libraries of hypothetical zeolites, MOFs and COFs. These hypothetical materials can improve the overall understanding of structure-performance relationships and identify potential candidates that do not exist in the literature, inspiring their synthesis and providing new design ideas for future materials. For example, Wilmer *et al.* developed a database containing 137,953 hypothetical MOF structures from a diverse library of ligand and metal building blocks that were combined according to applied geometric rules.[78] The database was screened using GCMC simulations to calculate the CH_4 storage capacity at 35 bar and 298 K over three stages: (1) all 137,953 were screened in a short simulation to identify the top 7000 MOFs, (2) these 7000 MOFs were screened in a longer simulation to identify the top 350 MOFs, (3) the remaining 350 MOFs were then screened in a long simulation. In the 3rd stage of calculations, the top 300 MOFs were found to possess volumetric uptakes that were greater than the world-record holder, PCN-14. Furthermore, 75% of the top candidates (volumetric uptake ≥ 205 cm^3 cm^{-3}) were found to contain methyl, ethyl, or propyl functional groups. In the final stages of their study, the authors identified an isostructural derivative of PCN-14 with methyl functionalised linkers that had recently been reported as MOF NOTT-107 by Lin and co-workers.[18] Wilmer et al. synthesised NOTT-107 and their measured CH_4 adsorption isotherms were in good agreement with their simulations, validating the predictions of

their screening.

1.4.1 Membrane screenings

In order to evaluate the separation performance of different porous membranes, it is important to employ efficient methods that can rapidly estimate the permeability and selectivity. In previous work, Krishna and van Baten employed the Maxwell-Stefan formalism to estimate the particle fluxes and membrane selectivity $S_{perm,i/j}$ of CO_2 and CH_4 across 12 zeolite membranes.[92] By assuming that the permeate side of a membrane is under vacuum conditions such that the downstream molecular loadings are negligibly small, Krishna and van Baten showed that for an equimolar mixture of components i and j, $S_{perm,i/j}$ can be approximated using the following equation:[92,93]

$$S_{mem,i/j} = S_{ads,i/j} \times S_{diff,i/j} = \frac{c_i}{c_j} \times \frac{D_i^{self}}{D_j^{self}} \tag{1.5}$$

where $S_{ads,i/j}$ and $S_{diff,i/j}$ are the adsorption and diffusion selectivities, respectively. $S_{ads,i/j}$ is calculated from the ratio of the equilibrium molar adsorbate loadings of each species at the feed side of the membrane. $S_{diff,i/j}$ is calculated from the ratio of the mixture self-diffusion coefficient values D^{self} - described in section 2.3.2. In addition to $S_{perm,i/j}$, they derived an expression for the permeability of each species:

$$P_i = \phi D_i^{self} \frac{c_i}{f_i} \tag{1.6}$$

where ϕ is a materials void fraction and P_i, D_i^{self}, c_i and f_i are the permeability, mixture self-diffusion coefficient, equilibrium gas loading and bulk phase partial fugacity of component i. In a later study, Keskin and Sholl modified these expressions to account for mixtures of arbitrary molar ratios:[94]

$$S_{mem,i/j} = \frac{c_i y_j}{y_i c_j} \times \frac{D_i^{self}}{D_j^{self}} \tag{1.7}$$

where y_i and y_j are the mole fractions of species i and j. Keskin and Sholl validated this approximative method by comparing their predictions of $S_{perm,i/j}$ for CO_2/CH_4, CH_4/H_2, and CO_2/H_2 mixtures in IRMOF-1 and CuBTC membranes, with previous work which employs more detailed calculations that evaluate mixture-adsorption isotherms and transport diffusion coefficients across various gas concentrations. While the approximative method accurately predicts membrane permeabilities for most mixtures, poor agreement was observed for CO_2/H_2 mixtures in CuBTC. In general, the approximative method is anticipated to perform better for systems where IAST can accurately predict the isotherm of the binary mixture. If this is not the case, a more rigorous set of detailed calculations are required to study the permeation process, including the evaluation of mixture transport diffusivities across several gas loadings. Over the past decade, the approximative methods of Krishna, van Baten, Keskin and Sholl have been employed to study various gas separations in both MOF,[95–106] and COF[88,107] membranes. In one example, Erucar and Keskin examined CH_4/H_2 separations in 173 MOFs from the CoRE MOF database.[95] In all 172 MOF membranes, the $S_{perm,CH_4/H_2}$ values are found to be lower than the $S_{ads,CH_4/H_2}$ values. This is because each MOF interacts with CH_4 more strongly than H_2, leading to high $S_{ads,CH_4/H_2}$. However, as H_2 is smaller, lighter and interacts weaker with the MOFs than CH_4, it can rapidly diffuse through the pores, leading to large $S_{diff,CH_4/H_2}$ values between 0.007 and 0.81 that favour H_2. The top 10 CH_4 selective candidates were identified as those possessing the highest $S_{perm,CH_4/H_2}$, ranging between 22 and 130. Some of these materials possess 1D pores which strongly confine the CH_4 molecules, leading to very high $S_{ads,CH_4/H_2}$ values up to 160.

1.4.2 Calculations at infinite dilution

As displayed in Table 1.1, a number of structural databases with tens of thousands of porous materials have been developed in recent years. With such large

numbers of potential candidates, it can be beneficial to determine an initial estimate of the membrane performance from calculations in the infinite dilution limit. This is an efficient way of rapidly screening materials and identifying top-performing candidates before employing a more detailed set of calculations. Haldoupis *et al.* demonstrated that in the infinite dilution limit, the permeability of a gas species, P_i^0, can be estimated from its Henry coefficient, K_i^0, and self-diffusivity, D_i^0:[108]

$$P_i^0 = K_i^0 \times D_i^0 \tag{1.8}$$

Hence, the membrane permeation selectivity in the limit of infinite dilution, $S_{perm,i/j}^0$ is reduced to:

$$S_{perm,i/j}^0 = \frac{K_i^0 \times D_i^0}{K_j^0 \times D_j^0} \tag{1.9}$$

Watanabe and Sholl previously demonstrated the application of this computational approach to screen 1163 MOFs for kinetic separations of CO_2/N_2 mixtures.[109] In 90% of the top materials, the authors report very large $S_{ads,CO_2/N_2}^0$ values in excess of 400, which is attributed to the larger quadrupole moment that exists in CO_2. Additionally, most MOFs possess $S_{diff,CO_2/N_2}^0$ values between 0.1 and 10, and contain very narrow pores with diameters smaller than 4 Å. Two exceptional candidates were found to possess very large diffusion selectivities with $S_{diff,CO_2/N_2}^0$ values of 441 and 104, respectively. The predicted $S_{perm,CO_2/N_2}^0$ values were used to form a Robeson plot and were compared against polymeric membranes using Robeson's 2008 upper bound. The top 10 identified materials possess $S_{perm,CO_2/N_2}^0$ values between 1200 and 26,200 and $P_{CO_2}^0$ values between 346 and 2.1 x 10^7 Barrer. To assess the impact of a real flue gas mixture, binary mixture adsorption isotherms were predicted for a 15/85 CO_2/N_2 mixture using classical grand canonical Monte Carlo simulations. The results indicated that the high $S_{ads,CO_2/N_2}^0$ values observed in the infinite dilution limit are also observed at higher pressures over a wide pressure range.

1.5 Thesis objectives and outline

The main objective of the research in this thesis is to employ numerous computational tools to predict the gas separation performance of different classes of porous solids in an efficient and high-throughput manner. This includes an investigation into how the structural properties and functionalities of different classes of porous materials impacts their gas adsorption and diffusion properties. While the methods presented in this thesis can be generally applied to a wide array of gas mixtures, a focus biogas upgrading is made due to the crucial applications of bio-methane as a source of renewable energy - discussed in more detail in chapter 4. This thesis is divided into six chapters and is structured as follows:

In chapter 2, an overview of the computational approaches employed in this thesis is provided. This includes a description of their use to study the gas separation properties of different materials and to characterise their physical properties.

While chapter 3 does not relate to the primary objectives in this thesis, it introduces the concept of "pore-filling contamination" (PFC) which has a widespread impact on the accurate surface area calculation of many porous materials from using the Brunauer–Emmett–Teller (BET) theory. In this work, molecular simulations are employed to measure the relative amounts of PFC in a diverse set of MOFs, providing; (1) insights into its relationship with the pore size of each material; (2) a more standardised method of comparing the surface areas of different materials.

In chapter 4, a multi-stage screening protocol is described to provide a high-throughput assessment of the biogas upgrading performance of approximately 70,000 MOF-based membranes. The relationship between the separation performance, structural properties and pore functionalities is examined. The top candidates of this work are employed to identify a set of structure-performance relationships that can be used for the future design of novel mem-

branes or employed to rapidly screen other structural databases.

In chapter 5, the multi-stage screening protocol introduced in chapter 4 is extended to assess the performance of porous COF-based membranes. A direct comparison with the previously investigated MOFs is made to assess how these classes of porous material function differently from one another, and whether they possess different relationships that govern high separation performance. Finally, molecular simulations are further employed to study the impact of feed pressure on the separation performance of eight different membranes.

Finally, chapter 6 provides a summary of the work in this thesis along with a few suggestions of potential avenues for future work.

Chapter 2

Computational Methods

In this chapter, an overview of the computational approaches that are commonly employed to characterise and study the adsorption and transport properties of porous materials is provided. This includes classical techniques such as Monte Carlo and molecular dynamics simulations, the force-fields that describe interactions in these systems and finally, methods for characterising the structural properties of porous solids.

2.1 Statistical Mechanics

Simulations are powerful tools that can provide microscopic information that is near-impossible to obtain from experimental methods such as instantaneous particle positions and velocities. However, we are often interested in understanding bulk properties that are of practical importance at the macroscopic level. In this section, we explore how statistical mechanics provides the bridge between these macroscopic properties of a physical system and the microscopic information that we observe during a simulation. To improve our understanding of this area, there are a number of key concepts to consider. Firstly, it is assumed that a physical system of interest can exist in a discrete set of microstates. For a classical system, each microstate defines the position and momenta of every particle and can be viewed as an instantaneous snapshot.

In addition, each microstate i has an associated value for various macroscopic quantities such as its total energy (E_i), volume (V_i) and number of particles (N_i). It is often more convenient to think of each microstate as a single point in "phase-space" (defined classically by position and momenta axes) - a system of N particles in D dimensions is described in $2ND$-dimensional phase-space.

From classical thermodynamics, the macroscopic state or macrostate of a physical system is described from a set of macroscopic quantities such as temperature (T), pressure (P) and volume (V). It is important to realise that for each macrostate, there are a number of different microstates that describe it. For example, gas particles in a box can be arranged into many different configurations describing several microstates. However these microstates may all possess the same macroscopic properties such as total energy (E) or volume (V), and thus describe the same macrostate. A collection of microstates that correspond to the same macrostate are referred to as an ensemble and these describe different physical systems of interest. Some of the most commonly employed ensembles include:[110]

- **The microcanonical ensemble** (NVE): The number of molecules, volume and potential energy of the system are fixed, describing an isolated system

- **The canonical ensemble** (NVT): The number of molecules, volume and temperature of the system are fixed, describing a system that is connected to a heat bath

- **The isothermal-isobaric ensemble** (NPT): The number of molecules, pressure and temperature of the system are fixed, describing a system connected to a piston which adjusts the volume of the system

- **The grand canonical ensemble** (μVT): The chemical potential, volume and temperature of the system are fixed, describing a system that is connected to a particle reservoir

Let us consider an isolated system with fixed E, V and number of particles N (i.e. one that is described by the micro-canonical ensemble). In order to calculate a property of interest for this system, we can average the property over the microstates in the micro-canonical ensemble. One of the fundamental postulates of statistical mechanics is that of equal *a priori* probabilities which states the following: An isolated system at equilibrium has an equal probability of being in any accessible microstate.[110] By defining the total number of microstates with energy E as $\Omega(E)$, the above postulate means that the probability (P_i) that our isolated system is in microstate i is given by:

$$P_i = \frac{1}{\Omega(E)} \tag{2.1}$$

This probability can be viewed as the amount of time spent in a specific state leading to a time-averaged property as produced in a molecular dynamics simulation (section 2.3). Alternatively, if we consider a set of identical replica systems which are in different microstates that correspond to the same macrostate, the probability can be viewed as the fraction of systems in a particular state. This is referred to as an ensemble-average and is produced from monte-carlo based methods (section 2.2). A system may be described as ergodic under the assumption that the time-average and ensemble average of a property are equal. Thus, an average calculated from exploring all accessible microstates of a single system sequentially in time, is assumed to be the same as an average calculated from the simultaneous measurement of a very large number of independent replica systems in equilibrium. In turn, this implies that the ordering in which each microstate is visited, does not affect the average of the studied property.[110]

For an ergodic system, a macroscopic property of interest A_{macro} can be calculated using ensemble averaging with the following equation:

$$A_{macro} = \langle A \rangle = \sum_i A_i P_i \tag{2.2}$$

where $\langle A \rangle$ denotes an ensemble average of property A, A_i is the measured value of property A in microstate i and P_i is the probability of observing the system in microstate i.

2.1.1 Entropy

Another significant outcome of the postulate of *a priori* probabilities is the statistical derivation of entropy (S). Let us consider that our isolated system is separated into two weakly interacting subsystems - a subsystem of interest (A) and its surroundings (B). The total energy of the system (E_T) is approximated as the sum of subsystem energies E_A and E_B. For a given value of E_A, the total number of microstates ($\Omega(E_T)$) is given by the product of $\Omega(E_A)$ and $\Omega(E_B)$. More conveniently, $\ln(\Omega(E_T))$ can be written as the sum of $\ln(\Omega(E_A))$ and $\ln(\Omega(E_B))$. Assuming that the subsystems can exchange energy with one another, we would like to know what the most likely distribution of the total energy is (i.e. what does the equilibrium state of the system look like?). Although equation 2.1 tells us that each microstate is equiprobable, it also tells us that Ω is a function of E. Therefore, the most probable distribution of energy will be the one which maximises $\Omega(\mathrm{E}_T)$:[110]

$$\left(\frac{\partial ln(\Omega(E_T))}{\partial E}\right)_{N,V,E} = 0$$

$$\left(\frac{\partial ln(\Omega(E_A))}{\partial E_A}\right)_{N,V,E} = \left(\frac{\partial ln(\Omega(E_B))}{\partial E_B}\right)_{N,V,E} \tag{2.3}$$

This suggests that Ω(E) is related to S which from the 2nd law of thermodynamics, reaches a maximum at equilibrium. Therefore, the microscopic origin of this law can be explained as the system evolving from a less probable macrostate to a more probable macrostate that contains a larger number of accessible microstates. The relationship between $\Omega(E)$ and S is expressed

through Boltzmann's entropy formula:[110]

$$S = k_B \; ln\Omega_T \tag{2.4}$$

where k_B is the Boltzmann constant. At equilibrium, there is no net flow of energy between A and B and they are said to be in thermal equilibrium with one another. This allows us to define the temperature (T) of the system using the following thermodynamic relation:[110]

$$\frac{1}{T} = \left(\frac{\partial S}{\partial E}\right)_{N,V} \tag{2.5}$$

2.1.2 The Boltzmann Distribution

Using the same system described in section 2.1.1, the probability (P_i) of observing subsystem A in microstate i with energy E_i is proportional to the number of microstates in subsystem B with energy E_T - E_i. This is expressed via the following equation:[110]

$$P_i = \frac{\Omega(E_T - E_i)}{\sum_j \Omega(E_T - E_j)} = \frac{e^{\left(\frac{S(E_T - E_i)}{k_B}\right)}}{\sum_j e^{\left(\frac{S(E_T - E_j)}{k_B}\right)}} \tag{2.6}$$

where the sum on the denominator is performed over all possible microstates available to subsystem B. Under the assumption that A and B interact weakly with one another, $E_i << E_T$ and therefore, S can be expanded about E_T:

$$\begin{aligned} S(E_T - E_i) &\approx S(E_T) - E_i \frac{\partial S}{\partial E} + ... \\ &= S(E_T) - \frac{E_i}{T} + ... \end{aligned} \tag{2.7}$$

Substituting equation 2.7 into equation 2.6 gives:

$$P_i = \frac{e^{-\beta E_i}}{\sum_j e^{-\beta E_j}} = \frac{e^{-\beta E_i}}{Z} \tag{2.8}$$

where:

$$\beta = \frac{1}{k_B T} \tag{2.9}$$

In equation 2.8, Z is the partition function which normalises the probabilities so that the total probability sums up to 1. More importantly, Z is the key component for calculating several macroscopic thermodynamic quantities as it describes all the statistical properties of a system. For a system with constant N, V and T, the Helmholtz free energy (F) can be calculated directly from Z using the following formula:[110]

$$F = E - TS = -k_B T \; ln(Z) \tag{2.10}$$

where E in this equation is the internal energy of the system. Knowledge of F can then be used to extract other macroscopic quantities including S, P and the chemical potential (μ). Depending on the choice of ensemble (i.e. which macroscopic variables to keep constant), various analogous thermodynamic potentials can be calculated including the Gibbs free energy (G), enthalpy (H) and the grand potential (Φ_G).[110]

Finally, the probability of finding subsystem A in microstate i (equation 2.8) can be modified to give the probability ($p(E_A)$ of finding subsystem A with energy E_A. This is useful as there may be several microstates with the same energy which corresponds to the same macrostate. This probability is expressed as:

$$P(E_A) = \frac{\Omega(E_A) e^{-\beta E_A}}{\sum_j \Omega(E_j) e^{-\beta E_j}} \tag{2.11}$$

Comparing with equation 2.4, this can be written as:

$$\begin{aligned} P(E_A) &= \frac{e^{\beta TS(E_A)} e^{-\beta E_A}}{\sum_j e^{\beta TS(E_j)} e^{-\beta E_j}} \\ &= \frac{e^{-\beta F_i}}{\sum_j e^{-\beta F_j}} \end{aligned} \tag{2.12}$$

While equation 2.12 is written for the canonical ensemble, it can be used

to express the probability across different ensembles by replacing F with the corresponding thermodynamic potential.

2.1.3 The Grand Canonical Ensemble

In the grand canonical ensemble, μ, V and T of the system are kept fixed while N is allowed to change. This is achieved by introducing new particles into the system from an external bulk reservoir, or by removing them. This is very similar to an adsorption experiment in which the adsorbent is exposed to a bulk fluid until an equilibrium is reached between the adsorbed fluid and the bulk fluid. The partition function for the grand canonical ensemble, $Z_{\mu VT}$, is the sum of all possible microstates that make up the ensemble for a system. Between each microstate, the energy of the system E_i and the number of molecules N_i can fluctuate. This means that the partition function consists of a summation over all combinations of these two elements:[110]

$$Z_{\mu VT} = \sum_i e^{\beta(\mu N_i - E_i)} = \sum_i (e^{\beta\mu N_i})(e^{-\beta E_i}) \tag{2.13}$$

Hence, the probability of observing microstate i within the grand canonical ensemble is:

$$P_i = \frac{(e^{\beta\mu N_i})(e^{-\beta E_i})}{Z_{\mu VT}} = \frac{(e^{\beta\mu N_i})(e^{-\beta E_i})}{\sum_i (e^{\beta\mu N_i})(e^{-\beta E_i})} \tag{2.14}$$

Substituting equation 2.14 into 2.2, we derive the following expression which determines an ensemble averaged property within the grand canonical ensemble $\langle A \rangle_{\mu VT}$:

$$\langle A \rangle_{\mu VT} = \sum_i A_i P_i = \frac{1}{Z_\mu VT} \sum_i A_i (e^{\beta\mu N_i})(e^{-\beta E_i}) \tag{2.15}$$

For a classical system, equation 2.15 can be rewritten in terms of an integral over all of phase space. Each point in phase space corresponds to a single microstate containing the coordinates r and momenta v of each particle in the system and the probability of observing each state is given by the probability

distribution *p(r,v)*:[110]

$$\langle A \rangle = \iint A(r,v)p(r,v)\,dr\,dv \tag{2.16}$$

The total energy of the system can be decoupled into a kinetic term that depends on the momenta of each particle, and a potential term that depends on the positions of each particle. The kinetic energy term E_k is derived from ideal gas theory which for a single monatomic particle can be expressed as:[110]

$$E_k = \frac{V}{\Lambda^3} \qquad where: \Lambda = h\sqrt{\frac{\beta}{2\pi m}} \tag{2.17}$$

where m is the mass of the particle, V is the simulation box volume, Λ is the thermal de Broglie wavelength and h is Planck's constant. For molecules such as diatomics and triatomics, additional contributions should also be included for the vibrational and rotational degrees of freedom, in addition to the translational energy contribution reported above. The potential energy of the system *U(r)* is expressed as a function of intra- and inter-molecular interactions which are commonly described by mathematical functions known as force-fields (described in section 2.4). Through substitution of the kinetic and potential terms, the probability distribution found in equation 2.14 can be expressed as:[110]

$$p(r) = \frac{1}{Z_{\mu VT}} \times \frac{V^N}{N!\Lambda^{3N}} \times (e^{\beta\mu N}) \times (e^{-\beta U(r)}) \tag{2.18}$$

Therefore, the classical ensemble average of property A can be expressed as:

$$\langle A \rangle_{\mu VT} = \frac{1}{Z_{\mu VT}} \frac{V^N}{N!\Lambda^{3N}} \int A(r)(e^{\beta\mu N})(e^{-\beta U(r)})\,dr \tag{2.19}$$

2.2 Monte Carlo methods

In order to solve equation 2.19, the property of interest must be sampled across a large number of microstates. Numerical integration schemes are often too expensive for any real system of interest leading to the use of Monte Carlo (MC) methods. In MC integration, the integral is evaluated across a series of randomly selected points in phase space providing an unweighted contribution to the overall integral. The problem with random sampling is that a very large proportion of the selected microstates have negligible Boltzmann factors leading to a low probability of being occupied. As such, these microstates have a negligible contribution to the integral and waste significant amounts of computational time to evaluate. In an alternative approach proposed by Metropolis *et al*, sampling is employed with a bias that leads to the preferential selection of microstates that contribute significantly to the integral (i.e. those with large Boltzmann factors).[111] Not only does importance sampling speed up the evaluation of the integral in equation 2.19, but also focuses on microstates with low energies which improves the convergence rate of the calculation.

A typical MC simulation consists of a random walk through phase space where a large number of microstates are sampled by applying small, random perturbations to the system. As such, new configurations of the system are only affected by the preceding configuration leading to the construction of a Markov chain. The probability of transitioning from an old configuration *(o)* to a new configuration *(n)* depends on:

- The probability of attempting a trial move: $a(o \rightarrow n)$
- The probability of accepting the trial move: $acc(o \rightarrow n)$.

This can be expressed in terms of a transition matrix $\pi(o \rightarrow n)$ where:[110]

$$\pi(o \rightarrow n) = a(o \rightarrow n) \cdot acc(o \rightarrow n) \tag{2.20}$$

As a system approaches equilibrium, the Metropolis scheme implements

a strict rule known as the detailed balance requirement which ensures a equilibrium distribution is not destroyed. This states that the number of moves from (o → n) must be identical to the number of moves from (n → o), such that:[111]

$$\pi(o \rightarrow n) \cdot p(o) = \pi(n \rightarrow o) \cdot p(n) \tag{2.21}$$

where *p(o)* and *p(n)* are the probabilities of observing the old and new configurations, respectively. In the original Metropolis scheme, *a(o → n)* was chosen to be a symmetric matrix such that *a(o → n) = a(o → n)*. Therefore, equation 2.21 can be rewritten as:

$$\frac{acc(o \rightarrow n)}{acc(n \rightarrow o)} = \frac{p(n)}{p(o)} \tag{2.22}$$

For an unbiased simulation, all microstates may be sampled with equal probability meaning that *acc(o → n)* and *acc(n → o)* are equal to 1 and the trial move is always accepted. When employing importance sampling, Metropolis *et al* defined *acc(o → n)* and *acc(n → o)* to be:[111]

$$acc(o \rightarrow n) = min(1, \frac{p(n)}{p(o)}) \qquad acc(n \rightarrow o) = min(1, \frac{p(o)}{p(n)}) \tag{2.23}$$

From equation 2.23, it is clear that if *p(n)* is greater than *p(o)* (i.e. state *n* has a larger Boltzmann factor and greater weight to the overall integral), then the trial move will always be accepted. If *p(o)* is greater than *p(n)*, the trial move may be accepted or rejected based on the relative difference in probability. In this case, the value of acc(o → n) is compared to a random number between 0 – 1 and accepted if acc(o → n) is greater. The advantage of choosing acc(o → n) in this way is that the partition function is completely eliminated from the calculation leading to lower computational expense and a faster convergence towards equilibrium.

2.2.1 Trial move acceptance criteria

As discussed previously in this chapter, the grand canonical ensemble allows for the number of molecules within the system to fluctuate. Therefore, a single-component grand canonical Monte Carlo (GCMC) simulation possesses four types of trial move that may perturb the system: particle translation, rotation, insertion or deletion.

During a translational perturbation, a randomly selected particle is displaced over a short distance within the simulation cell. As the number of molecules does not change in this type of perturbation, the acceptance criteria is simply a function of the energy difference between the old and new configurations. This is also true for particle rotations and the acceptance criteria for both of these moves can be written as:

$$acc(o \rightarrow n) = min(1, e^{-\beta(U(n)-U(o)}) \tag{2.24}$$

During an insertion move, a particle is randomly inserted into the simulation cell from an external particle reservoir. As the energy of the system and number of particles will change during this trial move, the acceptance criteria for this trial move will depend on both these factors. For insertion the acceptance criterion is:

$$acc(o \rightarrow n) = min(1, \frac{V}{\Lambda^3(N+1)} e^{-\beta(\mu-U(n)-U(o))}) \tag{2.25}$$

It is often more convenient to express the chemical potential μ of the system in terms of the bulk fluid fugacity f which can be calculated using an equation of state if the composition, temperature and pressure of the system are known:[110]

$$\mu = \frac{\ln(f\beta\Lambda^3)}{\beta} \tag{2.26}$$

Substituting equation 2.26 into 2.25 gives the following insertion acceptance

criteria:

$$acc(o \rightarrow n) = min(1, \frac{\beta f V}{(N+1)} e^{-\beta(U(n)-U(o))}) \tag{2.27}$$

A deletion move involves the removal of a randomly selected particle from the simulation cell. Like an insertion move, its acceptance criteria depends on both the energy of the system and number of particles:

$$acc(o \rightarrow n) = min(1, \frac{N}{\beta f V} e^{-\beta(U(n)-U(o))}) \tag{2.28}$$

In a multi-component GCMC simulation, an additional trial move known as identity swap may be used which attempts to replace a particle of one species with the particle of another. The acceptance criteria for this trial move is expressed as a combination of the insertion criteria for one particle and the deletion criteria for another particle:

$$acc(o \rightarrow n) = min(1, \frac{f_2 N_1}{f_1 (N_2+1)} e^{-\beta(U(n)-U(o))}) \tag{2.29}$$

2.2.2 Cavity and Energy Biasing

Large adsorbates occupy more space and often fit very tightly within the pore volume. This leads to a low probability of a successful insertion due to the potential overlap with neighbouring adsorbates or adsorbent atoms. To address this issue, a number of biasing techniques have been proposed such as cavity biasing, energy biasing and combinations of both. In cavity-bias GCMC,[112] particle insertions are no longer attempted at random and are biased to cavities or regions that can accommodate the adsorbate. In this method, a number of trial points are randomly selected across the simulation volume and tested to see whether they are inside a cavity of suitable radius, R_c (i.e. a space large enough to accommodate a newly inserted adsorbate). One of these points is randomly selected and a trial insertion is attempted with the following prob-

ability:

$$acc(o \rightarrow n) = min(1, P_c(N)\frac{\beta f V}{(N+1)}e^{-\beta(U(n)-U(o))}) \tag{2.30}$$

where $P_c(N)$ is the probability of finding a cavity with a radius of R_c or larger in a system of N molecules. In order to preserve detailed balance, a deletion is performed without bias by randomly removing a molecule from the system, with an acceptance probability:

$$acc(o \rightarrow n) = min(1, \frac{1}{P_c(N-1)}\frac{N}{\beta f V}e^{-\beta(U(n)-U(o))}) \tag{2.31}$$

For simulations of a LJ fluid, Mezei showed that cavity-bias insertions have up to an 8-fold increase in efficiency over random insertions.[112] In later work, Snurr *et al.* extended the cavity-bias methodology to develop an energy biasing scheme when studying aromatic hydrocarbon adsorption in an MFI zeolite.[113] This technique divides an adsorbent's unit cell into a 3-dimensional grid, assigning a weight to each voxel (3-dimensional grid point). The weight in voxel i (ρ_i) is determined by inserting a probe molecule at the centre of the voxel and evaluating the potential energy felt by the probe (U_i). This is then normalised over the total sum of voxel weights to give:

$$\rho_i = \frac{e^{-U_i\beta}}{\sum_j e^{-U_j\beta}} \tag{2.32}$$

An energy biased insertion is accepted with the following probability:

$$acc(o \rightarrow n) = min(1, \frac{1}{\rho_i}\frac{V_{voxel}}{V}\frac{\beta f V}{(N+1)}e^{-\beta(U(n)-U(o))}) \tag{2.33}$$

where V_{voxel} and V are the volumes of the voxel and simulation box, respectively. To preserve detailed balance, the deletion move is performed with a modified, unbiased acceptance probability:

$$acc(o \rightarrow n) = min(1, \rho_i\frac{V}{V_{voxel}}\frac{N}{\beta f V}e^{-\beta(U(n)-U(o))}) \tag{2.34}$$

Snurr *et al.* investigated the efficiency of energy biasing GCMC by simulating Ar adsorption on silicalite.[113] In their analysis, they observed that both cavity-biasing and energy-biasing lead to a substantial improvement of the insertion and deletion acceptance ratios. This could be increased further by applying both methods in the same simulation. However, the authors stated that the ultimate goal of this methodology is to improve the relative efficiency of the GCMC simulation. Therefore, it is important to balance the added computational cost with the gains in efficiency.

2.2.3 Generating an adsorption isotherm

At the beginning of a GCMC simulation, the simulation cell contains an empty adsorbent of interest. Unlike experiment, this material is usually considered as a perfect crystalline structure with no defects or adsorbed solvent molecules. After defining T and μ, the equilibration phase begins where different microstates in phase space are explored by perturbing the system and deciding whether to accept or reject the move based on the acceptance criteria defined in section 2.2.1. As seen in equation 2.12, the probability of observing the system with a specific energy is proportional to its free energy. This means that we observe moves in which *U(r)* can increase as well as decrease between two states. In the grand canonical ensemble, the free energy is represented by (Φ_G):

$$\Phi_G = E - TS - \mu N = F - \mu N \tag{2.35}$$

As the simulation progresses the system is said to be equilibrated when the free energy is minimised and the average properties of interest begin to fluctuate around some mean value. Over the remaining steps, the macroscopic properties of interest (*U(**r**)* and N) are sampled and averaged. The average value of N is then plotted as a single point on the simulated isotherm at the corresponding pressure. This method is then repeated to generate a full isotherm over the desired pressure range.

2.3 Molecular Dynamics

In many applications of porous materials, the rates of guest transport can have significant impact on the overall performance and efficiency of a process. For example, gas separations are governed by differences in transport rates between diffusing adsorbates, which may define the selectivity of a material. Transport rate can also be a limiting parameter; the rate of diffusion around the active site of a catalyst may have a large impact on the efficiency of the chemical process. In the confinement of a porous material, the transport behaviour of a guest may deviate strongly from its bulk behaviour. This can become even more complicated for materials that exhibit large degrees of structural flexibility or undergo phase changes in response to guest adsorption. Therefore, it is crucial to develop a comprehensive understanding of these processes in order to exploit their potential in different applications.

2.3.1 Simulation Algorithm

Molecular dynamics (MD) simulations are used to examine the time-dependant behaviour of a system. Unlike MC methods which produce ensemble-averaged properties, MD simulations yield time-averaged properties by visiting a series of microstates that are connected in time.[110] The initialisation of an MD simulation involves the assignment of particle positions and velocities at time, (t=0). Successive configurations of the system after a short time δt are then determined by integrating Newton's laws of motion to obtain a trajectory for each particle in the system. Like MC methods, the interactions between particles are typically described using an interaction potential. At a time t, the force acting on particle i at a position vector $\boldsymbol{r}_i$ can be determined from the gradient of the potential energy $U(r_i(t))$. This in turn, is related to the changes in $\boldsymbol{r}_i$ as a function of time:[110]

$$F_i = \frac{-\partial U(\mathbf{r}_i(t))}{\partial \mathbf{r}_i} = m_i \frac{d^2\mathbf{r}_i(t)}{dt^2} \tag{2.36}$$

The trajectory of each particle can be obtained by solving equation 2.36 using numerical integration algorithms at a specified time interval known as a time step δt. Many of these algorithms assume the positions, velocities and accelerations of each particle can be approximated by a Taylor series expansion - examples include the Euler, Verlet and velocity Verlet algorithms.[110] When setting up a MD simulation, it is important to choose an appropriate value for the δt - too small and not enough of phase space will be explored; too large and instabilities within the integration may occur. δt values of the order of femtoseconds are generally sufficient to capture fast dynamics including translations, vibrations and rotations. Another factor to consider is that most studies which examine the transport properties of small gases in porous solids are typically performed in a constant temperature ensemble. For these simulations, a thermostat algorithm is employed to ensure the average temperature of the system reaches a desired value - several algorithms have been proposed over the years including the Andersen, Berendsen and Nose-Hoover algorithms.[114–117] In this thesis, MD simulations are employed to study the diffusive behaviour of adsorbates in different porous solids.

2.3.2 Diffusion coefficients

When describing guest gas diffusion in a porous material, a number of different diffusion coefficients can be defined. The self-diffusion coefficient, D^{self}, describes the Brownian motion of individual particles and is calculated from the slope of the mean-squared displacement (MSD) using Einstein's relation:[110]

$$D^{self}(c) = \frac{1}{2dNt} \lim_{x\to\infty} \frac{d}{dt} \langle \sum_{i=1}^{N} (\mathbf{r}_i(t) - \mathbf{r}_i(0))^2 \rangle \tag{2.37}$$

where d is the dimensionality of the system, t is the observation time, c is the concentration of the adsorbed species and N is the number of adsorbates in the system. The Einstein relation is only valid in the long-time limit where the MSD scales linearly with time. This can be tested by plotting a log-

log plot of the MSD against observation time and measuring the slope which is equal to 1 in the diffusive region. It is important to separate the long-time diffusive behaviour from non-diffusive behaviour, which commonly occurs during the equilibration stage of the simulation. Alternatively, D^{self} can be calculated using the velocity autocorrelation function (VACF) using the Kubo-Green relation.[110]

In some cases, normal diffusive behaviour may not be observed over the timescale of the simulation. This is referred to as an anomalous diffusion process and is characterised by a non-linear relationship between the MSD and observation time. An extreme example of this occurs when the dimensionality and pore size of a porous material are decreased to the point where mutual passage of molecules is no longer possible. This is referred to as single file diffusion (SFD) and mainly occurs in non-intersecting, 1-dimensional channel structures where the width of the pores is comparable to the size of the adsorbates.[118] During SFD, the ordering of the molecules in the channel remains fixed and the movements of each adsorbate become strongly correlated with the movement of surrounding molecules. The concept of SFD has been studied using various theoretical methods including random walker models which show that the MSD increases linearly with the square root of time. This behaviour has also been studied experimentally[119–121] and using MD simulations,[122–124] indicating that single file behaviour is a complex issue and that some systems may exhibit single file and normal diffusive behaviour over different time scales.[125]

In the context of macroscopic diffusion, it is more convenient to define the transport diffusivity, D^t, which is the proportionality constant linking the macroscopic flux, N_{flux}, to the concentration gradient,∇c, described by Fick's Law:[63]

$$N_{flux} = -D^t(c)\nabla c \tag{2.38}$$

D^t is often described in terms of the corrected diffusivity, D^c, and a thermo-

dynamic correction factor, Γ, associated with the curvature of the adsorption isotherm:[94]

$$D^t(c) = D^c(c) \cdot \Gamma = D^c(c) \cdot \frac{\partial \ln(f)}{\partial \ln(c)} \tag{2.39}$$

where f is the bulk phase fugacity. D^c can be calculated from MD simulations using the following expression:[126]

$$D^c(c) = \frac{1}{2dNt} \lim_{x \to \infty} \frac{d}{dt} \left\langle \left(\sum_{i=1}^{N} (\mathbf{r}_i(t) - \mathbf{r}_i(0))\right)^2 \right\rangle \tag{2.40}$$

Unlike D^{self} which describes motion of individual particles, D^c is related to the collective centre-of-mass motion of all diffusing particles and must be calculated over a large number of independent trajectories. D^c is often referred to the single-component diffusivity used in the Maxwell-Stefan (MS) formalism of mass transport[127–129] It is worth noting that D^{self}, D^t and D^c are all functions of the adsorbate concentration and are only equal in the limit of zero loading.[127]

2.4 Force-fields

During a MC or MD simulation, the potential energy $U(\boldsymbol{r})$ of the system must be quickly but accurately evaluated during each step. This is usually achieved by employing a force-field which expresses $U(\boldsymbol{r})$ by a sum of mathematical functions describing the intra- and intermolecular interactions in the system. These can be further categorised into bonded interactions (stretching $U_{stretching}$, bending $U_{bending}$ and torsion $U_{torsion}$ terms) and non-bonded interactions (dispersive U_{LJ} and electrostatic $U_{electro}$ terms):

$$\begin{aligned} U(\mathbf{r}) &= U_{bonded} + U_{non-bonded} \\ &= U_{stretching} + U_{bending} + U_{torsion} + U_{LJ} + U_{electro} \end{aligned} \tag{2.41}$$

For simulations in this thesis, all adsorbates and porous solids were mod-

elled as rigid entities with fixed bond-lengths and angles. Consequently, all U_{bonded} terms are constant and changes in $U(\boldsymbol{r})$ occur as a result of non-bonded interactions.

2.4.1 Lennard-Jones Interactions

The 12-6 Lennard-Jones (LJ) function is one of the most commonly employed potentials to describe non-bonded dispersive interactions between particles. The potential energy $U(\boldsymbol{r}_{ij})$ between two interaction sites i and j is expressed as:[110]

$$U_{LJ}(\mathbf{r}_{ij}) = \sum_i \sum_j 4\epsilon_{ij} \left[\left(\frac{\sigma_{ij}}{\mathbf{r}_{ij}} \right)^{12} - \left(\frac{\sigma_{ij}}{\mathbf{r}_{ij}} \right)^{6} \right] \tag{2.42}$$

where ϵ_{ij} represents the potential well depth of interaction, $\boldsymbol{r}_{ij}$ represents their internuclear separation and σ_{ij} represents the collision diameter which is related to the size of the atoms. For the interactions between two different atom types, a set of mixing rules may be applied to determine the cross terms σ_{ij} and ϵ_{ij}. In this work, the Lorentz-Berthelot rules are applied:[130,131]

$$\sigma_{ij} = \frac{\sigma_{ii} + \sigma jj}{2} \qquad \epsilon_{ij} = \sqrt{\epsilon_{ii}\epsilon_{jj}} \tag{2.43}$$

The attractive term of the LJ potential decays as r^{-6} meaning that the interaction strength between two interaction sites becomes negligible after a short distance. To improve computational efficiency, the Lennard-Jones potential may be truncated at a specified cut-off radius r_c which sets $U(\boldsymbol{r}_{ij})$ to zero for interactions that occur over a separation greater than r_c. r_c should be appropriately chosen to balance the increased computational efficiency with the magnitude of error introduced into each calculation. One disadvantage of this method is that truncation introduces a discontinuity in the potential at r $= r_c$ which can introduce unphysical behaviour in MD simulations that require derivatives of $U(\boldsymbol{r}_{ij})$. This can be solved by shifting the potential to remove

the discontinuity, such that:[110]

$$U_{LJ}(\mathbf{r}_{ij}) = \begin{cases} U_{LJ}(\mathbf{r}_{ij}) - U_{LJ}(r_c) & \mathbf{r}_{ij} < r_c \\ 0 & r > r_c \end{cases} \tag{2.44}$$

For the study of MOFs, COFs and ZIFs, dedicated force-fields that describe host-guest interactions are scarce due to the wide chemical diversity of these materials. Instead, many studies employ general force-fields such as the universal force-field (UFF),[132] DREIDING,[133] or combinations of both. These force-fields contain parameters that were estimated from general rules based on the element, hybridisation, and connectivity for most elements in the periodic table. Another popular choice is the all-atom, optimised potentials for liquid simulations (OPLS-aa) force-field.[134] Unlike DREIDING or UFF, OPLS-aa was developed to study organic liquids and was parametrised to reproduce their bulk thermodynamic and structural properties. As such, each element possesses multiple sets of parameters which are able to describe different chemical environments of organic liquids. In all of these force-fields, pairwise dispersive interactions are modelled using a 12-6 LJ function and each force-field provides the homonuclear pair parameters, σ_{ii} and ϵ_{ii}.

Guest-guest interactions are typically described by force-fields which have been parametrised to reproduce the thermophysical and structural properties of adsorbates in the bulk phase. One of the most popular examples of these is the TraPPE family developed by Siepmann and co-workers,[135,136] a transferable and highly accurate set of force-fields used in the simulations of hydrocarbons, small gases and organic molecules. The parameters in these force-fields are typically found through empirical fitting to vapour-liquid coexistence curves (VLCC), liquid densities, critical temperatures, and vapour pressures across multiple temperatures and/or compositions. Small molecules such as CO_2, N_2, O_2, He and NH_3 are modelled with rigid bonds, however larger adsorbates with intrinsic flexibility are modelled with added bonded terms. For

some molecules (e.g CH_4, CH_3, CH_2 and CH groups), a united-atom (UA) approach is employed to represent multiple atoms by a single interaction site or pseudo-atom.[136] This improves the computational efficiency of the force-field with a small sacrifice in accuracy.

2.4.2 Electrostatic Interactions

For polar or quadrupole containing species, the calculation of electrostatic interactions is important. These are typically calculated by assigning point charges q to each interaction site, so that the electrostatic energy between two charges q_i and q_j separated by a distance $\boldsymbol{r}_{ij}$ can be expressed using the following Coulombic potential:

$$U_{coul}(\mathbf{r}_{ij}) = \sum_i \sum_j \frac{q_i q_j e^2}{4\pi\epsilon_0 r_{ij}} \tag{2.45}$$

where e is the elementary charge (e = 1.602 x 10^{-19} C) and ϵ_0 is the vacuum permittivity (ϵ_0 = 8.854 x $10^{-12} A^2 s^4 kg^{-1} m^3$). Unlike the LJ potential, the electrostatic interaction between two point charges is considered long-ranged in nature - decaying as r^{-1}. For a periodic system, this type of interaction can not be truncated using a cut-off scheme and must be evaluated in full. In this work, the Ewald summation technique is employed which splits equation 2.45 into a sum of real and Fourier contributions terms.[137] In this method, each point charge in the system is superimposed with an oppositely charged Gaussian distribution of width $\sqrt{2/\alpha}$.[110] This creates a series of screened, short-ranged charges that can be efficiently summed in real space. The screening charge is then superimposed with another set of Gaussian charges which nullify the effect of the first set of screening charges. The potential due to these charges can be represented by a Fourier series and is solved in reciprocal space. Finally, a self-interaction term is included to account for a compensating Gaussian charge acting on its own site. Therefore, the electrostatic energy $U_{elec}(\boldsymbol{r}_{ij})$ for

a system of N particles can be expressed as:[110]

$$U_{Ewald}(\mathbf{r}_{ij}) = \frac{e^2}{4\pi\epsilon_0}\Big(\frac{1}{2}\sum_{k\neq 0}\sum_{i=1}^{N}\sum_{j=1}^{N}\frac{4\pi q_i q_j}{Vk^2}e^{[i\mathbf{k}\cdot(\mathbf{r}_i-\mathbf{r}_j)]}e^{\left(\frac{-k^2}{4\alpha}\right)} - \sqrt{\frac{\alpha}{\pi}}\sum_{i=1}^{N}q_i^2 + \frac{1}{2}\frac{q_i q_j}{\mathbf{r}_{ij}}erfc\left(\sqrt{\alpha}\mathbf{r}_{ij}\right)\Big) \tag{2.46}$$

In this equation, V is the volume of the simulation cell, $\mathbf{k}$ is equal to $\frac{2\pi}{L}(l_x, l_y, l_z)$ where L is the unit cell length of a cubic box and l_x, l_y, l_z are the Fourier space lattice vectors.

In order to compute electrostatic interactions between species, knowledge of the atomic partial charge (APC) distribution is required. It is important to realise that APCs are not physical observables, meaning that they cannot be directly measured. In order to estimate their values, a number of different schemes can be applied with varying degrees of accuracy. The computational cost of these schemes differs considerably, and the choice is mainly governed by the size of the system or number of individual structures to be studied. For many adsorbates, the APCs assigned to each atom are already determined as part of the force-field parametrisation process to ensure they reproduce equilibrium properties (i.e. VLCCs). For porous adsorbents, the most reliable methods of determining the APCs are based on QM electronic structure calculations which calculate their values based on population analysis (e.g. Mulliken[138], Löwdin charges,[139] and natural charges population analysis[140]) or by partitioning the electron density distribution into atomic contributions (e.g. Bader,[141] Hirshfeld and iterative Hirshfeld schemes.[142])

Another popular approach is to use the electrostatic potential (ESP) of the adsorbent to derive APCs that fit the QM ESP on selected grid points. The CHELPG[143], RESP[144] and Merz-Kollman[145] schemes are examples of algorithms which employ this methodology and mainly differ from one another by the choice of grid points used to calculate the ESP. One of the limitations of these schemes is that they poorly describe the charges on buried atoms,

located far from the ESP surface. Buried atoms can possess a range of physical or unphysical APCs which reproduce the ESP with similar accuracy. In addition, these methods are applied to clusters which are assumed to provide an accurate representation of the ESP in the periodic structure. As such, the size of the cluster and how cleaved bonds are terminated can have a non-negligible impact on the predicted charge distribution. These issues can be addressed by using methods that employ penalty functions to combat unphysical charges and periodic calculation such as the REPEAT and periodic-RESP schemes[144,146]. In recent years, Manz and Sholl developed the density derived electrostatic and chemical (DDEC) method which has become one of the most popular choices for characterising MOF APCs from QM calculations.[147]

One of the natural drawbacks of QM calculations is the high cost of each electronic structure calculation. For many porous adsorbents, both cluster and periodic models may require several hours of compute time to obtain the APCs. For identifying the adsorption properties in a large number of structures, this is extremely demanding and has motivated the development of faster approximate methods. One example of these computationally cheaper methods is the semi-empirical charge equilibration (Qeq) scheme of Rappe and Goddard.[148] This popular algorithm is based on Sanderson's concept of electronegativity equalization and assumes that certain properties of isolated atoms are similar to those bonded within a molecule. Therefore, the APCs of a system in a specific geometry may be rapidly obtained from the ionisation potentials, electron affinities and atomic radii of its isolated atoms using a truncated second-order Taylor series expansion.

A number of variants of the Qeq algorithm have been proposed which modify the reference state of the Taylor expansion and extend the algorithm to periodic systems. In this work, the extended charge equilibration scheme (EQeq) of Wilmer *et al.*[149] is frequently used. This method centres the Taylor expansion of metal centres on a non-neutral oxidation state leading to a different APC distribution than in the original Qeq scheme. In a recent re-

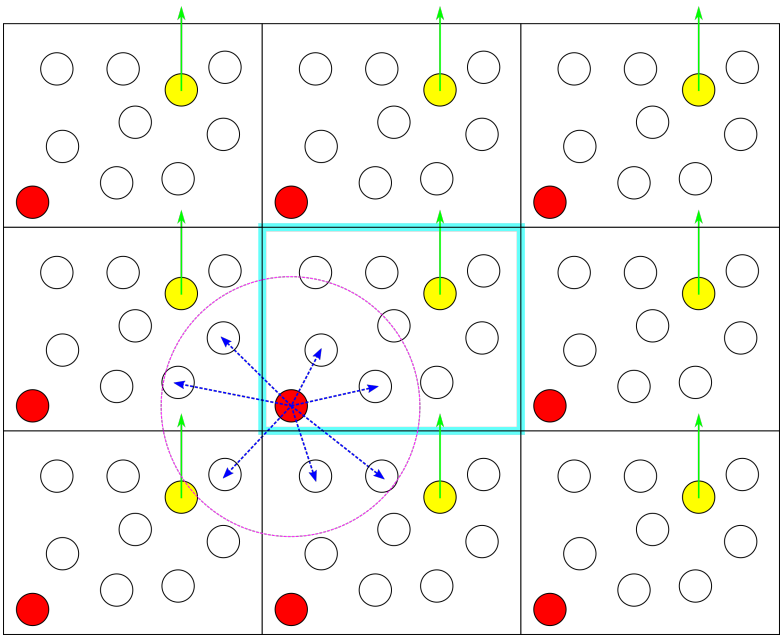


Figure 2.1: *Periodic boundary conditions shown for a 2 dimensional system containing circular particles. Under the minimum image convention, a cut-off (pink dashed circle) set to half the smallest dimension of the primary simulation cell (cyan box) is employed and interactions between a particle and its nearest images are evaluated (blue arrows). A particle leaving the simulation cell on one side will be replaced with a periodic image on the opposite side as depicted by the yellow circle.*

view by Ongari et al.[150] the APCs of 2388 MOFs derived using the various Qeq schemes were directly compared with DDEC charges. The authors noted that the choice of a non-neutral atom reference state for the Taylor expansion leads to a lower discrepancy with the DDEC derived APCs and is essential for estimating the APC distribution in alkali metals.

2.4.3 Periodic Boundary Conditions

Atomistic simulations are typically performed on small systems that contain hundreds or thousands of particles, many of which lie near the surfaces of the simulation cell. In order to account for the surface effects experienced by these particles and to ensure accurate sampling of bulk properties, an appropriate set of boundary conditions should be chosen. In many cases, periodic boundary conditions (PBCs) may be employed which surround the primary simulation cell with an infinite number of images across all dimensions - a 2-dimensional example is given in Figure 2.1. If a particle leaves the simulation cell on one

side, it is replaced by a periodic image which enters the simulation cell on the opposite side. In order to calculate the correct number of pair interactions, the minimum image convention is employed, which only considers interactions between each particle and its closest periodic images[110]. In order to enforce this convention and to stop molecules interacting with periodic images of themselves, a cut-off radius (r_c) is specified. Typically, the value of r_c is set to half the smallest dimension of the primary simulation cell, thereby ignoring interactions that occur over a separation greater than r_c.

2.5 Structural Characterisation

In this section, various computational approaches for characterising the structural properties and pore topology of porous materials are discussed.

2.5.1 BET Surface Area

The specific surface area (SSA) is one of the most important physical properties of an adsorbent for gas storage and separation applications. It is routinely estimated by applying the theory of Brunauer, Emmett and Teller (BET theory) to gas adsorption isotherms.[151] Developed in 1938, BET theory extends on Langmuir's work[152] by explaining the physical adsorption of gases onto surfaces through multi-layer adsorption. In Langmuir theory, the following main assumptions are applied:[152]

1. The surface is a plane comprised of identical sites which are energetically equivalent with respect to the adsorption energy

2. Adsorption at one site is independent of the occupancy of neighbouring sites

3. Only one adsorbate per site

4. Adsorbates form a monolayer and cannot act as sites for other adsorbates.

BET theory builds on these by introducing the following assumptions:[153]

1. Adsorbates can form layers in which each adsorbate acts as a single site for another adsorbate. At the saturation limit, the number of adsorbed layers tends to infinity.

2. Adsorbate-adsorbate interactions are only considered between adjacent layers

3. The enthalpy of adsorption for the first layer is greater than other layers.

4. The enthalpy of adsorption for the second layer and above is equal to the enthalpy of liquefaction (this suggests that the influence of host-guest interactions decay quickly past the first layer)

To estimate the SSA of an adsorbent, BET theory is employed to calculate the amount of gas forming an adsorbed monolayer on the surfaces of the adsorbent. This quantity, referred to as the monolayer capacity, is typically extracted from N_2 adsorption experiments at 77 K. However, other gases such as Ar and CO_2 are also commonly used. From the adsorption isotherm, the monolayer capacity can be calculated using the linearised BET equation:

$$\frac{p}{V(p_0 - p)} = \frac{1}{V_m C} + \left(\frac{C-1}{V_m C}\right)\frac{p}{p_0} \tag{2.47}$$

where p_0 is the saturated pressure of the adsorbate gas, p is the partial pressure of the adsorbate gas at equilibrium conditions, V is the volume of gas adsorbed at the equilibrium pressure p, V_m is the volume of gas adsorbed to produce a monolayer on the surface, and C is a dimensionless constant related to the heats of adsorption for the adsorbed monolayer on the surface.

Using the BET equation, V_m can be calculated from regression analysis over a restricted linear region of the BET plot. In the original publication, Brunauer, Emmett and Teller studied several catalysts, supports and adsorbents which possess type II N_2 adsorption isotherms due to their mesoporosity.[5] In these materials, they found that the BET plots typically became linear

between $0.05 \leq p/p_0 \leq 0.35$. While this range may be suitable for mesoporous adsorbents, there are many zeolites, MOFs, porous polymer networks (PPNs) and COFs which possess microporosity. In microporous materials, surface coverage and pore filling occur at much lower pressures, typically below a relative pressure of 0.05. Furthermore, the BET plots of adsorbents that combine micropores with mesopores may contain multiple linear ranges, making it more difficult to identify the most appropriate region. The location and extent of these regions will depend on both, the adsorbent and the adsorbate, making it important to have a consistent method for reporting BET surface areas. To address these issues, Rouquerol et al. devised a series of consistency criteria for selecting an appropriate linear range:[153]

1. Only a range where $V(p_0 - p)$ increases monotonically with p/p_0 should be selected.

2. The value of constant C resulting from linear regression should be positive.

3. V_m should correspond to a relative pressure that falls within the selected linear region.

4. The relative pressure corresponding to the monolayer loading calculated from BET theory $\left(\frac{1}{\sqrt{C}+1}\right)$ should be equal to the relative pressure determined in criterion (3) with a tolerance of 10 - 20 %.

After calculating V_m, the SSA A_{BET} is determined using the following formula:

$$A_{BET} = \frac{\sigma N_A V_m}{m_s} \tag{2.48}$$

σ is the adsorption cross-sectional area of the adsorbate, N_A is Avogadro's constant and m_s is the mass of the adsorbent sample. Brunauer and Emmett suggested that σ could be calculated from the liquid density in the bulk liquid

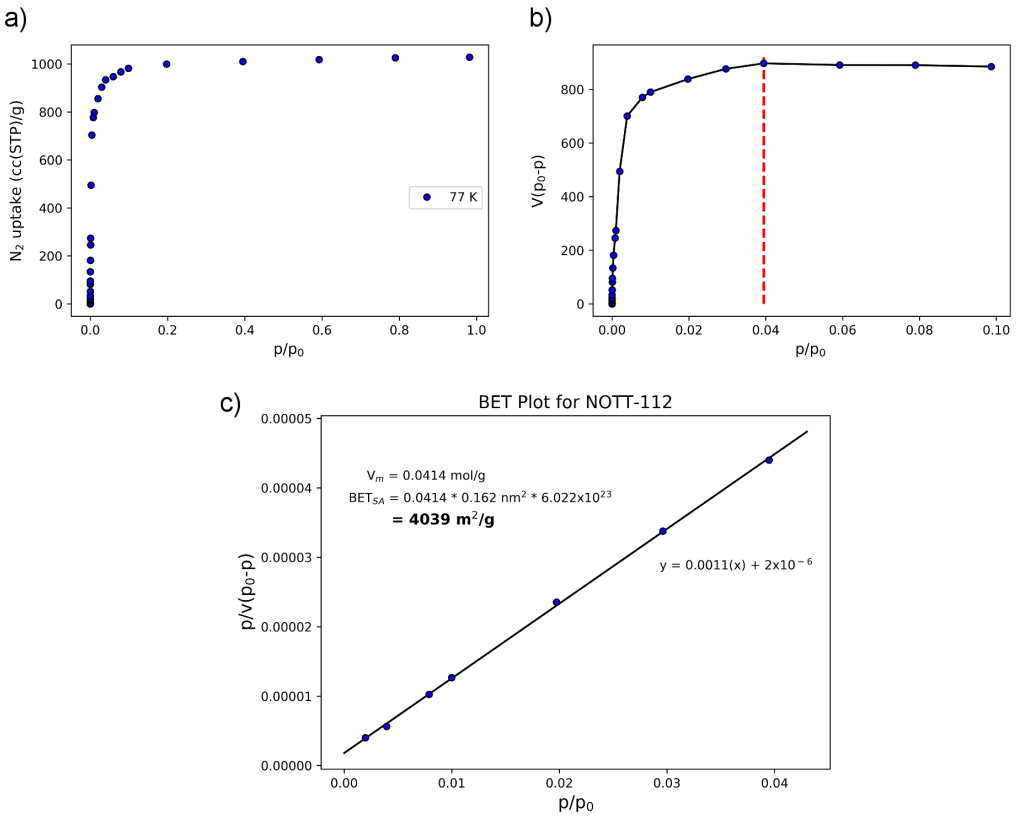


Figure 2.2: *(a) A simulated N_2 isotherm at 77 K for NOTT-112; (b) The corresponding Rouquerol consistency plot in which the maximum at a relative pressure of $\approx$ 0.04 is depicted by the dashed red line; (c) The BET plot and linear regression analysis that leads to the BET surface area calculation of NOTT-112.*

state, as:[6]

$$\sigma = f\left(\frac{M}{\rho N_A}\right)^{\frac{2}{3}} \tag{2.49}$$

Where f is a packing factor, ρ is the liquid adsorbate density and M is the mass of the adsorbate. It is commonly assumed that the arrangement of the adsorbed monolayer is hexagonal close-packing, making $\sigma = 0.162$ nm^2 for a nitrogen molecule at 77 K.

GCMC simulations can be employed to simulate adsorption isotherms for BET analysis. GCMC simulations normally use perfect crystal structures that are free of defects or collapsed pores, which may exist in the experimental sample. As such, the computational BET analysis gives an estimate of the theoretical upper limit to SSA. This is especially useful for materials such as MOFs, where the upper limit can be used to determine the effectiveness of the activation procedure. Figure 2.2 provides a breakdown of the overall

BET calculation using the Rouquerol consistency criteria. In this example, the NOTT-112 MOF[154] (see section 3.1 - Figure 3.1) is selected for demonstration, however the same principles can be applied to any material of interest. After calculating the adsorption isotherm from GCMC simulations (Figure 2.2a), the 1st Rouquerol criterion is applied to produce the plot given in Figure 2.2b. After identifying the relative pressure at which $V(p_0\text{-}p)$ no longer increases monotonically, the linearised BET equation from equation 2.47 can be plotted over the appropriate restricted range that incorporates all Rouquerol criteria (Figure 2.2c). Linear regression analysis can then be employed to determine the value of V_m and hence the SSA.

2.5.2 Geometric Surface Area

For high-throughput studies which contain thousands of materials, the BET method is too expensive to estimate the SSA of each material in a time-efficient manner. Therefore, it is more beneficial to employ efficient but faster methods that can calculate the structural properties geometrically. In this context, a geometric surface area can be determined mathematically from the atomic coordinates of the porous material alone. Depending on the application of the material, a number of different surface areas may be defined independently.

The accessible surface area (ASA) is calculated from the total area that is available to a probe molecule travelling across the surfaces of a material. Lee and Richards were the first to describe an algorithm for estimating the ASA of ribonuclease-S, lysozyme and myoglobin.[155] Their program computes the ASA by drawing an arc, centred around each protein atom, with a radius equal to the sum of the protein atom and solvent molecule radii. Regions of the arc which do not overlap with any other protein atoms are deemed accessible and the total ASA is therefore proportional to the summed length of accessible regions. This algorithm has been made more efficient over the years. Shrake and Rupley introduced a series of uniformly distributed grid test points around

each atom to speed up the calculation.[156]

In this work, the method of Gelb and Gubbins is employed which uses a Monte Carlo procedure to estimate the ASA of a material.[157] In this approach, a test probe is randomly placed at locations surrounding the surface of each atom and tested for overlap with any other atoms in the porous glass. The fraction of insertions that do not overlap with other atoms are then used to calculate the ASA.

2.5.3 Pore volume and Void Fraction

For many gas storage applications, the specific pore volume (PV) and void fraction (VF) are also important structural properties that govern the available volume of the unit cell which adsorbates can occupy. Experimentally, the PV can be derived from N_2 adsorption isotherms using the Gurvich rule.[5] This rule assumes that at the saturation pressure, the density of N_2 adsorbed in the pores is equal to its liquid density. The VF can be calculated from the product of the PV and unit cell density. Computationally, there are a number of different definitions of the PV that can be calculated from Monte Carlo based algorithms, including the geometric PV (GPV) and helium PV (HPV).

The GPV is fairly intuitive and is calculated by sampling a large number of test insertions for overlap with structural atoms. Test points may be generated at random or be situated on a 3-dimensional grid. The fraction of insertions that do not overlap with the adsorbent are multiplied by the total unit cell volume to get the GPV. This approach typically uses a dimensionless hard sphere probe; however, larger radii may be used to calculate the PV accessible to the centre of the probe. The next type of PV that is commonly determined is the HPV, which has importance in the conversion between absolute and excess adsorption.[158] The calculation of the HPV is previously discussed in the works of Myers, Monson and Talu, who demonstrated that in the limit of low pressure, the absolute adsorption second virial coefficient of a porous

adsorbent (B^a) can be calculated as:[159,160]

$$B^a = \frac{1}{m} \int e^{-\beta U(\mathbf{r})}\, d\mathbf{r} - V_g \tag{2.50}$$

where m is the mass of the adsorbent, $U(\boldsymbol{r})$ is the helium-surface interaction energy for a single helium atom, and $V_g$is the specific HPV. At room temperature, the adsorption of helium is considered negligible, therefore:

$$V_g = \frac{1}{m} \int e^{-\beta U(\mathbf{r})}\, d\mathbf{r} \tag{2.51}$$

The above integral can be estimated using the Widom insertion technique,[110] which samples the helium-solid interaction energy across the pore space. Consequently, the HPV will be sensitive to the choice of force-field and the temperature used in the simulation. While a standard temperature of 298 K is typically used, direct comparison with experimental work will be achieved using the same specified temperature.

2.5.4 Pore size distribution

Another important property when characterizing porous solids is the pore size distribution (PSD). A number of experimental methods exist for analysing the PSD of a porous material such as mercury porosimetry,[161] NMR cryoporometry[162] and small-angled X-ray/neutron scattering (SAXS and SANS).[163,164] Gelb and Gubbins developed a cheap and exact way of determining the PSD geometrically.[165] Their algorithm uses a Monte Carlo simulation to generate a series of random test points within the pore space of a material. At each test point, the largest sphere that contains the test point and does not overlap with atoms of the structure is recorded. By dividing the total radius range into a series of small bins, a cumulative pore volume function can be determined over a large number of insertions. This is a monotonically decreasing function that corresponds to the volume of void space that is coverable by spheres of

a given radius or smaller. The PSD is then determined from the derivative of this function with respect to the sphere radius.

In this work, an alternative approach is employed to sample the PSD using a stochastic ray tracing algorithm. In this method, the void space of a material is sampled by firing rays across the void space in random directions.[166] In an unconstrained approach, the initial positions of each ray are selected from within the probe accessible void space and are terminated once they intersect with the surfaces of the material. In an unconstrained approach, the initial position can be selected from any point within the unit cell and each ray is allowed to pass through the surfaces and explore multiple void regions until it reaches a maximum length threshold. In this approach, only the lengths of each ray that pass through void spaces contribute to the final histogram.

2.5.5 Topological features

The structural properties defined so far give little indication of the topology of a porous network. Depending on the class and composition of a porous material, the pore network can possess varying shapes and connectivity. Therefore, its characterisation is essential to gain an understating of how certain topological features impact adsorption and transport properties. To establish the pore connectivity within a given material, a number of approaches[108,167] have been proposed that employ a grid-based analysis using the Hoshen-Kopelman algorithm.[168] In these methods, the unit cell of a material is uniformly discretised into a number voxels and a probe particle of a given size is inserted at the centre of each one. If the inserted probe does not overlap with any framework atoms, then the voxel is considered accessible. After each voxel has been sampled, the Hoshen-Kopelman labelling algorithm groups accessible voxels together into clusters. If a cluster connects two opposite points across the entire length of a unit cell, it is referred to as a spanning cluster, which under periodic boundary conditions, represents a diffusion path of in-

finite length. This algorithm can efficiently identify pore channels and cages that exist within a structure and whether they are interconnected with one another. In addition, this algorithm provides an efficient way of evaluating the pore-limiting diameter (PLD) and largest cavity diameter (LCD) of a material. The PLD corresponds to the largest probe diameter that can freely diffuse through a material (i.e. the narrowest part of a spanning cluster). The LCD corresponds to the largest probe diameter that can be placed inside the pore system of a material without overlapping with framework atoms. Both of these dimensions are highly important for understanding diffusion in gas separation processes as they define what kinds of adsorbate are accessible to the pores and how well mixtures can pass one another. The results from this method are dependent on the 3-dimensional grid spacing used in the calculation; as the size of the spacing is reduced, the level of uncertainty in the predictions decreases.

An alternative approach is to use Voronoi decomposition, which provides a graph representation of the void space in a porous material.[169] In this method, the space closest to each of the framework atoms is divided into a series of polyhedral cells. The faces, edges and vertices of these cells correspond to planes, lines and nodes that are equidistant between neighbouring atoms. The Voronoi network mapped by the edges and vertices of each cell corresponds to the pore system in the material and can be analysed to extract geometrical descriptors such as the PLD, LCD, ASA, PV and VF. This methodology is implemented into the Zeo++ software package developed by the Harancyzk group and is commonly employed for high-throughput characterisation of large structural databases.[169]

Chapter 3

Pore-Filling Contamination in Metal-Organic Frameworks

Abstract

The surface areas of porous materials are routinely determined using the Brunauer-Emmett-Teller (BET) method. However, BET surface areas are often susceptible to errors from the pore-filling contamination (PFC) effect. PFC typically occurs in MOFs that possess multiple pores, which adsorb gas at different relative pressures leading to an appreciable overlap of surface adsorption and pore-filling across the different pores. As BET theory cannot distinguish between the molecules adsorbed onto the surfaces and those in the pore centres, additional molecules are erroneously considered part of the monolayer, leading to an over-estimated BET surface area. In this chapter, the impact of PFC across different materials is assessed including how it influences experimental results within the literature - For this, the strategy of increasing specific surface areas by replacing phenyl rings with alkyne groups is studied.

3.1 Introduction

Metal-organic frameworks (MOFs) represent a large group of porous coordination polymers that contain metallic-based building blocks that are bridged

together by polydentate organic ligands.[170] These form series of 3-D crystalline frameworks which typically possess ultra-high surface areas and porosities[14]. The wide variety of inorganic and organic moieties makes it hypothetically possible to design a near-infinite number of MOFs. Great flexibility in the design of a MOFs structure is highly desirable for its selective functionality towards adsorption based applications, such as energy storage[171] or carbon sequestration[172]. For these applications, it is crucial that MOF materials provide high and efficient uptake of adsorbates, and the use of open metal sites[173–175] has been shown to provide strong adsorption sites at low pressures, where uptake is governed by the strength of host-guest interactions. In addition, low pressure uptake can be improved through the inclusion of functionalised ligands[176,177] or through post-synthetic modification of the framework[19]. At higher pressures, uptake is correlated with the amount of the surface area and pore volume provided by the adsorbent. Therefore, the accurate estimation of these structural properties becomes increasingly important in understanding the mechanisms of adsorption.

As organic ligands make up the majority of a MOFs structure, their shape and size contribute significantly to the amount of surface area formed. By expanding the size of the organic ligand, a framework with larger surface area, pore volume and porosity may be created. In many examples, this expansion is achieved by bonding multiple phenyl rings together, forming part of an isoreticular series of MOFs[18,34,178]. While this method is effective, previous work has shown that using multiple, "area efficient" alkyne groups is a better approach to increase MOF surface areas[179]. By employing the latter strategy, two new MOFs, **NU-109** and **NU-110**, have been produced with specific surface areas (SSA) exceeding 7000 m^2/g; two of the largest values recorded in the literature. Since this publication[179], a number of MOFs and other porous materials have been designed with alkyne units forming a core part of their structures[180–183]. One of these structures, **NU-111**, developed by Hupp and co-workers,[184] possesses large dendritic ligands that contain six alkyne linkers

coordinated through copper paddlewheel nodes to form a cubic framework with **rht** topology (Figure 3.1). Hupp and co-workers find that **NU-111** has a BET surface area of about 5000 m^2/g, almost 20% larger than that of **NOTT-119**,[185] an isoreticular MOF that replaces each alkyne group with a phenyl ring (Figure 3.1a). This suggests that the strategy of replacing phenyl rings with alkyne groups may be beneficial for increasing the SSA of MOFs. These conclusions were later supported by Bichoutskaia *et al* who computed the ASAs of a hypothetical series of MOFs with **rht** topology.[186] For the seven MOFs considered in this study, the results also indicate that substituting phenyl rings with alkynes groups leads to a general increase in SSA.

In an earlier set of studies, Zhou and co-workers synthesised **PCN-16**[187] and **PCN-46**[188] MOF structures which coordinate tetra-topic carboxylate ligands through copper paddlewheel nodes, forming an **nbo** topology. The resulting framework possesses a rhombic unit cell formed from a combination of short spherical and long ellipsoidal cages (Figure 3.2b). Furthermore, the ligands used to form **PCN-16** and **PCN-46** were designed with one and two alkyne moieties, respectively (Figure 3.2a). By replacing these alkynes moieties with a phenyl ring, the isoreticular **NOTT-101** MOF is formed as synthesised by Schröder and co-workers[18]. The BET surface areas of **PCN-16**, **PCN-46** and **NOTT-101** are 2273, 2500 and 2316 m^2/g, respectively, further demonstrating examples where MOF SSAs may be increased through the replacement of phenyl rings with alkyne functional groups.

The SSAs of MOFs are routinely determined by applying the Brunauer, Emmett and Teller (BET) theory[151] to N_2 gas adsorption isotherms. As mentioned previously in chapter 2, the BET theory aims to explain the physical adsorption of guest molecules through the formation of adsorption layers. The surface area of a MOF is calculated by determining the amount of guest molecules, which form a single adsorbed layer across the pore surfaces. This quantity, referred to as the monolayer capacity, is typically extracted from N_2 gas adsorption experiments performed on the activated MOF sample. Alter-

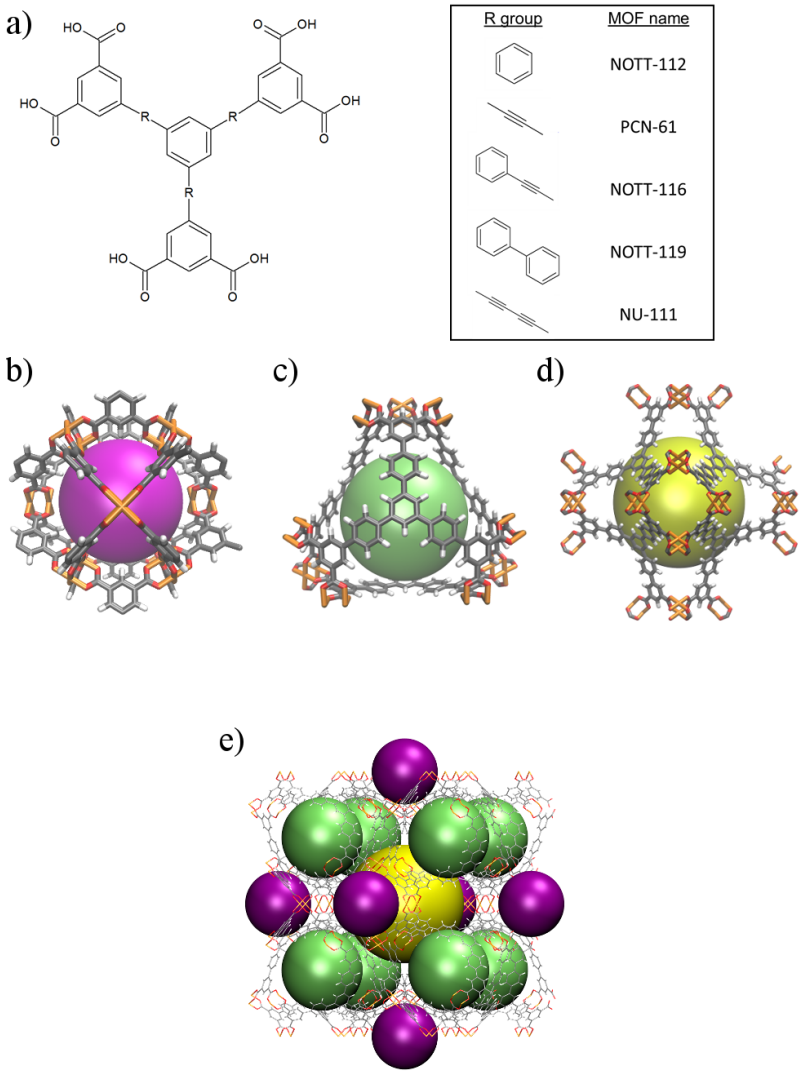


Figure 3.1: *Examples of MOFs with* ***rht*** *topology: (a) schematic of the hexacarboxylate ligands used; (b-d) constituent small spherical, medium tetrahedral and large octahedral pores; (e) a combined cubic unit cell as formed in* ***NOTT-112****. Atom colour scheme: Cu = Orange, C = grey, H = white, O = red.*

natively, a N_2 gas adsorption isotherm can be simulated using classical GCMC simulations.

While BET theory provides a means of comparing the surface areas of different materials, the underlying assumptions of the theory tend to be inapplicable for several porous materials. For example, BET theory assumes that gases physically adsorb onto surfaces forming multiple layers, of which an infinite number exist at the saturation pressure. By applying Langmuir theory to each layer, it assumes all sites are energetically homogenous and that adsorbate-adsorbate interactions and co-operative adsorption events do

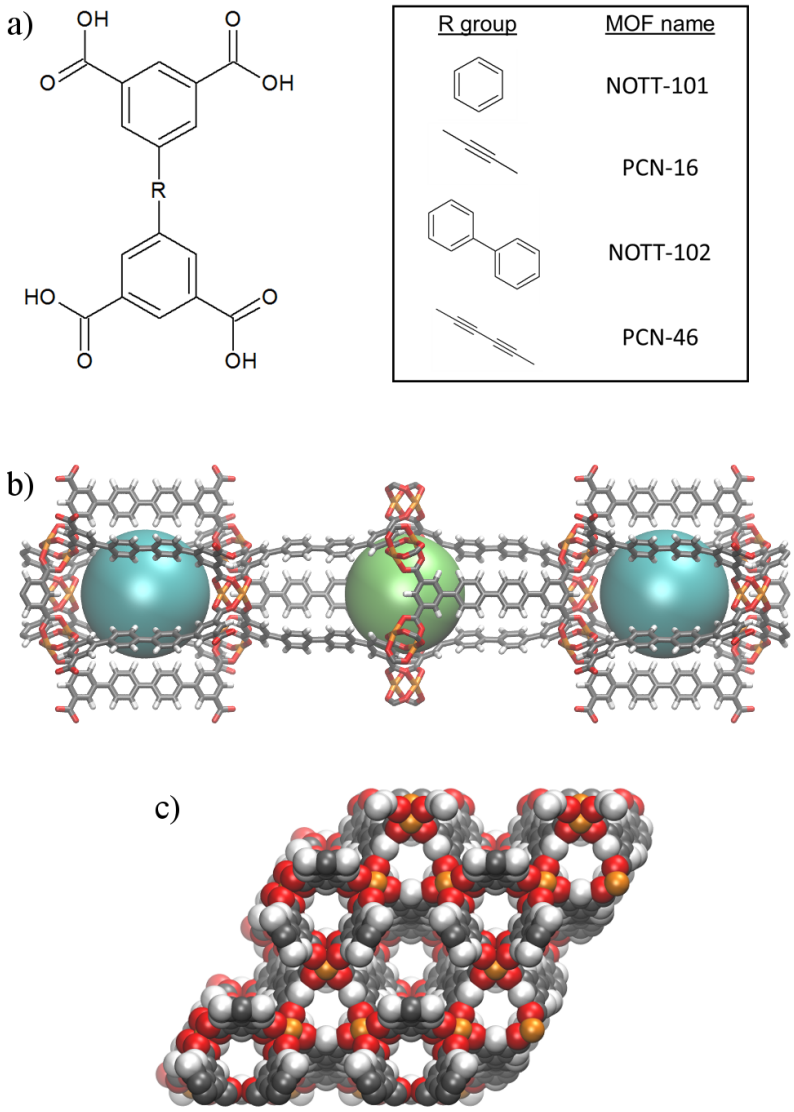


Figure 3.2: *Examples of MOFs with* ***nbo*** *topology: (a) schematic of the tetracarboxylate ligands used; (b) constituent small spherical (cyan) and large ellipsoidal (green) pores; (c) a combined rhombic unit cell that forms the hexagonal crystal structure of* ***nbo*** *MOFs, as formed in* ***NOTT-102****.*[18]

not impact the adsorption process.[189] It is clear that these assumptions oversimplify the adsorption process and are more appropriate for describing an ideal gas adsorbing onto a solid surface. In reality, many adsorbents possess finite sized pores which contain a great deal of heterogeneity with respect to the adsorption energy. For many of these materials, it has also been demonstrated that gas adsorption is more appropriately described by a pore-filling mechanism rather than layer-by-layer formation.[190] Consequently, this can influence the arrangement of the adsorbed gas, resulting in a range of σ values

that provide different estimations of the SSA.[1] This has lead to many additional questions regarding the physical meaning of the BET surface area and whether the method is valid for systems such as microporous adsorbents. To address these questions, Walton and Snurr used molecular simulations to calculate BET surface areas in six microporous IRMOFs.[191] Although simulation snapshots indicated a pore-filling mechanism in these materials, the authors reported very good agreement between the BET surface areas and the accessible surface area (ASA) determined using geometric methods. This agreement was further improved upon application of the consistency criteria proposed by Rouquerol *et al.* (see section 2.5.1), thus indicating the importance of identifying the correct linear region of the BET plot. In a later study, Bae and co-workers[192] extended on Walton and Snurr's research,[191] by expanding the range of porous materials to zeolites and MOFs that contain a combination of ultra-micropores ($d \leq 7$ $\AA$) and super-micropores (d in the region of 7 - 20 $\AA$). They reported consistent findings that showed good agreement between the BET and ASAs when applying the consistency criteria. Similarly, simulation snapshots indicated that gas adsorption did not form distinct layers, further demonstrating the weakness of this assumption in BET theory.

Despite fulfilment of the consistency criteria, it has recently[193,194] been shown that many MOF BET surface areas can be erroneously overestimated. This inaccuracy is due to a process known as 'pore-filling contamination' (PFC) which typically affects MOFs containing multiple pores of different sizes. In these materials, N_2 gas adsorbs in each pore at different relative pressures and can lead to an overlap between surface saturation and pore-filling adsorption. Consequently, the causes a large amount of N_2 to be included into the monolayer capacity calculation, despite being located in the centre of the pore cavities, leading to an over-estimated value of the BET surface area. Using experimental methods, it is extremely challenging to establish and quantify how PFC affects the BET calculation, as the exact locations of each adsorbed nitrogen molecule are required. In recent years, GCMC simulations (chapter

2.2) have been extensively used as a tool to study the adsorption thermodynamics of porous solids[195]. The quality and accuracy of these simulations is determined by the choice of force-field (chapter 2.4) used to describe the chemical interactions within the system. If a good match is observed between the experimental and simulated isotherms, then it is commonly assumed that the force-field can provide an accurate description of the underlying chemical interactions within the system.[196] This permits the accurate and precise extraction of adsorbate positions within the porous material from simulation snapshots, thus providing a reliable method of quantifying the amount of PFC within the BET surface area calculation.

In the beginning of this chapter, two methods of quantifying PFC are presented in order to assess its impact on the BET surface area calculation of nine MOFs (Figures 3.1 and 3.2). These methods are then employed to determine how PFC may influence the experimental surface areas of these MOFs - Each MOF was specifically chosen to focus on the process of replacing linker phenyl rings for alkyne moieties. In the subsequent section, PFC analysis is performed for a much larger array of MOFs, providing an in-depth insight into the relationship between the amount of PFC and the pore size of each structure. For each MOF studied in this work, cif files were obtained from the Cambridge Structural Database (CSD) with all solvent molecules and disordered atoms removed prior to simulation.[84]

3.2 Methods for quantifying PFC in MOFs

3.2.1 Computational Details

The nine MOFs employed in this section are previously shown in Figures 3.1 and 3.2. The theoretical BET surface areas of all nine MOFs are determined from simulated N_2 gas adsorption isotherms at 77 K. These are obtained from GCMC simulations that are performed using the Multi-Purpose Simulation

Code of Snurr *et al.*[197] Input fugacities for each simulation are calculated using the Peng-Robinson equation of state.[198] Simulations include random translation and rotation moves, as well as, energy biased insertion and deletion moves (see section 2.2.2). Each simulation involves an equilibration stage of 6 $\times$ 10^6 steps followed by a production stage of 9 $\times$ 10^6 steps for each pressure point. Frameworks are treated as rigid species with their atoms fixed in their crystallographic coordinates. For the framework atoms, LJ parameters are taken from the DREIDING force field[133] or UFF[132] for those which are missing from DREIDING. The N_2 adsorbate is treated as a rigid three-site species, where two nitrogen atoms are bound to a non-interacting and dimensionless centre of mass atom. The LJ parameters and (atomic) partial charges for the N_2 adsorbates are taken from the TraPPE force-field.[135] All LJ interactions are calculated with a truncated cut-off distance of 15.0 Å, and electrostatic interactions are handled using the Ewald summation technique.[137] Previous work has shown that N_2-MOF electrostatic interactions play a minor role in the adsorption of N_2 and are therefore, not included.[191] All BET surface areas are calculated using the consistency criteria devised by Rouquerol et al.[153] (section 2.5.1 and Figure 2.2). In addition, each MOFs accessible surface area (ASA) is calculated using the Poreblazer tool kit of Sarkisov and Harrison[167] using a spherical nitrogen site probe whose parameters are taken from the TraPPE force-field. A full list of force-field and BET fitting parameters may be found in Appendix A-1 and A-2. For each GCMC simulation, the statistical uncertainty in the number of adsorbed molecules is estimated by splitting the production phase into 20 equally-sized blocks and calculating the standard deviation. In all cases, the standard deviation is calculated to be smaller than 0.6% resulting in error bars on each isotherm that are smaller than the symbol size.

To quantify the amount of PFC present in each BET calculation, snapshots from GCMC simulations are analysed. To determine whether a N_2 molecule is in contact with the pore walls, a nearest neighbour algorithm that

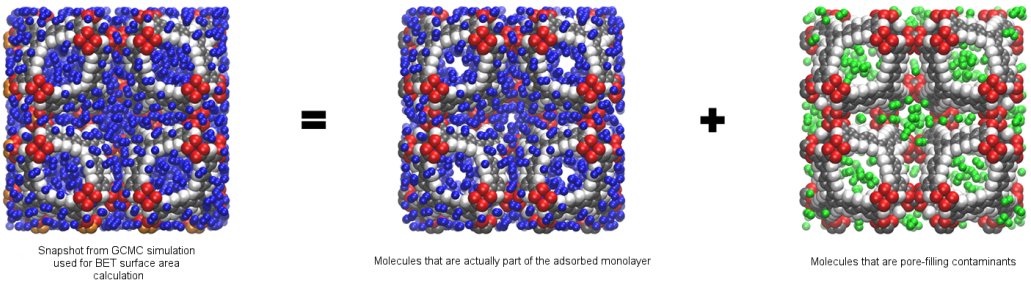


Figure 3.3: *An example of how PFC is quantified from GCMC simulation snapshots of* ***NOTT-112****. This method employs a k-dimensional tree nearest neighbour algorithm to determine the distance between each N_2 molecule and the framework surface. Equation 3.1 is then used to classify molecules as pore-filling contaminants or part of the adsorbed monolayer*

.

uses a k-dimensional tree is employed to calculate the shortest distance between each adsorbate atom and the framework. Once the distance and identity of the closest framework atom is known, the following tolerance δ_{ij} can be calculated[194]:

$$\delta_{ij} = D_{ij} - 2^{\frac{1}{6}}\sigma_{ij} \tag{3.1}$$

where D_{ij} is the inter-atomic distance between adsorbate atom i and framework atom j, and $2^{\frac{1}{6}}\sigma_{ij}$ is the LJ potential minimum distance for the atom pair. Based on previous work by Gomez-Gualdron *et al.*,[194] a N_2 molecule is deemed to be in contact with a framework atom if $\delta_{ij} \leq 1\mathring{A}$, thus providing a tolerance for small translational and rotational fluctuations. An example of the output from this calculation is shown below in Figure 3.3 for **NOTT-112**. For each MOF, a single snapshot taken from the end of the production phase was employed to calculated the PFC-corrected surface area. While, multiple snapshots could in theory be used to estimate the uncertainty in the surface area, the very small error bars on each isotherm should lead to a near-negligible difference that has little impact on the overall conclusions of the study.

3.2.2 PFC in rht and nbo MOFs

The experimental and simulated surface areas of the nine investigated MOFs are recorded in Table 3.1. In general, good agreement is observed between

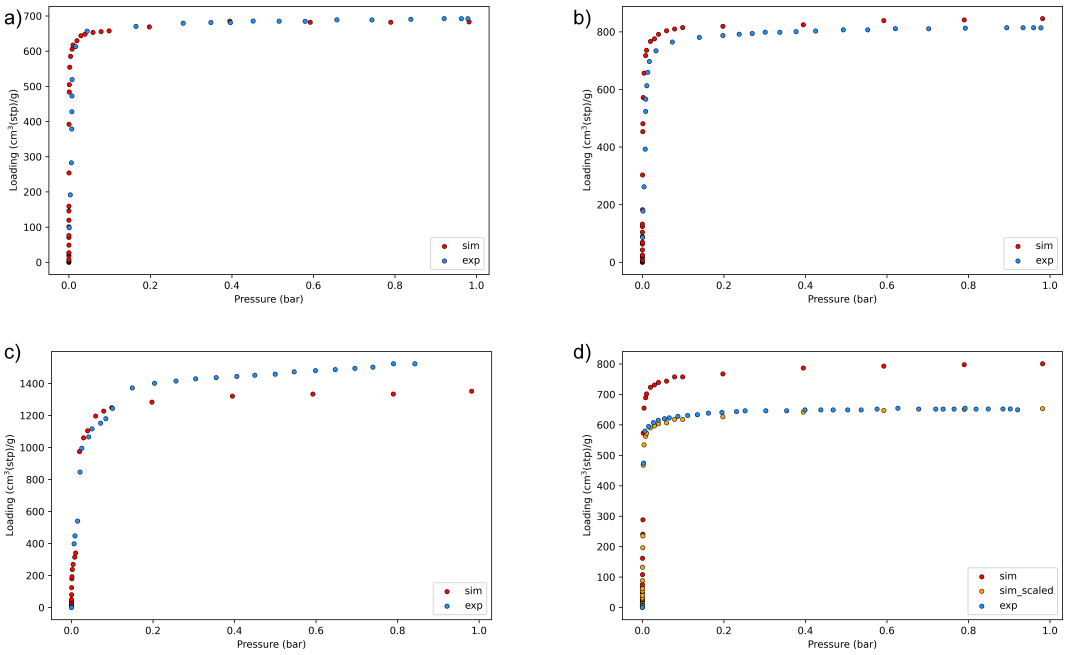


Figure 3.4: *Examples of the experimental and simulated N_2 gas adsorption isotherms at 77 K for (a)* ***NOTT-101****, (b)* ***NOTT-102****, (c)* ***NU-111*** *and (d)* ***PCN-46***

.

the experimental and simulated BET surface areas with simulations typically predicting a larger surface area than the experimental value. This is because the simulations use perfect crystal structures that are free of defects, adsorbed solvent molecules or collapsed regions of framework which to some extent, may be found in experimental structures. To investigate this further, the difference in specific pore volume (SPV) of the experimental and simulated structures is calculated from the amount of N_2 which they adsorb at $\frac{p}{p_0} \approx 0.99$. The ratio of these values can then provide a scaling factor that can be applied to the simulated adsorption isotherms. For the majority of investigated MOFs, the difference in the SPV is relatively small ($< 5\%$), however, for **PCN-46** the difference in SPV is much larger and can not be considered negligible (experiment - 1.01 cm^3/g, simulated - 1.24 cm^3/g). By rescaling the adsorption isotherm based on the ratio of the experimental and simulated SPVs (Figure 3.4 d), a much better agreement is observed between the adsorption isotherms. Furthermore, a new BET surface area of 2554 m^2/g is calculated from the rescaled isotherm which is in excellent agreement with the experimental value

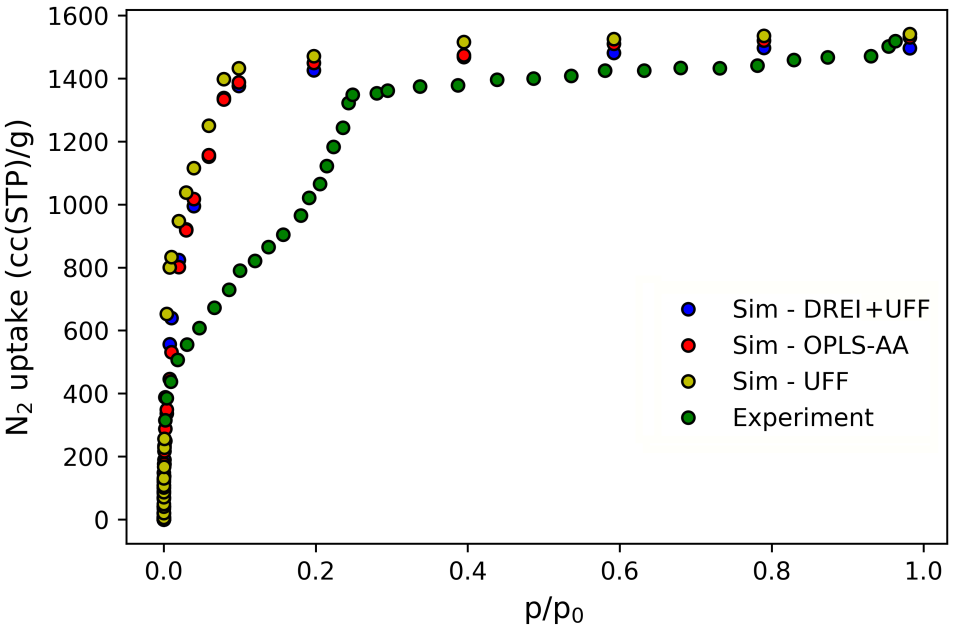


Figure 3.5: *Comparison of experimental (green circles) N_2 gas adsorption isotherm for NOTT-119 with predictions from GCMC simulations employing DRIEIDING and UFF (blue circles), the OPLS-all atom force-field (red circles) and the UFF (yellow circles).*

of 2500 m^2/g. Despite it's success, it should be reminded that the scaling factor does not provide an exact correction between the simulated and experimental results. For example, the accuracy of the simulated adsorption isotherm is also strongly dependent on the accuracy of the employed intermolecular potential. While this correction appears to work well for **PCN-46**, it was observed that many of the investigated MOFs in this work have small differences between their experiment and simulated SPVS. Interestingly, the SPV of NU-111 is found to be approximately 14% smaller than its experimental value, resulting in a smaller N_2 uptake near to p^0 (Figure 3.4 c). Therefore these differences elude to different deficiencies in the simulation model such as the presence of defects that increases the SPV or even subtle changes to the crystal structure that are not capture by a rigid model.

In the case of **NOTT-119**, a larger than anticipated discrepancy between the experimental and simulated BET surface areas is found. Upon inspection of the adsorption isotherms, it is clear that the experimental isotherm of **NOTT-**

119 shows type IV behaviour with a pore filling step at $\frac{p}{p_0} = 0.25$ (Figure 3.5). However, the simulations using a combination of DREIDING and UFF predict a sharp increase in nitrogen adsorption at $\frac{p}{p_0} < 0.08$ followed by a plateau in loading. This shape is more consistent with a type Ib isotherm, which is usually recorded for materials with wide micropores[1]. It should be noted that type I isotherms are also frequently observed in the experimental and simulated adsorption isotherms of many other investigated MOFs (Figure 3.4) According to BET theory, monolayer formation is predicted to occur at $\frac{p}{p_0} \approx 0.11$, correlating to a 68% or $\approx$ 560 cc(STP)/g difference in N_2 gas loading between the experimental and simulated uptakes. Simulations using generic force-fields such as OPLS-aa[134] and UFF also fail to capture the correct experimental isotherm shape. Despite this disagreement, simulation snapshots were collected as it is later demonstrated that they can still remain useful for the trend analysis.

The surface areas recorded in Table 3.1 show that for the **rht** topology, the BET method tends to predict larger values than the geometric method, while the opposite trend is observed for the **nbo** topology. It is believed that these trends arise as a consequence of PFC, which leads to overestimation of BET surface areas in some MOFs. To verify this, simulation snapshots at the pressure of monolayer formation (determined from the consistency criteria) are analysed using a nearest neighbour algorithm. Molecules in contact with the pore walls are part of the BET monolayer and are highlighted in blue, while pore-filling contaminants are highlighted in green (Figure 3.6).

For MOFs with the **nbo** topology, small amounts of PFC are observed which can be attributed to the narrow micropore widths in these materials. The surface adsorption of N_2 in these MOFs saturates the majority of the pore, leaving minimal space for a few additional molecules to adsorb. Of the four MOFs, **PCN-16** possesses the smallest amount of PFC, in which 3.00 N_2 molecules per unit cell (2.6%) are erroneously included into the calculation of the monolayer capacity. As the linker size is increased, a small increase in

Table 3.1: A list of the experimental and simulated surface areas for each of the nine investigated MOFs

					pore-filling contamination analysis			
		BET SA (m^2/g)			method 1		method 2	
MOF	topology	exp	sim[a]	ASA[b] (m^2/g)	SA (m^2/g)	%[c]	SA (m^2/g)	%[c]
NOTT-101	**nbo**	2316	2738 ± 6	3110 ± 17	2556	3.9	2894	3.4
PCN-16		2273	2611 ± 6	2772 ± 12	2596	2.6	2772	2.6
NOTT-102		2942	3348 ± 9	4084 ± 9	3242	4.9	3520	4.6
PCN-46		2500	3129 ± 9	3487 ± 9	3066	5.3	3245	7.3
NOTT-112	**rht**	3800	4039 ± 36	3689 ± 3	3568	14.0	3794	15.8
PCN-61		3000	3512 ± 10	3419 ± 3	3268	12.7	3470	10.9
NOTT-119		4118	6022 ± 221	4476 ± 5	4397	29.5	4475	31.4
NOTT-116		4664	5276 ± 74	4296 ± 5	4171	22.6	4319	25.3
NU-111		5000	5249 ± 58	4559 ± 7	4275	19.4	4522	23.2

SA - surface area; ASA - accessible surface area; [a] error calculated from linear regression analysis; [b] error calculated over 10 independent Monte Carlo runs; [c] (number of pore-filling contaminants divided by the total number of adsorbed nitrogen molecules) x 100%.

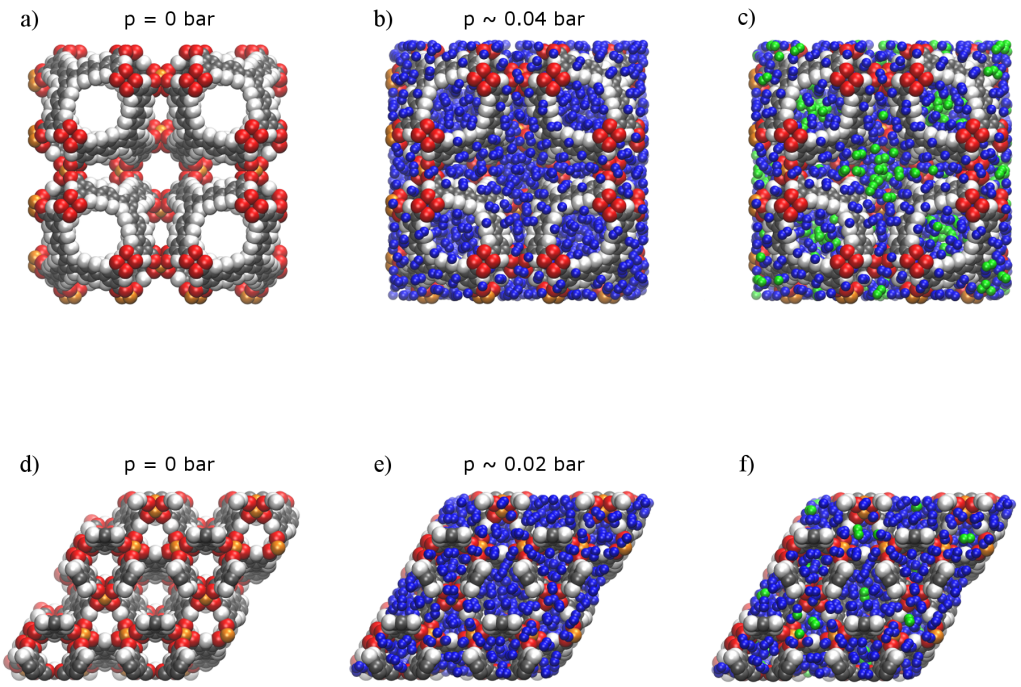


Figure 3.6: *Illustration of pore-filling contamination in* ***NOTT-112*** *(a-c) and* ***NOTT-102*** *(d-f): empty unit cells of* ***NOTT-112*** *(a) and* ***NOTT-102*** *(d) along the c-axis; a snapshot of the unit cell corresponding to monolayer formation at* $\frac{p}{p_0}$ *= 0.0395 bar for* ***NOTT-112*** *(b) and at* $\frac{p}{p_0}$ *= 0.0197 bar for* ***NOTT-102*** *(e);* N_2 *molecules which contribute to pore-filling contamination are highlighted in green (c), (f),* N_2 *molecules in each snapshot are scaled to 60% of their van der Waals size.*

the amount of PFC affecting the BET calculation is observed. **NOTT-101**, **PCN-46** and **NOTT-102** contain 5.00, 8.00 and 9.25 N_2 molecules per unit cell, respectively, which contribute to PFC; the positions of these molecules are typically found to reside at the centre of each pore as illustrated in Figure 3.7.

In contrast to these trends, the snapshots of MOFs with the **rht** topology show much larger proportions of PFC. These MOFs contain three different pore types, whose diameters range between 1.0 and 2.4 nm. Consequently, surface adsorption in the larger pores can overlap quite strongly with pore-filling or saturation of the smaller pores, leading to high levels of PFC. Although the consistency criteria were employed for all calculations, the snapshots at the monolayer formation pressure indicate that pore-filling can occur in the largest pore, even before surface saturation (Figure 3.8). The overlap of surface

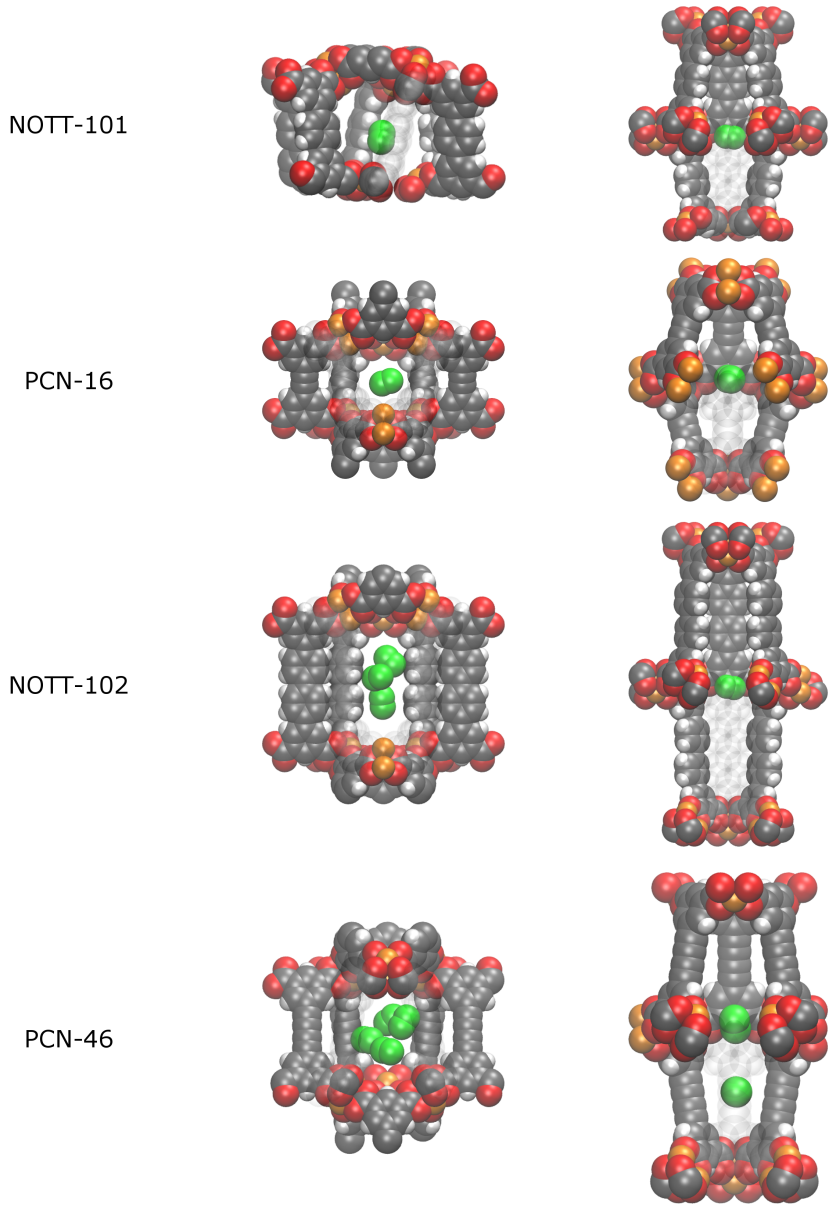


Figure 3.7: *Example positions of pore-filling contaminant N_2 molecules (highlighted in green) in the small and large pores of MOFs with the* ***nbo*** *topology*

adsorption with pore-filling is also evident from the BET C values of the **rht** MOFs. These range from 191 to 682, suggesting a vague boundary between mono-layer and multi-layer adsorption, increasing the likelihood of observing PFC. By combining these pieces of evidence, it becomes clearer why large proportions of PFC are observed in each snapshot of the **rht** MOFs. Of the five **rht** MOFs studied, **PCN-61** possesses the smallest amount of PFC. While only 12.6% of the adsorbed N_2 molecules are found to be pore-filling contaminants, this equates to 95 N_2 molecules per unit cell in absolute terms - ten

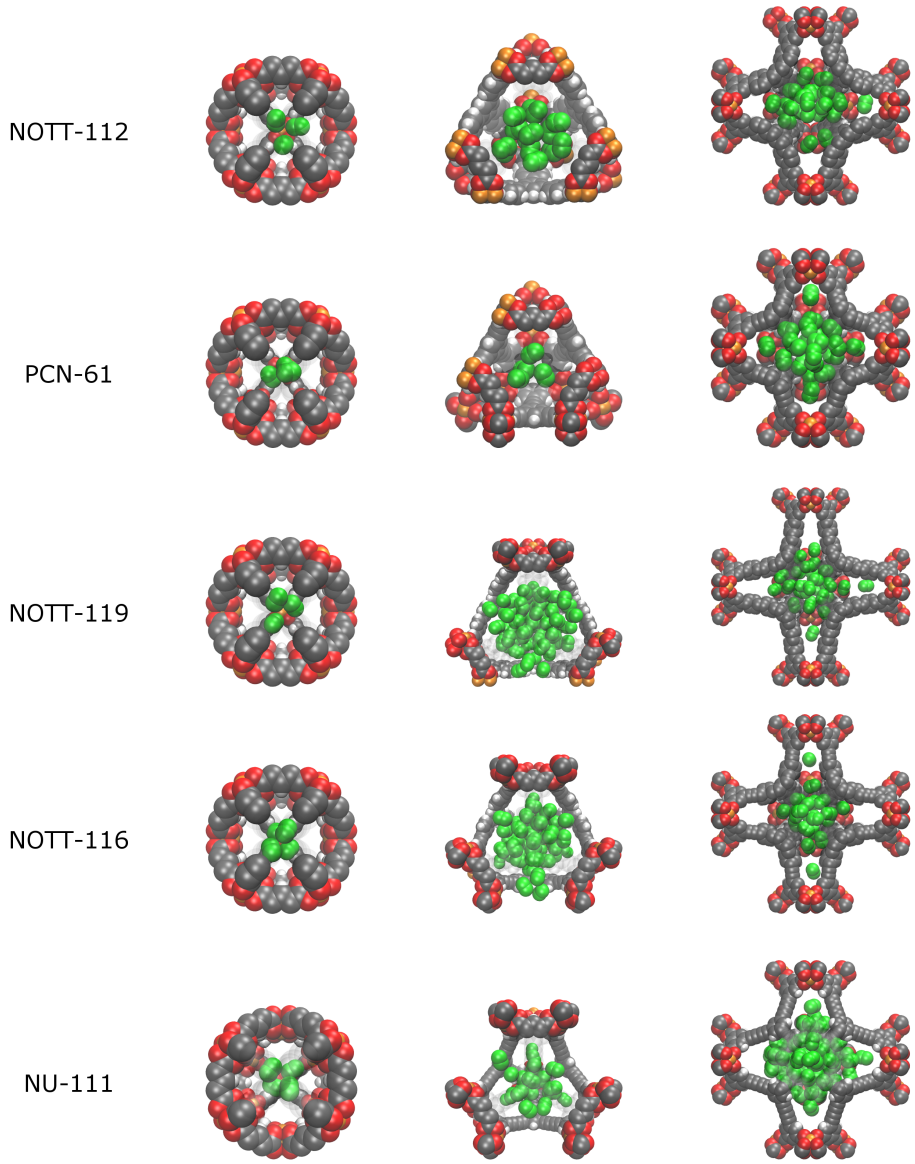


Figure 3.8: *Example positions of N_2 molecules (highlighted in green) that contribute to pore-filling contamination in the small (spherical), medium (tetrahedral) and large (octahedral) pores of MOFs with the* ***rht*** *topology*

times larger than the worst affected **nbo** MOF, **NOTT-102**. In the selected MOFs with **rht** topology, the amount of PFC also rises with increasing ligand length and pore size, i.e. **PCN-61** < **NOTT-112** < **NU-111** < **NOTT-116** < **NOTT-119**. The large proportions of PFC recorded for **NOTT-119** are expected to be over-estimated, based on the mismatch in shapes of the experimental and simulated isotherms. However, based on the other four MOFs with **rht** topology, PFC is still expected to have a large impact on the accuracy of the **NOTT-119** BET surface area.

Although each monolayer capacity has been derived from linear regions that fulfil or minimise the error within the consistency criteria, it has been shown so far that the BET surface area can still be susceptible to error from PFC. This evidence prompts a more accurate determination of the BET surface area by recalculating its value after the removal of any pore-filling contaminant N_2 molecules (referred to as method 1 in Table 3.1). For the MOFs with **nbo** topology, the corrections to the BET surface areas are quite subtle, ranging from 15 – 180 m^2/g. However, for the MOFs with **rht** topology, large reductions in surface area are observed, with **NOTT-119**, **NOTT-116** and **NU-111** decreasing by more than 1000 m^2/g. While this correction leads to a general improvement, there are still some noticeable differences between each materials ASA and their corrected BET surface areas. As discussed previously, most BET calculations assume that the adsorbed monolayer occupies the surface in a close-packed state. However, this packing may be changed or influenced across different surfaces leading to a different value of the nitrogen adsorption cross-section area, σ. A more in-depth discussion of this point is made in Appendix A-3. In previous work,[194] it has been shown that the accuracy of this assumption may be improved by using snapshots at the saturation pressure, p_0. At p_0, it is expected that the N_2 adsorbed in the pores packs like a liquid, such that the previously used σ value is more accurate and can be used to estimate the maximum number of N_2 molecules that form a close packed monolayer. This method has also been shown to give very similar surface areas to the geometric ASAs, over a range of different topologies. The monolayer capacity from this method can be calculated by counting the total number of N_2 molecules in contact with the pore walls at p_0. As such, the method relies very little on the assumptions of the BET theory and the calculation uses a very similar methodology to that of a geometric calculation. The surface areas determined using these monolayer capacities correspond to a more accurate upper limit of surface area, that can be achieved from a perfect crystal structure. This method was employed in this study to observe the difference that is

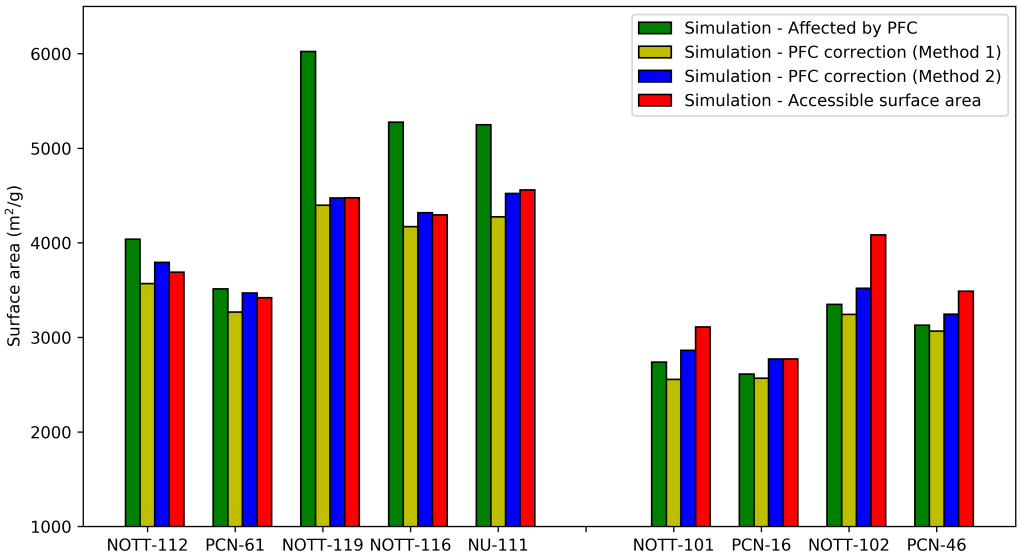


Figure 3.9: *Comparison of the simulated surface areas for each investigated MOF.*

made to the corrected surface area when the packing of the monolayer is also considered. This is referred to as method 2 in Table 3.1 and 3.2.

Using method 2, an excellent agreement between the ASAs and the PFC corrected surface areas is observed for all nine MOFs (Figure 3.9). This suggests that these surface areas provide a more accurate characterisation than those affected by PFC. For a few MOFs, the PFC corrected surface areas are found to be larger than their geometric ASAs. As many ASA calculations use hard-sphere probes, it can mean that the probe is not always able to fully access certain areas of the framework. However, these areas may be fully accessible to the softer N_2 molecules used in GCMC simulations, leading to an overall larger surface area. While the agreement between the geometric method and method 2 is very good, the computational expense of method 2 is much greater than it is for calculating an ASA. However, the use of a hard-sphere probe for the ASA calculation does not always provide accurate surface areas. As a result, method 2 can be used to verify the ASA results and it provides an alternative method for calculating accurate surface areas when the geometric method fails to do so. Alternatively, the corrections applied using method 1 are able to provide surface areas in satisfactory agreement with the ASA of the MOFs with **nbo** topology and excellent agreement for the MOFs with **rht**

topology.

3.2.3 Phenyl-Alkyne substitutions

With the excellent agreement between the ASA and PFC-corrected surface areas, it is now possible to accurately study how the SSA of a MOF changes when replacing phenyl rings with alkyne moieties. Due to the good agreement between the experimental surface areas and the simulated values before correcting for PFC, these findings can provide a fresh insight into the influence which PFC has had on the experimental trends. For this analysis, the PFC-corrected surface areas from method 2 are employed as they also provide an better overall agreement with the ASA of each studied MOFs.

Table 3.2 contains experimental and simulated results that measure the difference in surface area between MOFs containing phenyl moieties and MOFs that replace them for alkyne groups. A positive change in Table 3.2 implies that the SSA is increased by substituting the phenyl groups for alkynes, while a negative change implies a decrease in the SSA. It may be noted that the comparison of two experimental surface areas can be influenced by both PFC and the quality of the sample. The presence of defects, adsorbed solvent or collapse regions of framework may be present in one sample more than others, leading to a biased comparison. However, by using perfect crystals and accounting for PFC, a more balanced comparison can be made, which in this work can be used to assess the efficiency of replacing phenyl moieties with alkyne groups. Due to the small amounts of PFC present in each MOF with **nbo** topology, a good agreement between the experimental and simulated BET surface areas is generally observed, regardless of any PFC corrections to the surface area (Table 3.2). In contrast, the higher levels of PFC present in each MOF with **rht** topology is expected to strongly influence the SSA calculation, which will also impact how efficient the strategy of replacing phenyl rings for alkynes groups is. In these MOFs, it is expected that the comparisons

Table 3.2: Comparison of the changes in surface area that occur from substituting phenyl rings for alkyne groups

			change in SA (m^2/g)			
			BET SA [c]		PFC corrected SA	ASA
MOFs[a] [*]	topology	A:P [b]	exp	sim	sim - method 2	sim
NOTT-101 → PCN-16	nbo	1:1	–43	–338	–122	–338
NOTT-101 → PCN-46		2:1	+184	+377	+351	+377
NOTT-102 → PCN-46		1:1	–442	–219	–275	–597
NOTT-112 → PCN-61	rht	1:1	–800	–527	–324	–270
NOTT-112 → NU-111		2:1	+1200	+1210	+728	+870
NOTT-119 → NOTT-116		1:1	+546	–746	–156	–180
NOTT-119 → NU-111		1:1	+882	–733	+47	+83
NOTT-116 → NU-111		1:1	+336	–27	+263	+203

[*] alkyne based MOFs shown on the right of column, phenyl based MOFs shown on the left of column. The arrow indicates the direction of transformation when replacing ligand phenyl rings for alkynes; [a] differences shown in columns 4 – 6 are reported by subtracting the surface area of alkyne based MOF from the phenyl based MOF.; [b] ratio showing the number of alkynes replacing each phenyl per ligand, e.g. 2:1 means 2 alkynes have replaced one phenyl; [c] simulated surface areas are those which are not corrected for pore-filling contamination; PFC – pore-filling contamination; SA – surface area; ASA – accessible surface area; exp – experimental surface areas; sim – simulated surface areas.

generated from the ASAs and PFC-corrected surface areas provide a more reasonable assessment of this strategy, which appears to be less efficient than previously suggested through experimental analysis.

For both topologies, the changes to the SSA are strongly dependent on the number of substituted alkynes. To help explain these trends, the SSA is expressed using a different representation that uses the product of the number of unit cells per gram and the total surface area of each MOFs unit cell. These quantities can be directly extracted from the crystal structure and the computation of the surface area, making it simple to compare how the unit cell, mass and total surface area change when substituting phenyl rings with alkyne groups (Table 3.3). As a single phenyl ring has more than three times the mass of an internal alkyne, replacing any phenyl with three or less alkynes results in a reduced unit cell mass and an increase in the number of unit cells per gram. The SSA is also dependent on the total surface area of the unit cell - In general, this is affected by the size of the ligands and their accessibility for adsorption. As each alkyne is smaller than each phenyl ring, the coupling of multiple alkynes is required to increase the unit cell surface area when replacing phenyl rings. For example, **PCN-46** has two alkyne groups and **NOTT-101** has one phenyl ring per ligand. By coupling two alkynes together, **PCN-46** has a lower mass and longer ligand length than **NOTT-101**, affording a larger unit cell surface area, a greater number of unit cells per gram and a larger SSA (Table 3.3).

When a phenyl ring is substituted for a single alkyne, the decrease in unit cell mass is generally too small to offset the decrease in the unit cell surface area, resulting in a reduction in SSA. However, **NU-111** shows an exception to this trend when compared with **NOTT-119** - experimental analysis suggests that the BET surface area of **NU-111** is $\sim$20% larger than **NOTT-119**. In this work, it is shown that the BET surface area of **NU-111** and **NOTT-119** can be overestimated by PFC, and that these MOFs possess very similar SSAs. This result is also confirmed by comparing their ASAs, which show a

Table 3.3: A list of the calculated contributions to the SSA, crystal structure symmetry and dimensions for each MOF

MOF	UC per gram (x10^{19})	total ASA of UC (Å^2)[a]	total PFC–corrected SA of UC (Å^2)	crystal symmetry	a (Å)	c (Å)
NOTT-101	12.65	2459 ± 13	2288	hexagonal	18.6297	38.4920
PCN-16	14.02	1976 ± 9	1976		18.8370	32.1200
NOTT-102	11.06	3693 ± 8	3183		18.4335	52.3640
PCN-46	13.35	2612 ± 7	2430		18.2386	42.0490
NOTT-112	1.92	19261 ± 18	19813	cubic	47.0050	–
PCN-61	2.28	15020 ± 12	15244		42.7958	–
NOTT-119	1.55	28792 ± 34	28787		56.2960	–
NOTT-116	1.78	24077 ± 28	24203		51.6700	–
NU-111	2.09	21772 ± 32	21595		48.8930	–

[a] error in ASA is calculated over 10 independent Monte Carlo simulations; ASA – accessible surface area; PFC – pore-filling contamination; SA – surface area

small 83 m^2/g difference between the two MOFs. Close inspection of Table 3.3 indicates that the unit cell surface areas of **NU-111** and **NOTT-119** differ by ~7000 $Å^2$, equating to a 24% reduction in surface area. However, this is met by a reduction in unit cell mass which provides **NU-111** with an additional 5.4×10^{18} unit cells per gram (~35% increase over **NOTT-119**). The overall impact is that the reduction in unit cell surface area is marginally offset by the reduction in mass which provides the small increase in the SSA observed in Table 3.3.

From the results shown in Tables 3.2 and 3.3, the substitution of phenyl rings for alkynes can be viewed as a valid approach to increasing SSA in two scenarios. The first scenario is when a single phenyl ring is substituted for two or more alkyne groups. This provides an increase in unit cell surface area and a decrease in mass, resulting in a large SSA change. However, if the reduction in mass is large enough to compensate the reduction in unit cell surface area, it is also possible to observe increases in the SSA from substituting phenyls and alkynes in a 1:1 ratio. Although, this remains a valid approach to increasing SSA, the results from the simulations suggest that this process is not as efficient as previously suggested from experimental BET analysis.

3.2.4 Conclusions

In summary, GCMC simulations were employed to determine how PFC affects the BET surface area calculation of nine MOFs. While, the experimental and simulated BET surface areas generally agree, a poorer agreement between the simulated BET surface areas and accessible surface areas is observed. Assuming this to be the effect of PFC, GCMC simulation snapshots were used to measure the amounts of PFC in each MOF by calculating the distance of each N_2 molecule from the pore walls. The molecules which do not adsorb onto the pore walls were classified as pore-filling contaminants and deemed responsible for the over-estimation of the BET surface area. As each MOF

with **nbo** topology considered in this work possesses narrow micropores, PFC provides a negligible difference to their BET surface areas. However, a much larger overestimation of the surface area is found for MOFs with **rht** topology due to the multiple pore sizes which are susceptible to large amounts of PFC. Correcting the BET calculation for the effects of PFC is achieved by using two methods - in the first method, each pore-filling contaminant is simply removed and the monolayer that remained in the snapshots at the predicted monolayer formation pressure is used to recalculate the surface area. Due to the poor assumption of the monolayer packing in this method, an alternative approach which uses snapshots from the saturation pressure is also employed. By removing the molecules that are classed as pore-filling contaminants in these snapshots, a denser monolayer is observed which provides a more accurate calculation of the surface area using a close-packed monolayer assumption. This method employs a similar methodology to a geometric surface area calculation. The PFC-corrected surface areas that are obtained from the second method are found to be in excellent agreement with the ASAs, validating the results that are obtained from both of these methods. In addition, the short amount of time required to assess PFC in a GCMC snapshot suggests that this analysis could be routinely calculated for many adsorbents. While, the experimental BET surface area of a MOF may be affected by its crystal quality and the frameworks susceptibility to PFC, these simulated surface areas provide a fair even comparison between each investigated MOF, eliminating any deceptive trends that may arise as a result of PFC. Overall, the simulation results show that replacing phenyls with smaller alkynes is a valid approach to increasing the SSA when multiple alkynes are used. However, the relative gain in SSA is generally much smaller than predicted from experimental results. This is rationalised by expressing the SSA as a product of the number of unit cells per gram and the total unit cell surface area, showing how alkynes provide much lighter unit cells, which is the main driving force for the gains in SSA.

3.3 Analysing the PFC effect in small and large pores

In the section 3.2, two methods were presented to quantify and account for the amount of PFC that affects the BET surface area calculation of a material. While only a small number of MOFs were studied, it became clear that PFC impacts MOFs differently depending on their structural properties. To better understand the link between the PFC effect and the pore size of different materials, this chapter is concluded with a short investigation in which the BET surface area of large, diverse set of MOFs is performed. The main objectives of this investigation can be summarised into the following queries:

- How does the influence of PFC change as a function of pore size?
- Can the BET linear regression analysis of different materials provide information on their relative amounts of PFC?
- How well do the different methods of SA calculation compare to one another for different materials?

In order to facilitate the selection of a diverse set of materials, the MOFs in this study were chosen from a group of top-performing materials that were identified during a high-throughput screening study for biogas upgrading, as described in chapter 4. With the additional consideration of the computational time required to compute a full N_2 adsorption isotherm in each structure, a total of 1248 MOFs were selected for this study. These were separated into a small pore diameter (SPD) and large pore diameter (LPD) group based on their LCD. The SPD group of MOFs contains 1143 structures with pore diameters ranging between 4.1 Å and 15.0 Å, while the LPD contains 105 structures with pore diameters ranging between 15.0 Å and 30.8 Å. The small number of MOFs in the LPD arises from two reasons: 1) the screening described in chapter 4 primarily identified microporous materials as top performing candidates for

biogas upgrading; 2) mesoporous MOFs require substantially longer simulation times to simulate full N_2 isotherms than microporous MOFs due to their larger gas uptake properties. Therefore, a much smaller sample of MOFs in the LPD group was selected but still provides a respectable sample size to compare and contrast with the SPD group of materials.

3.3.1 Computational Details

The BET surface area of each MOF in this study is calculated using the same computational setup described in section 3.2.1 with a few changes. Given the high-throughput nature of this work, it became more appropriate to employ the RASPA simulation package of Dubbeldam *et al* for GCMC simulations.[199] Adsorption isotherms that are computed using both software packages were found to be in excellent agreement with one another, as demonstrated for NOTT-101 in figure 3.10. In addition, the UFF is employed to describe all LJ interactions with a cut-off of 12.8 Å to improve the computational efficiency of the calculations. A single GCMC simulation consists of 2000 initialisation cycles followed by 2000 production cycles - 1 cycle is equal to min(N, 50) steps, where N is the number of adsorbates within the simulation cell. A geometry-based analysis of structural properties such as the PLD, LCD and ASA is performed for each MOF using the high-throughput Zeo++ software package.[169] A recent study by Sarkisov and co-workers[200] has shown that these software packages are able to reproduce many structural properties such as the ASA, PV, PLD and LCD in excellent agreement with one another. For the remainder of this chapter, a method X surface area corresponds to a PFC-corrected BET surface area using method X, where X = 1 or 2.

3.3.2 Small pores: $(4.1\mathring{A} \leq \boldsymbol{d} \leq 15.0\mathring{A})$

The SPD group of MOFs in this study contains 1143 structures with calculated BET surface areas ranging between 92 and 2989 m^2/g. Using the two previ-

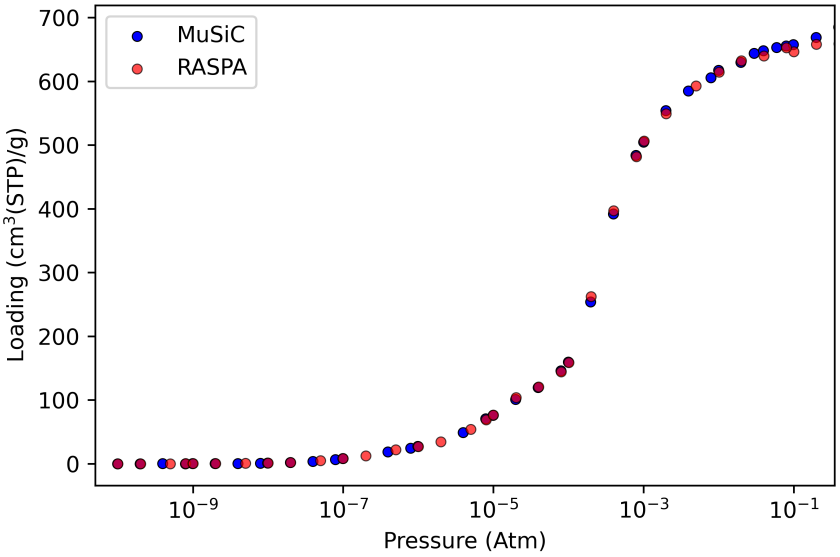


Figure 3.10: *A comparison of simulated N_2 adsorption isotherms for NOTT-101 using the MuSiC (blue circles) and RASPA (red circles) software packages.*

ously described methods in section 3.2.2, each BET surface area is adjusted to account for the effects of PFC. In general, it is clear that these materials are susceptible to relatively low levels of PFC giving rise to the very close agreement between the BET surface areas and the PFC-corrected surface areas using method 1 or method 2 (Figure 3.11). For the comparison with method 1 surface areas (Top of Figure 3.11), each MOF is coloured based on the the difference between the BET and PFC-corrected surface areas. Upon close inspection, 715 MOFs are found to possess a difference that is smaller than 20 m^2/g and 687 of these have no PFC contribution at all, implying that these difference may arise from the error in the linear regression analysis.

In the remaining 428 MOFs, PFC has a non-negligible impact on their BET surface areas with many of the larger contributions occurring in MOFs that possess LCD's $\geq$ 10Å (Figure 3.12). One notable example is MIL-68(Fe) (REFCODE: XADCOW) which possesses a BET surface area of 1669 m^2/g. This material consists of chains of $Fe(OH)_2(O)_4$ SBUs that extend along the c-axis and are coordinated by terephthalate ligands, affording small triangular and large hexagonal pores (Figure 3.13a). The simulated N_2 adsorption

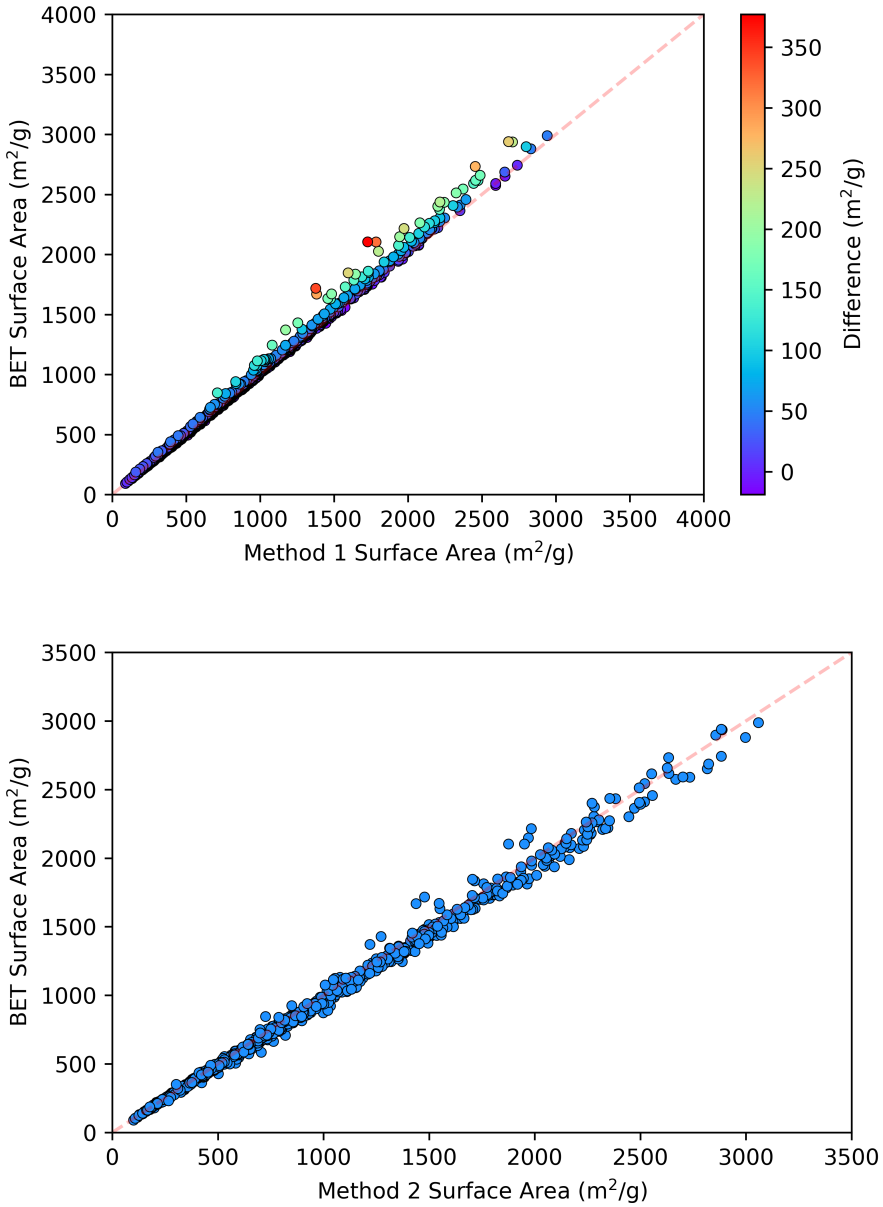


Figure 3.11: *A comparison of the BET surface areas and PFC-corrected surface areas using method 1 (top) and method 2 (bottom) in 1143 MOFs. Each point represents a different MOF structure and the colour is attributed to the difference between the two surface areas*

isotherm for this MOF is shown at the top of Figure 3.13, showing a shape that is consistent with a type I isotherm. The small step between 10^{-9} and 10^{-7} bar corresponds to the filling of the small triangular pores, while the larger step beginning at 10^{-5} bar corresponds to adsorption in the larger hexagonal pores. By applying the PFC-correction scheme to each point on the isotherm, the monolayer loading can be tracked as a function of pressure (green points).

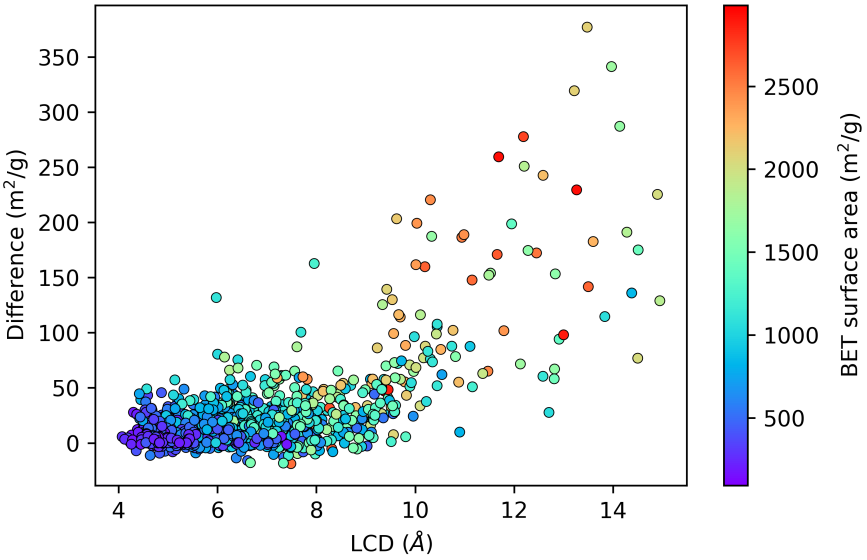


Figure 3.12: *A plot of the difference between a MOFs BET and method 1 surface areas BET surface area versus it's LCD for 1143 MOFs. The colour of each point corresponds to the BET surface area of the MOF.*

At approximately 2 $\times$ 10^{-3} bar, there is a deviation between the monolayer loading and the total amount of gas adsorbed indicating the presence of pore-filling contaminants. The BET surface area calculation predicts the pressure of monolayer formation ($P_{monolayer}$) at approximately 0.02 bar (red dashed line), indicating that the presence of pore-filling contaminants. Analysis of the GCMC simulation snapshots at $P_{monolayer}$ shows sizeable quantities of N_2 situated near the centre of the hexagonal pores (Figure 3.13b,d) which contribute to the surface area overestimation by 287 m^2/g. Removing these from the calculation leads to a method 1 surface area of 1382 m^2/g - in excellent agreement with the materials ASA of 1442 m^2/g. Furthermore, as the monolayer loading near plateaus at $P_{monolayer}$, there is only a small 56 m^2/g difference when accounting for the monolayer packing as seen in the method 2 PFC correction.

After activation at 573 K for 24 hours, the experimental BET surface area of MIL-68(Fe) is determined to be 665 m^2/g - much smaller than the simulated values in this work.[201] The authors attributed the differences between experimental and simulated values to two main factors: (1) the DMF solvent molecules may not be able to fully evacuate the pores leading to partial acti-

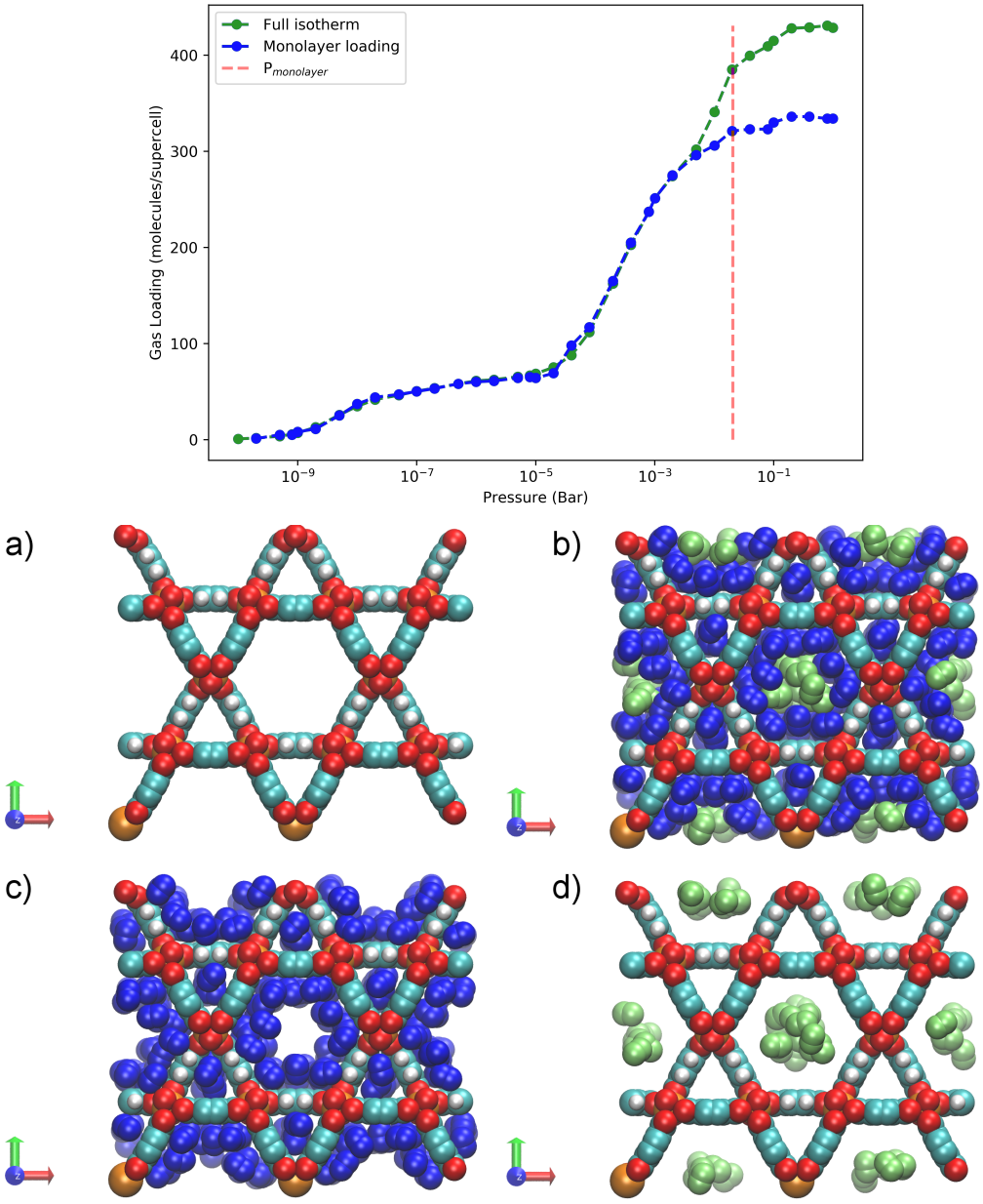


Figure 3.13: *Top - Simulated N_2 adsorption isotherm for MIL-68 at 77 K for the full gas loading (green) and monolayer molecules only (blue). The red dashed line corresponds to the pressure of predicted monolayer formation; Bottom - Images of from GCMC snapshots of the empty MIL-68 (a), and at $P_{monolayer}$ showing the relative amounts of monolayer and pore-filling contaminant molecules (b-d); Colour scheme: White = H, Red = O, Cyan = C, Orange = Fe, Blue = N_2 molecules that form part of the adsorbed monolayer, Lime = pore-filling contaminant N_2 molecules*

vation of the MOF; (2) N_2 molecules may find it difficult to diffuse into the triangular channels which is limited by the slow rotation of the phenyl rings at such low temperatures. As a rigid and idealised crystal structure is employed in this work and the small triangular pores are not physically blocked in each simulation, then it is expected that the N_2 adsorbates will be able to fully

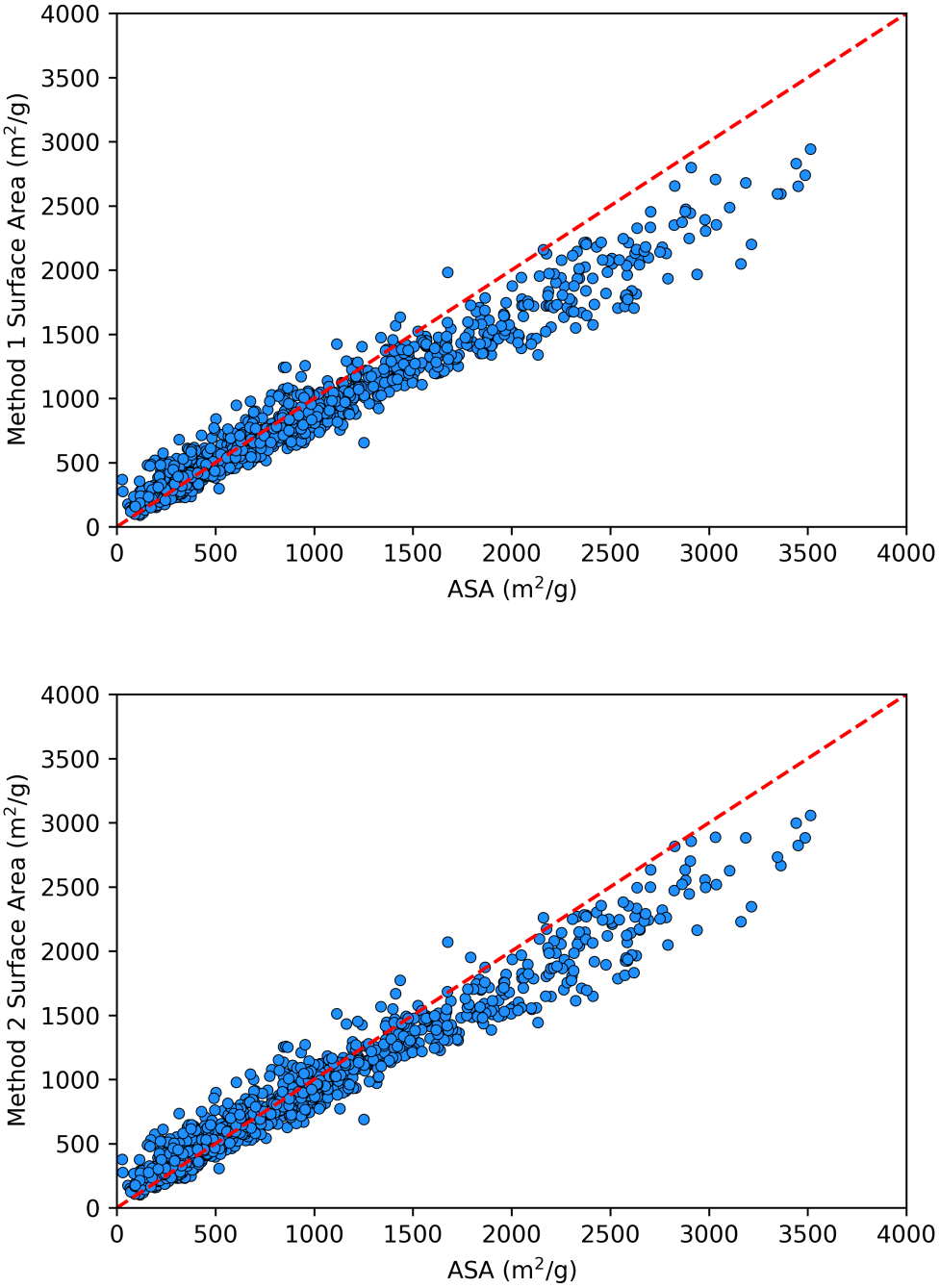


Figure 3.14: *A comparison of the PFC-corrected surface areas using method 1 (top) and method (2) with the ASAs of 1143 MOFs. The red dashed line is the line of unity where y=x*

occupy the channels. GCMC snapshots at $P_{monolayer}$ reveal that up to 8 N_2 adsorbates are able to occupy each of the smaller triangular pores per supercell - equating to a surface area of approximately 275 m^2/g.

In addition to the comparison with the BET surface area, the method 1 and method 2 surface areas are also compared with the geometrically calculated

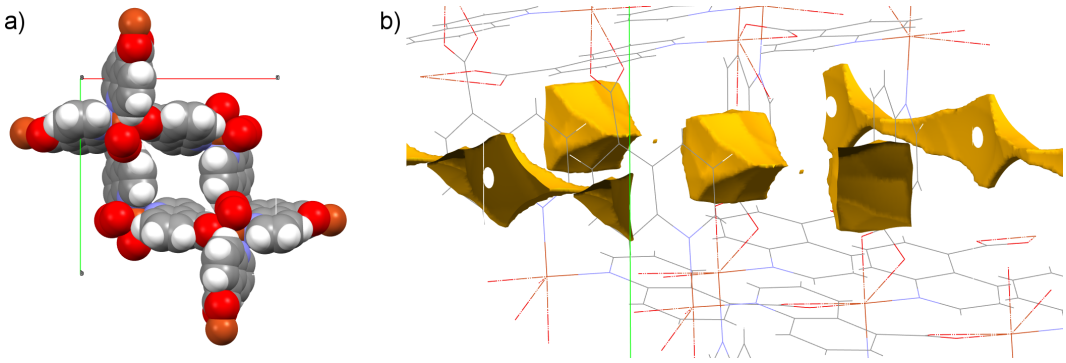


Figure 3.15: *a: unit cell of ARAJEK along the c-axis; b: image showing the volume that is accessible to the N_2 sized probe (yellow regions) in ARAJEK. Colour scheme: White = H, Red = O, Grey = C, Orange = Cu*

ASAs (Figure 3.14). For 701 MOFs, the ASA is calculated to be greater than the method 1 and method 2 surface areas. This arises from the idea that the geometric calculation provides a surface area based on the accessibility of a single probe. However in the GCMC simulations, the adsorbates are influenced by their interaction with the surface and each other which can change the geometry and efficiency of their packing, leading to a smaller predicted surface area.

In the remaining 442 MOFs, the opposite trend is observed where the ASA is calculated to be smaller than the PFC-corrected surface areas. The difference between these surface areas range from 0.52 - 420 m^2/g, although 63% have a relatively small difference below 100 m^2/g. The largest difference is recorded for ARAJEK, which possesses method 1 and method 2 surface areas of 680 and 736 m^2/g respectively, and an ASA of 316 m^2/g. This MOF consists of Cu(II) ions that coordinate quinoline-5-carboxylate ligands to afford a series of square 1-dimensional pores (Figure 3.15) with a PLD and LCD of 3.99 and 6.26 Å, respectively. The ASA calculation performed with Zeo++ indicates that this MOF has a number of pockets that are inaccessible to the probe that have a total surface area of 261 m^2/g. Overall, the surface area of the accessible and inaccessible regions totals 577 m^2/g. It is important to note that GCMC simulations can insert molecules into regions that are inaccessible to hard-sphere particles. Furthermore, the 'softer' nature of the particles can allow

GCMC molecules to pass through small windows that are also inaccessible to hard-sphere particles. Overall, this can lead to a larger surface area than recorded by the geometric calculation.

3.3.3 Large pores: (15.0 $\AA \leq d \leq$ 30.8 $\AA$)

The LPD group in this study contains 105 MOFs with pore diameters in the large micropore and small mesopore range. As such, these materials possess a larger set of BET surface areas than the SPD group, ranging between 902 and 7711 m^2/g. Another difference between the SPD and LPD groups is their BET C parameters which are related to the host-guest interaction strength and provide useful insight into the shape of the isotherm in the BET range. A high value of C (i.e. ≥ 200) is typically associated with high-energy surface sites or the filling of narrow micropores, whereas a low C value (i.e. ≤ 200) indicates that there may be overlap between monolayer and multi-layer adsorption.[5] Therefore, the C value can be used as a rough estimate to ascertain which systems may be susceptible to PFC.

As depicted in Figure 3.16, the SPD group possess very large C values which frequently exceed a value of 10^5 for MOFs with an LCD between 4 and 8 Å. In contrast, 89 MOFs in the LPD group possess a C value that is smaller than 831, corresponding to the smallest C value recorded for the SPD group of MOFs. Both plots show a decaying distribution in which the difference in surface area (an indicator of the amount of PFC) decreases with larger BET C values. Of the previously mentioned 89 MOFs that possess a C value smaller than 831, 57 possess a C value ≤ 200 which suggests these materials are highly susceptible to PFC. To test this idea, the BET surface area of each MOF was adjusted to account for the effects of PFC and are compared in Figure 3.17. For the method 1 surface area comparison, MOFs that posses a C value smaller than 200 are represented by star markers, while those with a C value greater than 200 are represented by circles. While the SPD group exhibited relatively

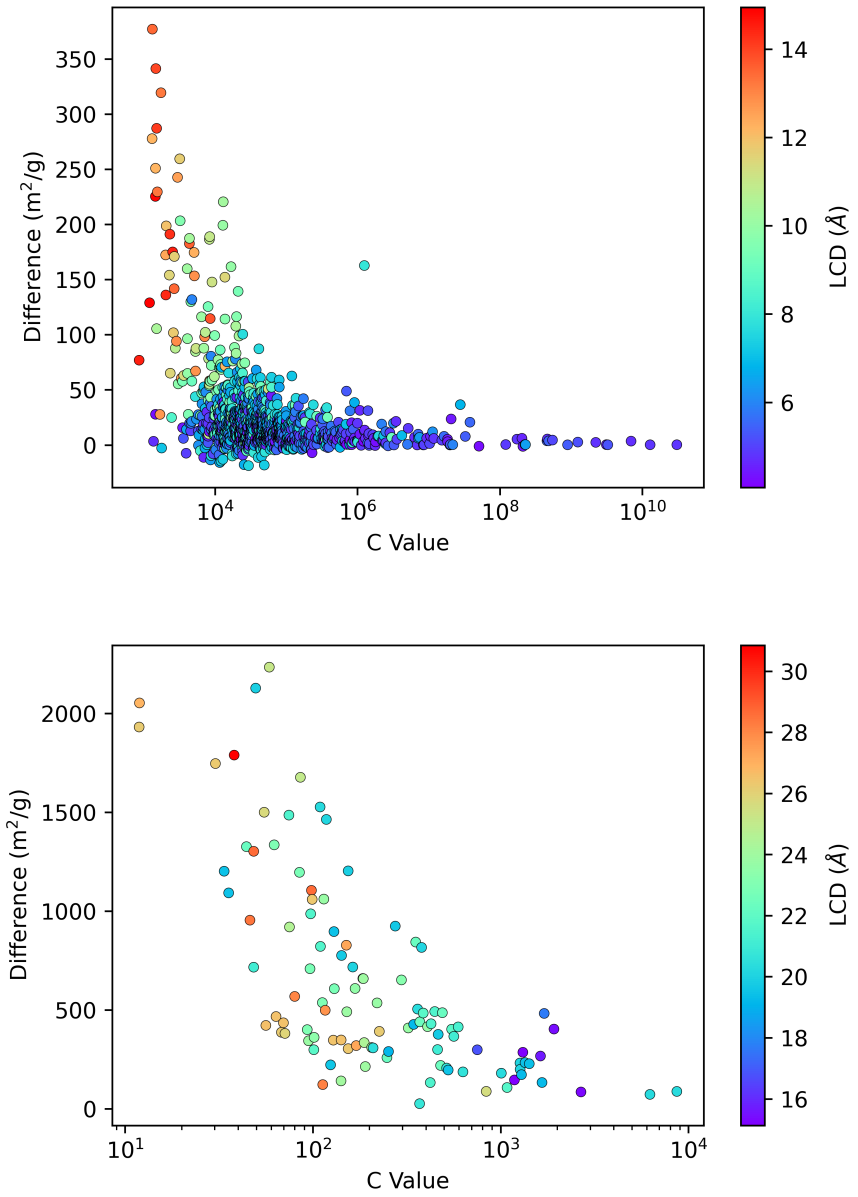


Figure 3.16: *Plots of the surface area difference (BET vs method 1) as a function of the BET C parameter for each MOF in the SPD (top) and LPD (bottom) groups. The colour of each point corresponds to each MOFs LCD.*

small differences between the BET and method 1 surface areas, the LPD group have substantially larger differences due to the higher levels of PFC. A total of 64 MOFs in the LPD group have larger differences than any MOF in the SPD group, of which 21 have a BET surface area that is overestimated by 1000 - 2250 m^2/g and a C value ≤ 200. This reinforces the idea that the C value can be used to initially determine whether a system will be susceptible to PFC.

The two largest BET surface areas in the LPD group belong to AVAKAL02

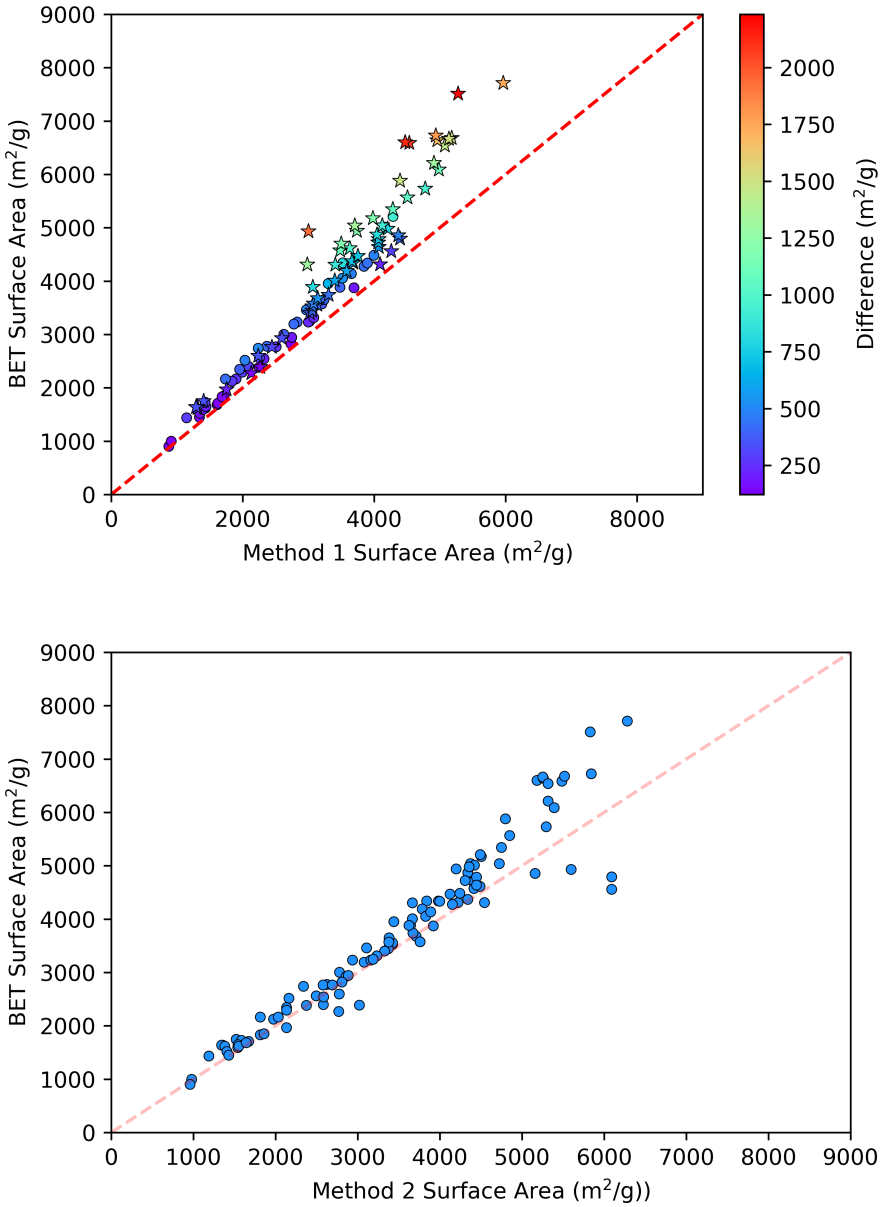


Figure 3.17: *A comparison of the BET surface areas and PFC-corrected surface areas using method 1 (top) and method 2 (bottom) in 105 MOFs. Each point represents a different MOF structure and the colour is attributed to the difference between the two surface areas. The starred structures correspond to those with a C value smaller than 200.*

(7711 m^2/g) and AVAKEP02 (7512 m^2/g), also known as DUT-64 and DUT-77, respectively. Both MOFs contain large icosahedral mesopores that are built from twelve Cu(II) paddle-wheel units and eight ligands.[202] Each of these connected by smaller micropores that are each made from four paddle-wheel units and four ligands (Figure 3.19). Due to the ultra low density of these materials (0.25 g/cm^3), attempts to activate these materials have been unsuccessful

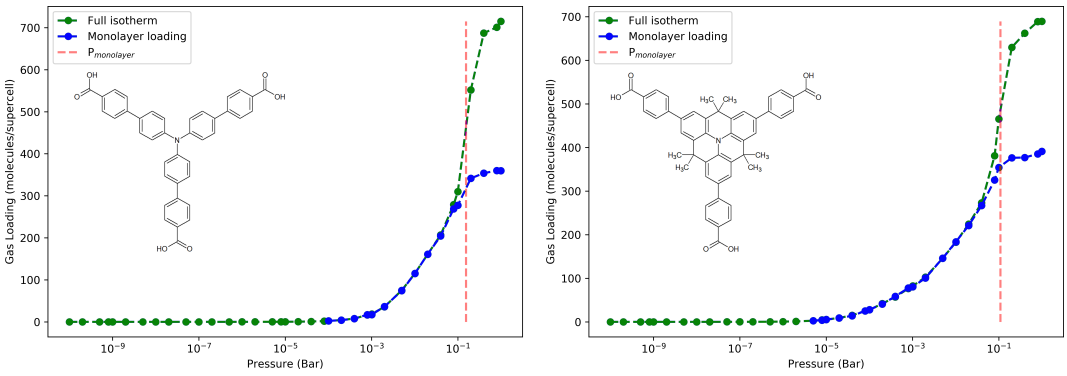


Figure 3.18: *Simulated N_2 adsorption isotherms for a 1x1x1 'supercell' AVAKAL02 (left) and AVAKEP02 (right) at 77 K. Isotherms are recorded for all the adsorbed gas molecules (green) and only those that form part of the adsorbed monolayer (blue) - $P_{monolayer}$ is given by the red dashed line. The hexatopic ligands that create each MOF are shown on the inset of each plot.*

leading to framework collapse. Therefore, computational tools can be applied to provide insight into the theoretical structural properties of these materials. The simulated N_2 adsorption isotherms for these materials are shown in Figure 3.18 - the shape of these indicate type IV isotherms despite the log plot appearance. On each of these isotherms, the monolayer loading calculated from each simulation and the predicted pressure of monolayer formation ($P_{monolayer}$) is also plotted to help visualise how PFC affects these systems. In both cases, $P_{monolayer}$ lies on a steep part of the isotherm and indicates that PFC contributes notably to the surface area calculation. This is further verified from simulation snapshots at $P_{monolayer}$ (Figure 3.19). Both MOFs show large proportions of pore filling contaminants occupying the regions between neighbouring pores and forming a second adsorption layer within the mesopores; overall, this accounts for nearly 30% of the total BET surface area. By applying PFC corrections to the BET surface areas of DUT-64 and DUT-77, a much improved agreement is observed between the ASAs (6227 and 5898 m^2/g), method 1- (5965 and 5278 m^2/g) and method 2-corrected surface areas (6281 and 5829 m^2/g).

Finally, the PFC-corrected surface areas of each MOF in the LPD group are compared with their ASAs in Figure 3.20. Similarly to the SPD group, a large proportion of structures (74%) possess greater ASAs than their PFC-

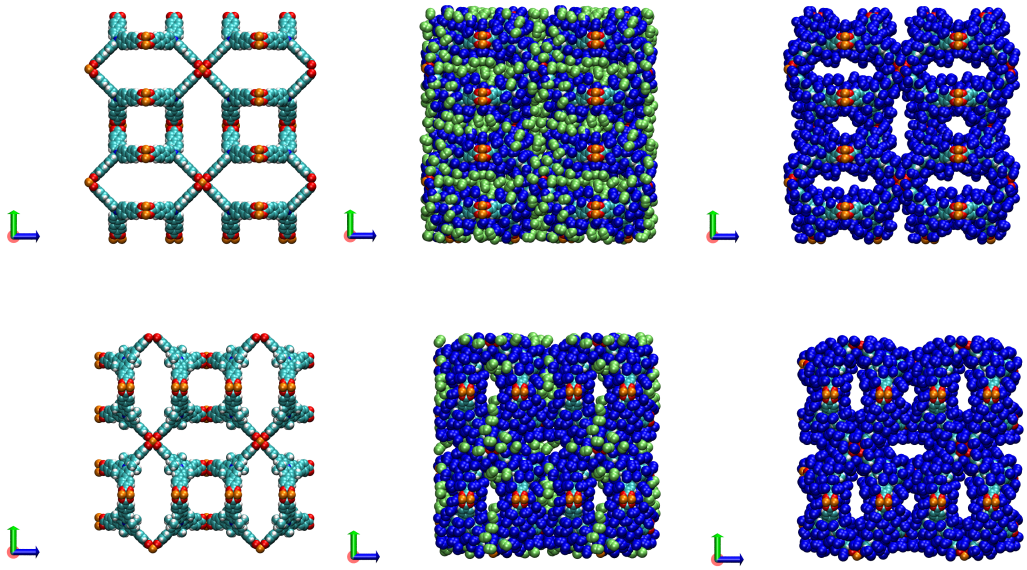


Figure 3.19: *GCMC simulation snapshots of AVAKAL02 (top row) and AVAKEP02 (bottom row) indicating the empty porous host (left), N_2 adsorbed at $P_{monolayer}$ (middle) and the adsorbed monolayer at $P_{monolayer}$ (right); Colour scheme: White = H, Red = O, Cyan = C, Orange = Cu, Blue = N_2 molecules that form part of the adsorbed monolayer, Lime = pore-filling contaminant N_2 molecules*

corrected surface areas. To reiterate, the geometric calculation provides the accessibility of a single hard-sphere probe and is providing little information on how the softer 'real' molecules may pack on the surface or how they will be influenced by surface heterogeneity with respect to the adsorption energy. In contrast to the SPD group, the monolayer packing density is found to play a more substantial role when applying PFC corrections to the surface area of MOFs in the LPD group. One of the most extreme cases to demonstrate this is observed in XAHPUT, a MOF containing large tetracarboxylates with orthogonal chiral diethoxy- functional groups which coordinate to Cu(II) ions forming paddle-wheel SBUs. The 3-D framework contains long square pore channels along the c-axis resulting in a large PFC-corrected surface area of 4261 m^2/g after applying method 1. Close inspection of the GCMC simulation snapshots at $P_{monolayer}$ (0.1 bar) indicate that over 94% of the adsorbed N_2 forms part of the monolayer, however this only accounts for approximately 70% of the monolayer loading found at p^0 suggesting that: (1) The packing of the monolayer at $p_{monolayer}$ is much sparser than at p^0; and/or (2) There are a number of vacant surface sites that may still be occupied by adsorbing

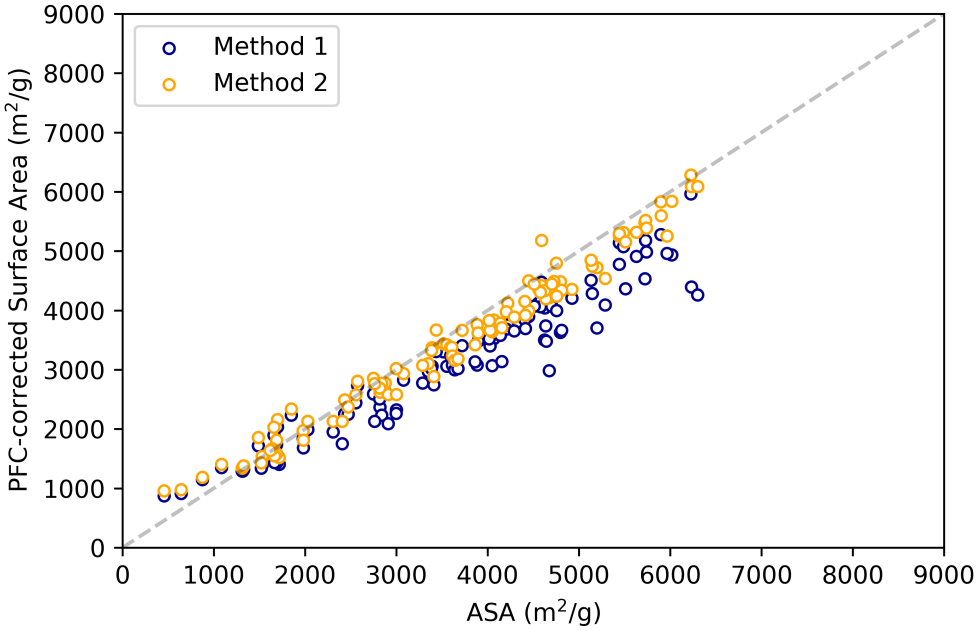


Figure 3.20: *A comparison of the PFC-corrected surface areas using method 1 (blue points) and method 2 (orange points) with the ASAs of 105 MOFs. The red dashed line represents the line of unity where y=x*

N_2 molecules. In comparison to the snapshots taken at p^0 (Bottom of Figure 3.21), it is clear that the packing density of the monolayer increases between 0.1 and 1 bar, leading to a method 2 surface area of 6090 m^2/g which is in excellent agreement with the ASA of 6299 m^2/g.

For systems like XAHPUT, simply removing the pore-filling contaminants from the BET calculation (method 1) may not provide an accurate assessment of the surface area unless the sparser packing of the monolayer is accounted for. In addition to improving the accuracy of the close-packed assumption, the advantage of applying the method 2 correction (i.e. removing PFC from snapshots at p^0) in these scenarios is that it provides a great deal of insight regarding the arrangement and maximum occupation of the monolayer, thus providing a better picture of the upper limit of surface area that can be accessed by softer 'real' adsorbates.

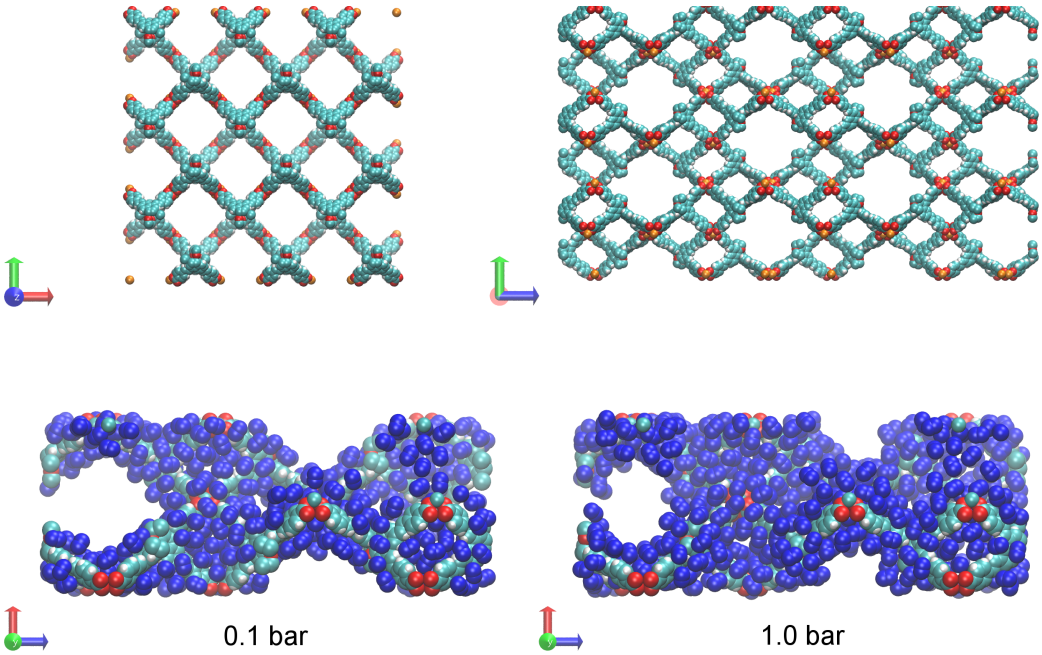


Figure 3.21: *GCMC simulation snapshots of the empty XAHPUT structure along the c and a axes (top). In addition, snapshots of the adsorbed monolayer are shown at 0.1 and 1.0 bar (bottom); Colour scheme: White = H, Red = O, Cyan = C, Orange = Cu, Blue = N_2 molecules that form part of the adsorbed monolayer*

3.3.4 Conclusions

In this work, the link between the PFC effect and the pore size of different materials was investigated using a diverse set of 1248 MOFs. The main findings of this investigation can be summarised into the following statements:

- The influence of PFC in small pore systems is generally negligible; in many cases the difference between BET and PFC corrected surface areas arise from error in the linear regression analysis. However, exceptions have been observed and even microporous MOFs have been shown to require attention for accurate surface area measurements.

- MOFs containing large pores are generally more susceptible to PFC than those with small pores.

- The BET C parameter can be employed to identify MOFs with appreciable monolayer/multilayer adsorption overlap, thus providing a quick assessment of whether PFC is expected to influence the BET calculation.

- The monolayer packing is demonstrated to be a crucial aspect for accurate SA measurements; this is why in general, the method 2 correction scheme gives excellent agreement with ASA.

- The ASA is generally larger than the PFC-corrected surface areas as a result of the close-packed monolayer assumptions used by BET theory; i.e. the packing geometry of the GCMC particles is influenced by their interactions with the surface and each other leading to non-uniform distributions which can lower the overall accessibility of the surface to other adsorbates.

- In some MOFs, GCMC simulations can insert molecules into regions that are inaccessible to hard-sphere particles. In addition, the 'softer' nature of the GCMC particles can allow them to pass through small windows that are also inaccessible to hard-sphere particles. Overall, this can lead to a larger surface area than recorded by the geometric calculation.

Chapter 4

A high-throughput screening of MOF-based membranes for biogas upgrading

Abstract

Applications of biomethane as a source of renewable energy and transport fuel rely heavily on successful implementation of purification methods capable of removing undesirable impurities from biogas and increasing its calorific content. Metal–organic frameworks (MOF) are competitive candidates for biogas upgrading due their versatile range of attractive physical and chemical properties which can be utilised in membrane materials. In this work, a high-throughput screening protocol is presented and demonstrates its capability for quickly extracting some of the most promising MOF-based membranes with exceptional gas separation performance from the Cambridge Structural Database (CSD).

4.1 Introduction

Agricultural, industrial and municipal wastes are some of the many feedstocks which, in the absence of oxygen, can be broken down to form biogas - a mixture of gases composed of CH_4 (50-65%), CO_2 (35-50%) and small amounts of trace

gases such as H_2S, N_2, H_2 and NH_3.[203] The composition of biogas is largely dependant on the waste substrate and the conditions under which substrate digestion occurs.[204] Raw biogas has a high calorific content between 5000 - 7000 kcal/m^3, making it ideal for heat and electricity generation.[205] Through separation of its components, biogas can be upgraded to provide an enriched source of CH_4, further improving its calorific content for utilisation in the transport sector. This process is essential as high levels of CO_2 lower the calorific content of the fuel. In addition, small concentrations of H_2S (< 50 ppm) have been shown to corrode through metal pipes, making raw biogas unsuitable for standard combustion engines.[206]

In industry, there are many techniques that can be employed to upgrade biogas including absorption, adsorption and cryogenic distillation methods. Absorption methods involve the capture of impurities by dissolving them in a solvent at elevated pressure, or by reacting them with an inorganic/amine based solution.[207] Adsorption methods make use of molecular sieves, activated carbon and zeolites to separate out biogas due to differences in affinity between the biogas components and the adsorbent bed. The contaminants are usually adsorbed at high pressure from the biogas stream, leaving a CH_4 stream to pass over the adsorbent bed. The bed can then be regenerated by reducing the pressure which desorbs the contaminants. These are the core principles underlying pressure-swing adsorption methods (chapter 1.3.1) used to separate gaseous mixtures.[208] Similar principles can also be employed using changes in temperature, known as temperature-swing adsorption. Finally, as each biogas component condenses at different temperatures and pressures, one can use cryogenic distillation to separate contaminants.[209]

These methods can provide high CH_4 purity typically between 90-99%, however, they can be quite energy intensive, suffering from high investment, operation and/or maintenance costs.[210] One of the most promising and cheaper alternatives is to use membrane materials to separate gas components through differences in permeation. While a lot of progress has been made in the devel-

opment of synthesis methods for existing polymer and inorganic based membranes,[211–213] the discovery of new materials which can rival the separation performance of existing membranes is also a key area of research.[214–216] One example of these materials are metal-organic frameworks (MOFs): a rapidly growing hybrid class of porous materials that are self-assembled from inorganic clusters (known as secondary building units) and organic ligands. Due to the diverse nature of their building blocks, MOFs can offer a versatile range of attractive physical and chemical properties such as high porosity and large surface area.[217] Furthermore, these properties are highly tunable by choosing appropriate building blocks, making MOFs competitive over traditional porous material.

When fabricating MOF thin films or membranes, a number of different strategies may be employed, such as direct growth, layer-by-layer growth, seeded growth or chemical solution deposition.[218,219] The development of these synthetic routes has led to the construction of continuous membranes for many different applications. An example of these applications is gas separations, including CO_2/CH_4 separation found in biogas upgrading. In an early study, Guerrero and co-workers prepared HKUST-1 membranes on porous alumina supports demonstrating a "twin copper source" technique.[220] Single component measurements indicated a moderate CO_2 permeability of 2.81×10^{-7} mol m^{-2} s^{-1} Pa^{-1}, however CO_2/CH_4 mixture permeability was not reported. Carrieon and Bohrman synthesised the first Bio-MOF-1 membranes supported on tubular stainless steel via the seeded growth technique.[221] The separation performance indicated large CO_2 permeability, up to 1.2×10^{-5} mol m^{-2} s^{-1} Pa^{-1}, but low CO_2/CH_4 selectivity of 2.6. Although these results were comparable to some traditional polymer membranes below the Robeson limit, the authors noted that synthesis optimisation could improve these parameters. Lee and coworkers prepared Ni-MOF-74 membranes on porous alumina supports using a layer-by-layer seeding technique, showing excellent affinity for CO_2 molecules due to the presence of open-metal sites (OMS).[222] Venna and Carreon pre-

pared ZIF-8 membranes also via seeded growth on porous alumina supports, displaying unprecedentedly high CO_2 permeability of 2.4×10^{-5} mol m^{-2} s^{-1} Pa^{-1} and selectivity values ranging between 4 and 7 for equimolar CO_2/CH_4 mixtures.[223] Huang and co-workers prepared 3-aminopropy-ltriethoxysilane (APTES) -functionalised ZIF-90 membranes, displaying a CO_2 permeability of 1.26×10^{-8} mol m^{-2} s^{-1} Pa^{-1} and a CO_2/CH_4 selectivity of 4.7.[224] Liu and co-workers developed highly c-orientated ZIF-69 membranes using an extended seeded growth approach. Their results show a CO_2/CH_4 selectivity and CO_2 permeability of 4.6 and 1.0×10^{-7} mol m^{-2} s^{-1} Pa^{-1}, respectively - an improvement over the performance of ZIF-69 membranes prepared via in-situ crystallisation due to an improved membrane microstructure.[225]

Huang and co-workers developed ZIF-95 membranes supported on APTES-modified alumina for separating gas mixtures containing H_2. Their study also showed excellent adsorption affinity for CO_2, indicating a good potential in CO_2 based separations.[226] In addition to these structures, the development of composite materials such as mixed matrix membranes (MMM) has been used as a strategy to combine the high separation performances of many zeolitic and MOF membranes with the facile and low processing costs of polymer membranes.[203,227–232]

Many of these experimental studies demonstrate the promising application of MOFs to biogas upgrading. However, they only cover a small fraction of the total number of MOFs that have been synthesised. In 2017, Moghadam and co-workers developed a series of criteria which estimates close to 70,000 MOF-like structures within the Cambridge structural database (CSD).[84] While this creates many opportunities for application-driven research, it is clearly not feasible to synthesise all of these structures. In such scenarios, high-throughput computational studies can be useful for accurately identifying top performing MOFs of a particular application (see chapter 1.4). Furthermore, they can provide insight and relationships that allow us to understand the link between structural properties and the performance of a MOF. In the literature,

there are a number of excellent high-throughput studies which investigate the CO_2 capture and separation properties of both experimental and hypothetical MOF adsorbents.[67,69,233–235] In contrast, there are far fewer studies which examine the membrane separation potential of MOFs, particularly focussing on CO_2/CH_4. This may be attributed to the higher computational cost of simulating gas permeability which requires both adsorption and diffusion calculations. In an early study, Erucar and co-workers tested several permeation models to compare predicted and experimental permeabilities in MMMs. With the best model, they screened a modest number of MOF-based MMMs, identifying trends between the choice of MOF filler particles and its effect on CO_2/CH_4 selectivity and CO_2 permeability.[236] Jiang and co-workers screened a large database containing hypothetical MOF membranes for CO_2/CH_4 and N_2/CH_4 separations. They identified MOFs with CO_2/CH_4 permselectivity exceeding 100 and CO_2 permeability greater than 10^4 Barrer (1 Barrer = 3.35×10^{-16} mol m^{-2} s^{-1} Pa^{-1}) . The top candidates were further examined for a ternary $CO_2/CH_4/N_2$ separation at 10 bar and 298 K.[237] Recently, Altintas, Erucar and Keskin screened MOF membranes to identify top performing MOFs that could be used as filler particles in MMMs and found that MOF-based MMMs have much higher CO_2 permeabilities and CO_2/CH_4 selectivities than the pure polymers.[238]

High-throughput studies which identify the "best" materials for separating CO_2 from CH_4 can provide a great deal of insight into biogas upgrading. However, for the production of high purity CH_4, it is also important to be able to selectively remove the smaller quantities of H_2S present in biogas streams. Additionally, many biogas streams contain water vapour which may potentially affect the separation performance and stability of many MOF membranes.[239] Therefore, it is important to try and address these issues to improve the viability of a promising material that has been identified via high-throughput screening.

In this work, a multi-stage screening methodology is designed to focus

on CO_2/CH_4 and H_2S/CH_4 separations across a range of hydrophobic MOF membranes from the CSD database. Therefore, top candidates will encompass high selectivity and permeability for CO_2 and H_2S which is essential for the biogas upgrading process. Additionally, the screening is expected to target a set of membranes with improved moisture stability due to their enhanced hydrophobic character. The study begins by filtering porous candidates based on the differences in their geometric properties. Then, an initial estimation of the ideal CO_2/CH_4 and H_2S/CH_4 selectivities and permeabilities is carried out at infinite dilution conditions. This is achieved by calculating Henry and diffusion coefficients from Monte Carlo and equilibrium molecular dynamics (EMD) calculations, respectively. Additionally, the impact of how different input parameters used to calculate partial charges via the extended charge equilibration (EQeq) scheme[149] is explored and how this can affect the physical nature of some MOFs charges and their overall separation properties. A selection of the top hydrophobic MOFs which exceed the Robeson upper bound are then exposed to a more accurate set of calculations under working conditions. Equimolar CO_2/CH_4 and H_2S/CH_4 grand canonical Monte Carlo (GCMC) and EMD simulations are employed to predict mixture selectivities and permeabilities at 298 K and 10 bar. The best membranes are then compared against literature zeolites, MOFs and MMMs to assess their overall performance and viability for biogas upgrading. Finally, the structural properties of 1183 hydrophobic membranes that lie above the Robeson limit are examined. This enables us to draw conclusions about the relationships which lead to exceptional separation performance, providing useful insight into the design of future membranes.

4.2 Computational Details

As of Nov 2018, the CSD MOF subset contains a total of 67,675 structures which are used in this study. Solvent molecules are removed from each struc-

ture using a python script readily available from the literature.[84] Geometric properties such as accessible surface area (ASA), pore limiting diameter (PLD), largest cavity diameter (LCD), pore volume (PV), void fraction (ϕ) and density are calculated using the Zeo++ software package, version 0.3.6.[169] ASAs are calculated using a 1.655 Å radius probe and 5000 monte-carlo (MC) insertions per atom, while PVs are calculated using a 0 Å radius probe and 50,000 insertions per unit cell. PLDs and LCDs are calculated from the largest inserted sphere that does not overlap with any framework atoms. Only frameworks that possessed non-zero ASAs are considered in this study. Furthermore, frameworks with PLDs $\leq$ 3.80 Å which will not permit the diffusion of each main biogas component are exlcuded, i.e. CH_4 (3.80 Å), CO_2, (3.30 Å) or H_2S (3.60 Å) - This leaves a diverse set of 7909 structures that are suitable for high-throughput screening.

The RASPA software package[199] is employed to calculate self-diffusivity (D^0), Henry constant (K^0) and heat of adsorption (Q^0_{st}) of CO_2, H_2S, CH_4 and H_2O at infinite dilution. K^0 is determined using the Widom insertion method at 298 K, using a total of 100,000 cycles - 1 cycle is equal to min(N, 20) steps, where N is the number of adsorbates within the simulation cell.[110] For calculations of D^0, EMD simulations in the NVT ensemble are employed. A timestep of 1 fs is used, and the number of equilibration and production cycles are set to 10,000 and 100,000, respectively. Heating is controlled using a Nosé-Hoover thermostat.[110] To mimic infinite dilution, adsorbate-adsorbate interactions are neglected and only framework-adsorbate interactions are considered. The statistical accuracy of infinite dilution conditions is improved by using 30 gas molecules per simulation. The initial positions of the gas molecules are determined using 1000 Monte Carlo initialization cycles. D^0 values are calculated using Einstein's relation as described in section 2.3.2 Based on previous work, materials where $D^0 < 10^{-8}$ cm^2/s are excluded as these values approach the limit of accurate characterisation of molecular diffusion from EMD simulations.[240] The gas permeability for each component i at infinite dilution (P^0_i) is

calculated from the product of its self-diffusivity and the Henry constant using equation 1.8. The ratios K_i^0/K_j^0, D_i^0/D_j^0 and P_i^0/P_j^0 of two components are then used to determine the ideal adsorption ($S^0_{\text{ads},i/j}$), diffusion ($S^0_{\text{diff},i/j}$) and membrane selectivity ($S^0_{\text{mem},i/j}$), respectively.

A hydrophobic subset of MOFs is identified by comparing $K^0_{\text{H}_2\text{O}}$ of each membrane against the hydrophobic ZIF-8 structure ($K^0_{\text{H}_2\text{O}} = 5.00 \times 10^{-6}$ mol kg^{-1} Pa). A membrane is considered hydrophobic if it possesses a $K^0_{\text{H}_2\text{O}}$ value that is smaller or equal to that of ZIF-8. This approach has been used previously to identify hydrophobic MOFs for hydrocarbon separations and toxic industrial chemical capture.[241,242] Only hydrophobic membranes above the 2008 Robeson bound[59] that are: 1) selective to H_2S and CO_2; 2) possess $P^0_{\text{CO}_2}$ and $P^0_{\text{H}_2\text{S}} > 2.5 \times 10^7$ Barrer are considered in the final phase of simulations where equimolar binary mixture GCMC and EMD simulations are employed at working conditions of 10 bar and 298 K.

For GCMC simulations, the number of initialization and production cycles is set to 10,000 each. Gas phase fugacities are calculated using the Peng-Robinson equation of state.[198] Due to the high cost of the EMD simulations, the LAMMPS software package is used to enable parallelisation of the calculations.[243] The initial states of each EMD simulation are determined from the loadings predicted in the GCMC simulations. In contrast to calculations at infinite dilution, both host - adsorbate and adsorbate - adsorbate interactions are included. A time step of 1 fs is employed with simulations running for a total of 1 ns (50% equilibration). Atomic coordinates for each adsorbate are recorded every 5 fs and are used to calculate the MSD using an in-house python code. This code calculates the MSD across multiple time origins at different correlation times.[110] This is visualised in Figure 4.1 in which the code uses multiple sampling windows with varying correlation times. These sample numerous initial and final states by *sliding* the window across the output frames. As such, lower correlation times can sample a larger number of pairs than higher correlation times. The MSD is then averaged across the sampled

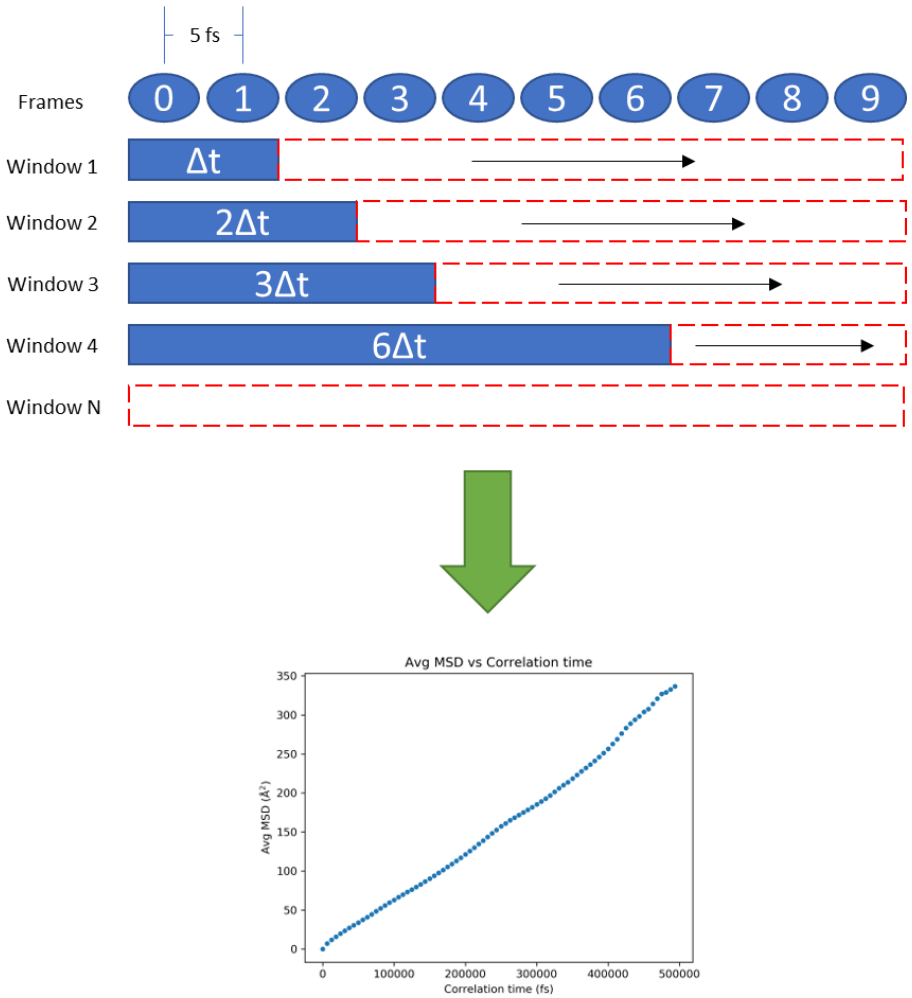


Figure 4.1: *Example of the post-processing window method used to calculate the MSD of gas molecules diffusing in MOF pores from EMD simulations.*

population and is plotted as a single point on a plot of the average MSD vs correlation time. The self-diffusivity is then calculated using Einstein's relation as described in section 2.3.2. A minimum of 5 independent trajectories are used to compute the mixture self-diffusivity of each component, and statistical uncertainty is estimated from the standard deviation using the mixture self-diffusivity from each trajectory. The gas permeability in the binary mixture is re-evaluated using expression 1.6.[93] The membrane selectivity ($S^{mix}_{\mathrm{mem},i/j}$) can then be calculated from the ratio of the gas permeabilities for components i and j of the binary mixture as P_i^{mix}/P_j^{mix}.

4.2.1 Force-Field Validation

The force-fields used to describe intermolecular interactions are formed from a Lennard-Jones (LJ) potential with a cut-off of 12.8 Å. Long-range Coulombic interactions are handled using the Ewald summation technique.[137] Cross-terms are calculated using the Lorentz-Berthelot mixing rules.[130,131] Frameworks are assumed to be rigid with atoms fixed in their crystallographic positions and modelled using the Universal Force-Field (UFF).[132] Atomic partial charges are assigned to framework atoms using the EQeq scheme available within the RASPA software package.[149] A list of oxidation states used in each EQeq calculation can be found in Appendix A. CO_2 and CH_4 molecules are modelled as a rigid 3-site and a single united-atom model, respectively, using LJ parameters and partial charges from the TraPPE force-field.[135,136] H_2O is modelled as a rigid 4-site using the TIP4P-Ew model[244] and H_2S is modelled as a rigid 4-site using parameters derived by Kristóf and co-workers.[245] A full list of force-field parameters may be found in Appendix A. For MOFs, so called "off-the-shelf" force-fields such as UFF are commonly employed to study adsorption and diffusion properties. These are typically combined with force-fields designed specifically for adsorbates to reproduce thermophysical properties, such as the TraPPE and TIP force-fields. This computational setup has been used extensively over the past 15 years and has been shown to give good agreement across a wide range of adsorbates and MOFs.[81,246,247] Furthermore, they have been previously validated for reproducing experimental membrane properties in a variety of CO_2 and CH_4 based separations.[248,249] In addition to these previous studies, similar calculations have been performed in this work which show good agreement between experimental and simulated CO_2 and CH_4 permeabilities (Figure 4.2a).

Unlike other small gases, studies into H_2S adsorption and separation are less documented than other small molecules such as CO_2 and CH_4.[252] In many MOFs, the formation of strong metal-sulphur bonds can lead to poor regen-

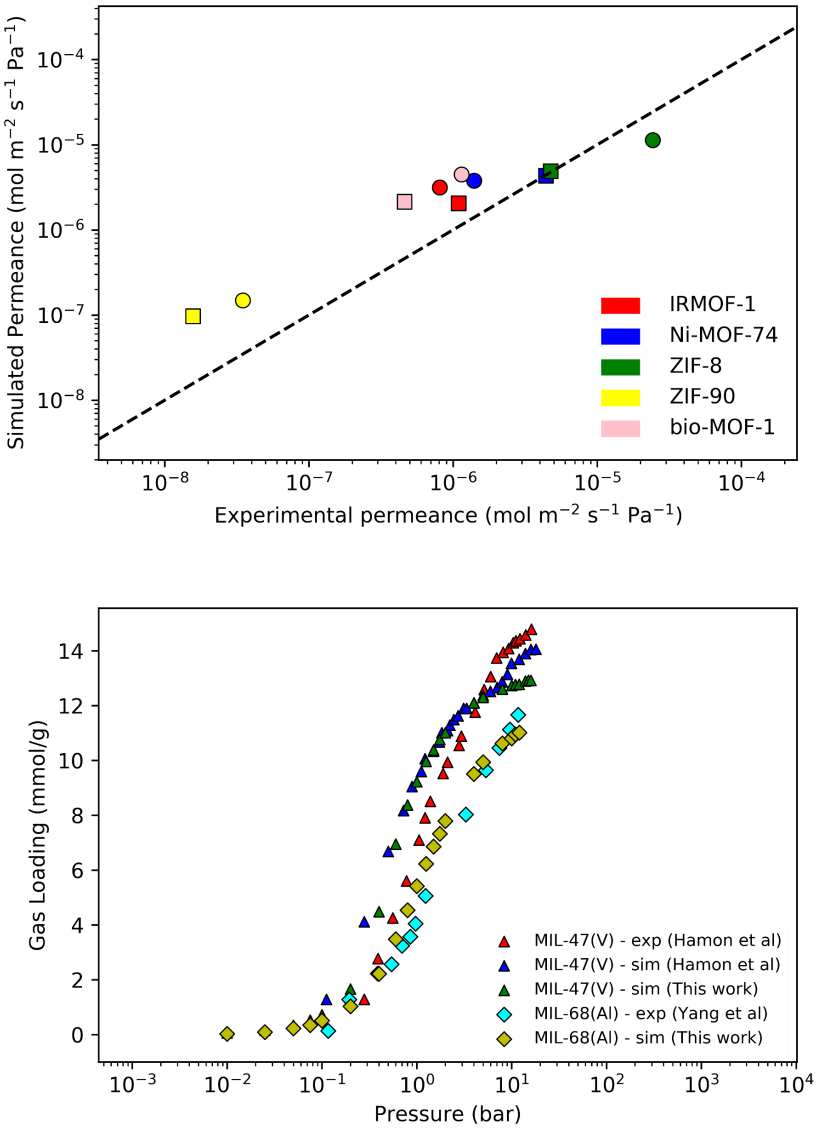


Figure 4.2: *a: Comparison of simulated and experimental CO_2 (circle symbols) and CH_4 (square symbols) permeances in selected MOF membranes. Experimental conditions may be found in Appendix B; b: Comparison of simulated and experimental H_2S uptakes in MIL-47 and MIL-68 MOFs at 303 K. Experimental data taken from Hamon et al[250] and Yang et al[251].*

eration of the empty host or even displacement of linkers causing loss of permanent porosity. Despite these issues, a small number of MOFs from the MIL family possess H_2S adsorption isotherms over large pressure ranges, which provide us the ability to validate the H_2S model. Our results on MIL-47(V) indicate good agreement with experimental results (Figure 4.2b) and similar agreement to simulations using a 3-site H_2S model employed by Hamon and coworkers.[250] Good agreement between theory and experiment is also achieved

for MIL-68(Al).[251] An evaluation test for H_2S permeability over a range of MOF membranes is not feasible with the current availability of experimental data.

4.2.2 Main assumptions and limitations

Before presenting the results of this screening, it is important to report and discuss the assumptions and limitations of the present computational methodology. For each MOF membrane, our calculations assume a perfect, rigid, defect-free crystal structure in which the solvent molecules are removed prior to simulation. As such, the results are expected to give an insight into the upper limit of permeation properties achievable in these materials. While this approximation has been used ubiquitously within the literature, it is important to realise that some membranes in the CSD subset may be sensitive to guest activation, leading to structural changes. In addition, the viability of a material that is identified in any high-throughput screening is also subject to its chemical and mechanical stability under different conditions, requiring additional simulations to assess this.

A limitation to the force-fields used in this work is that strong interactions between adsorbates and OMS are not captured, leading to under-prediction of the separation performance in these materials. Studies that have attempted to parametrise force-fields using quantum chemistry based calculations have successfully shown that this method can correctly capture host-guest interactions around OMS.[253,254] While this approach has been used at the high-throughput scale previously, it is a very costly process which can only target a small subset of MOFs possessing similar structural motifs (e.g. metal paddlewheels).[255,256] In this study, one of the main aims is to target a range of MOFs with a diverse set of structural properties, meaning that generic force-fields such as UFF will give the best compromise of accuracy and cost to achieve this.

With any computational study, calculated properties such as the adsor-

bate self-diffusivities are likely to be influenced by the computational setup that is employed. Firstly, it has been previously shown that in materials with small pore diameters, the rigid framework assumption generally leads to larger self-diffusivity coefficients than when using a fully flexible-model.[238] As such, many results from this work are expected to provide an over-estimate of the true self-diffusivity which will also affect any permeability calculations. In addition, the choice of thermostat is another important decision as the type of algorithm may influence the calculated transport properties. For example, Bussi and Parrinello discussed several stochastic algorithms and noted that the Langevin thermostat should not be used to compute dynamical properties, unless an extremely small friction parameter is employed. However, this leads to inefficient sampling and longer simulation times.[257] Basconi and Shirts reported that algorithms which are coupled to the systems kinetic energy and operate by scaling velocities (including the Nose-Hoover, stochastic velocity rescaling and Berendsen thermostats) can yield transport properties that are statistically indistinguishable from those calculated using the microcanonical ensemble.[258] Another consideration is the sampling length over which the self-diffusivity is calculated. While a 0.5 ns production length has been used in similar studies to the work in this chapter[240,248] and gives a good trade-off between the speed of each calculation in the screen and its accuracy, running for longer durations is also beneficial for further reducing the statistical uncertainty in the self-diffusivities and providing more conclusive evidence that the simulation is in the long-time region that is required by Einstein's relation.

Another source of error arises from finite-size effects. As discussed in section 2.4.3, a typical simulation box may contain thousands of atoms which is often much smaller than any real bulk system. As such, the finite size of the simulation box introduces a systematic error into the calculation of any property of interest. In an early study, Dunweg and Kremer showed that a polymer self-diffusion coefficient scales linearly with the inverse of the simulation box length.[259] As such, the self-diffusivity in the thermodynamic limit

can be extrapolated using regression analysis across multiple simulations with varying box lengths, thus eliminating finite-size effects. For most simulations that study bulk properties, the simulation box is often replicated using PBC's and a series of interaction cut-offs are introduced to truncate the total number of calculations. Although multiple calculations using different simulation box lengths can provide a more accurate estimate of the self-diffusivity in the thermodynamic limit, the computational cost of the simulation increases rapidly with particle number and is simply not feasible for some of the larger calculations that are performed in this study (i.e. those using multi-component mixtures and high pressures).

In this work, the EQeq scheme is employed which provides a quick and approximate method of determining APC's, as previously mentioned in section 2.4.2. It is an ideal scheme for high-throughput studies and previous work has demonstrated that the effect of the charges on predicted gas uptakes and heats of adsorption is very similar to QM derived DDEC charges.[150] More recently, Altintas and co-workers showed that the predicted gas diffusivities, permeabilities and membrane selectivities of several MOF membranes are very similar when using DDEC and Qeq based charge schemes.[260] However, they noted that deviations are particularly noted in MOFs with small pores. In this chapter, many of the top-performing materials are found to possess small pore diameters and therefore their results should be analysed with these limitations in mind. In some cases, it is likely that the screening may generate false-positive results in which a top-performing material is only identified as a result of the current approximations. To confirm the top-performing separation performance in these materials, a more accurate partial charge assignment scheme should be employed, though at greater computational expense.[260]

Finally, it is important to highlight that some materials are omitted in this screening due to unconverged APCs that arise from the EQeq scheme. Similarly, a number of materials are omitted due to poor separation performance which may arise from limitations in the employed models, thus leading

to a series of false-negative results. In particular, MOFs containing open-metal sites are likely to appear as false-negative results as general force-fields are not able to accurately model adsorbate interactions with open-metal sites, leading to inaccurate separation performances. Therefore, it is important to reiterate that the results and conclusions of this study should be analysed with the limitations of the current methodology in mind.

4.3 Results and discussion

4.3.1 Accuracy in evaluation of partial charges on metal sites

In the early stages of this screening, the distribution of partial charges were evaluated for 7909 MOFs using the EQeq method. Unlike the original Qeq method reported by Rappe et al[148], this method uses a neutral oxidation state Taylor expansion for ligand atoms, and a higher oxidation state Taylor expansion for metals. In some systems, the choice of Taylor expansion can be the difference between convergence to a physical set of partial charges or an unphysical set. In previous work, Ongari and co-workers compared the partial charges obtained from different charge equilibration methods against high quality density functional theory-derived DDEC charges for a large set of MOFs.[150] They showed that smaller deviations between the Qeq methods and DDEC charges were obtained when using a higher oxidation state for the metal centres present in the MOFs. Furthermore, using the data from DDEC charge distributions, they showed that by imposing an upper and lower atomic charge limit of +3 and -2 respectively, fewer structures containing unphysical charges were obtained from using the higher oxidation state Taylor expansion. In this work, MOFs with physical partial charges are obtained by applying two sets of criteria. Firstly, all MOFs containing atoms with a partial charge greater than +3.5 or less than -2 are removed. This criterion is closely based on the

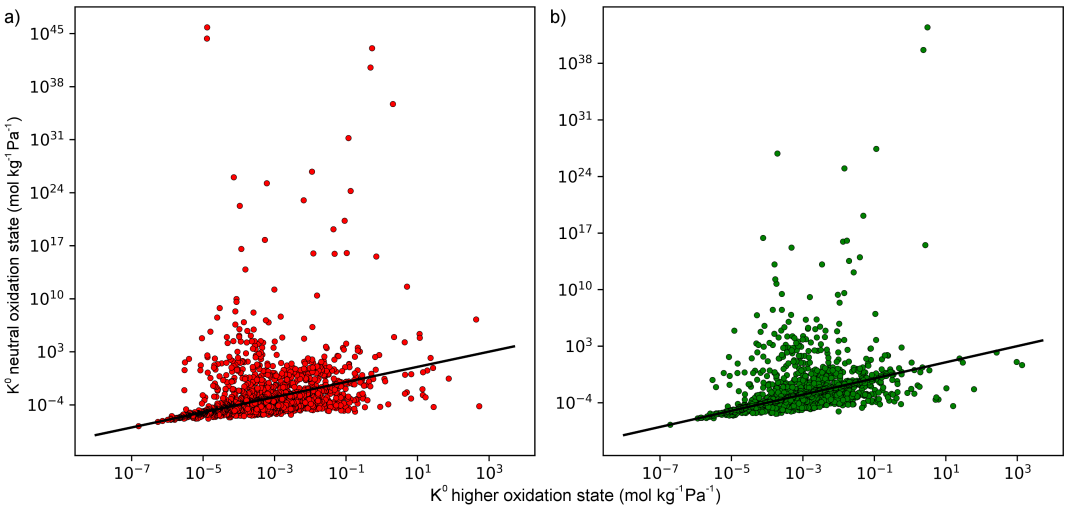


Figure 4.3: *Comparison of the Henry coefficients for CO_2 (red) and H_2S (green) in MOFs, predicted by using different sets of partial charges on metal sites. The y-axis corresponds to partial charges calculated using a neutral oxidation state on metal atoms, while the x-axis corresponds to partial charges calculated using a higher oxidation state on metal atoms.*

condition proposed by Ongari and co-workers, however, a slight buffer is added to the upper limit which is found to be useful for structures with highly charged metal centres containing Zr(IV). This criterion alone is found to be sufficient for identifying metals with unphysical charges but less so for ligand atoms such as carbon or hydrogen (Appendix C). Therefore, a stricter charge criteria is applied on C and H atoms to only allow MOFs with C and H charges between +1 and -1. A total of 800 MOFs are removed from the screening leaving 7109 MOFs to be taken forward into the first phase of high-throughput screening.

To demonstrate how the choice of Taylor expansion may influence the results, Figure 4.3 compares Henry coefficients for CO_2 and H_2S ($K^0_{CO_2}$ and $K^0_{H_2S}$) in MOFs used in this study for which a converged EQeq partial charge evaluation was achieved using both neutral and higher oxidation states of the metal atoms. For both CO_2 and H_2S, using the higher oxidation state Taylor expansion (x-axis) provides a narrower and more chemically meaningful spread of values for Henry coefficients. This is because the neutral oxidation state expansion has a higher propensity to provide structures with unphysical charges.[150] When using the neutral oxidation state Taylor expansion, the charge distributions in 76 MOFs which possess a $K^0_{CO_2} > 10^3$ mol kg^{-1} Pa^{-1},

(i.e. any value greater than the largest $K^0_{CO_2}$ predicted from using the higher oxidation state expansion) are analysed. The results indicate that 50% of these MOFs contain Li, Na or K atoms with charges ranging from +1.34 to +6.75, and 30% contain Nd atoms with charges ranging from +2.89 to +46.4. Consequently, the unphysical Coulomb interactions between CO_2 and these metals centres lead to large overestimation of $K^0_{CO_2}$. Using the higher oxidation state expansion, the Li, Na and K atoms in these MOFs have charges ranging from +0.55 to +0.71. Additionally, the Nd charges range between +1.45 and +2.46.

A total of 4418 MOFs (68%) have a larger $K^0_{CO_2}$ when using the higher oxidation state expansion instead of the neutral oxidation state expansion (Figure 4.3 left). However, in 81% of these MOFs, this increase in $K^0_{CO_2}$ is relatively small (1 to 10 times larger). Although this change is small, it is worth noting that the adsorption selectivity obtained from the ratio of the CO_2 and CH_4 Henry constants can be directly influenced by switching from one Taylor expansion to another. Similar trends are also observed for H_2S with 4013 MOFs (62%) possessing a larger $K^0_{H_2S}$ when using the higher oxidation state expansion. In 88% of these MOFs, $K^0_{H_2S}$ is 1 to 10 times larger compared to that calculated using the neutral oxidation state expansion. In general, these results demonstrate the importance of using a higher oxidation state Taylor expansion for metal atoms for generating a more accurate and physical set of partial charges.

4.3.2 Permeability at infinite dilution

Within the solution-diffusion model, the gas permeation across a membrane can be broken down into three steps: adsorption onto the membrane surface, diffusion through the membrane pore channels, and desorption from the membrane surface. Therefore, it is expected that differences in host-guest and guest-guest interactions for different biogas components will strongly influence the rate at which a component permeates through the membrane. For an initial

insight, calculations at very low concentrations (in the Henry region) are useful for comparing differences in permeation as Henry region adsorption thermodynamics is solely influenced by the strength of host-guest interactions. Figure 4.4 compares the diffusion coefficients and permeability for CH_4, CO_2 and H_2S in the Henry region in 6768 MOF membranes. Of the initial 7109 structures, 341 membranes are not included as they possess diffusion coefficients smaller than 10^{-8} cm^2/s.

For CH_4 gas, an increase in $P^0_{CH_4}$ is met with an increase in both $K^0_{CH_4}$ and $D^0_{CH_4}$, giving rise to the positive correlation shown in Figure 4.4a. For 5264 membranes, $D^0_{CH_4}$ lies between 10^{-3} and 10^{-4} cm^2/s, resulting in fast rates of diffusion which may be attributed to weak CH_4-MOF interactions. Although $K^0_{CH_4}$ values range between 8.91×10^{-3} mol kg^{-1} Pa^{-1} and 1.58×10^{-7} mol kg^{-1} Pa^{-1}, 81% of MOFs possess $K^0_{CH_4} < 3.00 \times 10^{-5}$ mol kg^{-1} Pa^{-1} also indicating weak CH_4-MOF interactions. Unlike CH_4 gas, both CO_2 and H_2S interact with MOF membranes through a combination of Van der Waals and electrostatic interactions. Therefore, on average, it is expected that CO_2-MOF and H_2S-MOF interactions will be stronger than CH_4-MOF interactions. Evidence of this can be seen in the range of $K^0_{CO_2}$ and $K^0_{H_2S}$ values which extend further than $K^0_{CH_4}$ to values as large as 10^3 mol kg^{-1} Pa^{-1} (Figures 4.4b and 4.4c). Furthermore, 76% of MOFs possess a $K^0_{CO_2}$ between 10^{-3} mol kg^{-1} Pa^{-1} and 10^{-5} mol kg^{-1} Pa^{-1} (70% for $K^0_{H_2S}$). Therefore, on average these gases diffuse slower than CH_4 through each MOF membrane. While 21% of MOFs possess $D^0_{CH_4} < 2.00 \times 10^{-4}$ cm^2/s, this increases to 63% and 66% when considering $D^0_{CO_2}$ and $D^0_{H_2S}$. The combination of these factors lead to a more negative looking correlation as presented in Figures 4.4b and 4.4c.

Of the 6768 MOFs included in our study, 67% possess Q^0_{st,H_2S} and Q^0_{st,CO_2} smaller than -25 kJ/mol. While these membranes are expected to strongly adsorb the main contaminants in biogas, the presence of water vapour in the biogas mixture may affect the stability of these membranes. In addition, water may act as a competitive adsorbate, resulting in different separation proper-

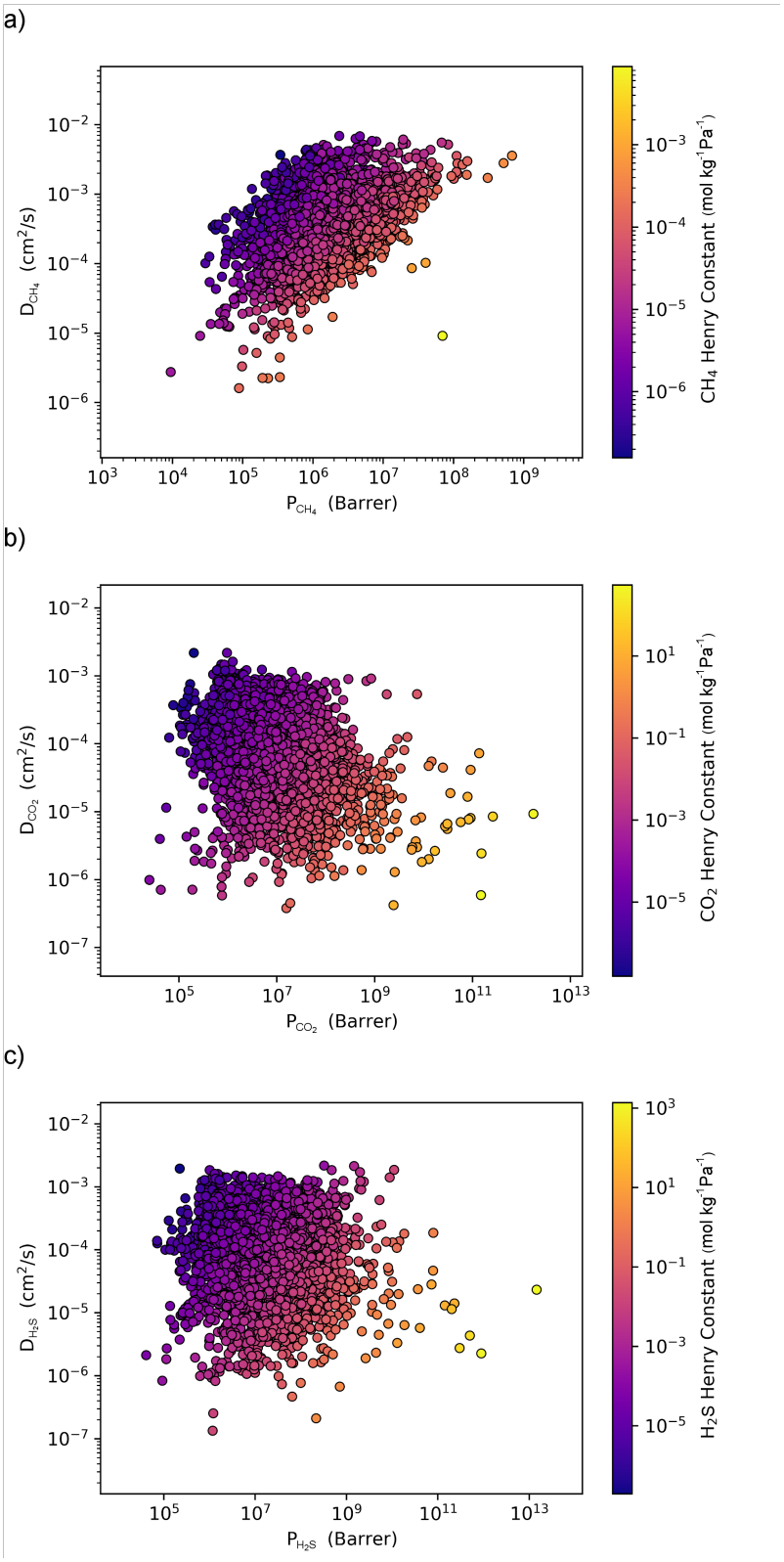


Figure 4.4: *The diffusion coefficient against permeability under infinite dilution conditions for a: CH_4, b: CO_2 and c: H_2S. Each point represents a different MOF and the colour corresponds to the magnitude of the Henry constant.*

ties. Of the MOFs which possess $Q^0_{st,\mathrm{H_2S}}$ and $Q^0_{st,\mathrm{CO_2}}$ < -25 kJ/mol, 70% possess $Q^0_{st,\mathrm{H_2O}}$ ¿ $Q^0_{st,\mathrm{H_2S}}$ or $Q^0_{st,\mathrm{CO_2}}$. As such, a hydrophobicity criteria is

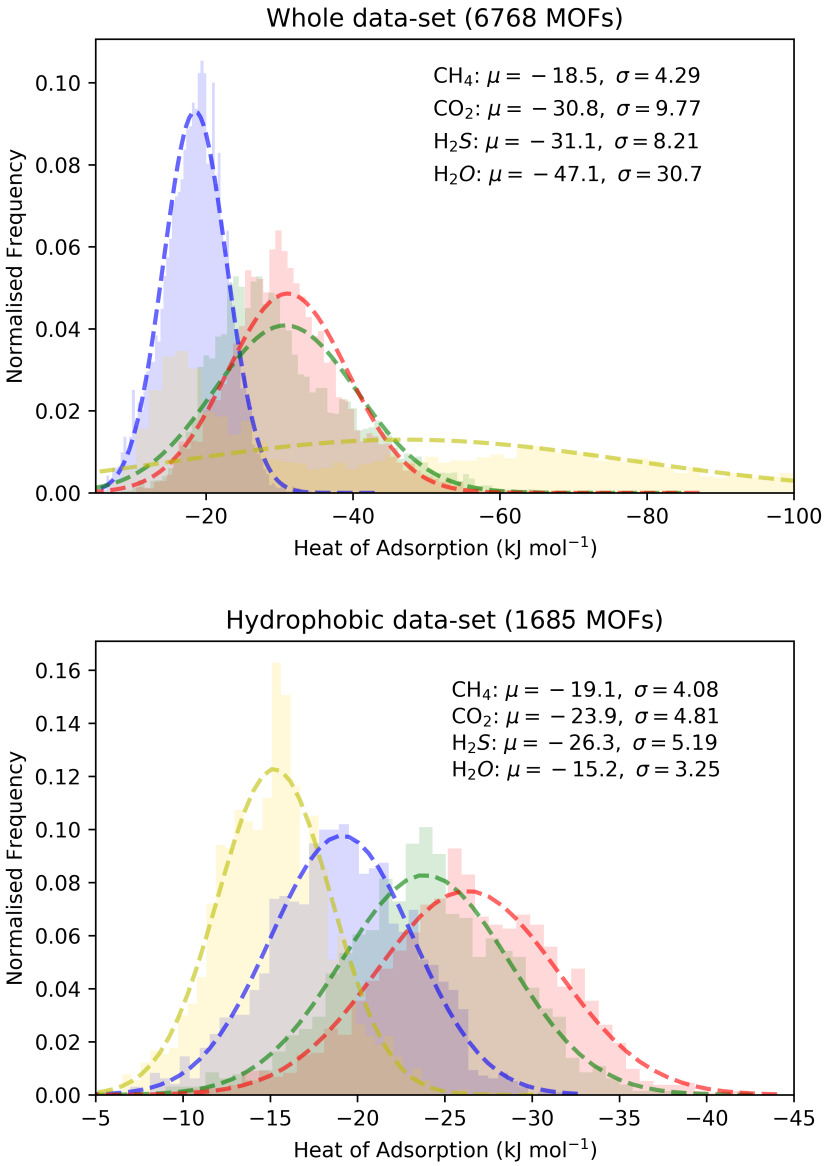


Figure 4.5: *Q^0_{st} distributions for CH_4 (blue), CO_2 (green), H_2S (red), and H_2O (yellow) in all 6867 MOFs (top) and in the 1685 hydrophobic subset (bottom). The mean (μ) and standard deviation (σ) of each distribution is displayed in each graph window.*

employed to identify promising membranes which are expected to possess improved hydrolytic stability. By doing so, the data set is reduced to 1685 MOF membranes and observe a decrease in the average $Q^0_{st,\mathrm{H_2O}}$ from -47.1 kJ/mol to -16.1 kJ/mol (Figure 4.5). Furthermore, less than 1% of the hydrophobic MOF dataset possess $Q^0_{st,\mathrm{H_2O}}$ values that are greater than $Q^0_{st,\mathrm{CH_4}}$, $Q^0_{st,\mathrm{CO_2}}$ or $Q^0_{st,\mathrm{H_2S}}$, compared to 59% in the original set of 6768 MOFs.

The permeability at infinite dilution for CH_4, CO_2 and H_2S is deter-

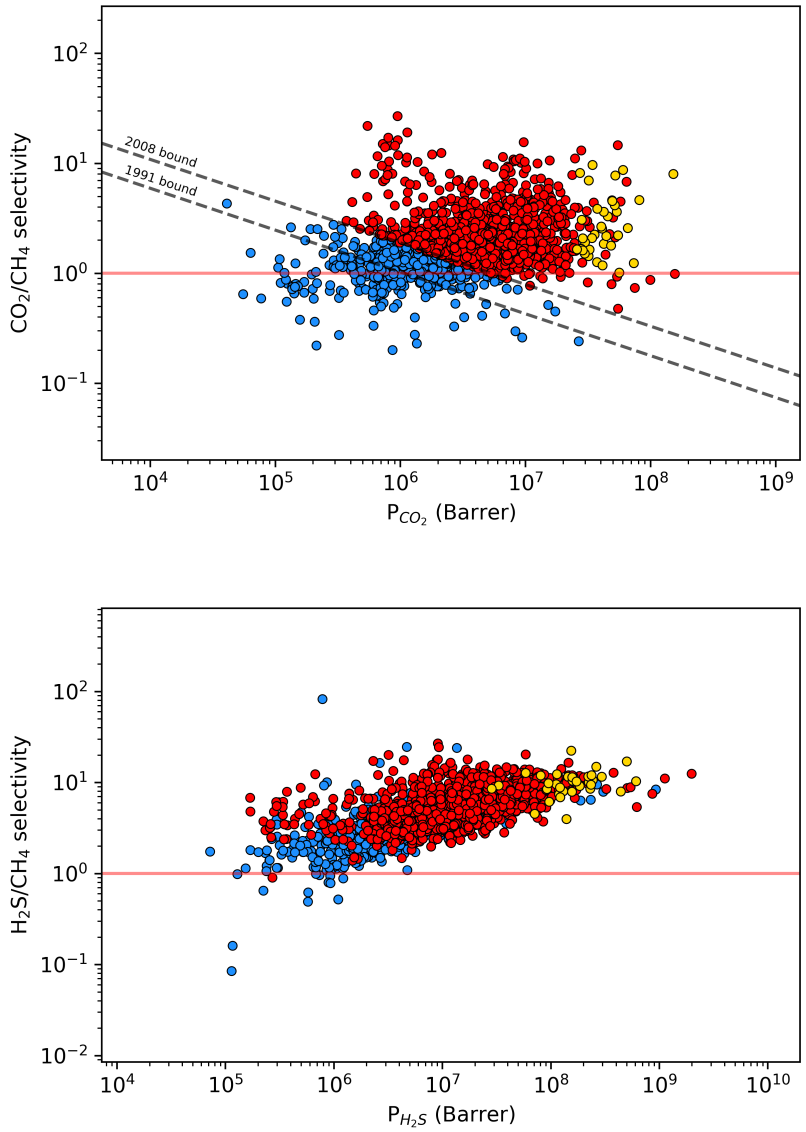


Figure 4.6: *Robeson trade-off plots for CO_2/CH_4 (top) and H_2S/CH_4 (bottom) ideal separations in 1685 MOFs. The CO_2/CH_4 Robeson 1991 and 2008 limits are used to compare performance of each MOF to some of the best polymer membranes. 1183 MOFs lie above the 2008 limit (red and yellow points) and 35 (yellow points) are used in the study of binary mixture separations at working conditions of 10 bar and 298K.*

mined for each of the remaining 1685 membranes. To assess the CO_2/CH_4 and H_2S/CH_4 separation performance of each membrane, Robeson plots are constructed as shown in Figure 4.6. For CO_2/CH_4 separation, the 1991 and 2008 Robeson upper bounds[58,59] are included to illustrate the performance of these MOFs relative to some of the best available organic polymer membranes. 1499 MOFs are found to be more selective for CO_2 gas with $S^0_{\mathrm{mem},CO_2/CH_4}$ val-

ues ranging between 1 and 26.9 and $P^0_{CO_2}$ values ranging between 4.10×10^4 Barrer and 1.56×10^8 Barrer. As seen in this study, MOFs have the potential to overcome the Robeson upper bound limit corresponding to the selectivity-permeability trade-off problem found in organic polymer membranes. Highlighted in red and yellow in Figure 4.6 are a total of 1183 MOFs that exceed the 2008 Robeson limit for CO_2/CH_4 separation. For H_2S/CH_4 separation, only 14 MOFs were found to be more selective for CH_4 than H_2S. The remaining 1671 possess $S^0_{mem,H_2S/CH_4}$ and $P^0_{H_2S}$ ranging from 1.03 to 82.3 and from 7.23×10^4 to 1.98×10^9 Barrer, respectively. Due to the limited availability of H_2S permeability data, an upper limit for the H_2S/CH_4 separation is not established. Therefore, the structures highlighted in red and yellow in Figure 4.6b correspond to the same structures as those shown in Figure 4.6a and are highlighted for comparative purposes.

Due to the large computational cost associated with modelling molecular dynamics at high pressure, this study focusses on MOF candidates that show the most promise from our calculations at infinite dilution conditions. Hence, unique MOF structures above the upper bound that are selective to CO_2 and H_2S with $P^0_{CO_2}$ and $P^0_{H_2S}$ greater than 2.50×10^7 Barrer are considered, leaving a total of 42 structures. Seven of these structures (CSD reference codes: CAFSUY, CAFTAF, COMDOY, CUMDIY, LODPOL, OHAKEO and SETQAL) are reported to collapse in response to activation or possess degrees of structural flexibility when exposed to different stimuli.[39,261–265] Therefore, the rigid structure approximation used in our calculations will not provide an accurate representation of the structure used under working conditions. Therefore, these structures are removed from the screening leaving a total of 35 unique membranes.

4.3.3 Separations at working conditions

With the remaining membranes, GCMC and EMD simulations are employed to study equimolar binary mixture separations of CO_2/CH_4 and H_2S/CH_4 at 10 bar and 298 K. Unlike calculations at infinite dilution, these simulations allow us to study the role of adsorbate-adsorbate interactions in biogas separation at operating conditions. One MOF structure (REFCODE: HONCIY) was removed from the screening as an accurate estimation of $D^{mix}_{CO_2}$ and $D^{mix}_{CH_4}$ was not possible within the timescale of its simulations.

A large decrease in gas permeability $P^{mix}_{CH_4}$, $P^{mix}_{CO_2}$ and $P^{mix}_{H_2S}$ is observed at working conditions, with values ranging between 10 and 10^5 Barrer (Figure 4.7). For 22 of the 34 MOFs, the values of both $S^{mix}_{mem,CO_2/CH_4}$ and $S^{mix}_{mem,H_2S/CH_4}$ are greater than their ideal selectivity at infinite dilution. With the inclusion of guest-guest interactions and increased gas loading under working conditions, the rate of diffusion for each component in the gas mixture is reduced leading to slower permeation rates. Furthermore, each component now competes against one another for adsorption sites which is not captured in the ideal calculations at infinite dilution. Under working conditions, the separation performance of 20 MOFs deteriorates such that they now lie below the 1991 and 2008 Robeson bounds (Figure 4.7 top). Of the remaining 14 MOFs, 6 lie between the 1991 and 2008 bounds and 7 lie above both bounds. These materials possess $S^{mix}_{mem,CO_2/CH_4}$ between 3.09 and 12.5, $P^{mix}_{CO_2}$ between 2.87×10^4 Barrer and 1.24×10^5 Barrer, $S^{mix}_{mem,H_2S/CH_4}$ between 25.0 and 123 and $P^{mix}_{H_2S}$ between 2.72×10^3 Barrer and 1.03×10^5 Barrer.

To determine how accurate the infinite dilution approximation is for estimating separation performance, the vertical distance (difference in selectivity) between each point on the Robeson plot and the 2008 upper limit is calculated for each membrane. This is then compared to a similar calculation performed on the Robeson plot at working conditions. These values are reported in Appendix B.4 (Table B.2) and show that in many cases, the separation

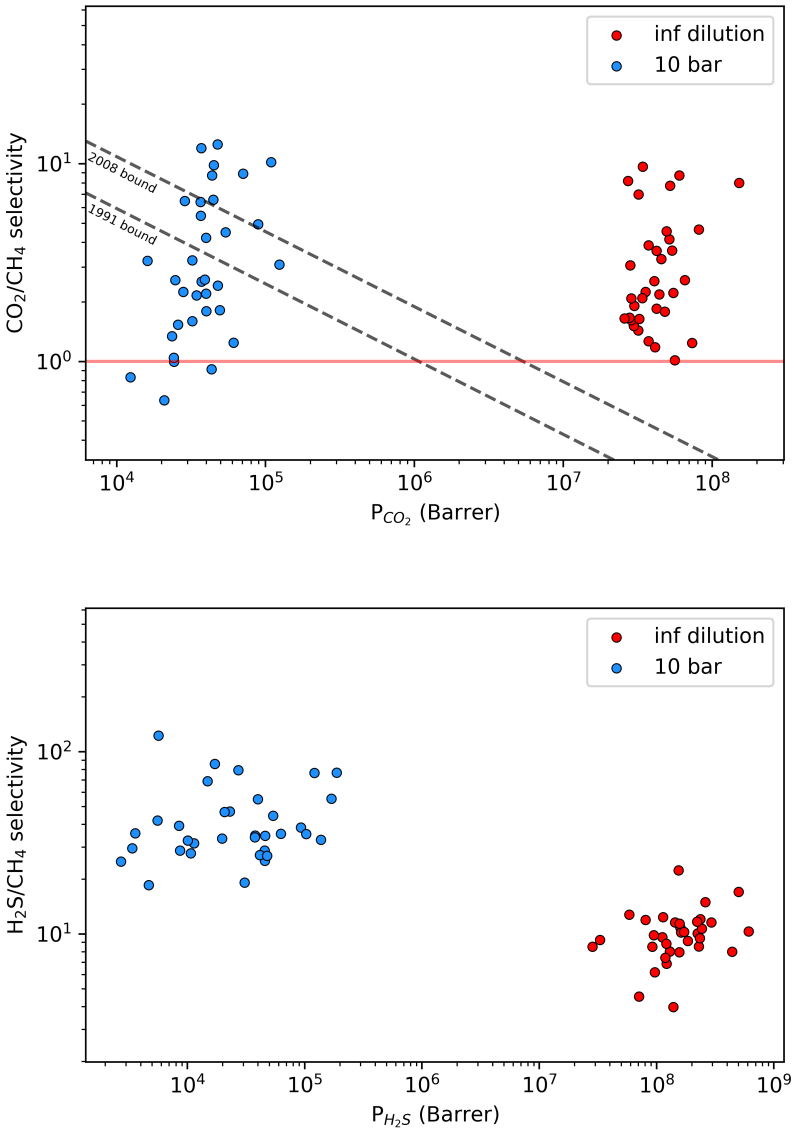


Figure 4.7: *Robeson trade-off plots comparing the CO_2/CH_4 (top) and H_2S/CH_4 (bottom) separation performance of 34 MOFs under infinite dilution (red) and at working conditions of 10 bar and 298 K (blue).*

performance of each MOF under working conditions can be quite different to those predicted under infinite dilution. As such, this highlights the importance of studying the behaviour of each MOF under working conditions and can be viewed as an essential step to improving the accuracy of the predicted separation performance.

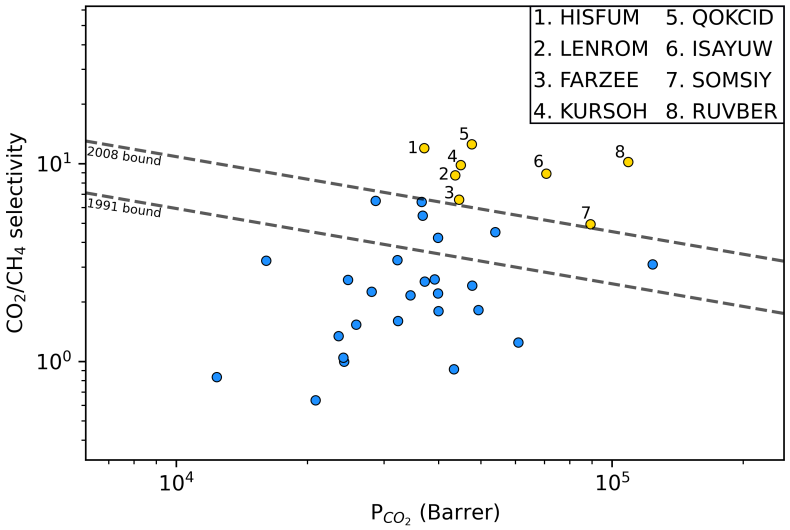


Figure 4.8: *Robeson trade-off plots at 298 K comparing the CO_2/CH_4 separation performance of 34 MOFs. The top 8 candidates identified in the proposed screening are highlighted as yellow points and labelled with the CSD reference code.*

4.3.4 Top candidates

When identifying the best candidates from these calculations, it should be noted that there are much larger concentrations of CO_2 to remove from a biogas stream than H_2S such that each MOFs performance should be weighted more heavily for CO_2/CH_4 separation than for H_2S/CH_4. For the remainder of this discussion, the top 8 MOFs are referred to as the top candidates identified by our high-throughput screening, and correspond to those which exceed the 2008 Robeson limit (Figure 4.8).

The geometric and physical properties summarised in Table 4.1 indicate that in these materials, LCDs are typically smaller than 6 Å, ASAs range from 164 to 1018 m^2/g, and void fractions (VF) are typically less than 0.5. Void analysis of the top candidates also shows that they all possess very similar structural characteristics, including one-dimensional pore channels as depicted in Figure 4.9. In order to determine the similarity between these materials beyond a visual inspection, one can also employ stochastic ray tracing to map the void space of each MOF onto a histogram. The similarity between a pair of structures can then be quantified by calculating the euclidean distance, as

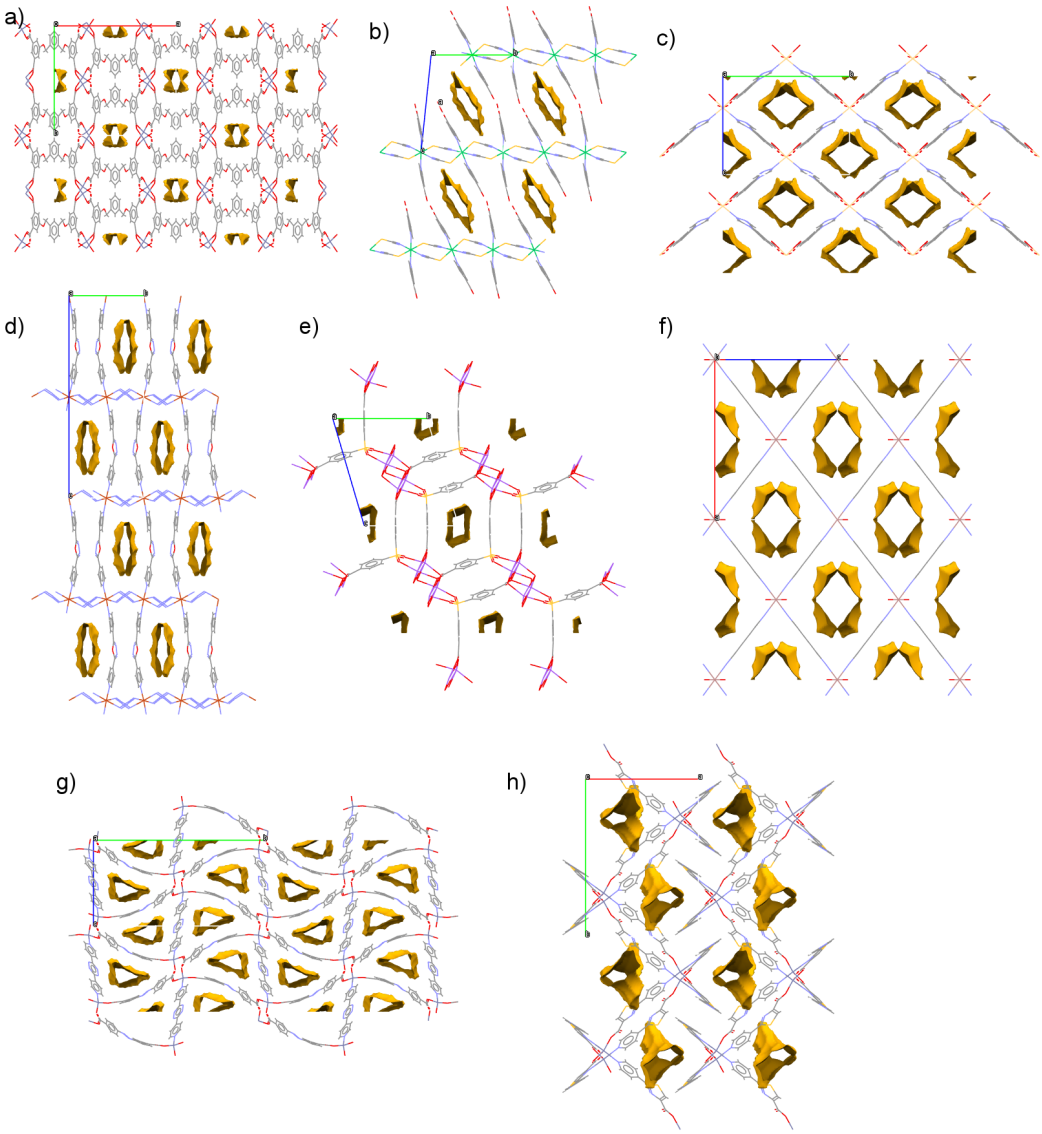


Figure 4.9: *Snapshots of the void space in the top structures determined from the contact surfaces of a 1.2 Å probe - QOKCID (a), FARZEE (b), RUVBER (c), ISAYUW (d), HISFUM (e), SOMSIY (f), KURSOH (g), LENROM (h).*

previously discussed in section 2.5.4. The resulting correlation plot for the top structures is shown in Figure 4.10, where a coefficient close to 0 means the pair of structures have very similar void space characteristics. For example, FARZEE and ISAYUW share the smallest coefficient of 0.145 - despite having very different compositions, they both possess narrow slit-type pores that share a common PLD and LCD. Consequently, their gas uptake and diffusion rates are quite similar across all investigated biogas components as displayed in Table 4.1.

Of the top 8 candidates, the MOF labelled QOKCID has the smallest

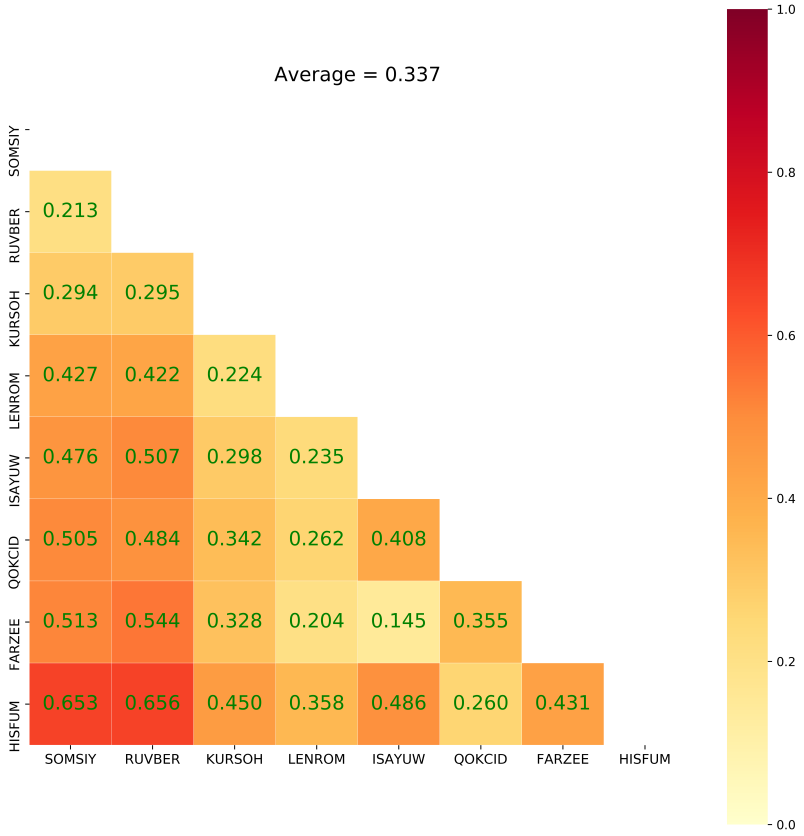


Figure 4.10: *Structural similarity plot for the top 8 MOFs identified in this study.*

LCD resulting in the lowest gravimetric and volumetric storage capacities for CO_2 and H_2S. In contrast, the MOF labelled RUVBER possesses the largest LCD allowing it to store more CO_2 and H_2S than most top candidates. It is known that pores with large diameters possess a large proportion of adsorption sites with weaker host-guest interactions, affecting their selectivity for contaminants. Despite this, RUVBER can still selectively adsorb both CO_2 and H_2S over CH_4 with large S_{ads}^{mix} values of 8.94 and 26.4 for CO_2/CH_4 and H_2S/CH_4 separations, respectively.

Diffusion coefficients $D_{CO_2}^{mix}$, $D_{CH_4}^{mix}$ and $D_{H_2S}^{mix}$ of the top candidates range from 4.38×10^{-5} cm^2/s to 7.87×10^{-7} cm^2/s. The average diffusion S_{diff}^{mix} for each binary mixture is fairly close to unity, ranging between 0.53 and 1.14 for

Table 4.1: Properties of the top 8 MOFs from GCMC and EMD simulations carried out at 10 bar and 298K

							— $\times 10^{-6}$ (cm^2/s) —							
REFCODE	PLD (Å)	LCD (Å)	ASA (m^2/g)	VF	n_{CO_2} (mol/kg)	n_{H_2S} (mol/kg)	$D^{mix}_{CO_2}$	$D^{mix}_{CH_4}$I	$D^{mix}_{H_2S}$	$D^{mix}_{CH_4}$II	$P^{mix}_{CO_2}$ (Barrer)	$S^{mix}_{CO_2/CH_4}$	$P^{mix}_{H_2S}$(Barrer)	$S^{mix}_{H_2S/CH_4}$
FARZEE	4.11	4.36	418	0.32	2.84	4.04	18.1	34.3	10.5	17.6	44582	6.56	37661	33.8
HISFUM	3.81	4.53	225	0.22	2.39	2.56	16.6	27.5	8.52	6.83	37063	11.9	20790	46.6
ISAYUW	4.32	4.59	376	0.31	2.80	3.46	28.4	32.5	19.9	22.7	70681	8.89	62670	35.3
KURSOH	4.60	5.22	674	0.43	4.55	3.61	13.2	11.6	3.67	4.31	45013	9.83	10136	32.7
LENROM	4.28	4.83	411	0.31	3.32	2.44	14.8	13.5	2.56	0.787	43673	8.72	5694	123
QOKCID	3.84	4.28	164	0.21	1.55	1.55	28.5	43.8	23.3	23.6	47688	12.5	39939	54.9
RUVBER	5.68	6.05	1018	0.51	5.58	6.05	27.1	24.7	10.8	11.3	108500	10.1	48046	26.8
SOMSIY	5.71	6.00	984	0.44	5.60	5.15	19.5	33.8	23.9	27.0	89295	4.93	103161	35.4

PLD = pore-limiting diameter; LCD = largest cavity diameter; ASA = accessible surface area; VF = void fraction; n_i = loading of adsorbate i obtained from 50:50 binary mixture GCMC; D^{mix}_i = diffusion coefficient of adsorbate i; $D^{mix}_{CH_4}$I is derived from CO_2/CH_4 simulations, and $D^{mix}_{CH_4}$II is derived from H_2S/CH_4 simulations; P^{mix}_i = permeability of adsorbate i; $S^{mix}_{i/j}$ = membrane selectivity for adsorbates i and j in the binary mixture.

CO_2/CH_4 mixtures and between 0.60 and 3.25 for H_2S/CH_4 mixtures. In the CO_2/CH_4 mixtures, CO_2 molecules interact more strongly with the framework than CH_4 resulting in a reduced degree of freedom that is reflected in their smaller self-diffusion coefficients. In the H_2S/CH_4 mixtures, the large gas loadings and high $S^{mix}_{\mathrm{ads},H_2S/CH_4}$ result in each CH_4 molecule being surrounded by a large number of contaminant molecules. This strongly influences the diffusion rate of CH_4 such that both H_2S and CH_4 molecules possess similar rates of diffusion through the pore channels. In general, $D^{mix}_{CO_2} \geq D^{mix}_{H_2S}$ because each MOF possesses a lower $S^{mix}_{\mathrm{ads},CO_2/CH_4}$ value than $S^{mix}_{\mathrm{ads},H_2S/CH_4}$. Consequently, a larger concentration of CH_4 is found in the pores during the CO_2S/CH_4 MD simulations which can collide with nearby CO_2 to help increase their diffusion rate.

4.3.5 Comparison with literature membranes

Next, $P^{mix}_{CO_2}$ and S^{mix}_{mem} of the top MOF candidates are compared to those of other porous membranes reported in the literature, which include pure zeolite-, MOF- and ZIF- based membranes, in addition to a number of novel MMMs (Table 4.2). Note that many studies report CO_2 separations over a range of conditions which may not be exactly the same as those used for biogas upgrading. However, these studies are still useful as they allow us to evaluate the separation performance of the MOF materials identified in the proposed screening. Some of the largest values of S^{mix}_{mem} were reported by Carreon[268] and Shi[269] for SAPO-34 membranes, and many of the reported MOF- and ZIF- based membranes possess $P^{mix}_{CO_2}$ of 10^4 Barrer to 10^5 Barrer and S^{mix}_{mem} ranging between 1 and 25. The formation of composite MMMs appears to improve S^{mix}_{mem} of many MOFs at the cost of lowering the value $P^{mix}_{CO_2}$ which typically range from 10s to 1000s of Barrer. However, it is clear from the studies reported in Table 4.2 that changes to the polymer and MOF loading can significantly alter the permeability, resulting in an additional level of con-

Table 4.2: Comparison of the top 8 MOFs identified by the proposed screening with literature zeolite, MOF and MMM based membranes

Material	$P^{mix}_{CO_2}$ (Barrer)	$S^{mix}_{mem,CO_2/CH_4}$	feed / permeate pressure (bar)	temp (K)	ref
H-ZSM-5	6.40	5.50	2.70 / 1.38	300	[266]
$Cu_2(bza)_4(pyz)$	4.48 x 10^3	25.0	1.50 / 1.00	293	[267]
SAPO-34	4.03 x 10^4	171	2.24 / 0.84	295	[268]
SAPO-34	4.84 x 10^4	186	2.40 / 1.00	295	[269]
HKUST-1	5.00 x 10^4	1.70	1.00 / 1.00	298	[220]
ZIF-8	3.63 x 10^5	5.10	1.38 / 0.99	295	[223]
Bio-MOF-1	5.14 x 10^4	2.50	1.38 / 0.99	298	[221]
ZIF-90 (modified with APTES ligand)	7.78 x 10^2	4.70	1.00 / 1.00	498	[224]
Ni-MOF-74	1.04 x 10^5	0.316	1.00 / 1.00	298	[222]
ZIF-69	1.22 x 10^4	4.60	1.00 / 1.00	298	[225]
20 wt% ZIF-8 @ Matrimid®5218	16.6	35.8	4.00 / 0.05	503	[270]
20 wt% SAPO-34 @ PU	28.7	25.6	12.0 (feed)	298	[271]
40 wt% NOTT-300(Al) @ Pebax®1657	395	36.3	10 bar (feed)	298	[272]
10 wt% ZIF-8 @ (10:90) PIM-1/6FDA-DAM	2891	26.6	3.00 / 1.00	308	[273]
20 wt% NH_2-MIL-53(Ti) @ PSF	29.3	29.5	3.00 (feed)	303	[274]
FARZEE	4.46 x 10^4	6.56	10.0 / vacuum	298	This work
HISFUM	3.71 x 10^4	11.9	10.0 / vacuum	298	This work
ISAYUW	7.07 x 10^4	8.89	10.0 / vacuum	298	This work
KURSOH	4.50 x 10^4	9.83	10.0 / vacuum	298	This work
LENROM	4.37 x 10^4	8.72	10.0 / vacuum	298	This work
QOKCID	4.77 x 10^4	12.5	10.0 / vacuum	298	This work
RUVBER	1.09 x 10^5	10.1	10.0 / vacuum	298	This work
SOMSIY	8.93 x 10^4	4.93	10.0 / vacuum	298	This work

trol over the permeation properties. In comparison, it appears that the top MOFs membranes identified in this work generally possess larger S^{mix}_{mem} and $P^{mix}_{\text{CO}_2}$ values. Furthermore, as these materials lie above the Robeson limit, their separation performance is competitive with traditional polymer membranes. As our simulations assume a perfect, defect-free crystal structure, the values of $P^{mix}_{\text{CO}_2}$ and S^{mix}_{mem} represent an upper limit of what may be achievable in these MOFs under the approximations made in these simulations. Despite this, the top MOFs in this work appear to show promise in separating biogas contaminants. Further insight which assesses the top membranes as filler particles in MMMs would be beneficial to establish whether their separation performance can be enhanced further.

4.3.6 Structure-Performance relationships

One of the main advantages of working with large data sets of structures is the ability to investigate the relationships between their performance and physical properties, which are crucial in the rational design of future materials. Generally, the separation performance for a class of materials can not be linked to an individual structural, physical or chemical property; it requires understanding of a complex interplay between all of them. Figure 4.6 shows that 1183 MOFs could pass the selectivity-permeability trade-off relationship described by the 2008 Robeson's upper bound. By comparing the structural properties of the MOFs in this study, three closely linked questions are considered: 1) Are there any common properties shared by these 1183 structures? 2) How do these properties account for the observed separation performance? and 3) Are there any relationships between the structural properties and the separation performance that will allow us to construct design principles for future MOFs?

Histogram distributions shown in Figure 4.11 for different structural properties of the 1183 MOFs indicate that many of these MOFs contain small pore

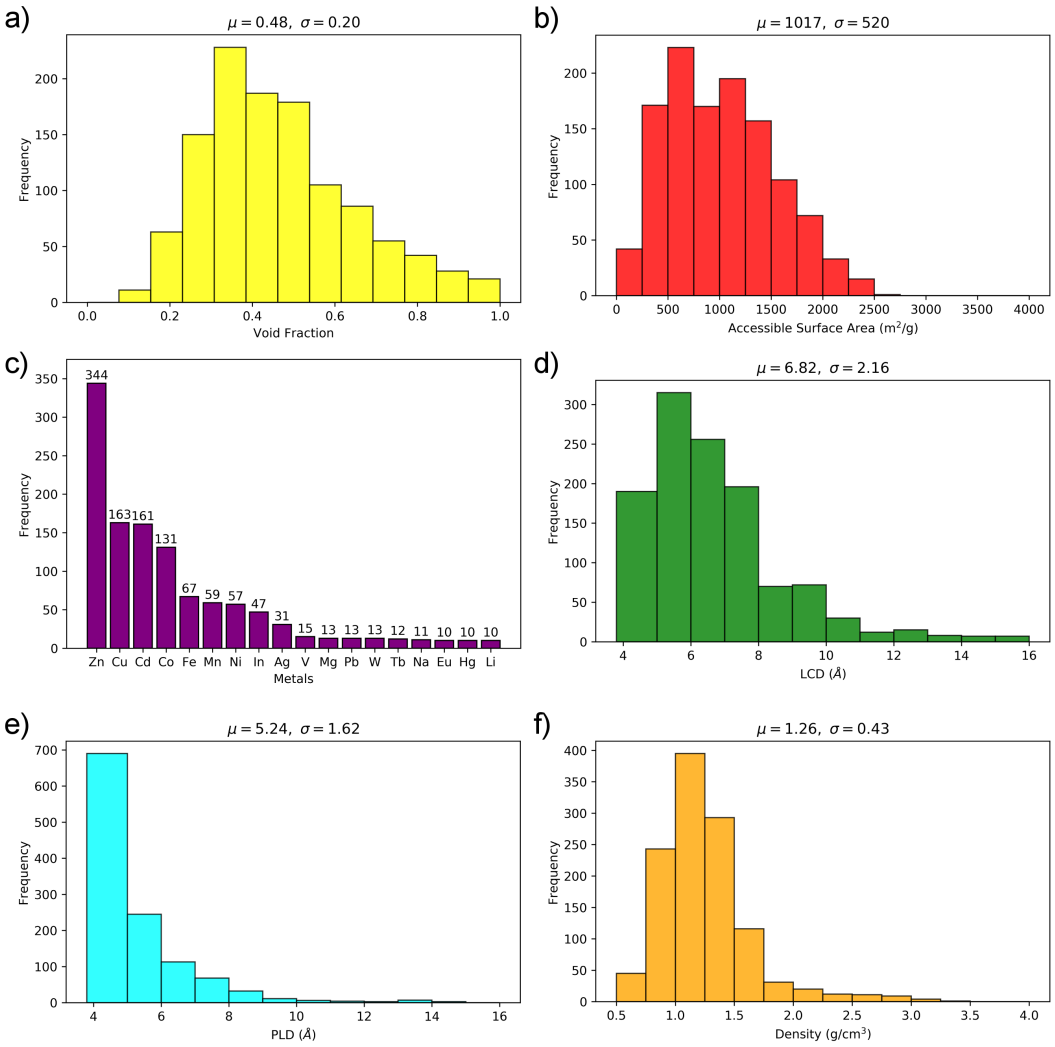


Figure 4.11: *Distributions of a) void fraction, b) accessible surface area, c) metals, d) largest cavity diameter, e) pore-limiting diameter, e) density in the 1183 MOFs above the Robeson upper bound (μ = mean, σ = standard deviation).*

sizes, with 80% of the structures having pore-limiting diameter (PLD) less than 6 Å and 81% possessing LCD below 8 Å. The ultra-microporous nature of many of these materials also leads to small ASAs with 68% found to possess an ASA less than 1250 m^2/g. Interestingly, the remaining 32% of materials make up 93% of the total hydrophobic MOFs that possess ASA exceeding 1250 m^2/g. However, most of these materials still have relatively small PLD's and LCD's, with only 159 structures exhibiting an LCD exceeding 8 Å and ASA larger than 1250 m^2/g. Large pores with high surface area can make it more difficult to separate mixtures through differences in binding affinity, making them undesirable for these types of separation. The porosity distribution indi-

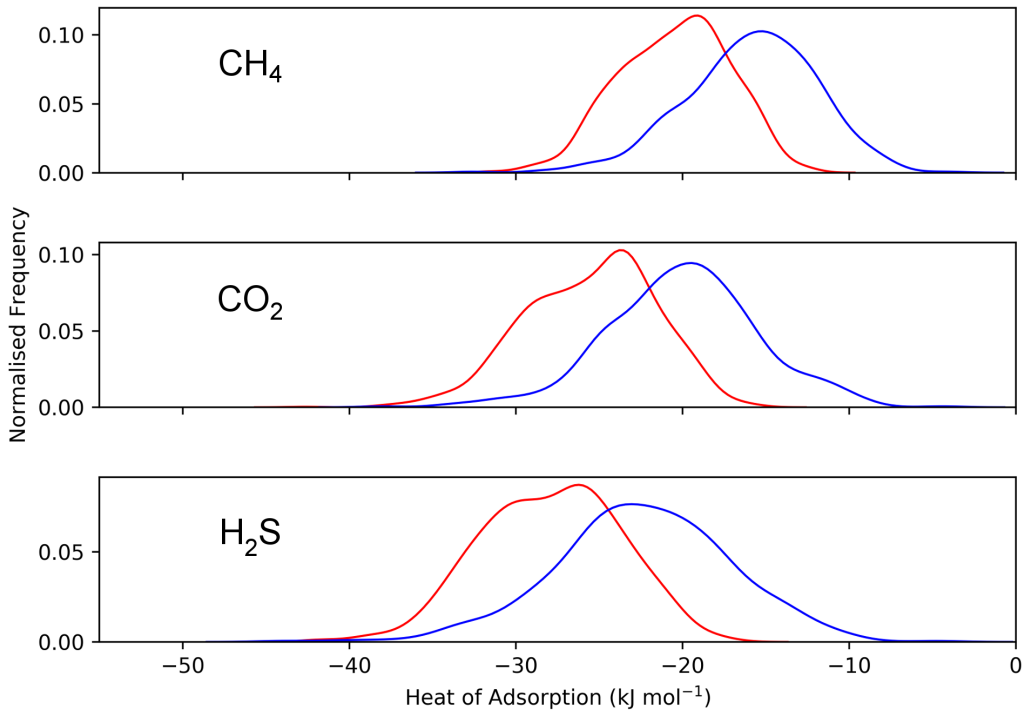


Figure 4.12: *Distribution of Q_{st}^0 for CH_4, CO_2 and H_2S in the MOFs above (red) and below (blue) the 2008 CO_2/CH_4 Robeson limit.*

cates that MOFs with low void fraction (VF) appear more frequently, with 42% possesing VF $<$ 0.4 and 61% $<$ 0.5. Analysis of the metals in each structure indicates that 29% of the structures are constructed from zinc based nodes, forming the most common metal ahead of cadmium (17%), copper (15%) and cobalt (10%). Furthermore, these four metals were exclusively found in 7 of the 10 top MOFs. In a recent study by Altintas and co-workers, it was shown that these four metals also frequently appear in the top membranes predicted for CH_4/H_2 separations.[248] Finally, the density distribution in Figure 4.11f shows that 64% of MOFs above the upper bound possess densities between 1 g/cm^3 and 1.5 g/cm^3. In summary, based on the calculations at infinite dilution, MOFs with PLD between 3.8 Å and 6 Å, LCD between 4 Å and 8 Å, ASA less than 1250 m^2/g, VF between 0.3 and 0.5 and density between 1 g/cm^3 and 1.5 g/cm^3 are found to appear most frequently in the top candidates of this computational screening for biogas separations and exhibit superior separation performance.

In order to verify the significance of these structure-performance relationships, it is useful to compare them with the structural property distributions from low-performing materials that lie below the 2008 Robeson bound. If structures below the upper bound also have similar distributions, then this suggests that these properties are not of significance and do not correlate with high performance. Interestingly, it is found that only 10% of membranes below the upper bound possess structural properties that are frequently observed in those above the upper bound (i.e. PLD between 3.8 Å and 6 Å, LCD between 4 Å and 8 Å, ASA less than 1250 m^2/g, VF between 0.3 and 0.5 and density between 1 g/cm^3 and 1.5 g/cm^3). Two of the most significant differences appear to be the PLD and LCD. In the low-performing subset of membranes, 42% possess a PLD smaller than 6 Å and 43% possess a LCD smaller than 8 Å. In contrast, this increases to 80% and 81% in membranes above the upper bound. In addition, only 29% of membranes below the upper bound possess a VF smaller than 0.5, in contrast to the 61% of structures above the upper bound. Finally, 32% of membranes below the upper bound possess a density between 1 and 1.5 g/cm^3, in contrast to 64% of membranes above the upper bound. These results suggests that the structure-performance relationships found from this study are significant and provide a good correlation with the superior separation performance.

Calculations of the isosteric heats of adsorption (Q^0_{st}) can provide useful insight into a MOFs affinity for different gas molecules. These can be directly linked to the strength of host-guest interactions which are related to structural properties such as pore diameter (PLD, LCD) and porosity (VF). The Q^0_{st} distributions for the MOFs above and below the 2008 Robeson upper bound are presented in Figure 4.12. For CH_4, CO_2 and H_2S, the distributions representing MOFs above the upper bound (red) lie further to the left than those below the upper bound (blue), implying that, in general, there are stronger host-guest interactions present in the MOFs above the upper bound. This is also reflected in the average values of $K^0_{CH_4}$, $K^0_{CO_2}$ and $K^0_{H_2S}$ which were a factor of

3.03, 3.90 and 4.73 larger for MOFs above the upper bound, respectively. From these results, a reduction in the rate of diffusion for each biogas component is expected to be observed. For the MOFs below the upper limit, the average $D^0_{\mathrm{CH_4}}$, $D^0_{\mathrm{CO_2}}$ and $D^0_{\mathrm{H_2S}}$ are found to be a factor of 1.87, 1.42 and 1.64 times larger than the MOFs above the upper bound. As permeability is calculated from the product of the solubility and diffusion properties of the material, it can be observed that the changes to K_i^0 outweigh the changes to D_i^0 and therefore, permeability and selectivity become larger for the MOFs above the upper bound.

4.3.7 Applying Structure-Performance relationships

While there are many screening studies in the literature that have determined a series of structure-performance relationships from their top-performing materials, far less have studied their future employment in the screening process to discover new materials. As a case study, some of the structure-performance relationships determined in this work are employed to streamline the discovery of top-performing biogas upgrading candidates from 134,162 hypothetical MOF structures that were previously constructed *in silico* from a library of chemical building blocks by Wilmer *et al.*[78] After applying the same geometric criteria described in section 4.2, an additional constraint is employed to involve some of the structure-performance relationships from section 4.3.6. In this case study, structures with a PLD $\geq$ 6 Å are subsequently removed from the screening, leaving a total of 40,773 MOFs. A test for hydrophobicity as described in section 4.2 is then applied to each material, in which a hydrophobic subset of 8978 MOFs is identified. For these MOFs, the CO_2/CH_4 and H_2S/CH_4 separation capabilities are determined under ideal conditions at infinite dilution allowing a quick assessment of their performance.

From the Robeson plots displayed in Figure 4.13, a total of 2395 MOFs are able to exceed the 2008 limit, with P_{CO_2} and P_{H_2S} ranging between 10^5 and

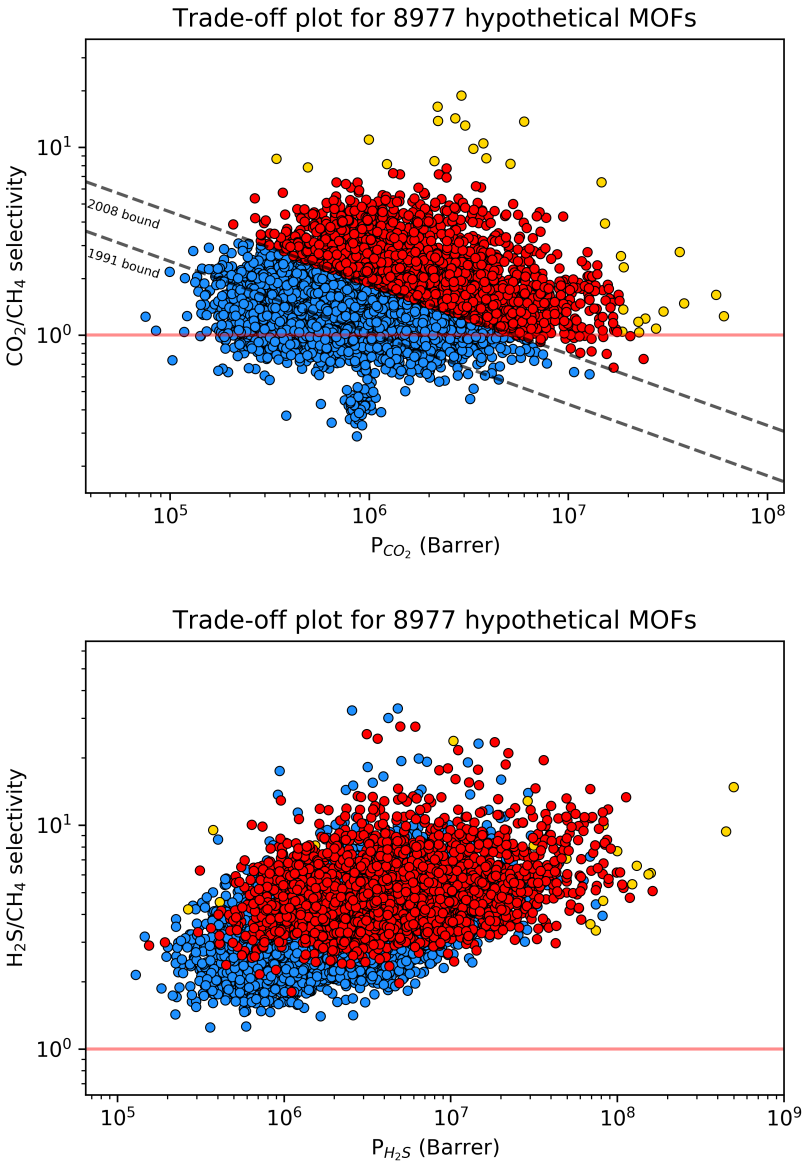


Figure 4.13: *Robeson trade-off plots for CO_2/CH_4 (top) and H_2S/CH_4 (bottom) ideal separations in 8977 MOFs. The CO_2/CH_4 Robeson 1991 and 2008 limits are used to compare performance of each MOF to some of the best polymer membranes*

10^9 Barrer, and S^0_{mem} ranging between 0.288 and 33.2. Unlike the real MOFs in section 4.3.2, far fewer candidates are observed with $P_{CO_2} \geq 10^7$ Barrer which was previously used to identify the top candidates in this screening. Therefore, top-performing candidates are selected from those above the 2008 limit that possess high selectivity, high permeability or a combination of both (highlighted in yellow). While there is potential for further study into these materials, this is beyond the scope of this case study which demonstrates that some structure-performance relationships can provide an additional screen-

ing stage to streamline the screening process. It is important to note that these structure-performance relationships are not an exact rule and that top-performing materials will likely exist with different structural properties. This is evident by the large proportion of candidates that were unable to surpass the 2008 and 1991 limits despite possessing similar pore sizes to those identified in the screening of real MOFs. Nevertheless, the application of a single relationship has been able to identify 2395 new candidates in a much shorter time than if the entire database was examined, highlighting a new route for expediting initial screening stages and reinforcing that structure-performance relationships can provide useful insight into the design of future membranes.

4.4 Conclusions

In this work, a multi-stage screening protocol was designed to identify the most promising porous MOFs for biogas upgrading. MOFs residing in the Cambridge structural database were pre-screened using a set of geometric criteria in order to remove structures with non-accessible surface area and pore diameter smaller than the individual components of biogas. The initial phase of screening predicted the single component permeation of CO_2, CH_4 and H_2S from adsorption and diffusion calculations at infinite dilution. In addition, Henry constants for the adsorption of H_2O were calculated for each structure to determine the relative levels of hydrophobicity. Only the top hydrophobic MOF structures which exceed the Robeson upper bound and are assumed to be the least affected by co-adsorption of H_2O molecules within the biogas stream were considered for the final phase of calculations. For these materials, mixture selectivity and permeability at 298 K and 10 bar were predicted from equimolar CO_2/CH_4 and H_2S/CH_4 simulations. The top 8 MOFs identified in this work possess selectivity and permeability that rivals that of polymer-, zeolite-, ZIF- and MMM- based membranes. At the operating conditions of 10 bar and 298 K, the predicted values of CO_2 permeability range between

3.71×10^4 Barrer and 1.09×10^5 Barrer, CO_2 selectivity between 4.93 and 11.9, H_2S permeability between 5.69×10^3 Barrer and 1.03×10^5 Barrer and H_2S selectivity between 32.7 and 123 for these top candidates. In addition, the structural properties of the 1183 hydrophobic membranes with membrane selectivity values above the Robeson limit were examined and indicate that MOFs with PLDs between 3.8 Å and 6 Å, LCDs between 4 Å and 8 Å, ASAs less than 1250 m^2/g, VF between 0.3 and 0.5 and density between 1 g/cm^3 and 1.5 g/cm^3 are exceptional candidates for biogas upgrading. To test how structure-performance relationships could be applied into future screenings, a final case study was employed to rapidly screen the hypothetical MOF database of Wilmer *et al*, containing 134,162 structures. Although the same protocol designed to screen the real MOF database was employed, an additional constraint that only screened MOFs with PLD $\leq$ 6 Åwas employed. This lead to the rapid discovery of 2395 hydrophobic candidates that were able to exceed the 2008 limit from calculations at infinite dilution. This demonstrates how the inclusion of previous structure-performance relationships into the initial geometric screening phase of the study can identify top-candidates in a much shorter time frame than if the entire database was screened. However, it should be noted that the application of these constraints may only apply to similar classes of porous material and at best, should be used as concise method of identifying similar candidates with exceptional separation performance.

Chapter 5

Evaluating COF-based membranes for biogas upgrading: A comparative study

Abstract

In this chapter, the previously designed high-throughput screening methodology is expanded to study covalent-organic frameworks as alternative membrane materials. After evaluating their separation performance, a comparative analysis of the top performing COF membranes is made with the top MOF membranes from chapter 4. Finally, a further investigation into the impact of biogas feed pressure is conducted across several porous COF and MOF membranes in order to optimise their separation performance.

5.1 Introduction

Covalent organic frameworks (COFs) represent an emerging class of nanoporous materials that solely consist of organic building blocks which are linked by covalent bonds via reversible condensation reactions. Unlike traditional zeolites, they display low porosities and a wide range of tunable pore sizes and surface areas from the highly abundant nature of their chemical building blocks.

Furthermore, they display excellent thermal and chemical stabilities across a wide range of environments unlike novel MOF materials. As such, they have attracted much attention for their potential suitability in gas storage, separation, catalysis, sensing and electronic device applications.[41–43,275]

Since their conception, the synthesis of continuous COF-based membranes has been a long-standing goal. However, many COF-based membranes suffer from difficult synthesis procedures; poor scalability; and insolubility across many solvents.[276] Furthermore, their growth is usually restricted into small domains as a result of internal defects.[277] One successful method of membrane fabrication involves exfoliation of bulk COFs into 2D nanosheets that are deposited onto a macroporous support. Recently, Li and co-workers prepared homogeneous and ultrathin COF-1 membranes supported on alumina.[278] Single-component permeation tests were conducted using He, H_2, N_2 and SF_6 at a feed and permeate pressure of 2 and 1 bar respectively. The authors reported a H_2 permeance of 1.62 x 10^{-6} mol m^{-2} s^{-1} Pa^{-1} and an ideal H_2/N_2 selectivity of 3.3. In a separate study, Ying *et al.* employed graphene-oxide nanosheets to assemble continuous and ultrathin CTF-1 membranes with highly tunable thickness's.[279] The single-component H_2 permeation results indicate fast permeances of 1.70 x 10^{-6} mol m^{-2} s^{-1} Pa^{-1} and large H_2/CO_2 selectivities of 17.4 at 298 K and a feed pressure of 3.0 bar. Furthermore, the separation performance of the prepared membranes was found to surpass the Robeson's 2008 upper bound, indicating the potential suitability of this membrane for clean-energy separations. Like many other membrane materials, there have been reports of incorporating COF materials into MMMs to increase their gas permeabilities and selectivities. Kang *et al.* prepared exfoliated nanosheets of NUS-2 and NUS-3 that were blended with polyetherimide (PEI) and polybenzimidazole (PBI) into MMMs.[280] The good compatibility between the COFs and polymers lead to a series of defect-free membranes with good mechanical properties that exhibited increased gas permeabilities and selectivities relative to the pure-polymer membrane. Furthermore, the incorporation of 20 wt%

of NUS-2 into PBI led to a H_2/CO_2 membrane selectivity up to 31.4 which was able to surpass the 2008 Robeson upper bound. Shan and co-workers reported the synthesis of MMMs with azine-linked ACOF-1 filler particles and the commercial Matrimid5218®. as a polymer matrix.[281] The good compatibility between the COF and polymer resulted in good adhesion and improved CO_2/CH_4 separation performance over the pure polymer. Using equimolar CO_2/CH_4 mixtures at 308 K and a feed pressure of 4 bar, a 16 wt% ACOF-1@Matrimid® MMM displays a CO_2 permeability of 15 Barrer and a CO_2/CH_4 permselectivity of approximately 32, rendering this membrane as a potentially good candidate for biogas separations.

One of the first computational examinations of mixture diffusion in COFs was performed by Keskin who studied the separation of CH_4/H_2 mixtures. This study showed how COFs may act as promising materials for membrane separations of CH_4/H_2 and that their separation performance may even rival that of several MOF- and zeolite-based membranes.[102] In more recent years, COF-based screenings have emerged across the literature. For example, Yan *et al* studied CO_2/CH_4 membrane separations in over 300 unique COFs.[88] The top materials identified in this work were modified with 10 kinds of functional groups in order to assess their impact on the separation process and to learn new design principles for future materials. The authors found that COFs decorated with halogen F and Cl groups occupy 50% of the best materials that exceed the 2008 Robeson's bound and possess membrane selectivities greater than 20. In addition, the authors expanded the study to assess each COFs performance as filler particles in a range of MMMs. In the past few months, Altundal *et al.* investigated the adsorbent- and membrane- separation performance of 295 COFs for flue gas separations involving CO_2/N_2 mixtures.[282] For PSA processes, the authors noted that the low densities of COF materials mean they generally possess higher working capacities than many MOF-based adsorbents. Furthermore, a number of COFs were found to exhibit higher adsorption selectivities than many commercially-used zeolites and activated

carbons. As for the membrane separations, the authors noted that COF membrane gas permeabilities were predicted to be similar to those of MOF membranes, but suffered from lower membrane selectivities that ultimately resulted in many membranes falling below the 2008 upper bound.

Overall, these studies show that COF-based membranes can provide desirable separation performances across a wide range of gas mixtures. Therefore in this chapter, the multi-stage screening protocol that was introduced in chapter 4 is further extended to study the CO_2/CH_4 and H_2S/CH_4 separation performance across a diverse set of COF membranes. The membrane properties of these materials will be directly compared with the top MOFs of section 4.2 to assess the viability and competitiveness of COFs as candidates for biogas upgrading.

5.2 Screening COF membranes for biogas upgrading

5.2.1 Computational Details

Unless specified, the calculations performed in each stage of the screening use the same computational setup as described previously in section 4.2. A total of 309 COFs are taken from the computation-ready experimental (CoRE) database v3.0 for use in this study.[107] Each structure is solvent-free and disorder-free making it suitable for direct use in computational calculations. After calculating the structural properties of each material, the initial set of 309 structures is refined to 296 structures by selecting those that possess non-zero ASAs and PLDs $\geq$ 3.80 Å. However, after assigning partial charges using the EQeq scheme and evaluating their distribution across each structure, only 284 structures are found to be viable based on the criteria previously defined in section 4.3.1.

Before screening these COFs, distributions of their structural properties

are plotted which reveal some similarities and differences to the set of MOFs screened in chapter 4 (Figure 5.1). Despite being made up from only 284 structures, this set of COFs display a wide diversity of pore sizes and surface areas; almost 50% are classed as mesoporous structures and many more are found to possess pore diameters that approach the microporous-mesoporous boundary. This is in stark contrast to the MOF candidates screened in chapter 4 in which only 1.4% of the initial 6768 MOFs possess an LCD $\geq$ 20 Å. As COFs are synthesised from light elements, their densities are expected to be much lower than most MOFs; therefore it is not surprising that the majority in this group lie between 0.25 and 0.75 g/cm^3. More than 80% of these structures can be classified as 2-D frameworks, many of which are built from expanded and conjugated building blocks that favour eclipsed stacking patterns leading to highly porous networks - this is captured by the high frequency of structures with VF between 0.7 - 1.0.

While it is possible that the top COFs to be identified in this study will possess similar structural properties to the top MOFs identified in chapter 4, it is similarly plausible that COF-based membranes could possess a different set of structure-performance relationships due the high proportion of materials with large micropores/small mesopores with large surface areas and porosities. Therefore, a comparison of the separation performance between both classes of materials will be made. Although it could be seen that the small number of COF structures in this database could bias the structure-performance relationships in this study, the CoRE-COF database is noted to contain the most complete collection of experimental COF structures from the literature.

5.2.2 Separations at infinite dilution

The presence of strong covalent bonds in COFs often results in robust frameworks that possess good thermal and chemical stability. However, COFs that are assembled from boroxine or boronate esters can often hydrolyse back into

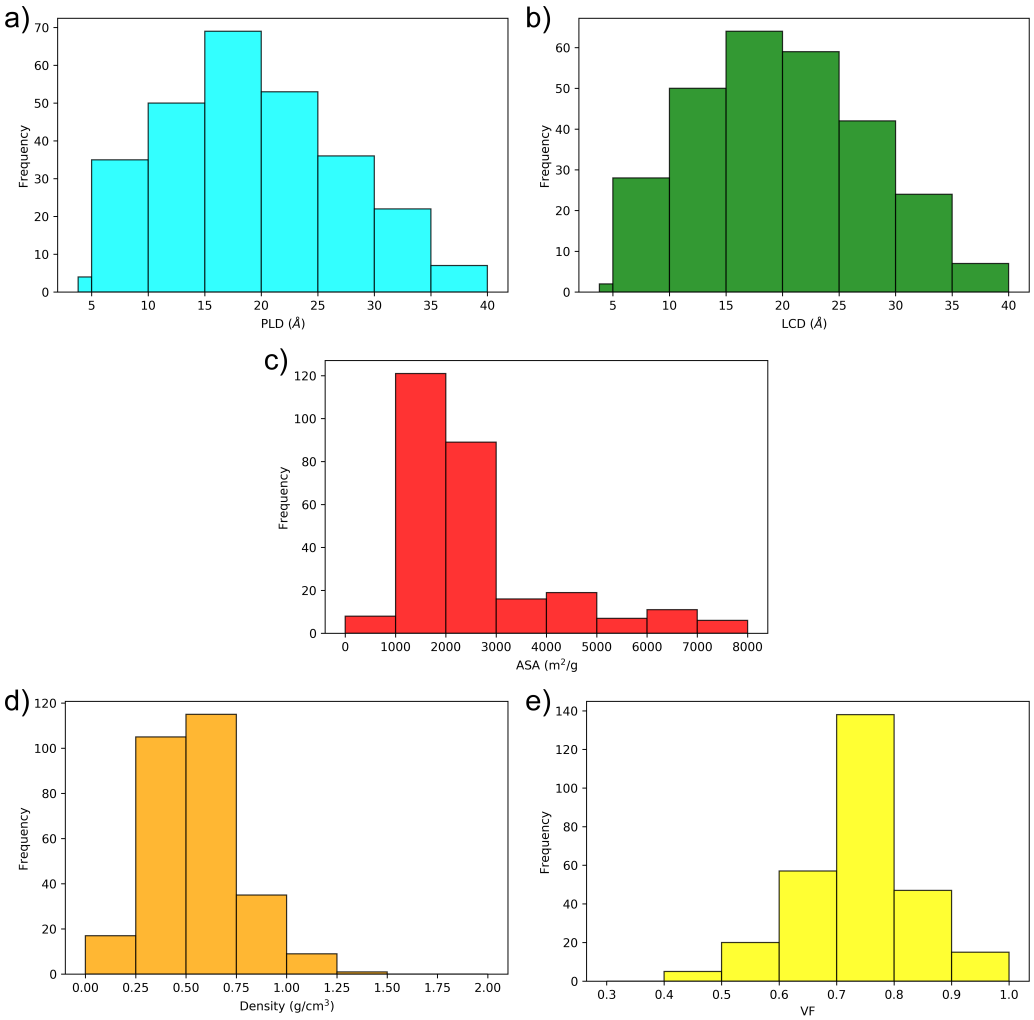


Figure 5.1: *Distributions of a) PLD, b) LCD, c) ASA, d) Density, and e) VF across the 284 COFs screened in this study.*

their acid and diol-based precursors in the presence of H_2O.[283,284] This is due to the strong electron-deficiency of the boron centers which makes them susceptible to nucleophillic attack. In this work, up to 30% of the investigated COFs are found to contain either boroxine or boronate ester linkages which may compromise their ability to separate bio-gas mixtures in the presence of H_2O vapour. Like previously in chapter 4, a hydrophobic criteria is enforced to eliminate structures susceptible to loss of function through hydrolysis or where H_2O adsorption could prove detrimental to the selectivity. While many COFs are considered to be hydrophobic due to their large content of aryl moieties, it will be later demonstrated that only 1 boronate-ester containing COF is identified in the top candidates and may be an exceptional candidate for separating

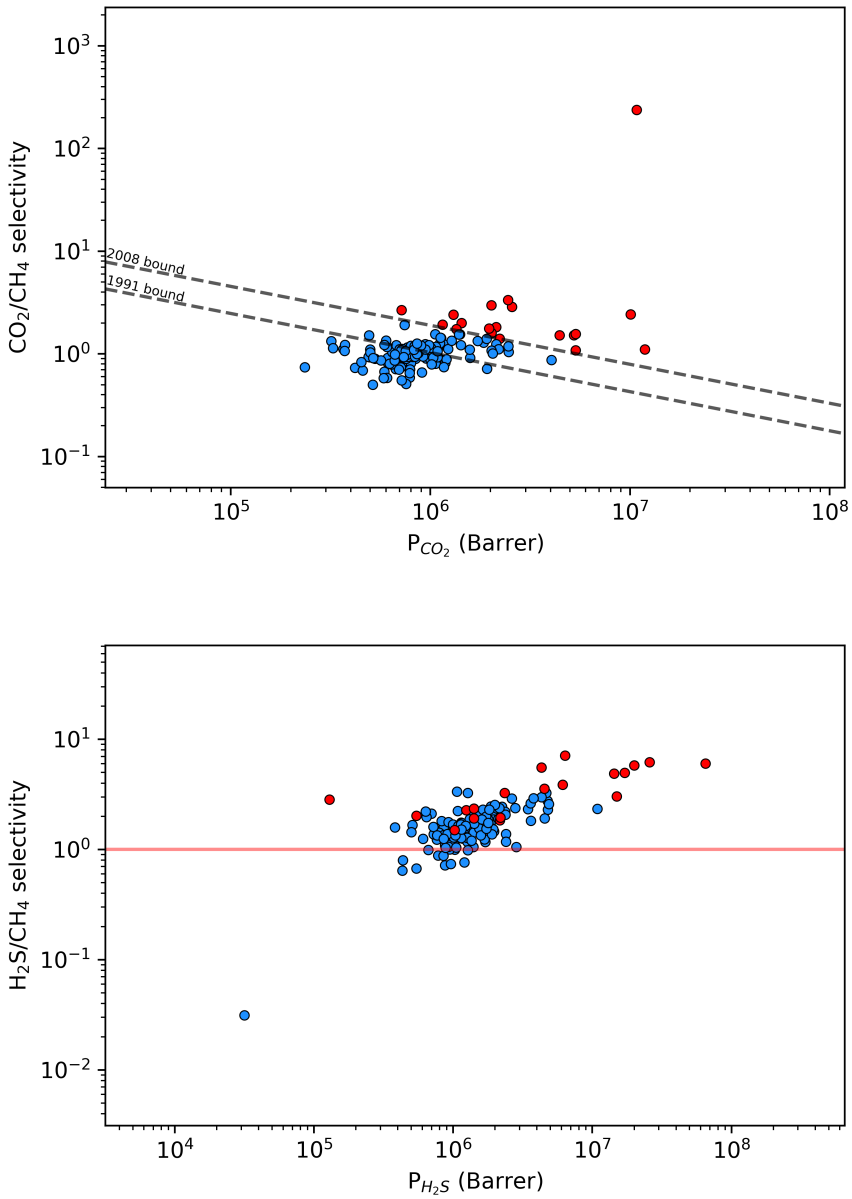


Figure 5.2: *Robeson trade-off plots for CO_2/CH_4 (top) and H_2S/CH_4 (bottom) ideal separations in 149 COFs. The CO_2/CH_4 Robeson 1991 and 2008 limits are used to compare performance of each COF to some of the best polymer membranes. 19 COFs lie above the 2008 limit (red points) which are used to study binary mixture separations at working conditions of 10 bar and 298K.*

bio-gas under dry conditions. Overall, 149 COFs are retained after applying this criteria and their permeability and selectivity for bio-gas contaminants is evaluated under infinite dilution conditions.

To assess the CO_2/CH_4 and H_2S/CH_4 separation performance of each membrane, Robeson plots are constructed as shown in Figure 5.2. For CO_2/CH_4 separations, $S^0_{\mathrm{mem},CO_2/CH_4}$ values range from 0.5 to 236, and $P^0_{CO_2}$ values range

from 2.36×10^5 Barrer and 1.19×10^7 Barrer - a total of 19 COFs exceed the 2008 Robeson limit. For H_2S/CH_4 separation, 28 COFs were found to be more selective for CH_4 than H_2S with $S^0_{\mathrm{mem},CH_4/H_2S}$ as high as 32. The remaining 121 possess $S^0_{\mathrm{mem},H_2S/CH_4}$ ranging from 1 to 7.10, and $P^0_{H_2S}$ from 3.17×10^4 to 6.51×10^7 Barrer, respectively.

Among the structures in Figure 5.2 are two interesting outliers. The first is OH-TAPH-COF which possesses a large ideal selectivity of 32 towards CH_4 over H_2S. This imine-linked 2-D COF is formed from the condensation reaction of 2,5-dihydroxyterephthalaldehyde (DHTA) and 5,10,15,20-tetrakis(4-aminophenyl)porphyrin (TAPH).[285] The potential for numerous $\pi-\pi$ stacking interactions leads to an eclipsed AA stacking arrangement with an interlayer spacing of approximately 6.75Å located between the porphyrin rings of each layer (Figure 5.3a & b). To rationalise the high CH_4 selectivity, MD snapshots from simulations at infinite dilution are analysed and show that H_2S molecules are attracted to the porphyrin sites between each layer (Figure 5.3c). Once occupied, the combination of strong dispersive and electrostatic interactions makes it much harder for H_2S molecules to vacate these sites and explore other regions of the framework, leading to a low $D^0_{H_2S}$ value of 7.53×10^{-7} cm^2/s. While CH_4 molecules are also attracted to the porphyrin sites, their host-guest interactions rely solely on dispersion leading to a weaker Q^0_{st} value (CH_4: -21.6 kJ/mol, H_2S: -30.8 kJ/mol). As such, CH_4 molecules are able to diffuse more freely across the framework ($D^0_{CH_4} = 3.07 \times 10^{-4}$ cm^2/s) and have been visualised interacting over different aryl sites (Figure 5.3d).

The second is AEM-COF-2 which possesses the largest $S^0_{\mathrm{mem},CO_2/CH_4}$ in this work of 236, and the only structure above the 2008 upper bound that contains a boronate ester linkage. AEM-COF-2 possesses a 2-D framework with an eclipsed stacking pattern from the condensation reaction between an arylene-ethynylene macrocycle and 1,4-benzenediboronic acid (Figure 5.4).[286] The framework topology affords a series of large hexagonal channels that are surrounded by six smaller triangular channels that are large enough to accom-

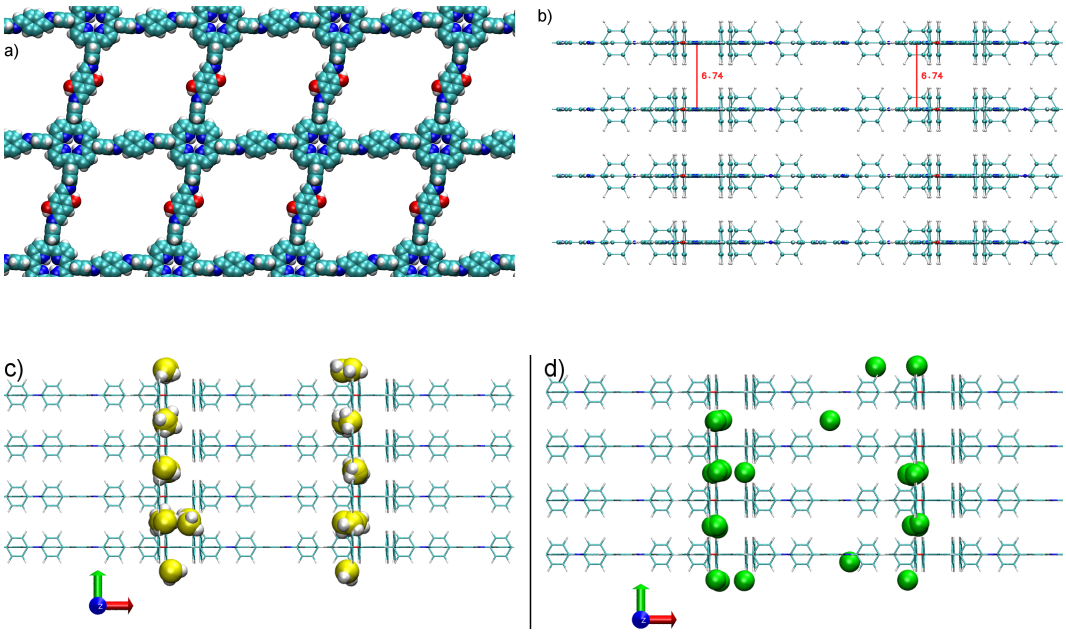


Figure 5.3: *Empty unit cells of OH-TAPH-COF - a 2-D COF with an porphyrin interlayer spacing of 6.75Å(a,b); MD simulation snapshots at infinite dilution conditions showing H_2S (c) and CH_4 (d) adsorbed on OH-TAPH-COF; Colour scheme: Cyan = C, White = H, Red = Oxygen, Blue = Nitrogen, Yellow = Sulphur, Green = Methane*

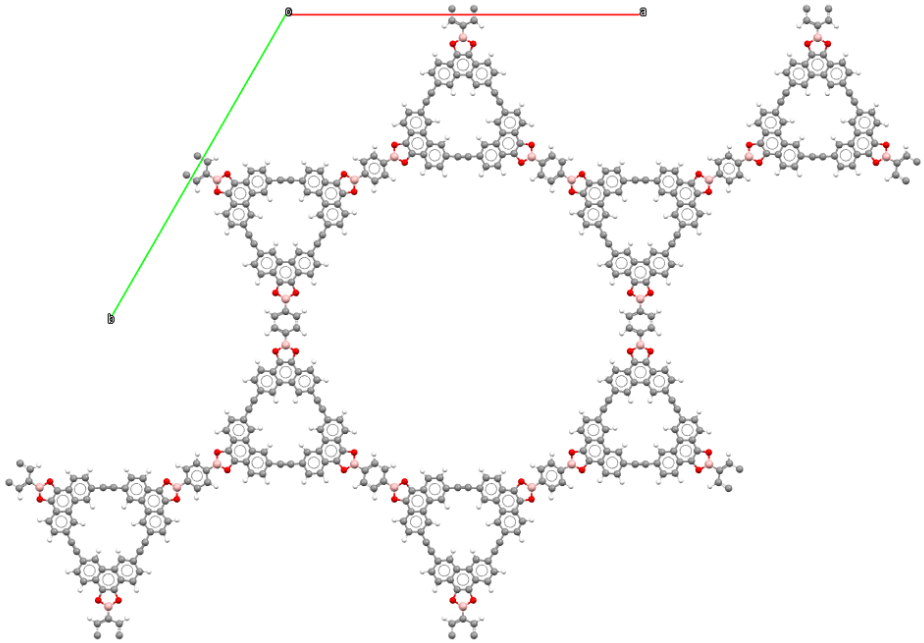


Figure 5.4: *Structure of the 2-D AEM-COF2 containing small triangular and large hexagonal pores.*

modate CH_4, CO_2, H_2S and H_2O molecules. Analysis of the simulations under infinite dilution conditions indicates that the exceptionally large $S^0_{\mathrm{mem},CO_2/CH_4}$ in AEM-COF-2 can be explained from the differences between host-guest in-

teractions. Both CH_4 and CO_2 possess relatively large Q_{st}^0 values of -31.5 and -36.6 kJ/mol, respectively, which are mainly attributed to the strong dispersive interactions from adsorbing in the small triangular pores. Additionally, CO_2 has a weak but repulsive electrostatic contribution which combined with its smaller diameter allows it to propel along the small triangular pores at a faster rate than CH_4. In contrast to the high CO_2/CH_4 selectivity, this material possesses a much smaller $S^0_{\mathrm{mem},H_2S/CH_4}$ value of 2.82. Unlike CO_2, the H_2S molecules experience a stronger dispersive interactions with the triangular pores, and a weak but attractive electrostatic contribution which limits their mobility along the channel. Despite the potential concerns with the hydrolytic stability of this framework, the predictions from these calculations suggest that AEM-COF-2 may be an ideal candidate for bio-gas separations involving dry feed gas and should be considered in the final phase of calculations.

5.2.3 Working conditions

With the 19 COF membranes that exceeded the 2008 upper bound, GCMC and EMD simulations are employed to study equimolar binary mixture separations of CO_2/CH_4 and H_2S/CH_4 at 10 bar and 298 K. In a similar manner to the screening in chapter 4, a general decrease in permeability and increase in selectivity is observed at working conditions relative to calculations at infinite dilution (Figure 5.5). Unfortunately, all 19 COFs fail to exceed the 2008 upper bound at working conditions suggesting inferior performance relative to many top polymer membranes. The values of $P^{mix}_{CH_4}$, $P^{mix}_{CO_2}$ and $P^{mix}_{H_2S}$ range between 106 and 1.54×10^6 Barrer, while the values of $S^{mix}_{\mathrm{mem},CO_2/CH_4}$ and $S^{mix}_{\mathrm{mem},H_2S/CH_4}$ range between 0.89 - 5.81 and 3.03 - 79.6, respectively.

In addition to studying general trends, Figure 5.5 can be adapted to show the specific changes to the permeability and selectivity of each COF; to demonstrate this, a focus on the CO_2/CH_4 Robeson plot is made where each structure is represented by a different colour or shade (Figure 5.6) Through this

assessment, we can highlight structures of interest which show very different behaviours at working conditions than when compared to their calculations at infinite dilution. For example, the CO_2/CH_4 membrane selectivity of AEM-COF-2 which previously was calculated to be 236 under ideal conditions drops considerably to 0.89 under working conditions, switching its selectivity towards CH_4. To understand these differences, MD simulation snapshots from the equimolar mixture simulations are shown in Figure 5.7. The main difference

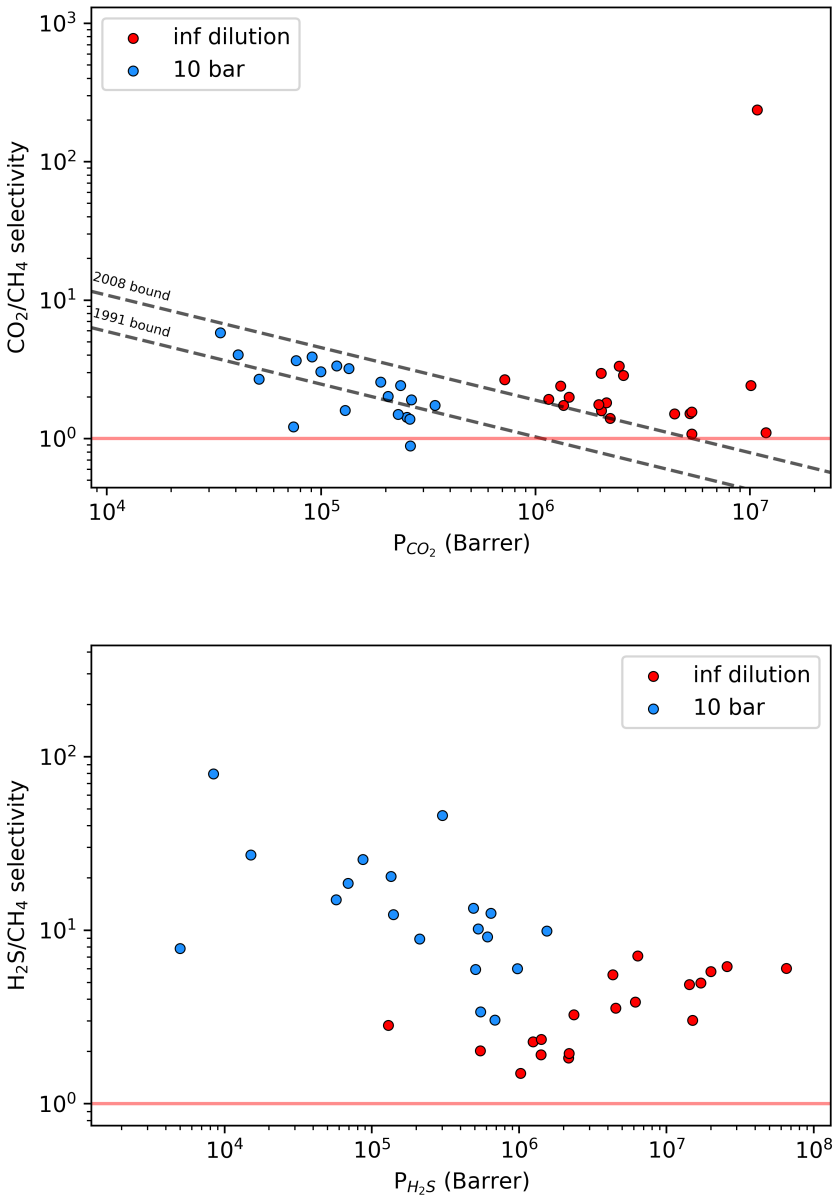


Figure 5.5: *Robeson trade-off plots comparing the CO_2/CH_4 (top) and H_2S/CH_4 (bottom) separation performance of 19 COFs under infinite dilution (blue) and at working conditions of 10 bar and 298 K (red).*

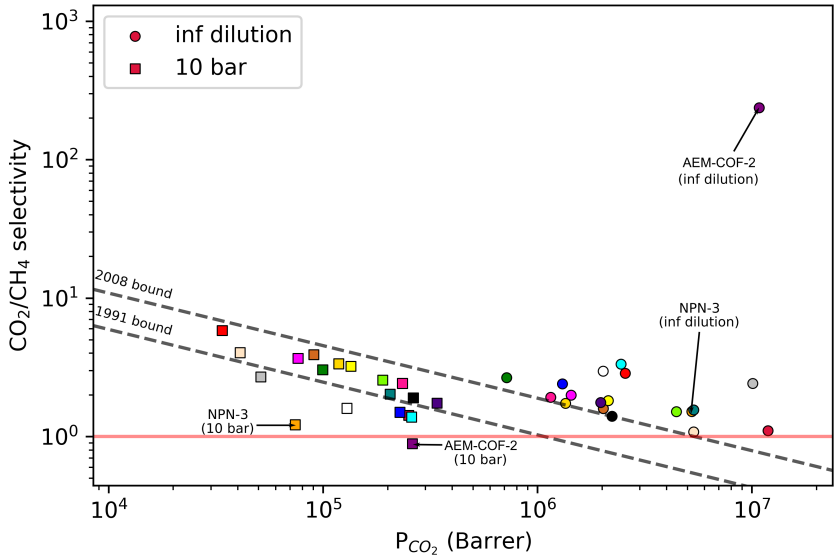


Figure 5.6: *Robeson trade-off plot comparing the CO_2/CH_4 separation performance of 19 COFs under infinite dilution (square symbols) and at working conditions of 10 bar and 298 K (circle symbols; Each COF is represented by a different colour or shade indicating how its separation performance varies between the infinite dilution and working conditions.).*

that can be observed at working conditions is that at $t = 0$, both the small triangular and large hexagonal pores are populated as opposed to just the small triangular pores at infinite dilution. During the simulation, CO_2 molecules diffuse along the pore channels and aggregate near the electro-positive boron atom sites of the B-O boronate ester linkages. As CH_4 interacts weakly with surface and does not have a specific site-preference, it is able to diffuse across the hexagonal pores at a much faster rate, leading to a high $S^{mix}_{diff,CH_4/CO_2}$ value of 1.81. Under working conditions, it can also be seen that the small triangular pores exhibit single file dynamics in which the ordering of the adsorbates is unable to change. In contrast to these behaviours, the adsorbates at infinite dilution favour adsorption into the small triangular pores which greatly favours CO_2 diffusion rates as previously described in this chapter. It can therefore be concluded that while there is a very large $S^0_{\mathrm{diff},CO_2/CH_4}$ value at infinite dilution, this reduces greatly at working conditions, thus reducing the overall $S^0_{\mathrm{mem},CO_2/CH_4}$ value.

Another highlighted structure is NPN-3 which shows a large decrease in

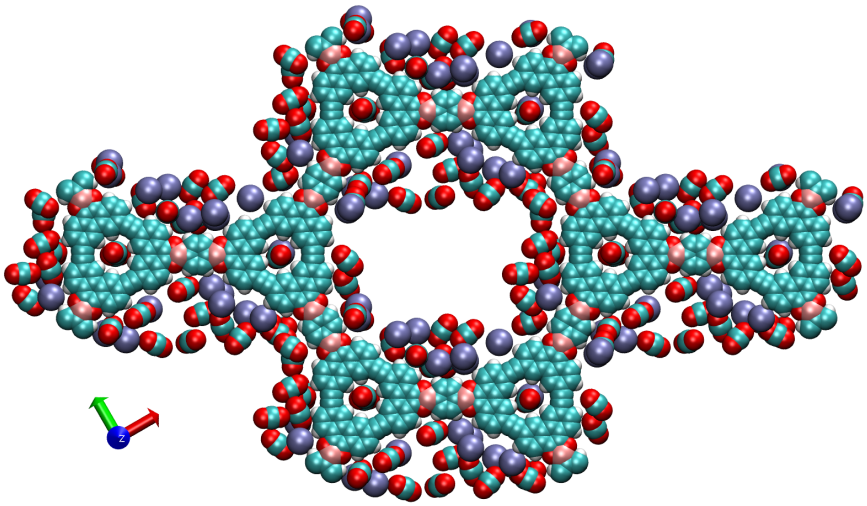


Figure 5.7: *Snapshot from an equimolar CO_2/CH_4 MD simulation in AEM-COF2; Colour scheme: Cyan = C, White = H, Red = Oxygen, Pink = Boron, Purple = CH_4*

P_{CO_2} from 5.25 × 10^6 Barrer at infinite dilution, to 7.43 × 10^4 Barrer at working conditions. To understand these changes, it is important to consider the structural properties of this material; NPN-3 is a 3-D COF with **dia** topology that is formed with a rare trans-azodioxy linkage from the self-addition polymerisation of 1,3,5,7-tetrakis(4-nitrosophenyl)adamantane.[287] It possesses six-fold framework interpenetration leading to greatly reduced PLD and LCD values of 5.44 and 6.14 Å, respectively. Consequently, the high adsorbate loadings at working conditions create densely packed pores that reduce the diffusion rate of both CH_4 and CO_2 from 8.28 × 10^{-5} cm^2/s and 6.03 × 10^{-5} cm^2/s at ideal conditions, to 6.68 × 10^{-5} cm^2/s and 2.05 × 10^{-5} cm^2/s in an equimolar mixture at working conditions (Figure 5.8b, c). Despite a modest increase in the adsorption selectivity from 2.07 to 5.40, the reduction in diffusion rate results in a large drop in permeability, as observed in Figure 5.6.

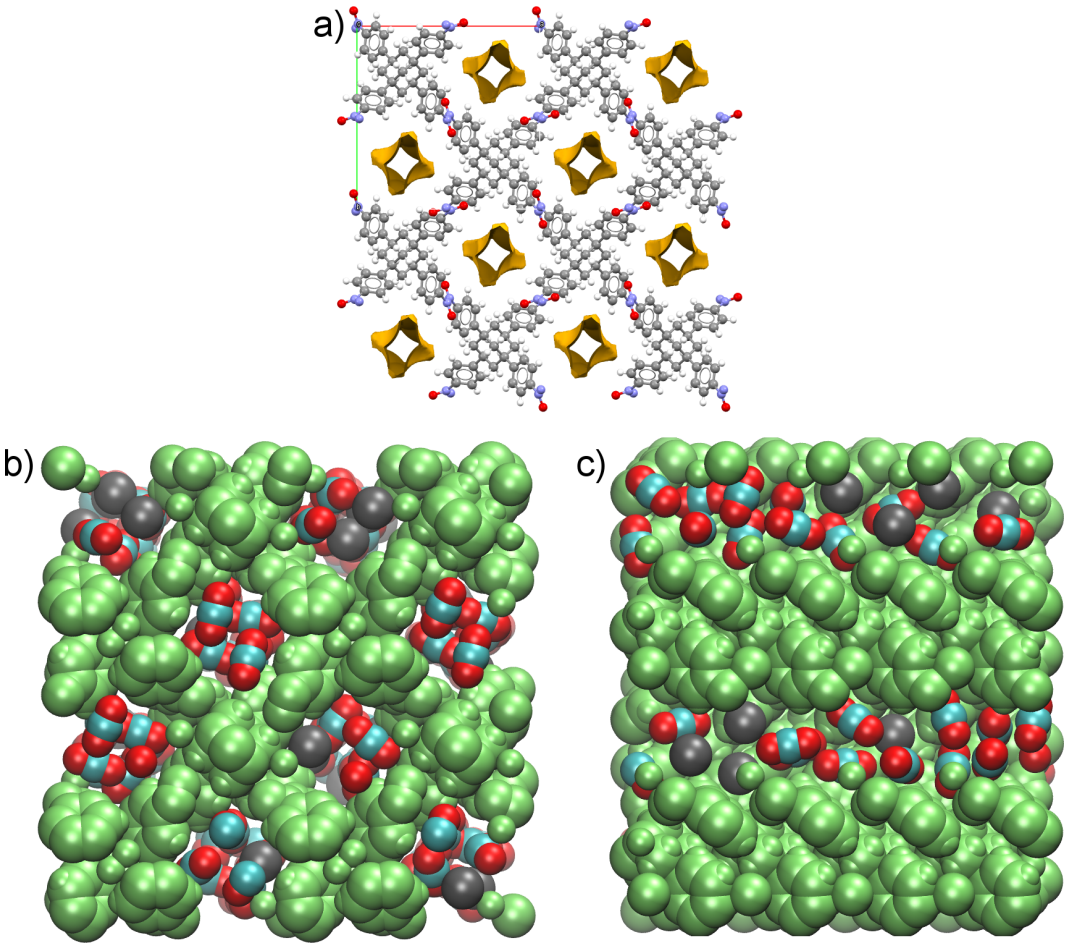


Figure 5.8: *(a) Structure of NPN-3 and its 1-D pore channels (yellow); (b,c) MD simulation snapshots showing the high adsorbate loadings of CO_2 and CH_4 in NPN-3 (framework is highlighted in green in order for a better contrast with the adsorbates); Colour scheme: Green = Framework, Red and Cyan atoms = CO_2, Black = CH_4*

5.2.4 MOF- and COF-based separation performance at working conditions

Before analysing the top COF candidates from this screening, the permeabilities and selectivities of the 19 COFs studied at working conditions are compared with the 34 MOFs from chapter 4 who also were studied under analogous conditions. As seen in Figure 5.9, both classes of materials exhibit a wide range of permeabilities and selectivities, however, the investigated COFs are generally found to possess larger $P^{mix}_{CO_2}$ and $P^{mix}_{H_2S}$ values while the investigated MOFs are generally found to possess larger $S^{mix}_{\mathrm{mem,CO_2/CH_4}}$ and $S^{mix}_{\mathrm{mem,H_2S/CH_4}}$ values. To help understand these trends, a kernel density estimate (KDE) of the LCD, VF and Q_{st} distributions is employed for the sets of MOFs and COFs (Figure

5.10). The 34 MOFs studied in chapter 4 show a relatively sharp and narrow LCD distribution centring around 5Å which indicates that these materials share very similar pore sizes. In contrast, the COF LCD distribution possess several peaks that indicate a diverse set of pore sizes with many appearing between 11 - 32 Å. The large number of structures with pore diameters near the mesoporous boundary also suggests high porosities which is further evidenced by the VF distribution that centres on 0.64. In contrast, the MOF subset

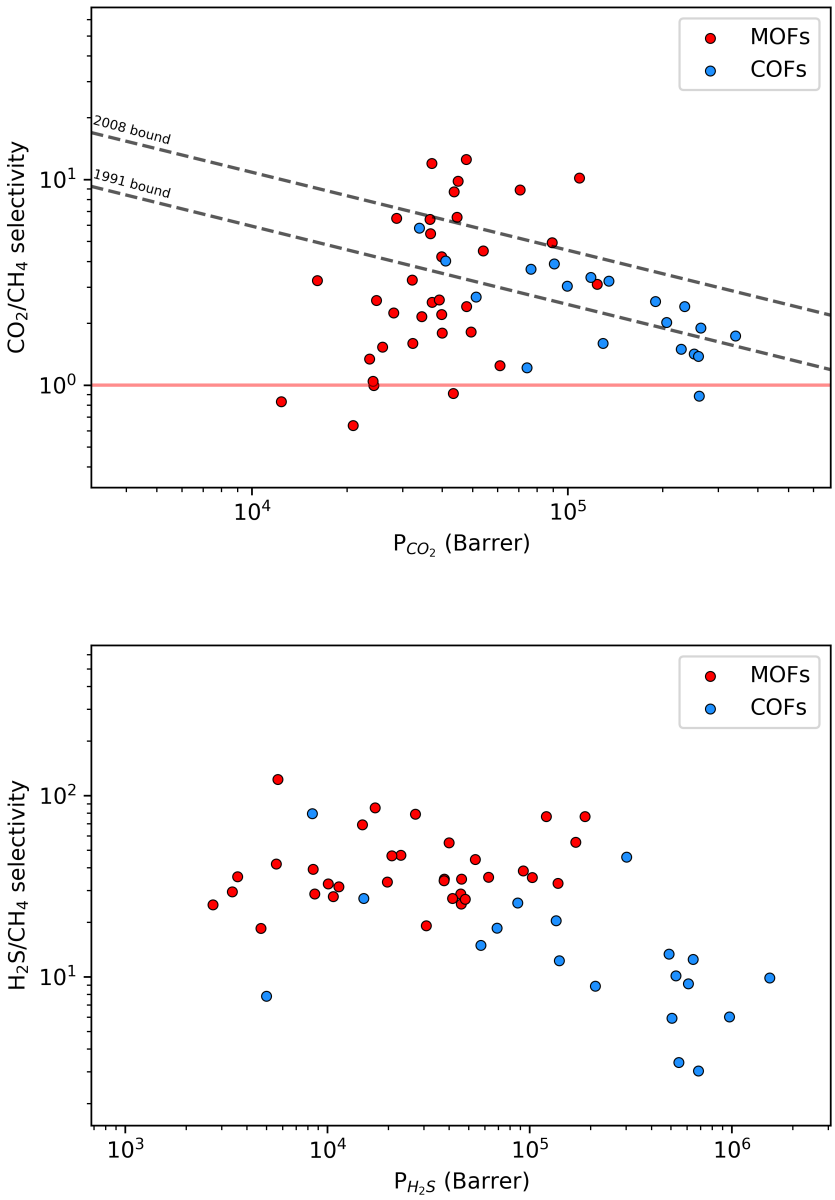


Figure 5.9: *Robeson trade-off plots comparing the CO_2/CH_4 (top) and H_2S/CH_4 (bottom) separation performance of the 34 MOFs (chapter 4) and 19 COFs (this study) that were investigated under working conditions of 10 bar and 298 K (red).*

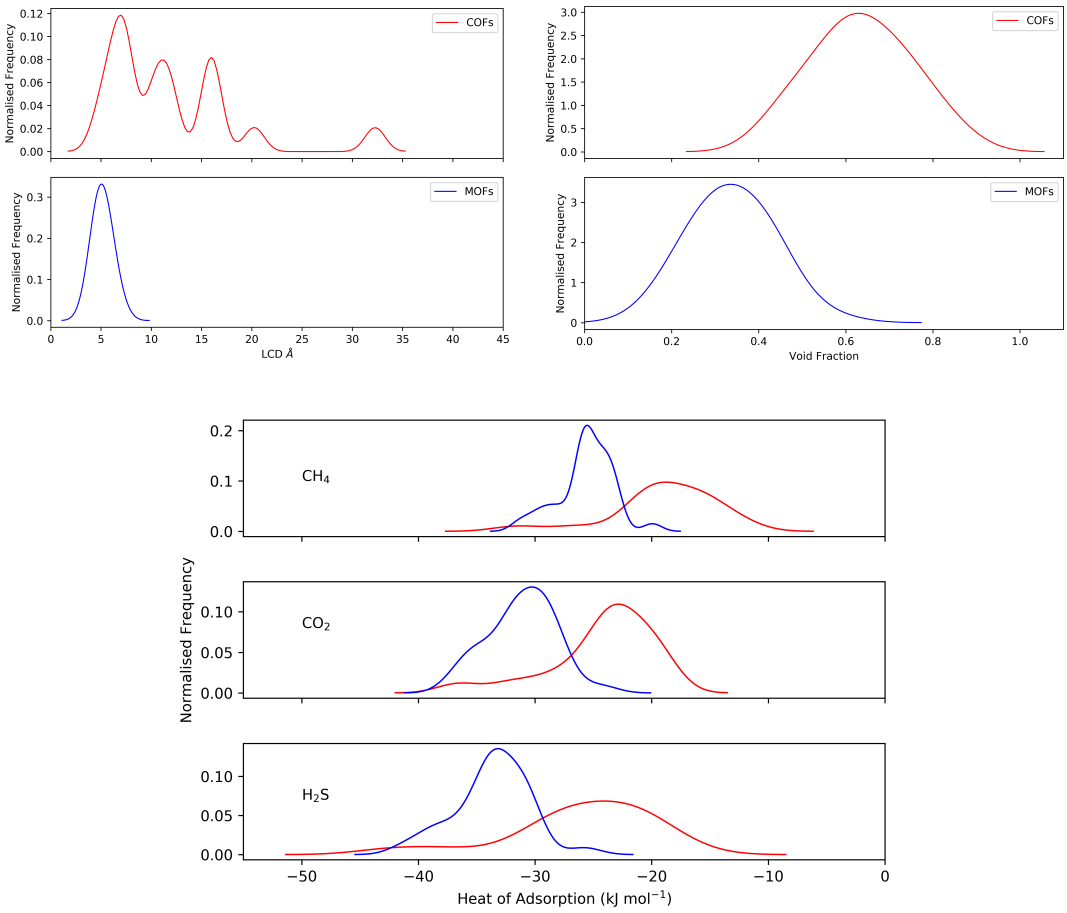


Figure 5.10: *KDEs of the LCD (top left); VF (top right); and Q_{st} distributions (bottom) in the 34 MOFs (blue lines) and 19 COFs (red lines) compared in this study.*

contains large numbers of structures with ultra-micropores ($d \leq 10$ Å) which is accompanied by lower porosities and a VF distribution that centres on 0.34.

So far the LCD and VF distributions suggest that the set of COFs generally possess larger pores with higher VF whereas the set of MOFs tend to possess narrow pores with lower VF. From these conclusions, it is expected that the confined pore space of the MOFs will be accompanied by strong host-guest interactions and a Q_{st} distribution which is shifted towards more negative values. Similarly a reverse argument may be made for the COFs in which the sparser pore space leads to weaker host-guest interactions. These hypotheses are both confirmed in the final distribution in Figure 5.10. In summary, the higher permeabilities observed for the COF set can be explained through

the large number of materials with weak host-guest interactions as a result of their large pore sizes. While this allows each adsorbate to diffuse more freely, these pores are generally less selective towards contaminant molecules. In contrast the narrow pore sizes exhibited by the set of MOFs typically possess stronger host-guest interactions which coupled with higher adsorbate densities per unit volume leads to lower diffusion rates and hence, lower permeabilities. It should be noted that there are some obvious exceptions to these general trends displayed in Figure 5.9. In particular, the previously described NPN-3 COF possesses a small PLD and LCD of 5.44 and 6.14 Å which contributes to its low gas permeabilities and also its exceptional $S^{mix}_{\mathrm{mem,H_2S/CH_4}}$ value of 78.0.

5.2.5 Top COF candidates

Despite being unable to exceed the 2008 upper bound, many COFs lay very close to the boundary. Therefore, the top COF candidates identified by this high-throughput screening are those between the 1991 and 2008 Robeson limits for CO_2/CH_4 separations. These correspond to the yellow points highlighted in Figure 5.11 and the identity of each COF can be found using the numbering scheme within the Figure. Furthermore, a summary of their geometric and physical properties may be found in Table 5.1. Due to their low densities, many of these materials are able to store larger gravimetric quantities of biogas contaminants than the top MOFs identified in chapter 4.

Diffusion coefficients $D^{mix}_{\mathrm{CO_2}}$, $D^{mix}_{\mathrm{CH_4}}$ and $D^{mix}_{\mathrm{H_2S}}$ of the top candidates range from 2.97×10^{-4} cm^2/s to 1.59×10^{-6} cm^2/s - many of the larger values arise as a consequence of the distribution of large pore diameters exhibited by these materials. For the CO_2/CH_4 mixture, a total of 10 structures possess $\mathrm{S}^{mix}_{\mathrm{diff}} \leq 1$ indicating that CH_4 molecules diffuse faster than CO_2 molecules; in the remaining 2 structures, $\mathrm{S}^{mix}_{\mathrm{diff}}$ is near to unity. For the H_2S/CH_4 mixtures, both $D^{mix}_{\mathrm{CH_4}}$ and $D^{mix}_{\mathrm{H_2S}}$ are generally observed to be smaller than $D^{mix}_{\mathrm{CH_4}}$ and $D^{mix}_{\mathrm{CO_2}}$ in the CO_2/CH_4 mixtures. As H_2S molecules generally interact more strongly

Table 5.1: Properties of the top 12 COFs from GCMC and EMD simulations carried out at 10 bar and 298K

							—— $\times 10^{-6}$ (cm^2/s) ——							
Name	PLD (Å)	LCD (Å)	ASA (m^2/g)	VF	n_{CO_2} (mol/kg)	n_{H_2S} (mol/kg)	$D^{mix}_{CO_2}$	$D^{mix}_{CH_4}$I	$D^{mix}_{H_2S}$	$D^{mix}_{CH_4}$II	$P^{mix}_{CO_2}$ (Barrer)	$S^{mix}_{CO_2/CH_4}$	$P^{mix}_{H_2S}$ (Barrer)	$S^{mix}_{H_2S/CH_4}$
DMTA-TPB4	4.92	5.57	605	0.47	3.44	4.78	14.9	13.4	4.67	6.77	33921	5.81	15095	27.0
CTF-FUM	6.02	6.74	1038	0.52	3.52	4.72	17.9	15.4	1.59	4.19	41057	4.01	4991	7.83
SIOC-COF-5	6.64	7.16	1562	0.61	6.03	9.50	26.4	28.4	12.3	22.7	76520	3.67	57449	15.0
TPE-COF-I	7.17	7.82	1795	0.60	8.77	12.3	21.5	27.2	11.4	22.8	90680	3.89	69021	18.6
HPB-COF	5.77	7.57	2384	0.65	5.49	9.16	42.6	47.1	35.1	39.6	99726	3.03	140276	12.3
3D-OH-COF	6.35	7.06	1939	0.60	5.98	10.7	41.0	45.2	16.5	18.9	118420	3.35	87227	25.6
MPCOF	9.78	10.3	1374	0.61	7.33	12.6	31.9	36.8	40.7	36.5	134939	3.20	302430	45.9
TPE-COF-II	10.9	11.7	2155	0.66	7.69	14.3	60.2	97.7	35.2	88.8	189822	2.55	210681	8.89
TPE-COF-III	15.9	16.3	2164	0.68	7.56	15.4	73.3	133	90.1	156	205693	2.03	528064	10.2
COF-DL229-6	9.67	10.2	3521	0.75	9.87	19.2	80.8	162	87.6	208	234798	2.41	506374	5.93
TPE-COF-IV	15.5	15.9	2695	0.73	8.31	16.5	99.0	179	112	170	263998	1.90	609827	9.15
COF-DL229-5	11.2	11.3	6638	0.80	10.6	29.8	136	234	214	297	340192	1.74	1540491	9.88

PLD = pore-limiting diameter; LCD = largest cavity diameter; ASA = accessible surface area; VF = void fraction; n_i = loading of adsorbate i obtained from 50:50 binary mixture GCMC; D^{mix}_i = diffusion coefficient of adsorbate i; $D^{mix}_{CH_4}$I is derived from CO_2/CH_4 simulations, and $D^{mix}_{CH_4}$II is derived from H_2S/CH_4 simulations; P^{mix}_i = permeability of adsorbate i; $S^{mix}_{i/j}$ = membrane selectivity for adsorbates i and j in the binary mixture.

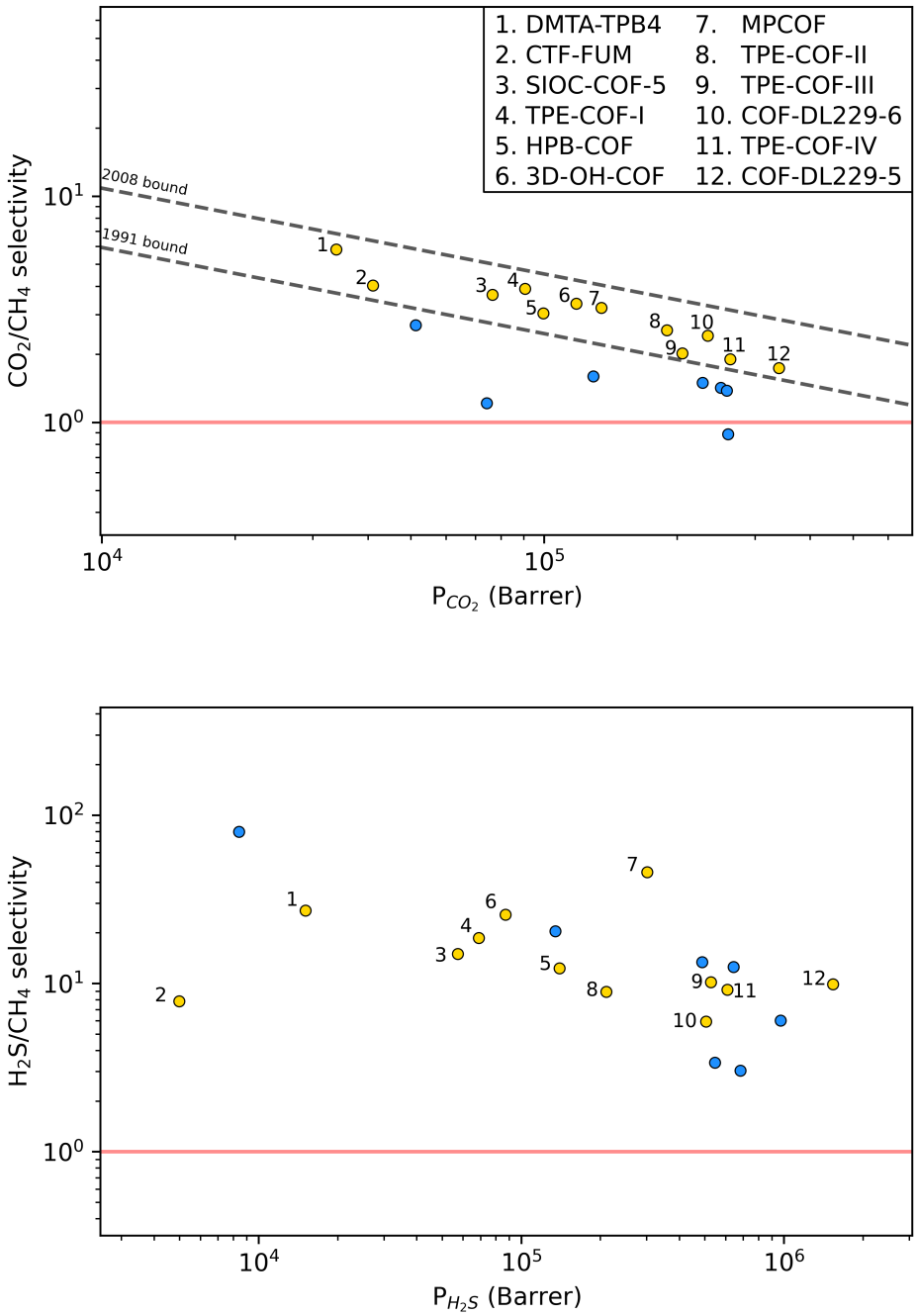


Figure 5.11: *Robeson trade-off plots at 298 K comparing the CO_2/CH_4 separation performance of 19 COFs. The top 12 candidates identified in the proposed screening are highlighted as yellow stars.*

with the framework than CO_2 molecules, their diffusion rate is expected to be smaller. Furthermore, these strong host-guest interactions lead to larger S_{ads} values which in turn, generates a higher adsorbate density within the pores, resulting in more frequent collisions and less available space for each molecule to diffuse into. Due to the larger S_{ads} values in the H_2S/CH_4 mixtures, the H_2S

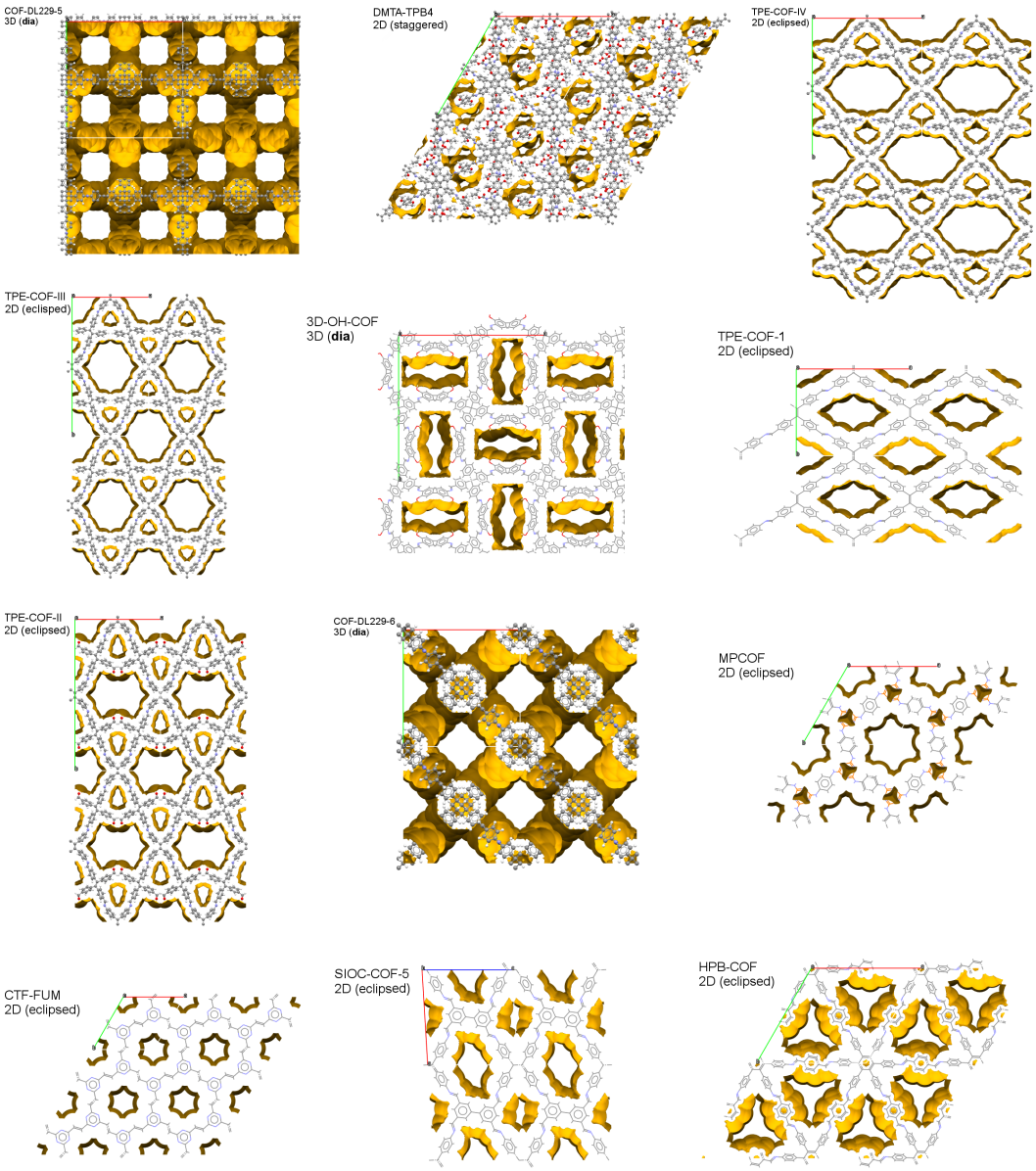


Figure 5.12: *Snapshots of the void space in the top structures determined from the contact surfaces of a 1.2Å probe*

molecules also have a greater impact in slowing down the faster CH_4 molecules which explains their overall slower diffusion rate in the H_2S/CH_4 mixtures.

The $S^{mix}_{\mathrm{mem},CO_2/CH_4}$ and $S^{mix}_{\mathrm{mem},H_2S/CH_4}$ values of the top candidates range between 1.74 - 5.81 and 5.93 - 45.9, respectively. In comparison with the top MOFs in chapter 4, these selectivities are generally lower which can be attributed to the MOFs narrower pore sizes and stronger interactions with metallic nodes leading to higher S^{mix}_{ads} values. The highest $S^{mix}_{\mathrm{mem},CO_2/CH_4}$ belongs to DMTA-TPB4; a 2-D imine-linked COF synthesised from the co-condensation

of a 1,3,5-tris(4-aminophenyl) benzene derivative and 2,5-dimethoxyterephthalaldehyde. The framework possesses a staggered 'ABC' stacking pattern, which greatly reduces the VF and provides strong adsorption sites for CO_2 molecules to interact with. Furthermore, this stacking pattern affords a set of narrow pores with PLD and LCD values of 4.92 and 5.57Å - the smallest values across the top candidates. The structure of DMTA-TPB4 and the remaining top materials are displayed in Figure 5.12. In total, 9 out of 12 materials are classified as 2-D structures with 8 displaying eclipsed stacking patterns and a diverse range of pore shapes. DMTA-TPB4 is the only 2-D COF in the top candidates to possess a staggered stacking arrangement which creates highly confined pores with some of the lowest PLD, LCD, ASA and VF values among the top COFs. However, the confined nature of these pores leads to the highest reported $S^{mix}_{\mathrm{mem,CO_2/CH_4}}$ and 2nd highest $S^{mix}_{\mathrm{mem,H_2S/CH_4}}$ values across the top COFs. The remaining 3 membranes are 3-D COF structures which as previously mentioned, are much rarer in the literature and CoRE-COF database than 2-D structures. It is noted that there are 19 3-D COF structures which make up 13% of the hydrophobic membranes investigated in this study. Therefore, it is believed that the representation of 3-D membranes in the top structures is rather similar to this, given the small subset of materials that lie above the upper bound.

Further inspection of each structure indicates that 10 out of 12 possess imine-based linkages. This is highly encouraging as imine-based COFs show exceptional stability across a wide range of organic solvents and are often insensitive to water, acidic and basic conditions.[288] As such, these are desirable properties for the development of robust membranes that can withstand a range of chemical environments, including the non-negligible H_2O content that is often present in bio-gas mixtures.

5.3 Investigating the impact of feed pressure

Throughout this thesis, high-throughput analysis has identified a number of MOF- and COF-based membranes that show promise for the application of biogas upgrading. These are based on a number of assumptions that simplify the separation process and also improve the computational efficiency of the screening. For example, the separation performance of each material is evaluated from equimolar binary mixtures of CO_2/CH_4 and H_2/CH_4. While the ability to separate both CO_2 and H_2S is essential, real biogas mixtures may contain numerous additional components with varying concentrations that may impact the gas permeability and selectivity of a membrane. Another example is that working conditions are often defined using a feed pressure and temperature of 10 bar and 298 K, respectively. However, studies on various polymer, inorganic and mixed-matrix membranes often report the separation performance of CO_2/CH_4 mixtures across a wide range of conditions, and usually indicate that small changes to the feed pressure, trans-membrane pressure drop or temperature can alter the transport properties of a membrane.[203] Therefore, it may be possible for membranes that have been previously overlooked to show improvement through optimisation of their working conditions. To explore this idea, the equimolar CO_2/CH_4 separation performance of 8 membranes is evaluated across numerous pressures intervals between 0.1 and 10 bar. The structures of each membrane employed in this study are shown in Figure 5.13 and consist of 4 MOFs and 4 COFs. Instead of focussing solely on top performing candidates, many of these structures are identified with average separation performance that may benefit from a change in working conditions. The COF set of membranes contains two previously met structures (AEM-COF-2 and DMTA-TPB4)[286,289] and two new structures (TpMA and TEMP-COF). TpMA is an imine-linked COF synthesised from the co-condensation of 1,3,5-triformylphloroglucinol (TFPG) and melamine building blocks.[290]. Each pore has three -OH moieties from each TFPG sub-units that

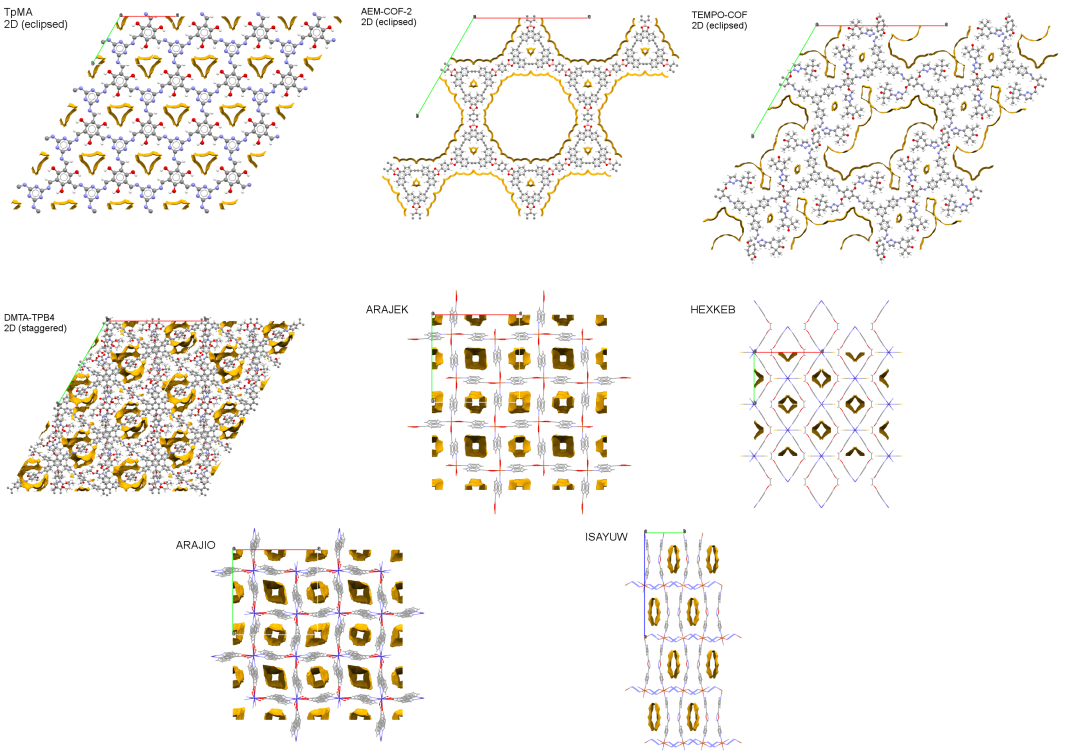


Figure 5.13: *The 8 structures employed to investigate how changes in feed pressure affect separation performance*

provide strong adsorption sites for CO_2 molecules to interact with. TEMPO-COF is another 2-D imine-linked COF that has recently been synthesised and exfoliated into redox-active COF nanosheets for lithium-ion battery technology.[291] Its framework is functionalised with large tetramethylpiperidine-1-oxyl (TEMPO) radicals that occupy a series of large 1-D hexagonal pore channels.

The MOF set of membranes consists of two Cu(II)- and two Co(II)-based frameworks with small pore channels that range between 4 - 6Å in diameter. ARAJEK and ARAJIO belong to the same family of MOFs and contain quinoline-5-carboxylate ligands which coordinate to Cu(II) and Co(II) ions respectively, affording a set of 1-D square channels with **sql** topology.[292] HEXKEB is an example of a Co(II) coordination compound containing flexible ethanediyl pyridinecarboxylates and thiocyanate ligands that exhibits a 1-D metallacyclic chain architecture.[293] The final structure (ISAYUW) is one of the oldest materials in this study and demonstrates the best separation performance of all 8 membranes at 10 bar and 298 K. ISAYUW contains chains of Cu(II) ions linked together through μ2-azido groups and an angular dipyridyl

bridging ligand (2,5-bis(4-pyridyl)-1,3,4-oxadiazole).[294] Using the results from both GCMC and MD simulations, the impact of feed pressure on the gas adsorption, diffusion and permeability properties, and its relationship with the structural properties of each membrane is assessed. The computational details for these simulations remains identical to those carried out at 10 bar in chapters 4.2 and 5.2.

5.3.1 Impact on adsorption behaviour

The multi-component adsorption isotherms for each investigated MOF and COF are shown in the top and bottom of Figure 5.14, respectively. These plots indicate the gravimetric gas uptake of each membrane which is a measure of the amount of gas adsorbed per kg of membrane. While it is true that COF membranes are typically lighter than most MOFs due to the lack of heavy transition metals, the gas uptake below 1 bar is generally larger in most MOF membranes due to their enhanced host-guest interaction strengths that arise from the more confined nature of their pores. Of the MOF membranes, ARAJEK and ARAJIO possess the highest CO_2 uptakes despite their unit cell masses being approximately 10-15% heavier than ISAYUW or HEXKEB. This is because their gas uptake per unit cell at 0.1 bar are higher than the gas uptake in ISAYUW or HEXKEB at 10 bar, increasing further at higher pressures and thus leading to the observed trends in Figure 5.14. Among the adsorption isotherms of the COF membranes are a number of interesting features that can be related to the physical properties of each material. The CO_2 isotherm for TpMa possesses one of the largest gradients between 0.1 and 1.0 bar due to the balance between: (1) Its enhanced host-guest interactions that result from its small pore diameters (PLD = 4.48Å; LCD = 4.73Å) and specific pore volume (0.35 cm^3/g); (2) Its low framework mass due to the small size of its melamine and TFPG building blocks. A similar argument can also explain the uptake in DMTA-TPB4, which exhibits an even sharper

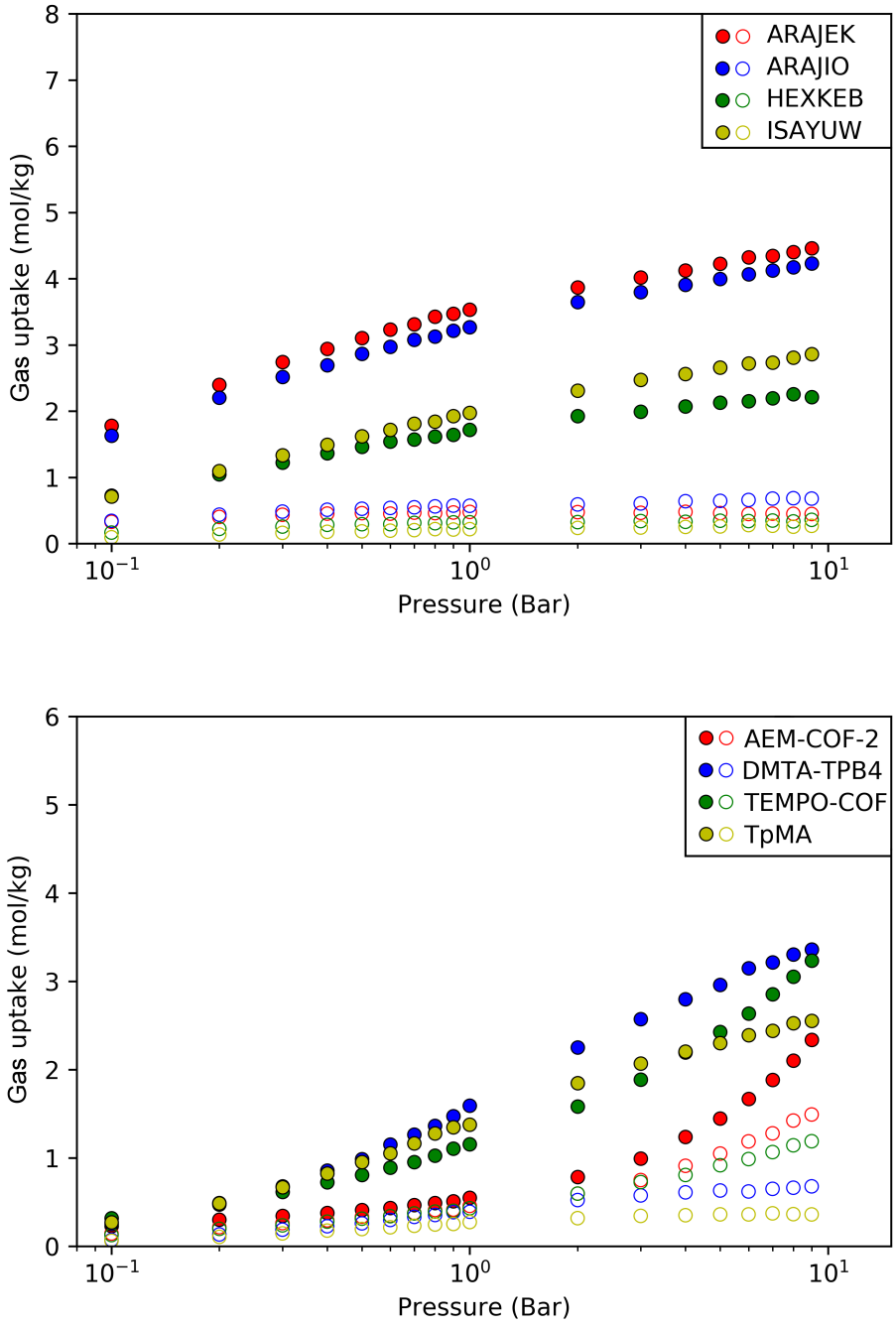


Figure 5.14: *Binary mixture adsorption isotherms from equimolar CO_2/CH_4 GCMC simulations on selected MOF (top) and COF(bottom) materials at 298 K; CH_4 - open symbols, CO_2 - closed symbols*

increase in CO_2 as a result of its 2-D staggered packing arrangement that strongly increases the host-guest interaction strength at the expense of its pore volume. In contrast, AEM-COF-2 exhibits low gas uptake between 0.1 and 1 bar but a sharp increase between 1 and 10 bar. This COF possesses the largest pore diameter (PLD and LCD = 32Å) and specific pore volume (1.22

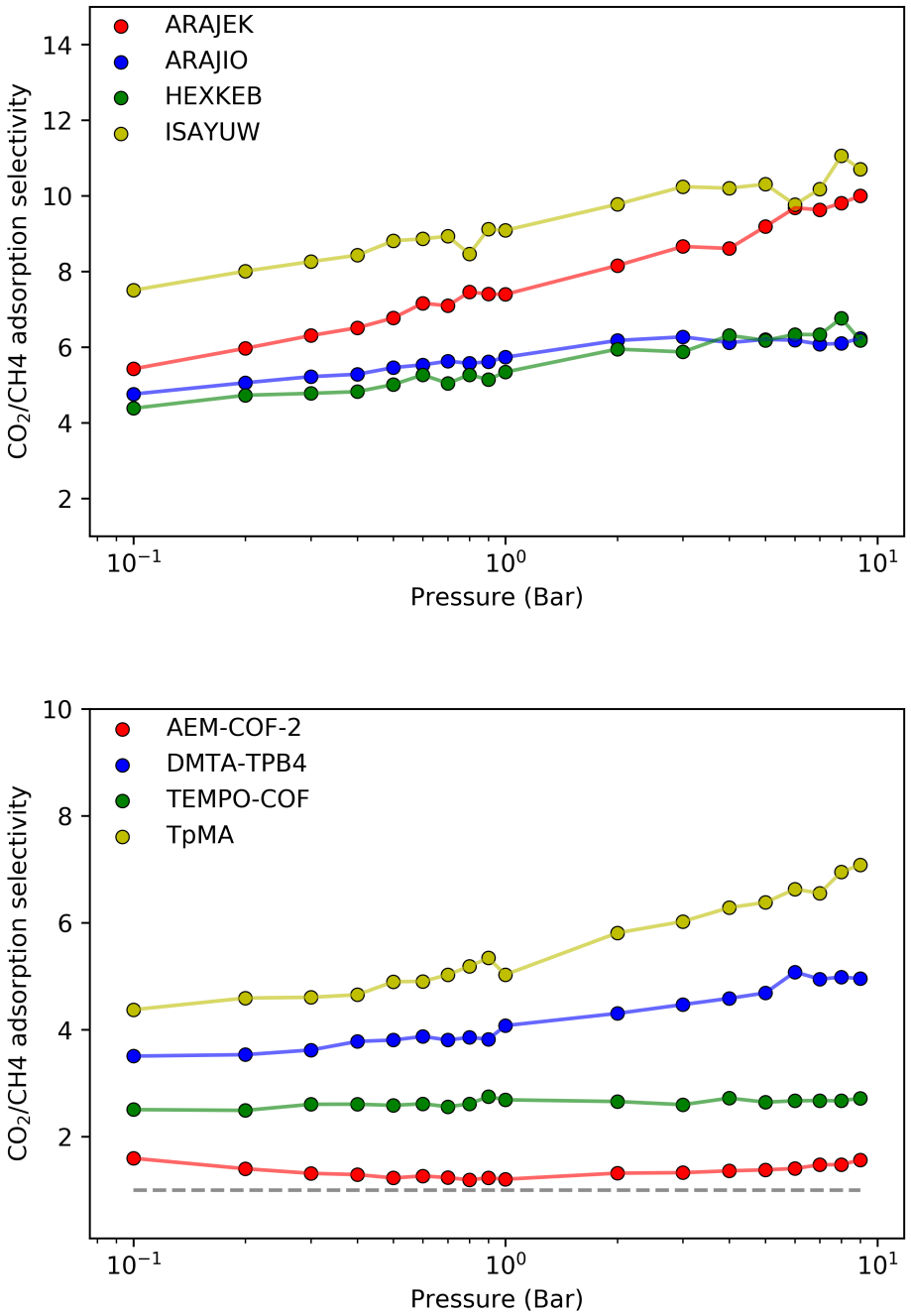


Figure 5.15: *Adsorption selectivity from equimolar CO_2/CH_4 GCMC simulations on selected MOF (top) and COF(bottom) materials at 298 K; Blacked dashed lines represents unity.*

cm^3/g) which gives it a higher storage capacity than any other investigated COF, but suffers from a relatively high unit cell mass due to the extended nature of the frameworks backbone.

In addition to adsorption isotherms, the corresponding S_{ads}^{mix} values from the equimolar GCMC simulations are plotted in Figure 5.15. All MOF mem-

branes show a general increase in S_{ads}^{mix} with pressure - ISAYUW exhibits the highest selectivity range from 7.5 to 11.0, while ARAJEK shows the largest gradient across the investigated pressure range. As for the COF membranes, TpMA and DMTA-TPB4 both show a general increase in S_{ads}^{mix} with increasing pressure as seen by the MOF membranes. In contrast, TEMPO-COF shows little change in S_{ads}^{mix} with values ranging between 2.5 - 2.7, and AEM-COF-2 exhibits a near-convex change in S_{ads}^{mix} approaching near unity. Overall, it appears that the adsorption selectivity does not drastically change with pressure but is an important consideration in materials with relatively small pores, such as those identified in this thesis. While separations performed at lower pressures may lead to slightly lower S_{ads}^{mix} values, the amount of adsorbed gas within the pores is expected to change their transport properties which will inherently effect the S_{mem}^{mix} and P^{mix}.

5.3.2 Impact on transport behaviour and membrane performance

To reduce the statistical error in the D_{self}^{mix} value, membranes with moderate S_{ads}^{mix} values often require large supercells that quickly increases the computational cost of each MD simulation. In order to reduce this cost, calculations of D_{self}^{mix} were only determined in each membrane at 0.1, 0.5, 1.0, 5.0 and 10.0 bar. These values were then fitted using a power law expression to determine the remaining D_{self}^{mix} values at regular intervals between 0.1 and 10 bar - An example of this fitting procedure is shown in Figure 5.16 for ARAJIO. The power law regression analysis provided excellent r^2 values across most membranes with values ranging between 0.94 - 0.99 for CO_2 and 0.94 - 0.99 for CH_4.

The predicted values of D_{self}^{mix} for each MOF and COF membrane are shown in the top and bottom images of Figure 5.17, respectively. In all structures, CO_2 interacts more strongly with the framework such that $D_{CO_2}^{mix} < D_{CH_4}^{mix}$ and

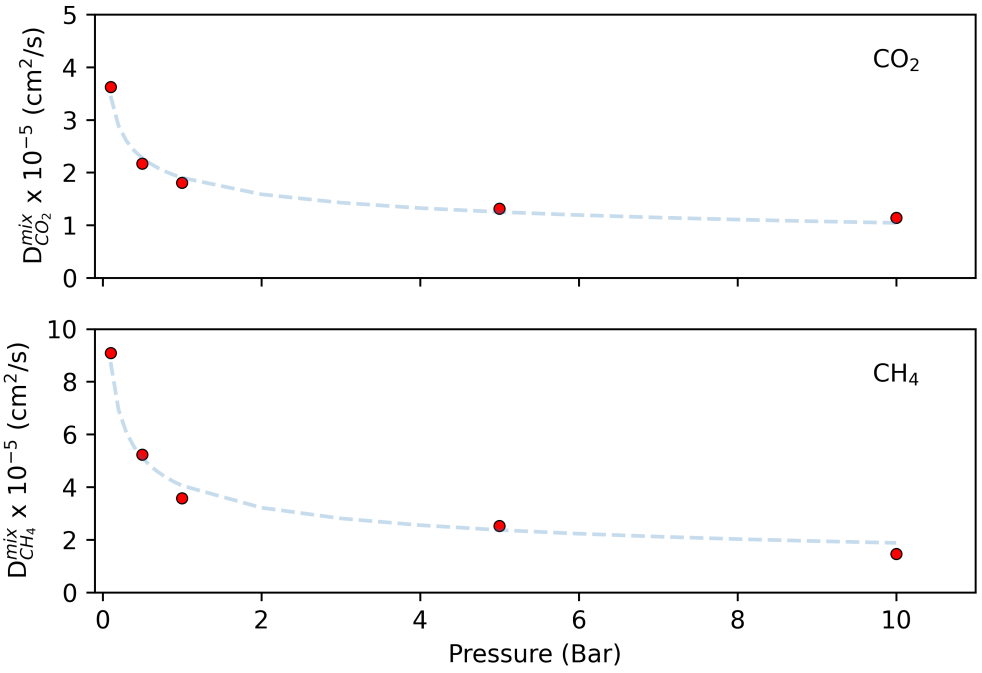


Figure 5.16: *Comparison of the self-diffusion coefficients of CO_2 and CH_4 in ARAJIO calculated directly from simulations (red points) and those estimated from regression analysis fitting (blue dashed lines).*

$S^{mix}_{diff,CO_2/CH_4}$ is ≤ 1. In all MOF membranes, a decrease in both $D^{mix}_{CO_2}$ and $D^{mix}_{CH_4}$ is observed with increasing feed pressure. However, plots of $S^{mix}_{diff,CO_2/CH_4}$ in Figure 5.18 indicate that $D^{mix}_{CO_2}$ and $D^{mix}_{CH_4}$ can decay at very different rates depending on the MOF membrane. For example, ISAYUW displays a steady increase in S^{mix}_{diff} from 0.64 to 0.96 over the investigated pressure range due to the faster decrease in $D^{mix}_{CH_4}$ over $D^{mix}_{CO_2}$. Although ARAJIO and ARAJEK are from the same family of MOFs, they exhibit different transport properties for equimolar CO_2/CH_4 mixtures. While both structures show $D^{mix}_{CH_4}$ and $D^{mix}_{CO_2}$ decreasing with increasing feed pressure, ARAJIO exhibits an increase in $S^{mix}_{diff,CO_2/CH_4}$ while ARAJEK exhibits a decrease in $S^{mix}_{diff,CO_2/CH_4}$ over the investigated pressure range. To rationalise these differences, we can refer back to the multi-component adsorption isotherms and $S^{mix}_{ads,CO_2/CH_4}$ plots in Figures 5.14 and 5.15. Firstly, ARAJIO has a lower $S^{mix}_{ads,CO_2/CH_4}$ across all investigated pressures resulting in a higher concentration of adsorbed CH_4 per unit cell than ARAJEK. These molecules possess weaker host-guest interactions and are lighter than CO_2 molecules, thus allowing them to diffuse at a faster

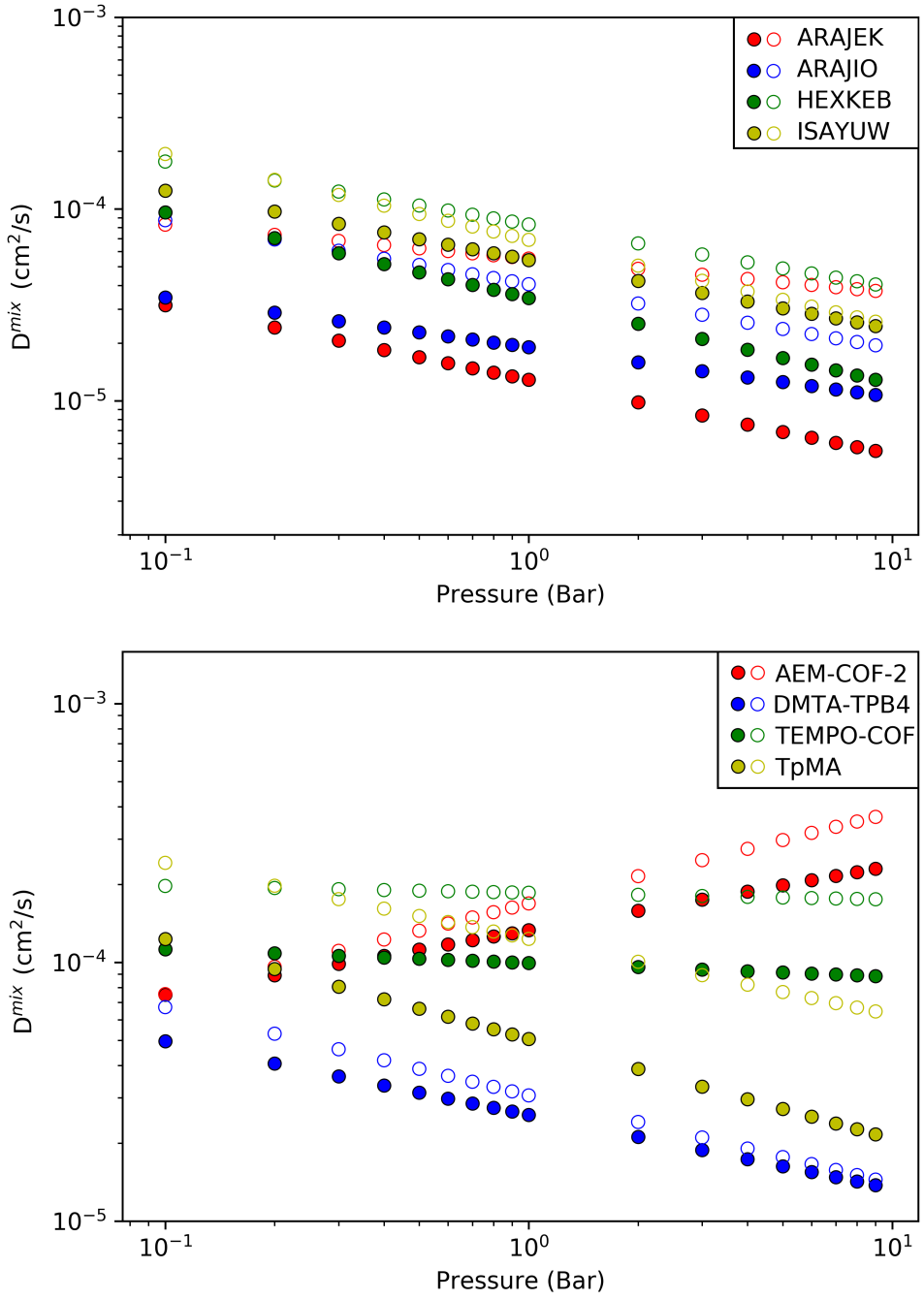


Figure 5.17: *Binary mixture self-diffusion coefficients of selected MOF (top) and COF(bottom) materials at 298 K as predicted from regression analysis models; CH_4 - open symbols, CO_2 - closed symbols*

rate. Within the mixture, the faster diffusing CH_4 molecules are able to speed up slow diffusing CO_2 molecules leading to a small decrease in $D^{mix}_{CH_4}$ and thus a small increase in $S^{mix}_{diff,CO_2/CH_4}$ from 0.40 to 0.56. In contrast, ARAJEK possesses a larger $S^{mix}_{ads,CO_2/CH_4}$ value across all investigated pressures resulting in a much lower concentration of adsorbed CH_4. As a result, CH_4 molecules have

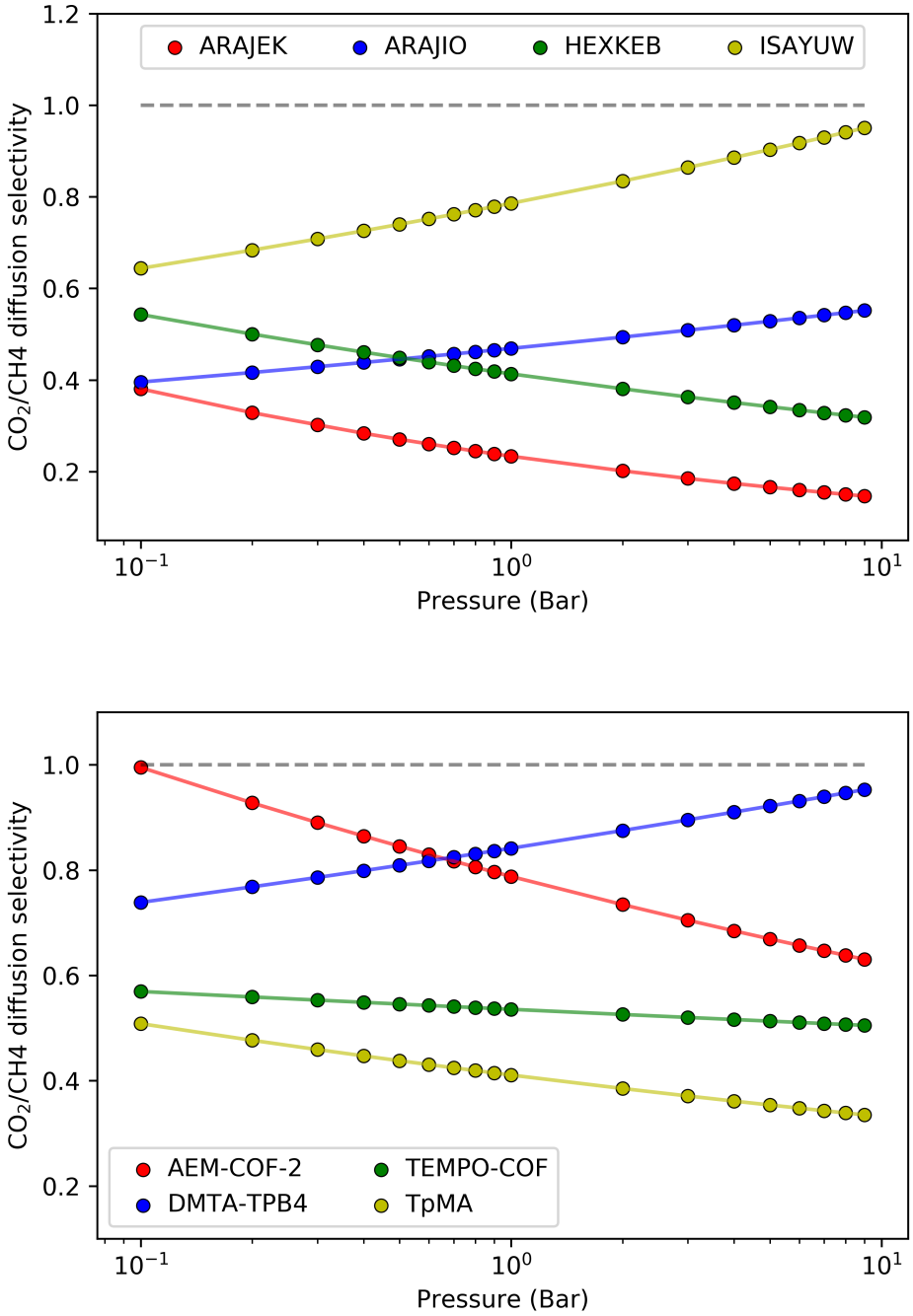


Figure 5.18: *Diffusion selectivity of selected MOF (top) and COF(bottom) materials at 298 K; Blacked dashed lines represents unity.*

less impact in speeding up the slow diffusing CO_2 molecules leading to the small decrease in $S^{mix}_{diff,CO_2/CH_4}$ from 0.38 to 0.14. The COF membranes in this study show some interesting variations of D^{mix}_{self} and S^{mix}_{diff} over the investigated pressure range. Like the 4 MOF membranes, TpMA, DMTA-TPB4 and TEMP-COF show decreases in $D^{mix}_{CO_2}$ and $D^{mix}_{CH_4}$ with increasing feed pressure.

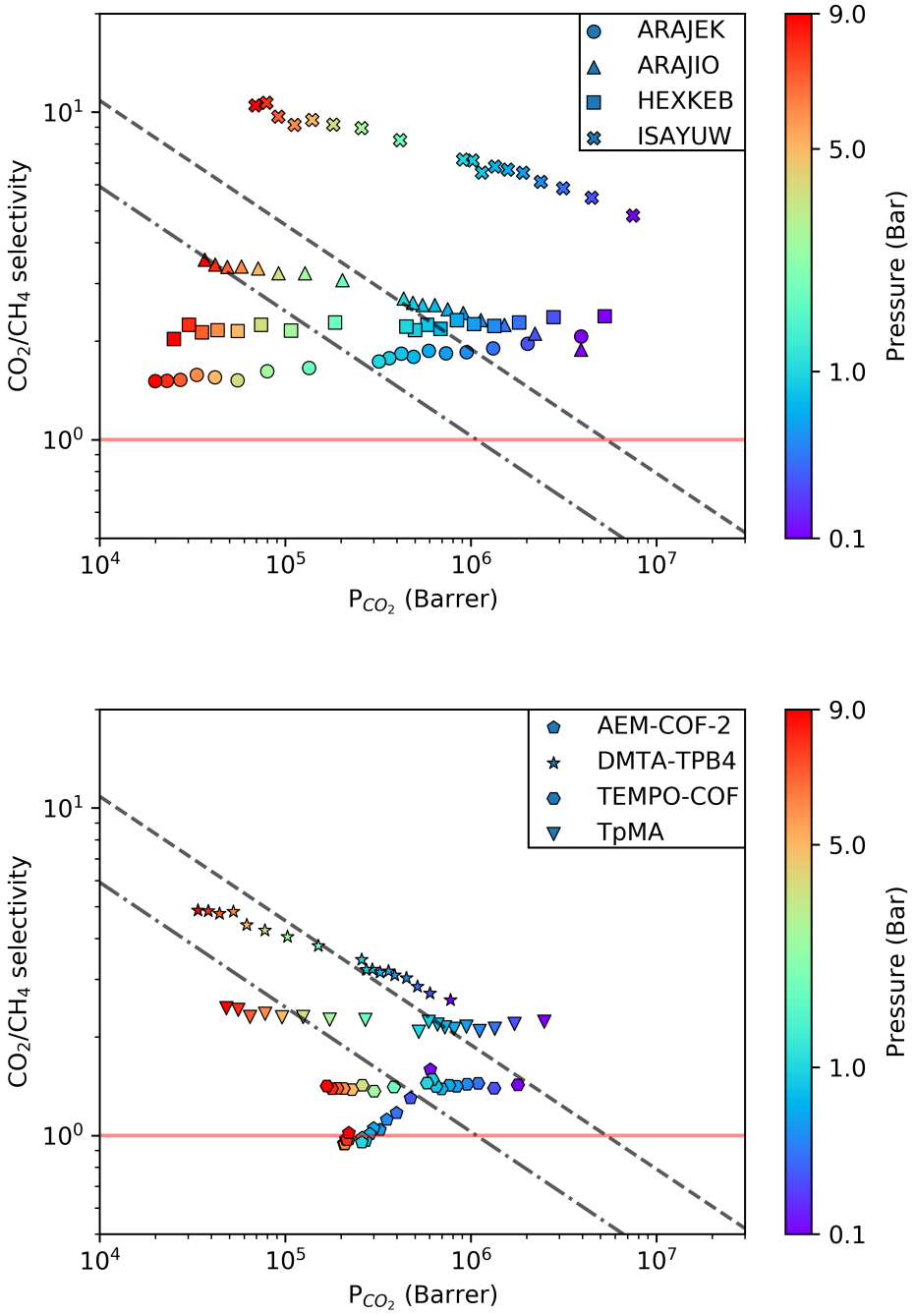


Figure 5.19: *Robeson trade-off plots at 298 K for CO_2/CH_4 mixtures in selected MOF (top) and COF(bottom) materials between 0.1 and 10 bar. The 1991 (dotted-dashed line) and 2008 (dashed line) upper bounds are included for comparison to top-performing polymer membranes.*

Due to its large pore concentration of CH_4 which can speed up slow diffusing CO_2, DMTA-TPB4 exhibits a small increase in $S^{mix}_{diff,CO_2/CH_4}$ from 0.74 to 0.96. While, TpMA exhibits a small increase in $S^{mix}_{diff,CO_2/CH_4}$ from 0.74 to 0.96 due to its large $S^{mix}_{ads,CO_2/CH_4}$ which results in a lower pore concentration of CH_4

that have less impact on speeding up nearby CO_2 molecules. In contrast to the other 7 membranes, AEM-COF-2 shows an increase in both $D^{mix}_{CH_4}$ and $D^{mix}_{CO_2}$ with increasing feed pressure. This is a consequence of its large hexagonal pores that show low selectivity for CO_2 ($S^{mix}_{ads,CO_2/CH_4}$ between 1.2 and 1.6). This results in a relatively high loading of fast diffusing CH_4 molecules that can collide with adsorbed CO_2 and release them into the large hexagonal channels.

The calculated gas uptakes and D^{mix}_{self} values are further used to predict the changes in S^{mix}_{mem} and P^{mix} as a function of feed pressure. These changes are plotted onto Robeson plots in Figure 5.19 and immediately showcase that the use of lower feed pressures can push many membranes above the 2008 Robeson limit. For example, all three MOF membranes that fall below the 1991 upper bound at 9 bar are able to cross the 2008 upper bound at lower working pressures - ARAJEK at ≈0.4 bar, HEXKEB at ≈0.7 bar and ARAJIO at ≈1.0 bar. By decreasing the pressure from 9 bar to 0.1 bar, P^{mix} is increased by large factors of 106, 108, 197 and 209 in MOF membranes ARAJIO, ISAYUW, ARAJEK and HEXKEB, respectively. Furthermore, ISAYUW and ARAJIO increase S^{mix}_{mem} by factors of 2.2 and 1.9, while ARAJEK and HEXKEB slightly decrease S^{mix}_{mem} by factors 0.73 and 0.85. Similar behaviours are also observed for the COF membranes with DMTA-TPB4 and TpMA crossing the 2008 upper bounds at ≈2 and 0.8 bar, respectively. The general trends suggests that a reduction in the operating pressure can significantly optimise a membrane's $P^{mix}_{CO_2}$ value for CO_2/CH_4 separations, with little impact to its $S^{mix}_{mem,CO_2/CH_4}$.

5.4 Conclusions

In this study, the multi-stage high-throughput methodology introduced in chapter 4 has been extended to assess the performance of porous COFs for biogas upgrading. A total of 309 COFs from the CoRE-COF database were initially considered which was quickly reduced to 284 after applying a series

of geometric criteria to remove structures with non-accessible surface area and pore diameter smaller than the individual components of biogas. Based on calculations at infinite dilution, a total of 19 hydrophobic COFs are found to exceed the CO_2/CH_4 Robeson upper bound and were considered for a final round of calculations that re-evaluated the separation performance at working conditions of 10 bar and 298 K. These COFs display membrane $P^{mix}_{CO_2}$ between 3.39×10^4 and 3.40×10^5 Barrer, $S^{mix}_{mem,CO_2/CH_4}$ between 0.89 and 5.81, $P^{mix}_{H_2S}$ between 4.99×10^3 and 1.54×10^6 Barrer and $S^{mix}_{mem,H_2S/CH_4}$ between 3.03 and 79.5. Comparison with the MOFs screened at working conditions in chapter 4 indicate that the COFs in this study generally possess higher gas permeabilities but lower membrane selectivities. This due to the larger number of COF structures that possess large pore sizes and weak host-guest interactions which allow each adsorbate to diffuse more rapidly at the expense of the selectivity towards contaminant molecules. Despite the inability of each COF to overcome the 2008 upper bound, there were many candidates that were very close and were therefore identified as the top candidates. These predominantly consist of 2-D materials with eclipsed stacking patterns and robust imine linkages that provide good thermal and chemical stability. Unlike MOF-based membranes, the low densities of these COFs result in higher predicted gravimetric uptakes of contaminant molecules, while their higher average PLD and LCD values result in faster D^{mix}_{self} values up to 10^{-4} cm^2/s. While many of the structure-performance relationships identified in chapter 4 do not generally apply to the top COFs, there are a few structures with narrow pore channels (DMTA-TPB4, CTF-FUM and SIOC-COF-5) that fit the description of these relationships and are able to rival with some of the previously presented literature membranes from table 4.2. The balance of high permeability, low - moderate selectivity and good thermal and chemical stability demonstrates that COF-based membranes may be a viable competitor for biogas upgrading. Finally, a number of MOF- and COF-based membranes were selected to investigate how their membrane separation performance could be optimised by

changing the feed pressure of the biogas mixture. Overall, a number of membranes that fall short of both the 1991 and 2008 Robeson upper bounds were able to exceed both when decreasing the feed pressure to lower values between 0.1 and 1.0 bar. An expanded study with a more diverse set of membrane structural properties would be highly beneficial to improve understanding of the relationships between the changes in membrane separation performance with feed pressure, and the structural properties of the material.

Chapter 6

Summary, conclusions and future outlook

Separation processes play significant roles in many areas of every day life, including carbon capture, petrochemical separation, toxic gas removal, water purification and clean-energy applications.[49–51] Membrane-based separations offer a cheap and efficient process that make use of organic polymers, molecular sieves and other inorganic materials to separate mixture components through differences in their affinity and transport properties. In recent years, novel framework materials such as MOFs and COFs have been intensely studied as they offer a versatile and highly tuneable range of attractive physical and chemical properties. However, their vast chemical space often makes it infeasible to synthesise and test each new material. With the modern advances of technology, computational modelling has become a ubiquitous and powerful tool across material science from structural characterisation to accurate predictions of the adsorption and transport properties of several gases through different porous media. Therefore, the design of high-throughput methodologies which rapidly assess the performance of novel membrane materials is highly desirable for the rapid identification of top-performing materials and their properties that can guide future synthetic progress.

6.1 Overview of chapter 3

The Brunauer-Emmett-Teller (BET) theory of gas adsorption is employed ubiquitously in materials science to calculate the surface area of porous solids. However, this method can largely over-estimate the surface area due pore-filling contamination (PFC). This typically affects structures with varying pore sizes, which adsorb gases at different relative pressures, so that monolayer formation and pore-filling can overlap across the different pores. In chapter 3, two methods were introduced to determine the impact of which PFC has on the BET surface area calculation of nine MOFs. In general, the PFC-corrected surface areas of each material were in much better agreement with the ASA than those calculated from BET theory alone (i.e. no PFC correction). Furthermore, these corrections allow for a fairer comparison of the surface areas of different materials than when using experimental data which may be compromised by PFC and also the crystal quality. In particular, this work demonstrated that replacing phenyl rings with alkynes is a valid approach to increasing the specific surface area of a MOF. However, the relative gain in specific surface area is generally much smaller than predicted from experimental studies.[184]

The short calculation time required to assess PFC makes it possible to analyse thousands of structures in a relatively short time period. In the second-half of chapter 3, 1248 MOFs were used to study the relationships between structure and PFC. Most notably, the results indicated that MOFs with pore diameters greater than 16 Å are generally more susceptible to PFC than those with smaller pore diameters. Furthermore, the BET C parameter can provide an indicator of structures that possess an appreciable overlap of monolayer/multilayer adsorption. Another main observation was that the ASA of most investigated MOFs was generally larger than their PFC-corrected surface areas, as a result of the close-packed monolayer assumption used by BET theory. As such, the packing geometry of the GCMC particles are influenced by their interactions with the surface and each other, leading to non-uniform

packing distributions that may lower the accessibility of the surface to other adsorbates. One of the main suggestions that could improve the agreement between the ASA and PFC-corrected surface areas is the use of a noble gas such as argon instead of N_2 for the BET calculation. Argon may be more beneficial as its atomic nature and absence of a permanent multipole eliminates any orientational effects on the packing. For some systems, the use of pore-blocking methods may be required for regions that are fully accessible under the assumptions of a simulation, but in reality are inaccessible due to the PLD in these materials. This is expected to largely impact materials in which the ASA is smaller than the PFC-corrected surface area.

The methods for correcting PFC that are presented in this chapter could provide the foundations for future studies that improve the accuracy of experimental BET calculations. This could start with the building of a database of porous solids which contains several structural descriptors (pore volume, diameter, topology, e.t.c) and predicted adsorption isotherms. One of the goals of this database may be to train an algorithm to predict the appropriate PFC correction based on these descriptors. In turn this would allow a correction to be estimated for experimental isotherms which would improve the estimate of a structures BET surface area without the need for any GCMC simulations. This of course is dependant on generating a set of highly accurate simulated isotherms and accounting for any errors associated with the experimental crystal sample quality. Studies of a similar concept are already beginning to emerge in the literature[295] and point to a new avenue for rapid and accurate characterisation of structural properties.

6.2 Overview of chapter 4

Biomethane derived from biogas can be used as source for energy storage and transport applications. In recent years, membrane technology has received much attention as a promising alternative to conventional methods of separa-

tion due to its lower costs and high purity yield. However, one of the main challenges of designing new membranes is to identify properties that lead to high selectivity and gas permeability that can compete with traditional polymer membranes used in industry. In chapter 4, a multi-stage high-throughput methodology was designed to identify the most promising porous MOFs for biogas upgrading. In addition to their separation capabilities, the relative levels of hydrophobicity of each candidate were determined to address the stability concerns of some MOFs in the presence of H_2O. The separation performance of the top hydrophobic MOFs was then re-evaluated under working conditions, revealing a total of 8 membranes which possess selectivities and permeabilities rivalling that of top polymer-, zeolite-, ZIF- and MMM- based membranes found in the literature.

With any computational screening like the one presented in this chapter, it is always important to reiterate that they are based on several assumptions and limitations that affect the analysis of the results. As previously discussed in section 4.2.2, one of the main limitations that can affect the reliability of this screening is the use of general force-fields which are unable to correctly describe host-guest interactions in MOFs containing open-metal sites (OMS). In the most recent version of the CoRE MOF database,[85] it was estimated that approximately 34% of structures contain atleast one OMS. As many of the structures in the CoRE MOF database also appear in the CSD, it is clear that there is a large proportion of structures that may be excluded from top-performing candidates with the current methodology. Nevertheless, there are numerous successful screening studies in which the predicted top candidates have been validated with experimental work using similar methodologies to the one in chapter 4.[89,296] In recent years, there has been developments in the generation of new force-fields for MOFs for the prediction of structural and dynamic properties.[297,298] However, it is more difficult and highly expensive to develop transferable force-fields for MOFs that accurately describe host-guest interactions. This is because they often rely on a large number of *ab initio*

calculations which become impractical for studying diverse sets of structures. Furthermore, the transferability of these parameters is often localised to chemically similar systems or adsorbates.[254,299–301] That being said, if the limit of transferability of these parameters is tested across a wide array of systems, it is possible that some of the current parameters could be used to accurately treat collections of challenging systems with similar chemical functionalities within future screening studies.

Another consideration for screening studies of MOF-based membranes is the stability of the identified top candidates. In this work, this was included within a very simple assumption that hydrophobic membranes have good chemical stability with respect to H_2O adsorption. Therefore, these materials were targeted by the screening criteria. For a more rigorous assessment, the mechanical properties of the membrane should also be investigated. In a previous study involving 3385 MOFs and 41 unique topologies, it was shown that parameters such as framework topology and the nature of the building blocks can have significant impact on properties such as the bulk modulus.[302] This is especially important for the processability of MOF-based membranes in order for them to rival polymer materials which currently dominate the commercial market.

Finally, the structure-performance relationships obtained in this study can help experimental synthesis of new membranes by narrowing the chemical search space in which these materials are designed from. In the past few years, machine learning (ML) algorithms have become an integral part of data science for generalising patterns and making predictions across large data sets. By combining geometric descriptors of each investigated MOF with the results calculated in this study, there is the potential to build a training set which can be used by ML algorithms to more accurately define structure-performance relationships or even predict properties, such as adsorbate loadings, heats of adsorption and selectivities for new candidates.[303–307] If the ML model is successful, this could improve the computational cost of screening future candi-

dates as this would remove the time required to fully simulate each of these properties using GCMC and EMD simulations.

6.3 Overview of chapter 5

Due to their low porosities; tuneable pore sizes; and display of excellent thermal and chemical stabilities across a wide range of environments, porous COFs may also be suitable candidates for gas separations such as biogas upgrading. In chapter 5, the previously designed high-throughput methodology from chapter 4 was further extended to assess the separation performance of 309 porous COFs. Unlike MOF membranes, the COFs were found to exhibit higher gas permeabilities but lower membrane selectivities as many of the COF structures possess larger pore sizes than the investigated MOFs in chapter 4. Many of the top COF candidates possess 2-D frameworks with eclipsed stacking patterns and robust imine linkages that provide good thermal and chemical stability. However, none were able to exceed the 2008 upper bound under the current working conditions, leading to the idea that these parameters could be optimised for each structure. Further investigation employing 8 different MOF- and COF-based membranes indicated that a number of membranes that fall short of the 1991 and 2008 Robeson upper bounds are able to exceed both when decreasing the feed pressure to lower values between 0.1 and 1.0 bar. Overall, the balance of high permeability, moderate selectivity and good thermal and chemical stability demonstrates that COF-based membranes may be a viable competitor for biogas upgrading.

In addition to feed pressure, there are a number of other process parameters that could be studied which also affect the separation process. These include permeate pressure, temperature and adsorbate mole fraction in which other trace gases could be included into the mixture to study their behaviour and impact on the separation performance. Additionally, this study assumes that a single separation process takes place whereas in reality, there may be

numerous cycles before a target purity is reached. The current working conditions for biogas separation are likely chosen to balance efficiency and cost when using polymer membranes. Therefore, the benefit of fully investigating each process parameter is that we can develop a better understanding of how they impact the separation performance of new membrane materials, and how they may be optimised for commercial benefit. As such, these investigations should employ a diverse set of membrane structural properties in order to build structure-performance relationships.

For most of these parameters, the current methodology used in chapters 4 and 5 would be sufficient. However, for studying permeate pressure, the current methodology that is based of the work of Krishna *et al*, assumes that the gas loading in the permeate stream is negligible.[93] Consequently, this allows the permeability to be expressed solely in terms of the gas loading at the feed pressure and self-diffusion coefficient of the adsorbate. For permeate pressures that are not under vacuum conditions, a shell model is often employed to approximate the concentration gradient and estimate the state state flux.[60] Unlike the high-throughput method, these simulations require transport diffusion coefficients that are more costly to evaluate from mixture EMD simulations than self-diffusion coefficients. In recent years, non-equilibrium methods have become more viable with developments such as concentration gradient driven molecular dynamics that are able to simulate membrane separations at the microsecond time scale.[308,309] While the application of such methods into high-throughput screenings has yet to be realised, the method demonstrates an alternative approach to studying membrane separations under various different working conditions.

Finally, the work presented in chapters 4 and 5 could be expanded further by evaluating the potential of the top candidates as filler particles in mixed-matrix membranes (MMMs). Over the past decade, MMMs have received a great deal of attention as they combine the ideal processability and mechanical properties of polymers with the high selectivity and good thermal and chemi-

cal stabilities of many porous materials.[310] In a previous study, it was shown that MOFs with high selectivity in their pure form can lead to MMMs with significantly improved separation performance over the pure polymeric membrane.[311] While the moderate selectivity of the top COF candidates in chapter 5 may limit their potential in MMMs, this line of investigation is still beneficial for understanding their influence as MMM components and how they compare to MOF-based MMMs - an area of research that is still developing within the literature.

Appendix A

Chapter 3 Appendix

A.1 Force-field parameters

Table A.1: Force-field parameters used in section 3.2

site	$\sigma(\mathring{A})$	ϵ (K)	q	Force-field
C	3.47	47.86	EQeq scheme	DREIDING
O	3.03	48.19	EQeq scheme	DREIDING
H	2.85	7.65	EQeq scheme	DREIDING
Cu	3.114	2.516	EQeq scheme	UFF
N	3.31	36.00	-0.482	TraPPE
COM	0.0	0.0	0.964	TraPPE

A.2 BET fitting parameters

Table A.2: BET fitting parameters for each investigated MOF from section 3.1

MOF	p/p_0 range	BET C Value	gradient	intercept	R^2
NOTT-101	0.0002 - 0.031	3544	1.59×10^{-3}	4.49×10^{-7}	1.0000
PCN-16	0.0002 - 0.030	4142	1.67×10^{-3}	4.02×10^{-7}	1.0000
NOTT-102	0.00004 - 0.039	1822	1.30×10^{-3}	7.14×10^{-7}	0.9999
PCN-46	0.0002 - 0.039	2500	1.39×10^{-3}	5.56×10^{-7}	0.9999
NOTT-112	0.0002 - 0.039	600	1.08×10^{-3}	1.80×10^{-6}	0.9996
PCN-61	0.0002 - 0.039	682	1.24×10^{-3}	1.82×10^{-6}	0.9999
NOTT-119	0.00004 - 0.099	71	7.13×10^{-4}	1.01×10^{-5}	0.9935
NOTT-116	0.008 - 0.08	144	8.20×10^{-4}	5.72×10^{-6}	0.9991
NU-111	0.019 - 0.08	191	8.25×10^{-4}	4.34×10^{-6}	0.9997

A.3 Method 1 and method 2 monolayer comparison

Table A-3 shows the number of N_2 molecules that form the adsorbed monolayer at $p_{monolayer}$ and p^0, corresponding to results from method 1 and method 2 of the PFC correction schemes in section 3.2. Based on the difference between these values, it is possible to estimate the adsorption cross-sectional area (σ) of the monolayer from method 1 that gives the same surface area as method 2. The values of σ range from 16.5 - 18.1 $\mathring{A}^2$ indicating that the monolayers that form at $p_{monolayer}$ are sparser than the corresponding monolayers that form at p^0 across all investigated MOFs. Therefore, the assumption of a close-packed monolayer from BET theory and the calculation of the SSA become less accurate. These results highlight how each investigated MOF influences the packing of the adsorbed monolayer in different ways and should be treated with care when employing the assumptions of BET theory.

Table A.3: BET fitting parameters for each investigated MOF from section 3.1

MOF	Number of monolayer molecules at $p_{monolayer}$	Number of monolayer molecules at p^0	Difference*	% Difference	Estimated cross-sectional area, σ ($\mathring{A}^2$)*
NOTT-101	499	565	66	11.7	18.1
PCN-16	457	488	31	6.35	17.2
NOTT-102	724	786	62	7.89	17.5
PCN-46	567	600	33	5.5	17.1
NOTT-112	1150	1223	73	5.97	17.2
PCN-61	886	941	55	5.84	17.1
NOTT-119	1746	1777	31	1.74	16.5
NOTT-116	1443	1494	51	3.41	16.8
NU-111	1260	1333	73	5.48	17.1

* - Difference column corresponds to the difference in the number of molecules at $p_{monolayer}$ and p^0; Estimated cross sectional area is the estimated area per molecule required for method 1 surface area to be equal to the method 2 surface area

Appendix B

Chapter 4 Appendix

B.1 UFF parameters, oxidation states and adsorbate force-field parameters

Element	O.S	ε (K)	σ (Å)	Element	O.S	ε (K)	σ (Å)	Element	O.S	ε (K)	σ (Å)	Element	O.S	ε (K)	σ (Å)
Ac	+3	16.6	3.10	Er	+1	3.52	3.02	N	0	34.72	3.26	Si	+4	202.27	3.83
Ag	+1	18.11	2.80	Es	+3	6.04	2.94	Na	+1	15.09	2.66	Sm	+1	3.13596	3.14
Al	+3	254.09	4.01	Eu	+1	4.03	3.11	Nb	+4	29.69	2.82	Sn	+2	285.28	3.91
Am	+3	7.04	3.01	F	0	25.16	3.00	Nd	+1	5.03	3.18	Sr	+2	118.24	3.24
Ar	0	93.08	3.45	Fe	+2	6.54	2.59	Ne	0	21.13	2.66	Ta	0	40.75	2.82
As	+3	155.47	3.77	Ga	+3	208.81	3.90	Ni	+2	7.55	2.52	Tb	+1	3.52	3.07
At	0	142.89	4.23	Gd	+1	4.53	3.00	Np	+4	9.56123	3.05	Tc	+2	24.1547	2.671
Au	+1	19.62	2.93	Ge	+2	190.69	3.81	O	0	30.19	3.12	Te	0	200.25	3.98
B	0	90.57	3.64	H	0	22.14	2.57	Os	0	18.62	2.78	Th	+4	13.08	3.03
Ba	+2	183.15	3.30	He	0	10.9	2.64	P	0	153.46	3.69	Ti	+4	8.55	2.83
Be	+2	42.77	2.45	Hf	+3	36.23	2.8	Pb	+2	333.59	3.83	Tl	+1	342.14	3.87
Bi	+3	260.63	3.89	Hg	+1	193.71	2.41	Pd	+2	24.15	2.58	Tm	+2	3.01934	3.006
Br	0	126.29	3.73	Ho	+1	3.52	3.04	Pm	+1	4.53	3.16	U	+3	11.07	3.02
C	0	52.83	3.43	I	0	170.57	4.01	Pr	+3	5.03	3.21	V	+4	8.05	2.8
Ca	+2	119.75	3.03	In	+3	301.39	3.98	Pt	+1	40.25	2.45	W	0	33.71	2.73
Cd	+2	114.72	2.54	Ir	0	36.73	2.53	Pu	+4	8.05156	3.05	Xe	0	167.04	3.92
Ce	+3	6.54	3.17	K	+1	17.61	3.40	Rb	+1	20.13	3.67	Y	+3	36.23	2.98
Cl	0	114.21	3.52	Kr	0	110.69	3.69	Re	0	33.21	2.63	Yb	+2	114.72	2.99
Cm	+3	6.54	2.96	La	+2	8.55	3.14	Rh	+2	26.67	2.61	Zn	+2	62.39	2.46
Co	+2	7.04	2.56	Li	+1	12.58	2.18	Ru	+2	28.18	2.64	Zr	+4	34.72	2.78
Cr	+3	7.55	2.69	Lu	+1	20.63	3.24	S	0	137.86	3.59				
Cs	+1	22.64	4.02	Mg	+2	55.85	2.69	Sb	+3	225.91	3.94				
Cu	+2	2.52	3.11	Mn	+2	6.54	2.64	Sc	+3	9.56	2.94				
Dy	+1	3.52	3.05	Mo	+4	28.18	2.72	Se	0	146.42	3.75				

Figure B.1: *List of force-field parameters and oxidation states used in simulations across this thesis*

Molecule	Atom	σ (Å)	ε (K)	q
CH_4	CH_4	3.73	148	0.000
CO_2	C	2.80	27.0	+0.700
	O	3.05	79.0	-0.350
H_2S	H	0.00	0.00	+0.250
	S	3.73	250	+0.400
	M	0.00	0.00	-0.900
H_2O	H	0.00	0.00	+0.52422
	O	3.16435	81.8994972	0.000
	M	0.00	0.00	-1.04844

Figure B.2: *List of force-field parameters used for modelling each adsorbate in chapters 4 and 5*

B.2 Experimental membrane conditions

Table B.1: List of experimental conditions used in comparison calculations

MOF	Membrane Thickness (μ m)	Gases	Temp (K)	Pressure (bar)	reference
IRMOF-1	25	CO_2, CH_4	298	1.06	[312]
Ni-MOF-74	25	CO_2, CH_4	298	1.80	[222]
ZIF-8	5	equimolar CO_2/CH_4 mixture	298	1.00	[223]
ZIF-90	20	CO_2, CH_4	473	1.00	[313]
Bio-MOF-1	15	equimolar CO_2/CH_4 mixture	298	1.00	[221]

B.3 Qeq partial charge criteria assessment

In recent work, Ongari and co-workers compared the charges obtained from different QEq variants against DDEC charges for 2338 MOFs.[150] Using data from DDEC charge distributions, they showed that by imposing an upper and lower atomic charge limit of +3 and -2 respectively, fewer structures containing unphysical charges were obtained from using the higher oxidation state Taylor expansion. While this charge criteria worked well for identifying metals with unphysical charges, it failed to identify some ligand atoms that possess unphysical or unrealistic charges (e.g. C charge between +2 and +3). This is shown in the following histograms where the atomic partial charge distributions of the 7779 MOFs were examined:

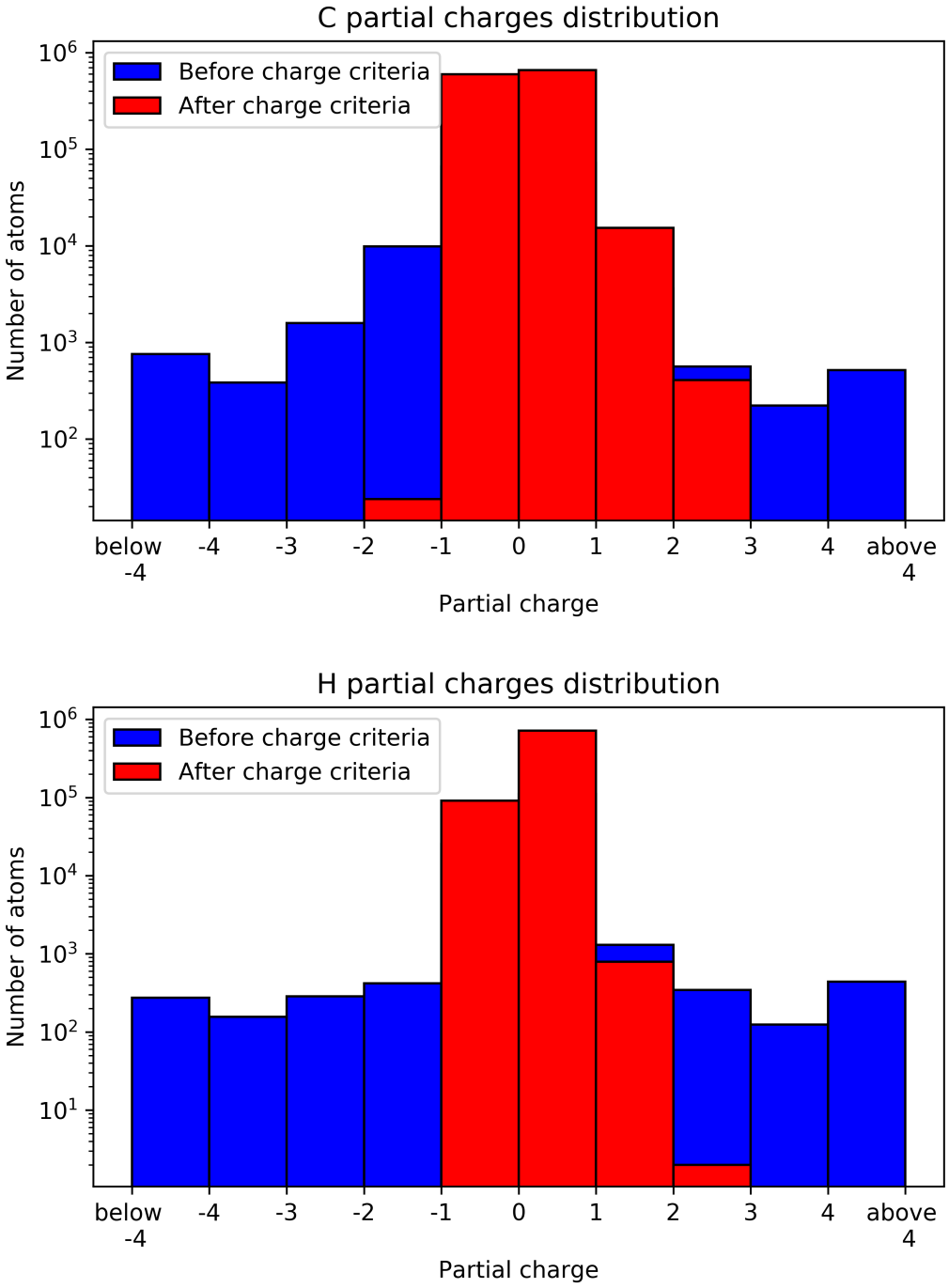


Figure B.3: *Histogram of the partial charge distribution on the C(top) and H(bottom) atoms of 7779 MOFs; Blue = Before applying the criteria of Ongari and co-workers, Red = After applying the criteria of Ongari and co-workers*

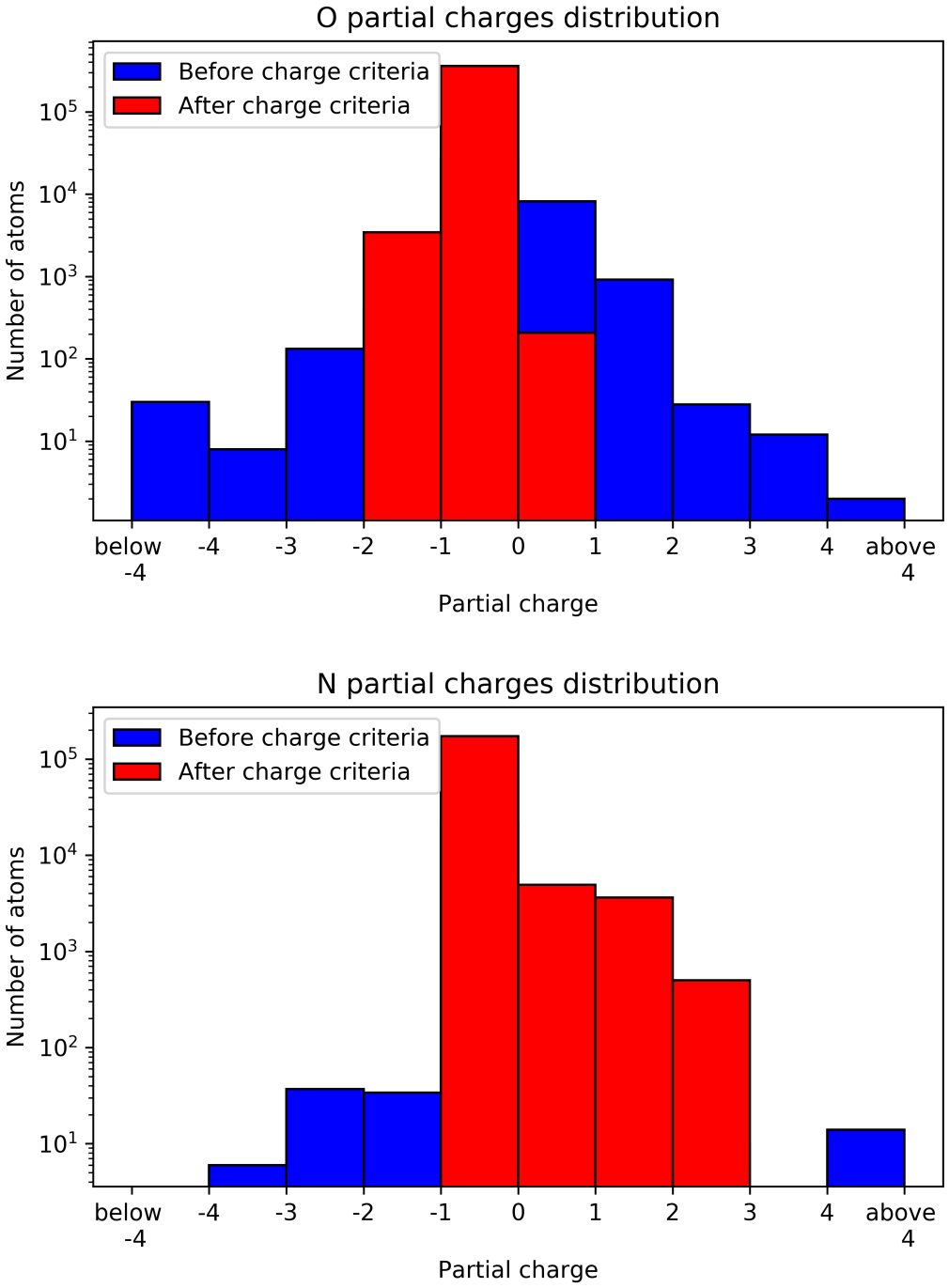


Figure B.4: *Histogram of the partial charge distribution on the O(top) and N(bottom) atoms of 7779 MOFs; Blue = Before applying the criteria of Ongari and co-workers, Red = After applying the criteria of Ongari and co-workers*

B.4 Infinite dilution calculation assessment

Table B.2: A list of the computed "distances" to the 2008 Robeson limit for each membrane studied at working conditions

MOF	Infinite dilution	Working Conditions
NEYBEZ	9.15	-6.03
LACFOM	8.31	-7.57
HISFUM	7.71	5.37
BUXJUB	7.63	-4.63
ARAJEK	7.32	-5.11
KUBJAU	6.48	-3.87
KAXQOR	4.29	-4.22
ISAYUW	4.12	3.72
ARAKAH	3.72	-0.24
SIVWUR	3.39	-9.17
ARAJIO	3.22	-1.17
QUQQEZ	3.17	-2.21
QEDZEG	2.85	-5.36
LIDZOP	2.53	-5.83
LENROM	2.19	2.52
FARZEE	2.08	0.41
TABZON	1.80	-1.23
EWETIL	1.76	-6.50
ETECOW	1.73	-3.58
PAVRIO	1.59	-6.72
KURSOH	1.55	3.69
EJIQIZ	1.39	-4.06
CICYUJ	1.39	-6.75
HEXKEB	1.35	-5.09
SUGWEX01	1.14	-0.80
QOKCID	1.13	6.52
SOMSIY	1.10	0.20
RITDEF	1.09	-4.11
JAQQEA	0.99	-5.31
ECIWOC	0.93	-3.72
JODGAM	0.87	-4.22
LIWPUE	0.79	-4.62
RUVBER	0.72	5.80
PAVLUU	0.60	-1.08

Bibliography

[1] F. Rouquerol, *Adsorption by powders and porous solids : principles, methodology and applications / F. Rouquerol [and four others]*, Kidlington, Oxford : Academic Press, Kidlington, Oxford, 2nd edn., 2014.

[2] M. Králik, *Chemical Papers*, 2014, **68**, 1625–1638.

[3] J. Rouquerol, D. Avnir, C. W. Fairbridge, D. H. Everett, J. H. Haynes, N. Pernicone, J. D. F. Ramsay, K. S. W. Sing and K. K. Unger, *Pure and Applied Chemistry*, 1994, **66**, 1739–1758.

[4] K. S. Sing and R. T. Williams, *Adsorption Science & Technology*, 2004, **22**, 773–782.

[5] M. Thommes, K. Kaneko, A. V. Neimark, J. P. Olivier, F. Rodriguez-Reinoso, J. Rouquerol and K. S. W. Sing, *Pure and Applied Chemistry*, 2015, **87**, 1051–1069.

[6] S. Brunauer and P. H. Emmett, *J. Am. Chem. Soc.*, 1937, **59**, 1553–1564.

[7] A. Nalaparaju, X. S. Zhao and J. W. Jiang, *The Journal of Physical Chemistry C*, 2010, **114**, 11542–11550.

[8] J. Weitkamp, *Solid State Ionics*, 2000, **131**, 175–188.

[9] W. Lowenstein, *Am. Mineral*, 1954, **39**, 92–96.

[10] J. Weitkamp, *Industrial & Engineering Chemistry Product Research and Development*, 1982, **21**, 550–558.

[11] R. Albuquerque and G. Calzaferri, *Chemistry – A European Journal*, 2007, **13**, 8939–8952.

[12] *U.S. Pat, US3702886A*, 1969.

[13] *Ch. Baerlocher and L.B. McCusker, Database of Zeolite Structures:*, http://www.iza-structure.org/databases/, Accessed: 1st May 2020.

[14] H. Furukawa, N. Ko, Y. B. Go, N. Aratani, S. B. Choi, E. Choi, A. z. Yazaydin, R. Q. Snurr, M. O'Keeffe, J. Kim and O. M. Yaghi, *Science*, 2010, **329**, 424–428.

[15] M. Eddaoudi, D. B. Moler, H. Li, B. Chen, T. M. Reineke, M. O'Keeffe and O. M. Yaghi, *Accounts of Chemical Research*, 2001, **34**, 319–330.

[16] H. Li, M. Eddaoudi, M. O'Keeffe and O. M. Yaghi, *Nature*, 1999, **402**, 276–279.

[17] O. M. Yaghi, M. O'Keeffe, N. W. Ockwig, H. K. Chae, M. Eddaoudi and J. Kim, *Nature*, 2003, **423**, 705–714.

[18] X. Lin, I. Telepeni, A. J. Blake, A. Dailly, C. M. Brown, J. M. Simmons, M. Zoppi, G. S. Walker, K. M. Thomas, T. J. Mays, P. Hubberstey, N. R. Champness and M. Schröder, *Journal of the American Chemical Society*, 2009, **131**, 2159–2171.

[19] Z. Wang and S. M. Cohen, *Chemical Society Reviews*, 2009, **38**, 1315–1329.

[20] Z. Yin, S. Wan, J. Yang, M. Kurmoo and M.-H. Zeng, *Coordination Chemistry Reviews*, 2019, **378**, 500–512.

[21] M. Ding, R. W. Flaig, H.-L. Jiang and O. M. Yaghi, *Chem. Soc. Rev.*, 2019, **48**, 2783–2828.

[22] X. Zhao, Y. Wang, D.-S. Li, X. Bu and P. Feng, *Adv. Mater.*, 2018, **30**, 1705189.

[23] S. Rojas, A. Arenas-Vivo and P. Horcajada, *Coord. Chem. Rev.*, 2019, **388**, 202–226.

[24] S. M. J. Rogge, A. Bavykina, J. Hajek, H. Garcia, A. I. Olivos-Suarez, A. Sepúlveda-Escribano, A. Vimont, G. Clet, P. Bazin, F. Kapteijn, M. Daturi, E. V. Ramos-Fernandez, F. X. Llabrés i Xamena, V. Van Speybroeck and J. Gascon, *Chem. Soc. Rev.*, 2017, **46**, 3134–3184.

[25] H. Wang, W. P. Lustig and J. Li, *Chem. Soc. Rev.*, 2018, **47**, 4729–4756.

[26] M. Rubio-Martinez, C. Avci-Camur, A. W. Thornton, I. Imaz, D. Maspoch and M. R. Hill, *Chemical Society Reviews*, 2017, **46**, 3453–3480.

[27] J. E. Mondloch, O. Karagiaridi, O. K. Farha and J. T. Hupp, *CrystEngComm*, 2013, **15**, 9258–9264.

[28] S. S.-Y. Chui, S. M.-F. Lo, J. P. H. Charmant, A. G. Orpen and I. D. Williams, *Science*, 1999, **283**, 1148–1150.

[29] V. K. Peterson, Y. Liu, C. M. Brown and C. J. Kepert, *Journal of the American Chemical Society*, 2006, **128**, 15578–15579.

[30] J. Getzschmann, I. Senkovska, D. Wallacher, M. Tovar, D. Fairen-Jimenez, T. Düren, J. M. van Baten, R. Krishna and S. Kaskel, *Microporous and Mesoporous Materials*, 2010, **136**, 50–58.

[31] L. Grajciar, A. D. Wiersum, P. L. Llewellyn, J.-S. Chang and P. Nachtigall, *The Journal of Physical Chemistry C*, 2011, **115**, 17925–17933.

[32] V. K. Peterson, P. D. Southon, G. J. Halder, D. J. Price, J. J. Bevitt and C. J. Kepert, *Chem. Mater.*, 2014, **26**, 4712–4723.

[33] N. C. Burtch, H. Jasuja and K. S. Walton, *Chemical Reviews*, 2014, **114**, 10575–10612.

[34] J. H. Cavka, S. Jakobsen, U. Olsbye, N. Guillou, C. Lamberti, S. Bordiga and K. P. Lillerud, *Journal of the American Chemical Society*, 2008, **130**, 13850–13851.

[35] Q. Yang, A. D. Wiersum, P. L. Llewellyn, V. Guillerm, C. Serre and G. Maurin, *Chemical Communications*, 2011, **47**, 9603–9605.

[36] S. Horike, S. Shimomura and S. Kitagawa, *Nature Chemistry*, 2009, **1**, 695–704.

[37] K. Uemura, R. Matsuda and S. Kitagawa, *Journal of Solid State Chemistry*, 2005, **178**, 2420–2429.

[38] T. Loiseau, C. Serre, C. Huguenard, G. Fink, F. Taulelle, M. Henry, T. Bataille and G. Férey, *Chemistry – A European Journal*, 2004, **10**, 1373–1382.

[39] R. El Osta, A. Carlin-Sinclair, N. Guillou, R. I. Walton, F. Vermoortele, M. Maes, D. de Vos and F. Millange, *Chem. Mater.*, 2012, **24**, 2781–2791.

[40] A. P. Côté, A. I. Benin, N. W. Ockwig, M. Keeffe, A. J. Matzger and O. M. Yaghi, *Science*, 2005, **310**, 1166.

[41] S.-Y. Ding and W. Wang, *Chemical Society Reviews*, 2013, **42**, 548–568.

[42] Z. Wang, S. Zhang, Y. Chen, Z. Zhang and S. Ma, *Chemical Society Reviews*, 2020, **49**, 708–735.

[43] S. Bi, C. Yang, W. Zhang, J. Xu, L. Liu, D. Wu, X. Wang, Y. Han, Q. Liang and F. Zhang, *Nature Communications*, 2019, **10**, 2467.

[44] X. Feng, X. Ding and D. Jiang, *Chemical Society Reviews*, 2012, **41**, 6010–6022.

[45] L. Zhu and Y.-B. Zhang, *Molecules*, 2017, **22**, 1149.

[46] M. S. Lohse and T. Bein, *Advanced Functional Materials*, 2018, **28**, 1705553.

[47] F. J. Uribe-Romo, J. R. Hunt, H. Furukawa, C. Klöck, M. O'Keeffe and O. M. Yaghi, *Journal of the American Chemical Society*, 2009, **131**, 4570–4571.

[48] X. Ma and T. F. Scott, *Communications Chemistry*, 2018, **1**, 98.

[49] H. Li, K. Wang, Y. Sun, C. T. Lollar, J. Li and H.-C. Zhou, *Materials Today*, 2018, **21**, 108–121.

[50] J.-R. Li, J. Sculley and H.-C. Zhou, *Chemical Reviews*, 2012, **112**, 869–932.

[51] J.-R. Li, R. J. Kuppler and H.-C. Zhou, *Chemical Society Reviews*, 2009, **38**, 1477–1504.

[52] *U.S. Pat, US2944627A*, 1958.

[53] C. A. Grande, *ISRN Chemical Engineering*, 2012, **2012**, 982934.

[54] N. Hedin, L. Andersson, L. Bergström and J. Yan, *Applied Energy*, 2013, **104**, 418–433.

[55] S. P. Nandi and P. L. Walker, *Separation Science*, 1976, **11**, 441–453.

[56] S. Basu, A. L. Khan, A. Cano-Odena, C. Liu and I. F. J. Vankelecom, *Chem. Soc. Rev.*, 2010, **39**, 750–768.

[57] M. Shah, M. C. McCarthy, S. Sachdeva, A. K. Lee and H.-K. Jeong, *Ind. Eng. Chem. Res.*, 2012, **51**, 2179–2199.

[58] L. M. Robeson, *J. Membr. Sci.*, 1991, **62**, 165–185.

[59] L. M. Robeson, *J. Membr. Sci.*, 2008, **320**, 390–400.

[60] E. Adatoz, A. K. Avci and S. Keskin, *Sep. Purif. Technol.*, 2015, **152**, 207–237.

[61] P. S. Goh and A. F. Ismail, *Desalination*, 2018, **434**, 60–80.

[62] J. A. Wesselingh and R. Krishna, *Mass Transfer in Multicomponent Mixtures*, Delft University Press, Delft, The Netherlands, 2000.

[63] A. Fick, *Annalen der Physik*, 1855, **170**, 59–86.

[64] R. Krishna and D. Paschek, *Separation and Purification Technology*, 2000, **21**, 111–136.

[65] A. L. Myers and J. M. Prausnitz, *AIChE Journal*, 1965, **11**, 121–127.

[66] K. S. Walton and D. S. Sholl, *AIChE Journal*, 2015, **61**, 2757–2762.

[67] C. E. Wilmer, O. K. Farha, Y.-S. Bae, J. T. Hupp and R. Q. Snurr, *Energy Environ. Sci.*, 2012, **5**, 9849–9856.

[68] N. S. Bobbitt, J. Chen and R. Q. Snurr, *The Journal of Physical Chemistry C*, 2016, **120**, 27328–27341.

[69] D. Wu, Q. Yang, C. Zhong, D. Liu, H. Huang, W. Zhang and G. Maurin, *Langmuir*, 2012, **28**, 12094–12099.

[70] D. Wu, C. Wang, B. Liu, D. Liu, Q. Yang and C. Zhong, *AIChE Journal*, 2011, **58**, 2078–2084.

[71] D. Dubbeldam, R. Krishna, S. Calero and A. z. Yazaydın, *Angewandte Chemie International Edition*, 2012, **51**, 11867–11871.

[72] M. W. Deem and J. M. Newsam, *Nature*, 1989, **342**, 260–262.

[73] M. W. Deem and J. M. Newsam, *Journal of the American Chemical Society*, 1992, **114**, 7189–7198.

[74] D. J. Earl and M. W. Deem, *Industrial & Engineering Chemistry Research*, 2006, **45**, 5449–5454.

[75] M. W. Deem, R. Pophale, P. A. Cheeseman and D. J. Earl, *The Journal of Physical Chemistry C*, 2009, **113**, 21353–21360.

[76] R. Pophale, P. A. Cheeseman and M. W. Deem, *Physical Chemistry Chemical Physics*, 2011, **13**, 12407–12412.

[77] C. Y., J. Camp, M. Haranczyk, B. J. Sikora, W. Bury, V. Krungleviciute, T. Yildrim, O. K. Farha, D. S. Sholl and R. Q. Snurr, *Chem. Mater.*, 2014, **26**, 6185–6192.

[78] C. E. Wilmer, M. Leaf, C. Y. Lee, O. K. Farha, B. G. Hauser, J. T. Hupp and R. Q. Snurr, *Nature Chemistry*, 2012, **4**, 83–89.

[79] R. L. Martin, L.-C. Lin, K. Jariwala, B. Smit and M. Haranczyk, *The Journal of Physical Chemistry C*, 2013, **117**, 12159–12167.

[80] J. Goldsmith, A. G. Wong-Foy, M. J. Cafarella and D. J. Siegel, *Chemistry of Materials*, 2013, **25**, 3373–3382.

[81] Y. J. Colón and R. Q. Snurr, *Chem. Soc. Rev.*, 2014, **43**, 5735–5749.

[82] D. A. Gómez-Gualdrón, Y. J. Colón, X. Zhang, T. C. Wang, Y.-S. Chen, J. T. Hupp, T. Yildirim, O. K. Farha, J. Zhang and R. Q. Snurr, *Energy & Environmental Science*, 2016, **9**, 3279–3289.

[83] Y. J. Colón, D. A. Gómez-Gualdrón and R. Q. Snurr, *Crystal Growth & Design*, 2017, **17**, 5801–5810.

[84] P. Z. Moghadam, A. Li, S. B. Wiggin, A. Tao, A. G. P. Maloney, P. A. Wood, S. C. Ward and D. Fairen-Jimenez, *Chem. Mater.*, 2017, **29**, 2618–2625.

[85] Y. G. Chung, E. Haldoupis, B. J. Bucior, M. Haranczyk, S. Lee, H. Zhang, K. D. Vogiatzis, M. Milisavljevic, S. Ling, J. S. Camp, B. Slater, J. I. Siepmann, D. S. Sholl and R. Q. Snurr, *Journal of Chemical & Engineering Data*, 2019, **64**, 5985–5998.

[86] R. L. Martin, C. M. Simon, B. Medasani, D. K. Britt, B. Smit and M. Haranczyk, *The Journal of Physical Chemistry C*, 2014, **118**, 23790–23802.

[87] R. Mercado, R.-S. Fu, A. V. Yakutovich, L. Talirz, M. Haranczyk and B. Smit, *Chemistry of Materials*, 2018, **30**, 5069–5086.

[88] T. Yan, Y. Lan, M. Tong and C. Zhong, *ACS Sustainable Chemistry & Engineering*, 2019, **7**, 1220–1227.

[89] P. Z. Moghadam, T. Islamoglu, S. Goswami, J. Exley, M. Fantham, C. F. Kaminski, R. Q. Snurr, O. K. Farha and D. Fairen-Jimenez, *Nature Communications*, 2018, **9**, 1378.

[90] J. K. Schnobrich, O. Lebel, K. A. Cychosz, A. Dailly, A. G. Wong-Foy and A. J. Matzger, *Journal of the American Chemical Society*, 2010, **132**, 13941–13948.

[91] C. E. Wilmer, O. K. Farha, T. Yildirim, I. Eryazici, V. Krungleviciute, A. A. Sarjeant, R. Q. Snurr and J. T. Hupp, *Energy & Environmental Science*, 2013, **6**, 1158–1163.

[92] R. Krishna and J. M. van Baten, *Chemical Engineering Journal*, 2007, **133**, 121–131.

[93] R. Krishna and J. M. van Baten, *J. Membr. Sci*, 2010, **360**, 323–333.

[94] S. Keskin, J. Liu, R. B. Rankin, J. K. Johnson and D. S. Sholl, *Industrial & Engineering Chemistry Research*, 2009, **48**, 2355–2371.

[95] I. Erucar and S. Keskin, *Journal of Membrane Science*, 2016, **514**, 313–321.

[96] Y. Basdogan, K. B. Sezginel and S. Keskin, *Ind. Eng. Chem. Res.*, 2015, **54**, 8479–8491.

[97] Z. Sumer and S. Keskin, *Journal of Nanomaterials*, 2016, **2016**, 12.

[98] Z. Sumer and S. Keskin, *Chemical Engineering Science*, 2017, **164**, 108–121.

[99] Y. Gurdal and S. Keskin, *The Journal of Physical Chemistry C*, 2013, **117**, 5229–5241.

[100] R. Krishna and J. M. van Baten, *Physical Chemistry Chemical Physics*, 2011, **13**, 10593–10616.

[101] C. Altintas and S. Keskin, *Chemical Engineering Science*, 2016, **139**, 49–60.

[102] S. Keskin, *The Journal of Physical Chemistry C*, 2012, **116**, 1772–1779.

[103] E. Atci and S. Keskin, *The Journal of Physical Chemistry C*, 2012, **116**, 15525–15537.

[104] J. Liu, S. Keskin, D. S. Sholl and J. K. Johnson, *The Journal of Physical Chemistry C*, 2011, **115**, 12560–12566.

[105] S. Keskin, *The Journal of Physical Chemistry C*, 2011, **115**, 800–807.

[106] T. N. Ozturk and S. Keskin, *The Journal of Physical Chemistry C*, 2014, **118**, 13988–13997.

[107] M. Tong, Y. Lan, Q. Yang and C. Zhong, *Chemical Engineering Science*, 2017, **168**, 456–464.

[108] E. Haldoupis, S. Nair and D. S. Sholl, *Journal of the American Chemical Society*, 2010, **132**, 7528–7539.

[109] T. Watanabe and D. S. Sholl, *Langmuir*, 2012, **28**, 14114–14128.

[110] D. Frenkel and B. Smit, *Understanding Molecular Simulation*, Academic Press, San Diego, 2nd edn., 2002.

[111] N. Metropolis, A. W. Rosenbluth, M. N. Rosenbluth, A. H. Teller and E. Teller, *The Journal of Chemical Physics*, 1953, **21**, 1087–1092.

[112] M. Mezei, *Mol. Phys.*, 1980, **40**, 901–906.

[113] R. Q. Snurr, A. T. Bell and D. N. Theodorou, *The Journal of Physical Chemistry*, 1993, **97**, 13742–13752.

[114] H. C. Andersen, *J. Chem. Phys*, 1980, **72**, 2384–2393.

[115] H. J. C. Berendsen, J. P. M. Postma, W. F. v. Gunsteren, A. DiNola and J. R. Haak, *The Journal of Chemical Physics*, 1984, **81**, 3684–3690.

[116] S. Nose, *J. Chem. Phys.*, 1984, **81**, 511–519.

[117] W. G. Hoover, *Physical Review A*, 1985, **31**, 1695–1697.

[118] L. Riekert, in *Sorption, Diffusion, and Catalytic Reaction in Zeolites*, ed. D. D. Eley, H. Pines and P. B. Weisz, Academic Press, 1970, vol. 21, pp. 281–322.

[119] V. Gupta, S. S. Nivarthi, A. V. McCormick and H. T. Davis, *Chem. Phys. Lett.*, 1995, **247**, 596–600.

[120] K. Hahn, J. Kärger and V. Kukla, *Physical Review Letters*, 1996, **76**, 2762–2765.

[121] V. Kukla, J. Kornatowski, D. Demuth, I. Girnus, H. Pfeifer, L. V. C. Rees, S. Schunk, K. K. Unger and J. Kärger, *Science*, 1996, **272**, 702–704.

[122] D. S. Sholl and K. A. Fichthorn, *Physical Review Letters*, 1997, **79**, 3569–3572.

[123] D. S. Sholl, *Chem. Phys. Lett.*, 1999, **305**, 269–275.

[124] D. S. Sholl and K. L. Cha, *J. Chem. Phys.*, 2000, **122**, 817–824.

[125] P. H. Nelson and S. M. Auerbach, *The Journal of Chemical Physics*, 1999, **110**, 9235–9243.

[126] D. Dubbeldam and R. Q. Snurr, *Molecular Simulation*, 2007, **33**, 305–325.

[127] A. I. Skoulidas and D. S. Sholl, *The Journal of Physical Chemistry A*, 2003, **107**, 10132–10141.

[128] R. Krishna and L. J. P. van den Broeke, *The Chemical Engineering Journal and the Biochemical Engineering Journal*, 1995, **57**, 155–162.

[129] D. Paschek and R. Krishna, *Langmuir*, 2001, **17**, 247–254.

[130] H. A. Lorentz, *Ann. Phys.*, 1881, **248**, 127–136.

[131] D. Berthelot, *Comptes Rendus Hebdomadaires des Séances de l'Académie des Sciences*, 1898, **126**, 1703–1855.

[132] A. K. Rappe, C. J. Casewit, K. S. Colwell, W. A. Goddard and W. M. Skiff, *J. Am. Chem. Soc.*, 1992, **114**, 10024–10035.

[133] S. L. Mayo, B. D. Olafson and W. A. Goddard, *The Journal of Physical Chemistry*, 1990, **94**, 8897–8909.

[134] W. L. Jorgensen, D. S. Maxwell and J. Tirado-Rives, *Journal of the American Chemical Society*, 1996, **118**, 11225–11236.

[135] J. J. Potoff and J. I. Siepmann, *AIChE J.*, 2001, **47**, 1676–1682.

[136] M. G. Martin and J. I. Siepmann, *J. Phys. Chem. B.*, 1998, **102**, 2569–2577.

[137] P. P. Ewald, *Ann. Phys.*, 1921, **369**, 253–287.

[138] R. S. Mulliken, *The Journal of Chemical Physics*, 1955, **23**, 1833–1840.

[139] P. Löwdin, *The Journal of Chemical Physics*, 1950, **18**, 365–375.

[140] A. E. Reed, R. B. Weinstock and F. Weinhold, *J. Chem. Phys.*, 1985, **83**, 735–746.

[141] R. F. W. Bader, *Acc. Chem. Res.*, 1985, **18**, 9–15.

[142] F. L. Hirshfeld, *Theoretica chimica acta*, 1977, **44**, 129–138.

[143] C. M. Breneman and K. B. Wiberg, *Journal of Computational Chemistry*, 1990, **11**, 361–373.

[144] C. L. Bayly, P. Cieplak, W. Cornell and P. A. Kollman, *J. Phys. Chem.*, 1993, **97**, 10269–10280.

[145] U. C. Singh and P. A. Kollman, *Journal of Computational Chemistry*, 1984, **5**, 129–145.

[146] C. Campañá, B. Mussard and T. K. Woo, *Journal of Chemical Theory and Computation*, 2009, **5**, 2866–2878.

[147] T. A. Manz and D. S. Sholl, *J. Chem. Theory Comput.*, 2010, **6**, 2455–2468.

[148] A. K. Rappe and W. A. Goddard, *J. Phys. Chem.*, 1991, **95**, 3358–3363.

[149] C. E. Wilmer, K. C. Kim and R. Q. Snurr, *J. Phys. Chem. Letters*, 2012, **3**, 2506–2511.

[150] D. Ongari, P. G. Boyd, O. Kadioglu, A. K. Mace, S. Keskin and B. Smit, *J. Chem. Theory Comput.*, 2019, **15**, 382–401.

[151] S. Brunauer, P. H. Emmett and E. Teller, *Journal of the American Chemical Society*, 1938, **60**, 309–319.

[152] I. Langmuir, *J. Am. Chem. Soc.*, 1918, **40**, 1361–1403.

[153] J. Rouquerol, P. Llewellyn and F. Rouquerol, in *Is the bet equation applicable to microporous adsorbents?*, ed. F. R.-R. J. R. P.L. Llewellyn and N. Seaton, Elsevier, 2007, vol. Volume 160, pp. 49–56.

[154] Y. Yan, X. Lin, S. Yang, A. J. Blake, A. Dailly, N. R. Champness, P. Hubberstey and M. Schröder, *Chem. Commun.*, 2009, 1025–1027.

[155] B. Lee and F. M. Richards, *Journal of Molecular Biology*, 1971, **55**, 379–IN4.

[156] A. Shrake and J. A. Rupley, *Journal of Molecular Biology*, 1973, **79**, 351–371.

[157] L. D. Gelb and K. E. Gubbins, *Langmuir*, 1998, **14**, 2097–2111.

[158] S. Brandani, E. Mangano and L. Sarkisov, *Adsorption*, 2016, **22**, 261–276.

[159] A. L. Myers and P. A. Monson, *Langmuir*, 2002, **18**, 10261–10273.

[160] O. Talu and A. L. Myers, *AIChE Journal*, 2001, **47**, 1160–1168.

[161] H. Giesche, *Particle & Particle Systems Characterization*, 2006, **23**, 9–19.

[162] J. Mitchell, J. B. W. Webber and J. H. Strange, *Physics Reports*, 2008, **461**, 1–36.

[163] A. P. Radlinski, M. Mastalerz, A. L. Hinde, M. Hainbuchner, H. Rauch, M. Baron, J. S. Lin, L. Fan and P. Thiyagarajan, *International Journal of Coal Geology*, 2004, **59**, 245–271.

[164] C.-S. Tsao, M.-S. Yu, T.-Y. Chung, H.-C. Wu, C.-Y. Wang, K.-S. Chang and H.-L. Chen, *J. Am. Chem. Soc.*, 2007, **129**, 15997–16004.

[165] L. D. Gelb and K. E. Gubbins, *Langmuir*, 1999, **15**, 305–308.

[166] M. Pinheiro, R. L. Martin, C. H. Rycroft, A. Jones, E. Iglesia and M. Haranczyk, *Journal of Molecular Graphics and Modelling*, 2013, **44**, 208–219.

[167] L. Sarkisov and A. Harrison, *Molecular Simulation*, 2011, **37**, 1248–1257.

[168] J. Hoshen and R. Kopelman, *Physical Review B*, 1976, **14**, 3438–3445.

[169] T. F. Willems, C. H. Rycroft, M. Kazi, J. C. Meza and M. Haranczyk, *Microporous Mesoporous Mater.*, 2012, **149**, 134–141.

[170] J. Kim, B. Chen, T. M. Reineke, H. Li, M. Eddaoudi, D. B. Moler, M. O'Keeffe and O. M. Yaghi, *Journal of the American Chemical Society*, 2001, **123**, 8239–8247.

[171] S. Ma and H.-C. Zhou, *Chemical Communications*, 2010, **46**, 44–53.

[172] Y.-S. Bae and R. Q. Snurr, *Angewandte Chemie International Edition*, 2011, **50**, 11586–11596.

[173] B. Chen, N. W. Ockwig, A. R. Millward, D. S. Contreras and O. M. Yaghi, *Angewandte Chemie*, 2005, **117**, 4823–4827.

[174] W. Zhou, H. Wu and T. Yildirim, *Journal of the American Chemical Society*, 2008, **130**, 15268–15269.

[175] Y.-S. Bae, C. Y. Lee, K. C. Kim, O. K. Farha, P. Nickias, J. T. Hupp, S. T. Nguyen and R. Q. Snurr, *Angewandte Chemie International Edition*, 2012, **51**, 1857–1860.

[176] B. Arstad, H. Fjellvåg, K. O. Kongshaug, O. Swang and R. Blom, *Adsorption*, 2008, **14**, 755–762.

[177] A. Henley, M. J. Lennox, T. L. Easun, F. Moreau, M. Schröder and E. Besley, *The Journal of Physical Chemistry C*, 2016, **120**, 27342–27348.

[178] M. Eddaoudi, J. Kim, N. Rosi, D. Vodak, J. Wachter, M. Keeffe and O. M. Yaghi, *Science*, 2002, **295**, 469.

[179] O. K. Farha, I. Eryazici, N. C. Jeong, B. G. Hauser, C. E. Wilmer, A. A. Sarjeant, R. Q. Snurr, S. T. Nguyen, A. z. Yazaydın and J. T. Hupp, *Journal of the American Chemical Society*, 2012, **134**, 15016–15021.

[180] B. Zheng, R. Yun, J. Bai, Z. Lu, L. Du and Y. Li, *Inorganic Chemistry*, 2013, **52**, 2823–2829.

[181] D. A. Gomez-Gualdron, O. V. Gutov, V. Krungleviciute, B. Borah, J. E. Mondloch, J. T. Hupp, T. Yildirim, O. K. Farha and R. Q. Snurr, *Chemistry of Materials*, 2014, **26**, 5632–5639.

[182] X. Wu, R. Wang, H. Yang, W. Wang, W. Cai and Q. Li, *Journal of Materials Chemistry A*, 2015, **3**, 10724–10729.

[183] X. Wu, L. Li, T. Fang, Y. Wang, W. Cai and Z. Xiang, *Physical Chemistry Chemical Physics*, 2017, **19**, 9261–9269.

[184] O. K. Farha, C. E. Wilmer, I. Eryazici, B. G. Hauser, P. A. Parilla, K. O'Neill, A. A. Sarjeant, S. T. Nguyen, R. Q. Snurr and J. T. Hupp, *Journal of the American Chemical Society*, 2012, **134**, 9860–9863.

[185] Y. Yan, S. Yang, A. J. Blake, W. Lewis, E. Poirier, S. A. Barnett, N. R. Champness and M. Schroder, *Chemical Communications*, 2011, **47**, 9995–9997.

[186] E. Bichoutskaia, M. Suyetin, M. Bound, Y. Yan and M. Schröder, *The Journal of Physical Chemistry C*, 2014, **118**, 15573–15580.

[187] D. Sun, S. Ma, J. M. Simmons, J.-R. Li, D. Yuan and H.-C. Zhou, *Chemical Communications*, 2010, **46**, 1329–1331.

[188] D. Zhao, D. Yuan, A. Yakovenko and H.-C. Zhou, *Chemical Communications*, 2010, **46**, 4196–4198.

[189] K. Sing, *Colloids and Surfaces A: Physicochemical and Engineering Aspects*, 2001, **187–188**, 3–9.

[190] J. L. C. Rowsell and O. M. Yaghi, *Journal of the American Chemical Society*, 2006, **128**, 1304–1315.

[191] K. S. Walton and R. Q. Snurr, *Journal of the American Chemical Society*, 2007, **129**, 8552–8556.

[192] Y.-S. Bae, A. z. Yazaydın and R. Q. Snurr, *Langmuir*, 2010, **26**, 5475–5483.

[193] H. Wang, X. Zeng, W. Wang and D. Cao, *Chemical Engineering Science*, 2015, **135**, 373–380.

[194] D. A. Gómez-Gualdrón, P. Z. Moghadam, J. T. Hupp, O. K. Farha and R. Q. Snurr, *Journal of the American Chemical Society*, 2016, **138**, 215–224.

[195] F.-X. Coudert and A. H. Fuchs, *Coord. Chem. Rev.*, 2016, **307**, 211–236.

[196] M. J. Lennox, M. Bound, A. Henley and E. Besley, *Molecular Simulation*, 2017, **43**, 828–837.

[197] A. Gupta, S. Chempath, M. J. Sanborn, L. A. Clark and R. Q. Snurr, *Molecular Simulation*, 2003, **29**, 29–46.

[198] D.-Y. Peng and D. B. Robinson, *Industrial & Engineering Chemistry Fundamentals*, 1976, **15**, 59–64.

[199] D. Dubbeldam, S. Calero, D. E. Ellis and R. Q. Snurr, *Mol. Simul.*, 2016, **42**, 81–101.

[200] L. Sarkisov, R. Bueno-Perez, M. Sutharson and D. Fairen-Jimenez, *Chem. Mater.*, 2020, **32**, 9849–9867.

[201] A. Fateeva, P. Horcajada, T. Devic, C. Serre, J. Marrot, J.-M. Grenèche, M. Morcrette, J.-M. Tarascon, G. Maurin and G. Férey, *European Journal of Inorganic Chemistry*, 2010, **2010**, 3789–3794.

[202] P. Muller, *CrystEngComm*, 2016, **18**, 8164–8171.

[203] X. Y. Chen, H. Vinh-Thang, A. A. Ramirez, D. Rodrigue and S. Kaliaguine, *RSC Adv.*, 2015, **5**, 24399–24448.

[204] S. Rasi, A. Veijanen and J. Rintala, *Energy*, 2007, **32**, 1375–1380.

[205] M. Harasimowicz, P. Orluk, G. Zakrzewska-Trznadel and A. G. Chmielewski, *J. Hazard. Mater.*, 2007, **144**, 698–702.

[206] P. Gosh, *Wet H2S Cracking*, 2007.

[207] E. Ryckebosch, M. Drouillon and H. Vervaeren, *Biomass Bioenergy*, 2011, **35**, 1633–1645.

[208] D. Ruthven, S. Farooq and K. Knaebel, *Pressure Swing Adsorption*, VCH Publishers, New York, 1994.

[209] A. M. Yousef, W. M. El-Maghlany, Y. A. Eldrainy and A. Attia, *Energy*, 2018, **156**, 328–351.

[210] U. of Vienna, *Biogas to biomethane technology review, Task 3.1.1. Institute of chemical engineering research, Divison thermal process engineering and simulation*, Intelligent energy europe report, 2012.

[211] N. Rangnekar, N. Mittal, B. Elyassi, J. Caro and M. Tsapatsis, *Chem. Soc. Rev.*, 2015, **44**, 7128–7154.

[212] J. Gascon, F. Kapteijn, B. Zornoza, V. Sebastián, C. Casado and J. Coronas, *Chem. Mater.*, 2012, **24**, 2829–2844.

[213] K. Xie, Q. Fu, G. G. Qiao and P. A. Webley, *J. Membr. Sci.*, 2019, **572**, 38–60.

[214] S. R. Venna and M. A. Carreon, *Chem. Eng. Sci.*, 2015, **124**, 3–19.

[215] M. Carta, R. Malpass-Evans, M. Croad, Y. Rogan, J. C. Jansen, P. Bernardo, F. Bazzarelli and N. B. McKeown, *Science*, 2013, **339**, 303–307.

[216] M. Vinoba, M. Bhagiyalakshmi, Y. Alqaheem, A. A. Alomair, A. Pérez and M. S. Rana, *Sep. Purif. Technol.*, 2017, **188**, 431–450.

[217] S. Yuan, L. Feng, K. Wang, J. Pang, M. Bosch, C. Lollar, Y. Sun, J. Qin, X. Yang, P. Zhang, Q. Wang, L. Zou, Y. Zhang, L. Zhang, Y. Fang, J. Li and H.-C. Zhou, *Adv. Mater.*, 2018, **30**, 1704303.

[218] N. Stock and S. Biswas, *Chem. Rev.*, 2012, **112**, 933–969.

[219] S. Qiu, M. Xue and G. Zhu, *Chem. Soc. Rev.*, 2014, **43**, 6116–6140.

[220] H. Guo, G. Zhu, I. J. Hewitt and S. Qiu, *J. Am. Chem. Soc.*, 2009, **131**, 1646–1647.

[221] J. A. Bohrman and M. A. Carreon, *Chem. Commun.*, 2012, **48**, 5130–5132.

[222] D.-J. Lee, Q. Li, H. Kim and K. Lee, *Microporous Mesoporous Mater.*, 2012, **163**, 169–177.

[223] S. R. Venna and M. A. Carreon, *J. Am. Chem. Soc.*, 2010, **132**, 76–78.

[224] A. Huang, Q. Liu, N. Wang and J. Caro, *Microporous Mesoporous Mater.*, 2014, **192**, 18–22.

[225] Y. Liu, G. Zeng, Y. Pan and Z. Lai, *J. Membr. Sci.*, 2011, **379**, 46–51.

[226] A. Huang, Y. Chen, N. Wang, Z. Hu, J. Jiang and J. Caro, *Chem. Commun.*, 2012, **48**, 10981–10983.

[227] D. Bastani, N. Esmaeili and M. Asadollahi, *J. Ind. Eng. Chem.*, 2013, **19**, 375–393.

[228] G. Liu, V. Chernikova, Y. Liu, K. Zhang, Y. Belmabkhout, O. Shekhah, C. Zhang, S. Yi, M. Eddaoudi and W. J. Koros, *Nat. Mater.*, 2018, **17**, 283–289.

[229] H. B. Tanh Jeazet, S. Sorribas, J. M. Román-Marín, B. Zornoza, C. Téllez, J. Coronas and C. Janiak, *Eur. J. Inorg. Chem.*, 2016, **2016**, 4363–4367.

[230] M. R. Khdhayyer, E. Esposito, A. Fuoco, M. Monteleone, L. Giorno, J. C. Jansen, M. P. Attfield and P. M. Budd, *Sep. Purif. Technol.*, 2017, **173**, 304–313.

[231] S. Basu, A. Cano-Odena and I. F. J. Vankelecom, *Sep. Purif. Technol.*, 2011, **81**, 31–40.

[232] G. Dong, H. Li and V. Chen, *J. Mater. Chem. A*, 2013, **1**, 4610–4630.

[233] Z. Qiao, K. Zhang and J. Jiang, *J. Mater. Chem. A*, 2016, **4**, 2105–2114.

[234] Z. Li, G. Xiao, Q. Yang, Y. Xiao and C. Zhong, *Chem. Eng. Sci.*, 2014, **120**, 59–66.

[235] E. Haldoupis, S. Nair and D. S. Sholl, *J. Am. Chem. Soc.*, 2012, **134**, 4313–4323.

[236] I. Erucar and S. Keskin, *Ind. Eng. Chem. Res.*, 2011, **50**, 12606–12616.

[237] Z. Qiao, C. Peng, J. Zhou and J. Jiang, *J. Mater. Chem. A*, 2016, **4**, 15904–15912.

[238] C. Altintas and S. Keskin, *ACS Sustainable Chem. Eng.*, 2019, **7**, 2739–2750.

[239] C. Wang, X. Liu, N. Keser Demir, J. P. Chen and K. Li, *Chem. Soc. Rev.*, 2016, **45**, 5107–5134.

[240] H. Daglar and S. Keskin, *J. Phys. Chem. C.*, 2018, **122**, 17347–17357.

[241] Z. Qiao, Q. Xu and J. Jiang, *J. Mater. Chem. A*, 2018, **6**, 18898–18905.

[242] P. Z. Moghadam, D. Fairen-Jimenez and R. Q. Snurr, *J. Mater. Chem. A*, 2016, **4**, 529–536.

[243] S. Plimpton, *J. Comp. Phys.*, 1995, **117**, 1–19.

[244] H. W. Horn, W. C. Swope, J. W. Pitera, J. D. Madura, T. J. Dick, G. L. Hura and T. Head-Gordon, *J. Chem. Phys.*, 2004, **120**, 9665–9678.

[245] T. Kristóf and J. Liszi, *J. Phys. Chem. B.*, 1997, **101**, 5480–5483.

[246] J. Yu, L.-H. Xie, J.-R. Li, Y. Ma, J. M. Seminario and P. B. Balbuena, *Chem. Rev.*, 2017, **117**, 9674–9754.

[247] R. B. Getman, Y.-S. Bae, C. E. Wilmer and R. Q. Snurr, *Chem. Rev.*, 2012, **112**, 703–723.

[248] C. Altintas, G. Avci, H. Daglar, E. Gulcay, I. Erucar and S. Keskin, *J. Mater. Chem. A*, 2018, **6**, 5836–5847.

[249] G. Avci, S. Velioglu and S. Keskin, *ACS Appl. Mater. Interfaces*, 2018, **10**, 33693–33706.

[250] L. Hamon, C. Serre, T. Devic, T. Loiseau, F. Millange, G. Férey and G. D. Weireld, *J. Am. Chem. Soc.*, 2009, **131**, 8775–8777.

[251] Q. Yang, S. Vaesen, M. Vishnuvarthan, F. Ragon, C. Serre, A. Vimont, M. Daturi, G. De Weireld and G. Maurin, *J. Mater. Chem.*, 2012, **22**, 10210–10220.

[252] M. S. Shah, M. Tsapatsis and J. I. Siepmann, *Chem. Rev.*, 2017, **117**, 9755–9803.

[253] L. Chen, C. A. Morrison and T. Düren, *J. Phys. Chem. C.*, 2012, **116**, 18899–18909.

[254] M. Fischer, J. R. B. Gomes and M. Jorge, *Mol. Simul.*, 2014, **40**, 537–556.

[255] C. Zhang, L. Wang, G. Maurin and Q. Yang, *AIChE J.*, 2018, **64**, 4089–4096.

[256] A. R. Kulkarni and D. S. Sholl, *J. Phys. Chem. C.*, 2016, **120**, 23044–23054.

[257] G. Bussi and M. Parrinello, *Computer Physics Communications*, 2008, **179**, 26–29.

[258] J. Basconi and M. Shirts, *J. Chem. Theory. Comput.*, 2013, **9**, 2887–2899.

[259] B. Dunweg and K. Kremer, *J. Chem. Phys.*, 1993, **99**, 6983 – 6997.

[260] C. Altintas and S. Keskin, *Mol. Syst. Des. Eng.*, 2020, **5**, 532–543.

[261] Y.-B. Dong, M. D. Smith, R. C. Layland and H.-C. zur Loye, *Chem. Mater.*, 2000, **12**, 1156–1161.

[262] M. Vougo-Zanda, J. Huang, E. Anokhina, X. Wang and A. J. Jacobson, *Inorg. Chem.*, 2008, **47**, 11535–11542.

[263] J. P. S. Mowat, J. A. Groves, M. T. Wharmby, S. R. Miller, Y. Li, P. Lightfoot and P. A. Wright, *J. Solid State Chem.*, 2009, **182**, 2769–2778.

[264] J. H. Park, W. R. Lee, Y. Kim, H. J. Lee, D. W. Ryu, W. J. Phang and C. S. Hong, *Cryst. Growth Des.*, 2014, **14**, 699–704.

[265] A. Aijaz, E. Barea and P. K. Bharadwaj, *Cryst. Growth Des.*, 2009, **9**, 4480–4486.

[266] J. C. Poshusta, R. D. Noble and J. L. Falconer, *J. Membr. Sci.*, 1999, **160**, 115–125.

[267] S. Takamizawa, Y. Takasaki and R. Miyake, *J. Am. Chem. Soc.*, 2010, **132**, 2862–2863.

[268] M. A. Carreon, S. Li, J. L. Falconer and R. D. Noble, *J. Am. Chem. Soc.*, 2008, **130**, 5412–5413.

[269] H. Shi, *New J. Chem.*, 2014, **38**, 5276–5278.

[270] Q. Song, S. K. Nataraj, M. V. Roussenova, J. C. Tan, D. J. Hughes, W. Li, P. Bourgoin, M. A. Alam, A. K. Cheetham, S. A. Al-Muhtaseb and E. Sivaniah, *Energy Environ. Sci.*, 2012, **5**, 8359–8369.

[271] G. Sodeifian, M. Raji, M. Asghari, M. Rezakazemi and A. Dashti, *Chin. J. Chem. Eng.*, 2019, **27**, 322–334.

[272] N. Habib, Z. Shamair, N. Tara, A.-S. Nizami, F. H. Akhtar, N. M. Ahmad, M. A. Gilani, M. R. Bilad and A. L. Khan, *Sep. Purif. Technol.*, 2020, **234**, 116101.

[273] J. Sánchez-Laínez, A. Pardillos-Ruiz, M. Carta, R. Malpass-Evans, N. B. McKeown, C. Téllez and J. Coronas, *Sep. Purif. Technol.*, 2019, **224**, 456–462.

[274] X. Guo, H. Huang, Y. Ban, Q. Yang, Y. Xiao, Y. Li, W. Yang and C. Zhong, *J. Membr. Sci.*, 2015, **478**, 130–139.

[275] X. Liu, D. Huang, C. Lai, G. Zeng, L. Qin, H. Wang, H. Yi, B. Li, S. Liu, M. Zhang, R. Deng, Y. Fu, L. Li, W. Xue and S. Chen, *Chemical Society Reviews*, 2019, **48**, 5266–5302.

[276] P. J. Waller, F. Gándara and O. M. Yaghi, *Accounts of Chemical Research*, 2015, **48**, 3053–3063.

[277] X.-H. Liu, C.-Z. Guan, S.-Y. Ding, W. Wang, H.-J. Yan, D. Wang and L.-J. Wan, *Journal of the American Chemical Society*, 2013, **135**, 10470–10474.

[278] G. Li, K. Zhang and T. Tsuru, *ACS Applied Materials & Interfaces*, 2017, **9**, 8433–8436.

[279] Y. Ying, D. Liu, J. Ma, M. Tong, W. Zhang, H. Huang, Q. Yang and C. Zhong, *Journal of Materials Chemistry A*, 2016, **4**, 13444–13449.

[280] Z. Kang, Y. Peng, Y. Qian, D. Yuan, M. A. Addicoat, T. Heine, Z. Hu, L. Tee, Z. Guo and D. Zhao, *Chemistry of Materials*, 2016, **28**, 1277–1285.

[281] M. Shan, B. Seoane, E. Rozhko, A. Dikhtiarenko, G. Clet, F. Kapteijn and J. Gascon, *Chemistry – A European Journal*, 2016, **22**, 14467–14470.

[282] O. F. Altundal, C. Altintas and S. Keskin, *Journal of Materials Chemistry A*, 2020, **8**, 14609–14623.

[283] H. Li, H. Li, Q. Dai, H. Li and J.-L. Brédas, *Advanced Theory and Simulations*, 2018, **1**, 1700015.

[284] W. Niu, C. O'Sullivan, B. M. Rambo, M. D. Smith and J. J. Lavigne, *Chemical Communications*, 2005, 4342–4344.

[285] S. Zhao, B. Dong, R. Ge, C. Wang, X. Song, W. Ma, Y. Wang, C. Hao, X. Guo and Y. Gao, *RSC Advances*, 2016, **6**, 38774–38781.

[286] H. Yang, Y. Du, S. Wan, G. D. Trahan, Y. Jin and W. Zhang, *Chemical Science*, 2015, **6**, 4049–4053.

[287] D. Beaudoin, T. Maris and J. D. Wuest, *Nature Chemistry*, 2013, **5**, 830–834.

[288] J. L. Segura, M. J. Mancheño and F. Zamora, *Chemical Society Reviews*, 2016, **45**, 5635–5671.

[289] J. Zhang, X. Han, X. Wu, Y. Liu and Y. Cui, *Journal of the American Chemical Society*, 2017, **139**, 8277–8285.

[290] S. He, Q. Rong, H. Niu and Y. Cai, *Chemical Communications*, 2017, **53**, 9636–9639.

[291] F. Xu, H. Xu, X. Chen, D. Wu, Y. Wu, H. Liu, C. Gu, R. Fu and D. Jiang, *Angewandte Chemie International Edition*, 2015, **54**, 6814–6818.

[292] K.-J. Chen, D. G. Madden, T. Pham, K. A. Forrest, A. Kumar, Q.-Y. Yang, W. Xue, B. Space, J. J. Perry IV, J.-P. Zhang, X.-M. Chen and M. J. Zaworotko, *Angewandte Chemie International Edition*, 2016, **55**, 10268–10272.

[293] K. Huang, Z. Xu, Y. Li and H. Zheng, *Crystal Growth & Design*, 2007, **7**, 202–204.

[294] M. Du, Y.-M. Guo, S.-T. Chen, X.-H. Bu, S. R. Batten, J. Ribas and S. Kitagawa, *Inorg. Chem.*, 2004, **43**, 1287–1293.

[295] A. Datar, Y. G. Chung and L.-C. Lin, *J. Phys. Chem. Lett.*, 2020, **11**, 5412–5417.

[296] Z. Chen, P. Li, R. Anderson, X. Wang, X. Zhang, L. Robison, L. R. Redfern, S. Moribe, T. Islamoglu, D. A. Gómez-Gualdrón, T. Yildirim, J. F. Stoddart and O. K. Farha, *Science*, 2020, **368**, 297–303.

[297] D. E. Coupry, M. A. Addicoat and T. Heine, *Journal of Chemical Theory and Computation*, 2016, **12**, 5215–5225.

[298] S. Bureekaew, S. Amirjalayer, M. Tafipolsky, C. Spickermann, T. K. Roy and R. Schmid, *physica status solidi (b)*, 2013, **250**, 1128–1141.

[299] C. Campbell, C. A. Ferreiro-Rangel, M. Fischer, J. R. B. Gomes and M. Jorge, *The Journal of Physical Chemistry C*, 2017, **121**, 441–458.

[300] C. Campbell, J. R. B. Gomes, M. Fischer and M. Jorge, *The Journal of Physical Chemistry Letters*, 2018, **9**, 3544–3553.

[301] H. Fang, H. Demir, P. Kamakoti and D. S. Sholl, *J. Mater. Chem. A*, 2014, **2**, 274–291.

[302] P. Z. Moghadam, S. M. Rogge, A. Li, C.-M. Chow, J. Wieme, N. Moharrami, M. Aragones-Anglada, G. Conduit, D. A. Gomez-Gualdron, V. Van Speybroeck and D. Fairen-Jimenez, *Matter*, 2019, **1**, 219 – 234.

[303] C. M. Simon, R. Mercado, S. K. Schnell, B. Smit and M. Haranczyk, *Chemistry of Materials*, 2015, **27**, 4459–4475.

[304] G. S. Fanourgakis, K. Gkagkas, E. Tylianakis, E. Klontzas and G. Froudakis, *The Journal of Physical Chemistry A*, 2019, **123**, 6080–6087.

[305] Y. Wu, H. Duan and H. Xi, *Chemistry of Materials*, 2020, **32**, 2986–2997.

[306] F. Gharagheizi, D. Tang and D. S. Sholl, *The Journal of Physical Chemistry C*, 2020, **124**, 3664–3670.

[307] J. Burner, L. Schwiedrzik, M. Krykunov, J. Luo, P. G. Boyd and T. K. Woo, *The Journal of Physical Chemistry C*, 2020, **124**, 27996–28005.

[308] A. Ozcan, C. Perego, M. Salvalaglio, M. Parrinello and O. Yazaydin, *Chem. Sci.*, 2017, **8**, 3858–3865.

[309] A. Ozcan, R. Semino, G. Maurin and A. O. Yazaydin, *Chemistry of Materials*, 2020, **32**, 1288–1296.

[310] T.-S. Chung, L. Y. Jiang, Y. Li and S. Kulprathipanja, *Progress in Polymer Science*, 2007, **32**, 483 – 507.

[311] S.-S. Chen, M. Chen, S. Takamizawa, M.-S. Chen, Z. Su and W.-Y. Sun, *Chem. Commun.*, 2011, **47**, 752–754.

[312] Y. Liu, Z. Ng, E. A. Khan, C.-B. Jeong H-K, Chung and Z. Lai, *Micropor. Mesopor. Mater.*, 2008, **118**, 296–301.

[313] A. Huang, W. Dou and C. Jurgen, *J. Am. Chem. Soc*, 2010, **132**, 15562–15564.